

DATENAKQUISITIONSENTWICKLUNG
UND UNTERGRUNDSTUDIEN FÜR DEN
WELTRAUMDETEKTOR AMS-02 UND
DEN CMOS-DETEKTOR MIMOSA-V

Mike Schmanau

Zur Erlangung des akademischen Grades eines
DOKTORS DER NATURWISSENSCHAFTEN
von der Fakultät für Physik der Universität (TH)
Karlsruhe

genehmigte

DISSERTATION

von

Dipl.-Phys. Mike Schmanau
aus Hemer

Tag der mündlichen Prüfung: 28.11.2008

Referent: Prof. Dr. Wim de Boer, Institut für Experimentelle Kernphysik

Korreferent: Prof. Dr. Thomas Müller, Institut für Experimentelle Kernphysik

Dissertation

**Data acquisition development
and background studies for
the space borne detector AMS-02 and
the CMOS detector MIMOSA-V**

Mike Schmanau

28.11.2008

Prof. Dr. Wim de Boer

Prof. Dr. Thomas Müller

to my wife, my family and my friends

*I like to thank you for the understanding considerateness during
the preparation of this thesis and hope you gain insight to
my time consuming work!*

Contents

1	Introduction	1
2	Physical interactions processes for particle detection	5
2.1	Charged particle detection	5
2.1.1	Energy losses by Ionization	5
2.1.2	Energy losses by Ionization in thin media	6
2.1.3	Bremsstrahlung	7
2.1.4	Multiple scattering	7
2.1.5	Pair annihilation	7
2.1.6	Cherenkov Radiation	8
2.1.7	Transition Radiation	8
2.2	Photon detection	11
2.2.1	Photoelectric Effect	11
2.2.2	Pair Production	12
2.2.3	Compton Scattering	12
3	The AMS-02 Detector on the International Space Station	15
3.1	Physical motivations for AMS-02	16
3.1.1	Search for antimatter	16
3.1.2	The age of cosmic rays and the density of the interstellar material	17
3.1.3	Indirect search for dark matter	18
3.2	Subdetectors of AMS-02	22
3.2.1	Time of flight detector (TOF)	22
3.2.2	Anti Coincidence Counter (ACC)	24
3.2.3	Transition Radiation Detector (TRD)	24
3.2.4	Silicon Tracker System (Tracker)	27
3.2.5	Ring Imaging Cherenkov Detector (RICH)	31
3.2.6	Electromagnetic Calorimeter (ECAL)	32
3.2.7	AMICA Star Tracker and GPS System	35
4	The AMS-02 TRD data acquisition electronics	37
4.1	The AMS-02 DAQ-system	37
4.1.1	Interfaces to the International Space Station	38
4.1.2	DAQ electronics communication (AMSWire/Can-/LeCroy-bus)	39
4.1.3	Common parts of the DAQ electronics (CDP/CDDC)	40
4.2	The TRD DAQ-system design and development	42
4.2.1	TRD front-end electronics (UFE/UTE/UHVD)	43
4.2.2	TRD DAQ and supply electronics (U-Crate)	44
4.2.3	Power distribution box (UPD)	49
4.3	The TRD electronics qualification and acceptance tests	57

4.3.1	Environmental Stress Screening (ESS)	58
4.3.2	Thermo Vacuum Test (TVT)	60
4.3.3	Test devices	61
4.3.4	TRD Test Environment	67
4.3.5	Performed test procedures	70
4.3.6	Results of the QM2 U-Crate and UPD S9011AU board level tests	73
4.3.7	Results of the QM1/2 and FM/FS UPD board-level tests	74
5	The AMS-02 TRD Monte-Carlo simulation	77
5.1	Beamtests with the TRD prototype	78
5.1.1	Beam test setup	78
5.1.2	The TRD prototype	80
5.1.3	Raw data analysis of the X7 beamtest	81
5.2	Rejection power analysis	82
5.2.1	Likelihood method	83
5.2.2	Cluster counting method	84
5.2.3	Rejection power mismatch between data and GEANT3	84
5.3	Diffractive background cross section in the TRD	86
5.4	GEANT4 simulation of the prototype beamtest	89
5.4.1	Beam profile adjustment	90
5.4.2	Simulation of gas-ionization	91
5.4.3	Simulation of transition radiation (TR)	93
5.4.4	Hadronic physics approaches in GEANT4	95
5.5	Analysis of data and simulations	97
5.5.1	Readout system parametrization for the simulations	97
5.5.2	Track-reconstruction and event selection cuts	97
5.5.3	Rejection power comparison between data and simulations	98
5.6	PYTHIA study of a possible TRD background	102
5.6.1	Generation of a prototype hit pattern	102
5.6.2	Background extraction from the prototype hit pattern	103
5.7	Conclusion of the GEANT4 and PYTHIA background simulation	106
6	The Mimosa-V Detector for the REGINS imaging project	107
6.1	CMOS pixel sensors as particle detector	107
6.1.1	The MIMOSA-V sensor	109
6.1.2	The back-thinned MIMOSA-V sensor	110
6.2	Radiation Damage in Silicon Sensors	112
6.2.1	Bulk Damage	112
6.2.2	Surface damage	112
7	The Mimosa-V longterm Data Acquisition	115
7.1	SUCIMA Data Acquisition System	115
7.1.1	The Data Acquisition Board "SUCIMA Imager"	115
7.1.2	The repeater and the hybrid	117
7.2	The MIMOSA-V DAQ software for realtime sparsification	118
7.2.1	Software settings inside "Set Parameters"	119
7.2.2	Initialization and raw data processing	120
7.2.3	Sophisticated LabView algorithms	121

8	The Mimosa V back-thinned for microarray imaging	125
8.1	Imaging constraints for ^{14}C and ^3H spectra	126
8.2	Imaging constraints for microarrays	127
8.3	Images of ^{14}C and ^3H standards for different activities	128
8.4	Differential imaging of nCi probes	130
8.5	Sensor resolution vs. object distance	132
9	Summary	135
A	Measured inclusive cross sections of $pp \rightarrow pX$ and $pA \rightarrow pX$	139
B	Parameters of the TRD prototype simulation	141
C	Additional comparison plots between data and simulations of the TRD prototype beamtest.	145
C.1	Proton beam profiles inside the TRD prototype	146
C.2	Plots for a detector gas density of 4.72 mg/cm^3	148
C.2.1	Accumulated proton energy depositions in the TRD prototype	148
C.2.2	Mop values of the accumulated proton layer distributions	151
C.2.3	Likelihood distributions	153
C.3	Plots for a detector gas density of 4.78 mg/cm^3	155
C.3.1	Accumulated proton energy depositions in the TRD prototype	155
C.3.2	Mop values of the accumulated proton layer distributions	158
C.3.3	Likelihood distributions	160
	Acknowledgements	163
	List of Figures	165
	Bibliography	175

Chapter 1

Introduction

This thesis deals with the development of particle detectors as well as the analysis of their responses and simulations of physical interactions inside of them. The covered detector designs reach from a large scale multi purpose detector with several sub-detectors for cosmic particle research to a small single type detector for microscopic imaging of molecules.

Since the discovery of cosmic rays by Victor Hess in 1912, physicists all over the world were interested in the origin of these particle and studied their nature with earthbound and airborne experiments. It was evident from the beginning, that access to the primary particles is only possible in the upper atmosphere or above. Already Victor Hess measured a first shrinking and suddenly rising ionization rate, while ballooning to higher and higher altitudes equipped with three Wulf electrometers. An effect nowadays known as resulting from interactions of galactic and intergalactic cosmic rays showering off in the earth atmosphere. These secondary particle showers can be measured with large ground detector arrays, as for example done by the KASKADE or the AUGER experiment. Due to large fluctuations, this detection principle has the disadvantage of a poor energy resolution for the primary particle and large uncertainties in their identification.

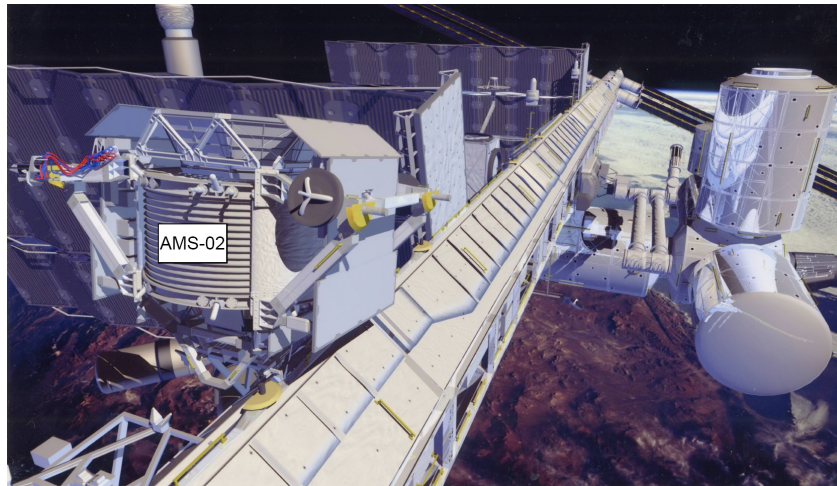


Figure 1.1: A drawing of the AMS-02 experiment mounted to the International Space Station (ISS) (by Lockheed Martin).

In contrast airborne experiments such as the Alpha Magnetic Spectrometer-02 (AMS-02) detector, discussed in this thesis, measure the composition and energy spectra of primary cosmic

rays in an energy range of 300 MeV to 3 TeV with much higher precision. The AMS-02 experiment will be mounted to the International Space Station (ISS), as shown in Fig 1.1. After its launch with the Space Shuttle AMS-02 will take data within a 3 years lasting mission. The collected high precision data will allow to refine the existing models of the acceleration and propagation of cosmic rays and will include signatures of eventually existing antimatter domains. With its modular design AMS-02 will measure lepton, hadron, gamma ray and nuclei spectra. Especially the first three types of spectra will confirm or rule out certain theoretical models about the nature of Dark Matter, known to exist in galaxies and making up about 80% of the mass of the universe. Compared to the LHC detectors at CERN the AMS-02 experiment is rather small, but has more subdetectors than any detector built so far. Moreover it will host the first large superconducting magnet in space, which is of special interest for the NASA, since such magnets may act as active radiation shield of crew compartments in future manned space missions to Mars. All detector components must be able to withstand the enormous vibration stress during the launch, but also the temperature cycles and the vacuum. Therefore, critical parts of AMS-02 have to be well protected and provided with redundancy, as no maintenance is possible during the lifetime of the experiment.

Chapter 3-5 of this thesis concentrate on the development of space-qualified readout electronics for the Transition Radiation Detector (TRD) of AMS-02 as well as on the necessary algorithms for the data analysis and simulation of this detector part. The Institut für Experimentelle Kernphysik at the University of Karlsruhe (TH) is responsible for the TRD electronics and actively involved in the design, qualification and production process since the engineering phase. During the engineering phase of the TRD in 2000 a beamtest was performed with a TRD prototype of the final design. By comparing analyzed beamtest data with a detector simulation, a not understood deviation was found. This motivated another iteration of the analysis and a comparison to a new simulation based on GEANT4, a simulation framework commonly used by today's HEP experiments. To obtain a deeper understanding of interactions inside the TRD, additional single process events generated by a HEP event generator were analyzed.

The development of a large scale detector for space is time consuming, because many production cycles and tests are necessary to achieve space qualification. Since all tests need to be done in specialized laboratories, the test periods depend on the available time slots for the facilities and large time gaps are unavoidable. This time was used to develop test equipment and to perform the mentioned data and simulation analysis.

Before the final TRD electronics acceptance test, the interims were used to participate in the development of an autoradiography device to detect radioactively labeled proteins on microarrays. This research topic was funded by the European Community inside the REGINS¹ project. The project used a back-thinned MIMOSA-V² detector for the imaging, a CMOS pixel array originally developed by the SUCIMA³ collaboration.

Today biochemistry is a strongly funded area of research. It helps to detect and defeat disease and further opens the opportunity to modify food products making grains growing in deserts possible or allows to lower temperature levels for chemical reaction by enzymatic catalyzers as used in washing powders. Since the development of DNA-microarrays by Stephen P. A. Fodor

¹REGINS, Regional standardised interface for a better integration of SMEs in the European economy (SME, small and medium-sized enterprises).

²MIMOSA, Minimum Ionizing particle MOS Active pixel sensor

³SUCIMA, Silicon Ultra fast Cameras for electron and gamma sources in Medical Applications, A project supported by the European Commission

in 1980, the analysis of DNA fragments and proteins can be often carried out automatically. For example microarrays allow to analyze 100.000 known genes inside probes of patient tissues. Protein-microarrays are more complicated to realize than for DNA ones, because the chemical activity of proteins as ligands depends on their folding and this is easily destroyed by irradiation (e.g. X-rays) or chemical labeling.

The contribution to the REGINS project, presented in chapter 6-8, was mainly related to the implementation of a fast data acquisition and sparsification software as an essential ingredient for the data handling. The experience gained from the development of a software for the TRD electronics test and the beamtest analysis software could be directly used for this project. Chapter 8 also includes some minor off-line data analysis of the recorded data, especially to show the performance of the used detector.

Chapter 2

Physical interactions processes for particle detection

Particle physics experiments measure particle observable by detecting small or total losses of their energy in materials. This chapter describes the physical process necessary to understand the principles of all different kinds of particle detectors used in this thesis.

2.1 Charged particle detection

When charged particles enter a detector material they suffer an energy loss by generating charges due to ionization, photons due to Bremsstrahlung, Cherenkov Radiation or Transition Radiation, or nuclear recoils. In general the losses are kept small by design. Only calorimetric detectors operate with strong losses, mainly due to ionization and Bremsstrahlung, to derive the particle energy from total losses or loss profiles.

2.1.1 Energy losses by Ionization

The dominant process for energy losses of low energy charged particles in matter is the ionization of atoms. Fig 2.1 depicts, that ionization losses are strong for low energies, then drop to a minimum ionization energy and rise logarithmically afterwards for relativistic particles. The losses can be calculated by the phenomenological formula of Bethe and Bloch (1930):

$$-\frac{dE}{dx} = \frac{4\pi}{m_e c^2} \cdot \frac{nz^2}{\beta^2} \cdot \left(\frac{e^2}{4\pi\epsilon_0}\right)^2 \cdot \left[\ln\left(\frac{2m_e c^2 \beta^2}{I \cdot (1 - \beta^2)}\right) - \beta^2 - \frac{\delta}{2} \right] \quad (2.1)$$

with E = the particle energy, x = the particle range in the material, c = the speed of light, $\beta = v/c$ with v = the particle velocity, z = charge number of the particle, e = the charge of the electron, n = the electron density of the material, I = the mean Ionization potential of the material, m_e = the rest mass of the electron, and δ = a density parameter, taking into account a shielding effect for the extended electrical field of relativistic particles.

As ionization potential "I" can be used the simple approximation $I \sim 13.5 \cdot Z \text{ eV}$ with Z the charge number of the material or the more accurate values from the ICRU¹ tables. Particles with energies above the minimum ionizations loss range ($E > 3 \times m_{particle}$) are called minimum ionizing particles (MIP), since the relativistic contributions are small. The exceptions make

¹ICRU, International Commission on Radiation Units and Measurements (www.icru.org)

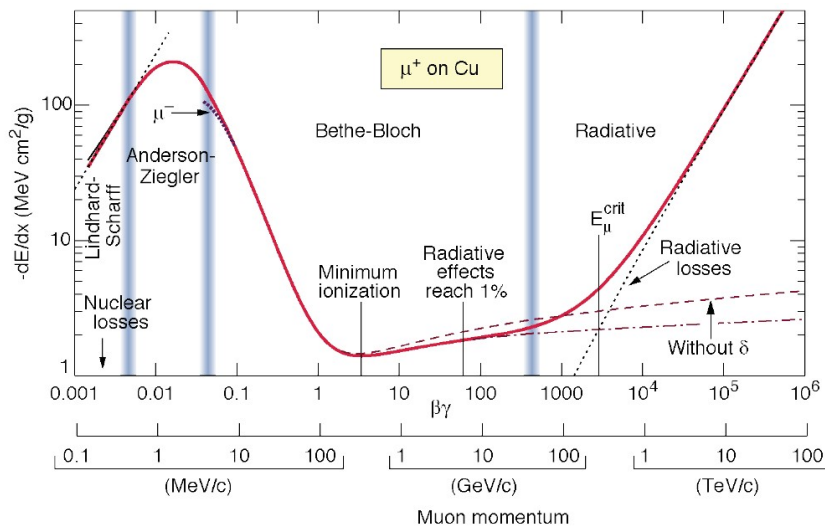


Figure 2.1: The mean energy loss of particles in matter described by the Bethe Bloch formula. This plot shows the loss for muons. For other particle masses the energy scale is just shifted and the radiative loss (Bremsstrahlung) is small for heavy particles [PDG02].

light charged particles, especially electrons and positrons, because their Bremsstrahlung is strong and therefore they are only MIPs in range of the Bethe-Bloch minimum. As shown in Fig 2.1 are the Bremsstrahlung contributions often included to the Bethe-Bloch formula, but then the resulting equation differs for electrons and positrons [Gru93].

2.1.2 Energy losses by ionization in thin media

The Bethe-Bloch equation just describes the most probable value of the deposited energy in the material. In reality the losses obey a Landau-distribution as discussed in chapter 5.4.2. The long tail of the resulting distribution originate from close to direct hits, which deposit much energy. For dense media it reshapes to a Gaussian-distribution, since the averaged energy deposition per hit becomes smaller for more frequent hits. In gases also appears a fraction of generated free charges, so called δ -electrons, which escape from the detector and therefore shrink the energy deposition by only adding there own ionization. A reason why the Landau tails are in general less strong as expected. The distribution of δ -electrons mit energy $T \gg I$ can be calculated by:

$$\frac{d^2N}{dTdx} = \frac{1}{2} K z^2 \frac{Z}{A} \frac{1}{\beta^2} \frac{F(T)}{T^2} \text{ mit } F(T) = (1 - \beta^2 T/T_{max}) \quad (2.2)$$

Due to low hits rates the energy deposition fluctuates statistically in thin media. To overcome the problems of such fluctuations, one can express the hits of particles as radiative processes (Absorption-, Compton scattering, etc.) [GW05], the so called Photo-Absorption-Ionization (PAI). The probability to absorb a photon with $E = h\omega$ is in good approximation by the

differential cross-section:

$$\frac{d\sigma}{d\omega} = \frac{\alpha}{\pi\beta^2|\epsilon(\omega)|^2} \left[\frac{\sigma_\gamma(\omega)}{\omega} \left(\ln \frac{2mv^2}{\omega|1-\beta^2\epsilon|} - \frac{\epsilon_1 - \beta^2|\epsilon|^2}{\epsilon_2} \arg(1 - \beta^2\epsilon^*) \right) + \frac{1}{\omega^2} \int_{I_1}^{\omega} \sigma_\gamma(\omega') d\omega' \right], \quad (2.3)$$

with the complex dielectric constant $\epsilon = \epsilon_1 + i\epsilon_2$ of the media and the cross-section σ_γ of the related photonic process. The energy-loss of a particle is given by the sum of all absorbed photon energies. Because this solution does not use a continuous mean free path like the Bethe-Bloch equation (ionization potential I), but determines the free path for each calculation step again, it also works for low hit rates in thin media. On the other hand this procedure causes much more computation overhead, especially if it is used for high hit rates in dense media. In this case the Bethe-Bloch formula is more suitable.

2.1.3 Bremsstrahlung

The main contribution for energy losses of light relativistic charged particles was first discovered by Konrad Röntgen in 1895 and is generally called Bremsstrahlung. They are strongly mass-dependent and therefore dominant for light leptons. A special kind of Bremsstrahlung is the synchrotron-radiation, where the retarding electric field of fast circling particles cause an emission of photons. Bremsstrahlung is produced when charged particles fall into matter and scatter on the electromagnetic potential of atoms. These potentials force the particles on curved trajectories leading to a shower of Bremsstrahlung-photons. The energy loss of electrons by Bremsstrahlung was first formulated in 1934 by Bethe and Heitler [BH34] as:

$$\frac{dE}{dx} = -4\alpha r_0^2 \cdot \frac{Z^2}{A} L \cdot \ln \frac{183}{Z^{1/3}} \cdot E \quad (2.4)$$

2.1.4 Multiple scattering

The multiple scattering process plays a minor role for most particle detectors and generally just reduces the momentum resolution. It accounts for energy losses by recoils due to multiple scattering of particles on the atomic potentials. The losses are small and only necessary for particles with less than 1 GeV energy.

2.1.5 Pair annihilation

Pair annihilation means an electron and positron annihilate into two photons. This process diminishes the efficiency of positron detection, because the resulting two photons are counted as background. The differential cross section of pair annihilation [WM02b] is given by :

$$\frac{d\sigma}{d\epsilon} = \frac{\pi r_0^2 Z}{\gamma - 1} \frac{1}{\epsilon} \left[1 - \epsilon + \frac{2\gamma\epsilon - 1}{\epsilon(\gamma + 1)^2} \right] \quad (2.5)$$

with $\gamma^{-2} = 1 + \beta^2$, E_a, E_b = the total e^+ , e^- -energy, $E_{tot} = E_a + E_b$, and $\epsilon = E_a/E_{tot}$. For $\gamma \gg 1$ follows $E_a \gg E_b \sim 0,511MeV \rightarrow \epsilon \sim 1$ and the differential cross section becomes small for large γ -factors.

2.1.6 Cherenkov Radiation

Relativistic charged particles ($\gamma > 1$) lead to emission of Cherenkov radiation while traversing a medium. Due to their charge they generate polarizations of the medium, shown by Fig 2.2. This polarizations lead to photon emissions and the radiation forms a Mach-cone in case the

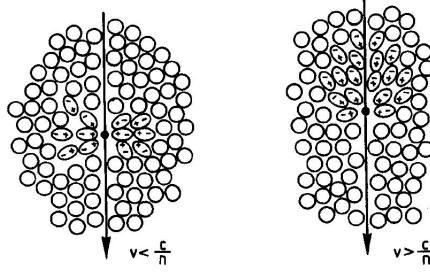


Figure 2.2: Polarization of media by traversing charged particles with different speed.

particles speed is faster than the speed of light in the traversed material. The appearing cone angle Φ is related to the particle speed and the speed of light $c' = c/n$ in the media with a refraction index n :

$$\cos \Phi = \frac{c'}{v} = \frac{1}{n\beta} \quad (2.6)$$

2.1.7 Transition Radiation

Transition radiation (TR) was first described by I. Frank and V. Ginsburg in 1946. TR originates from highly relativistic charged particle crossing the interface of two media with different dielectric constant, where the spontaneous change of the media polarizations causes the emission of photons [PDG02],[ESA00],[Gri01],[GS04],[GS06]. Ultra-relativistic ($\gamma > 1000$) charged particles generate transition radiation in the X-ray region (XTR). For X-ray photons the dielectric constant ϵ_i can be expressed by the plasma frequency approximation:

$$\epsilon_i(\omega) = 1 - \omega_{P,i}^2/\omega^2 = 1 - \xi_i^2 \quad (2.7)$$

with the plasma frequency $\omega_{P,i} = \sqrt{4\pi n_{e,i} e^2/m_e}$, where m_e is the electron mass and $n_{e,i}$ the number of electrons per volume of the medium i . In that case the angular distribution of the radiated photon intensity of a single interface can be written as:

$$\frac{d^2W}{d\omega d\Theta^2} = \frac{2\alpha\hbar\Theta^2}{\pi} \left(\frac{1}{\gamma^{-2} + \Theta^2 + \xi_1^2} - \frac{1}{\gamma^{-2} + \Theta^2 + \xi_2^2} \right)^2, \quad (2.8)$$

where $\alpha = e^2/\hbar c$ is the fine structure constant and $\hbar\omega$ the energy of the radiated photon. This expression is valid for high frequencies $\omega \gg \omega_{P,i}$ and small angles $\Theta \ll 1$. The distribution is sharply peaked in forward direction $\Theta \sim 1/\gamma$. Integration over Θ reveals the differential energy spectrum:

$$\frac{dW}{d\omega} = \frac{2\alpha\hbar}{\pi} \left[\left(\frac{\omega_1^2 + \omega_2^2 + 2\omega^2/\gamma^2}{\omega_1^2 - \omega_2^2} \right) \ln \left(\frac{\gamma^{-2} + \omega_1^2/\omega^2}{\gamma^{-2} + \omega_2^2/\omega^2} \right) \right]. \quad (2.9)$$

Further integration with respect to frequency leads to the total intensity at a single interface:

$$W = \frac{\alpha \hbar (\omega_1 - \omega_2)^2}{\pi (\omega_1 + \omega_2) \gamma}. \quad (2.10)$$

The proportionality to γ comes primarily from the hardening of the X-ray spectrum, not so much from an increasing photon number. The photon yield per interface is rather low and of the order of $\alpha \simeq 1/137$, but can be easily multiplied by a stack of many interfaces as used in transition radiation detectors. The short coherence length of generated X-ray TR forces the use of thin radiator materials in which case the TR of two interfaces needs to interfere constructively. Due to the short coherence length, X-ray photons are generally suppressed in radiators of Cherenkov detectors. For relativistic particles the amplitudes of the forward radiation from both interfaces are of same magnitude. Neglecting backward emission, reflections

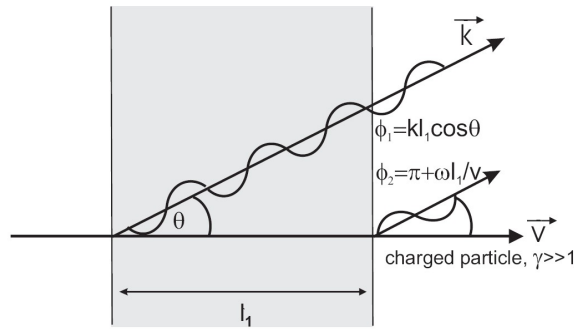


Figure 2.3: Constructive interference of TR photons from two interfaces of a material layer. [Hau05]

and changes of Θ caused by refraction, results in an electric field like:

$$\vec{E}(\omega, \vec{\Theta}) = \sum_{j=1}^n \cdot \vec{E}^j(\omega, \vec{\Theta}) e^{(-\sum_{i \geq j} \sigma_i + i\Phi_i)} \quad (2.11)$$

with \vec{E}^j the single surface amplitude, $e^{i\sigma_i}$ the absorption-factor in the i -th medium, $\vec{\Theta}$ the difference between the photon and the particle direction and Φ_i the phase difference due to the different photon and particle speed in the medium i . When the field created on the first interface reaches the second one, it has the phase $kl_i \cos \Theta$ with l_i the thickness of the medium. The second field, drawn in Fig 2.3, occurs later related to the particle velocity \vec{v} and has the phase $\pi + \omega l_i / v$. Here an additional factor π results from the opposed polarization on the second interface. By summation of the fields a modulating interface factor appears in the radiated intensity:

$$|e^{ik_i l_i \cos \Theta} - e^{i\omega l_i / v}|^2 = 4 \sin^2(l_i (k_i \cos \Theta - \omega / v) / 2) = 4 \sin^2(\Phi_i / 2). \quad (2.12)$$

Approximating $k_i = \sqrt{\epsilon_i} \omega / c \simeq (1 - \frac{1}{2} \xi^2) \omega / c$, $\cos \Theta \simeq 1 - \frac{1}{2} \Theta^2$, $\beta^{-1} \simeq 1 + \gamma^{-2} / 2$ and neglecting the small mixing terms leads to:

$$\Phi_i = (\omega l_i / 2c) (\gamma^{-2} + \Theta^2 + \xi_i^2) = \frac{l_i}{L_i} \quad (2.13)$$

with the coherence length:

$$L_i = \frac{c}{\omega} \frac{1}{\gamma^{-2} + \Theta^2 + \xi_i^2} \quad (2.14)$$

Formula 2.14 considers an even number of interfaces, otherwise a factor 2 appears in the nominator. Now the differential angular intensity of two interfaces can be calculated:

$$\frac{d^2W}{d\omega d\Theta^2} = \left(\frac{d^2W}{d\omega d\Theta^2} \right)_{single} \cdot 4 \sin^2(\Phi_i/2) = \frac{\alpha \hbar \Theta^2}{\pi} \left(\frac{\omega}{c} \right)^2 \text{Re} \left\{ R^{(121)} \right\} \quad (2.15)$$

with

$$R^{(121)} = 2(L_1 - L_2)^2 4 \sin^2 \left(\frac{l_2}{4L_2} \right). \quad (2.16)$$

Because the dielectric constant in non transparent media is described by $\epsilon_i(\omega) = 1 - \frac{\omega_{p,i}^2}{\omega^2} + i \frac{c}{\omega l_{abs,i}}$, one introduces the absorption-length $l_{abs,i}$, and the coherence length merges to the complex formation-zone:

$$Z_i = \frac{L_i}{1 - i \frac{L_i}{l_{abs,i}}}. \quad (2.17)$$

The partial absorption of destructive interfering photons elongates now the formation-zone. Typical formation-zones are in the order of 10–100 μm . With this transfer the complex factor $R^{(121)}$ in equation 2.15 looks like:

$$R^{(121)} = 2(Z_1 - Z_2)^2 \left[1 - \exp \left(\frac{il_2}{2Z_2} \right) \right] \quad (2.18)$$

Its worthwhile to note, that this transparent media relation follows from the approximation $l_{abs} \rightarrow \infty$ in equation 2.18. In this case the factor 2 neglected above appears.

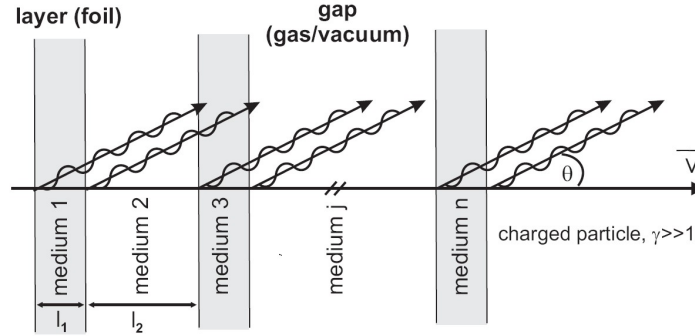


Figure 2.4: Rising TR yield by cascading many material layers.[Hau05]

Cascading n interfaces leads to the mentioned higher yield and is demonstrated by Fig 2.4. Therefore one needs to replace the complex factor $R^{(121)}$ with:

$$\langle R^{(n)} \rangle = 2(Z_1 - Z_2)^2 \left\{ n \frac{(1 - F_1)(1 - F_2)}{1 - F} + \frac{(1 - F_1)^2 F_2 [1 - F^n]}{(1 - F)^2} \right\} \quad (2.19)$$

and

$$F = F_1 F_2. \quad (2.20)$$

The media and gap thicknesses F_1, F_2 can be chosen arbitrarily. Irregular radiators (etc. fiber type) are well described by a gamma-distributed choice:

$$F_i = \int_0^\infty dt_i \left(\frac{\nu_i}{\bar{t}_i}\right)^{\nu_i} \frac{t_i^{\nu_i-1}}{\Gamma(\nu_i)} \exp\left[-\frac{\nu_i t_i}{\bar{t}_i} - i \frac{t_i}{2Z_i}\right] = \left[1 + i \frac{\bar{t}_i}{2Z_i \nu_i}\right]^{-\nu_i} \quad (2.21)$$

with the mean thickness \bar{t}_i of the media and the gap and the variance $\sigma = 1/\bar{t}_i \sqrt{\nu_i}$ between them; for foil type radiator F_1, F_2 stay constant. XTR appears for high γ -factors ($\gamma \sim 10^3$) and can be used for particle identification, as a positron with 3 GeV ($\gamma = E/M \sim 6000$) generates XTR, a proton of the same energy ($\gamma \sim 6$) does not. The AMS-02-TRD radiators are well described by the gamma distributed choice of F_i , as shown by a comparison between beam test data and GEANT4 simulation of a 20 GeV electron distribution in chapter 5.4.2.

2.2 Photon detection

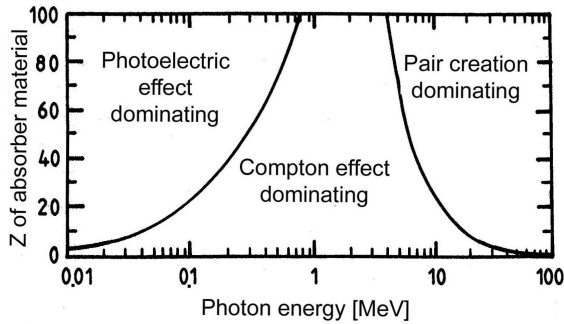


Figure 2.5: Dominating regimes of photon process dependent on their energy and the charge number of the absorber material. [Gru93]

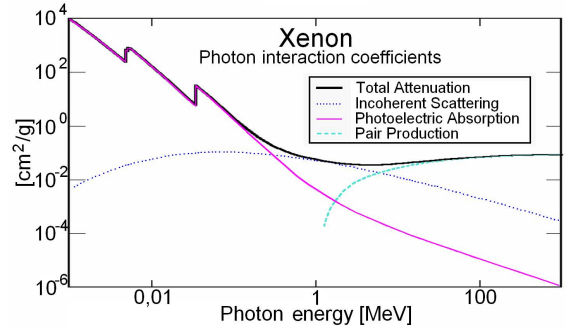


Figure 2.6: Contribution of photon processes to the interaction coefficient in Xenon gas. [NIS]

Photons which enter a detector material can either be totally absorbed due to the Photoelectric Effect or the Pair Production or undergo a Compton scattering. Fig 2.5 shows the energy domains of these three processes dependent on the charge number Z of the absorbing material. High Z materials are used for photon detection to benefit from the strong photon interaction rate by the Photoelectric Effect, like demonstrated by Fig 2.6.

2.2.1 Photoelectric Effect

The Photoelectric Effect was first explained by Albert Einstein (1905) with the quantization of photons $E = \hbar\omega$. An absorbed photon energy leads to the release of an atomic shell electron and the excess energy is transformed into kinetic energy of the released electron. The main contribution to this effect ($\sim 80\%$) comes from electrons of the atomic K-shell, because the conservation of energy and momentum is much easier fulfilled for strongly bound electrons. That is also the reason why the absorption of low energy photons in materials strongly depends

on the atomic number Z of the material. Walter Heitler calculated the total cross section for the K-shell as [Hei54]:

$$\sigma_{PH}(E) = \alpha^4 \cdot Z^5 \sqrt{32 \left(\frac{E_0}{E}\right)^7} \cdot \sigma_{Th} \quad (2.22)$$

with the fine structure constant α , the atomic number Z , the rest energy of the electron E_0 and the Thomson cross section $\sigma_{Th} = 8/3\pi r_0^2$.

2.2.2 Pair Production

The Pair Production starts for high energetic photons with $E > 2m_e c^2 + 2m_e/m_{nucleus}c^2$. In presence of a nuclear Coulomb field the photon irradiates into an electron positron pair with the cross section $\sigma_{pair} \sim Z^2$.

2.2.3 Compton Scattering

In the Compton scattering process a photon scatters on an electron of a absorber material and transfers a part of its energy, like shown by Fig 2.7. The final wavelength λ_f of the photon is

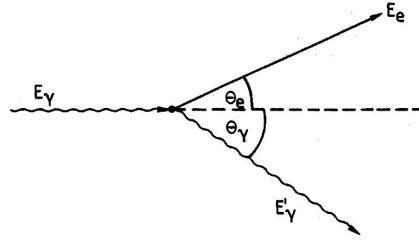


Figure 2.7: Compton scattering of a photon on an electron [].

increased by:

$$\Delta\lambda = \lambda_f - \lambda_i = \frac{h}{m_e c} \cdot (1 - \cos\theta_\gamma), \quad (2.23)$$

with the electron mass at rest m_e , c the speed of light, the scattering angle of the photon θ_γ and h the Plank number. Experimental verifications of this formula provided evidence, that photons are massless particles but nonetheless carry momentum. This formula also leads to the energy of the scattered photon E'_γ :

$$E'_\gamma = \frac{E_\gamma}{1 + \frac{E_\gamma}{m_e c^2} \cdot (1 - \cos\theta_\gamma)} \quad (2.24)$$

The small binding energies of atoms can be neglected in this scattering process and the cross sections per solid angle is given as:

$$\frac{d\sigma}{d\Omega} = \frac{r_0^2}{2} \cdot (1 + \cos^2\theta_\gamma) \quad (2.25)$$

with the classical electron radius r_0 . This simple classical formulation becomes quantum mechanical in the Klein-Nishina relation [WM02a]:

$$\frac{d\sigma}{d\Omega} = \pi r_0^2 \frac{m_0 c^2}{E_0} Z \left[\frac{1}{\epsilon} + \epsilon \right] \left[1 - \frac{\epsilon \sin^2 \theta}{1 + \epsilon^2} \right] \quad (2.26)$$

with $m_0 c^2$ = the electron mass, E_0 = the energy of the initial photons, E_1 = the energy of the final photons and $\epsilon = E_1/E_0$.

Chapter 3

The AMS-02 Detector on the International Space Station

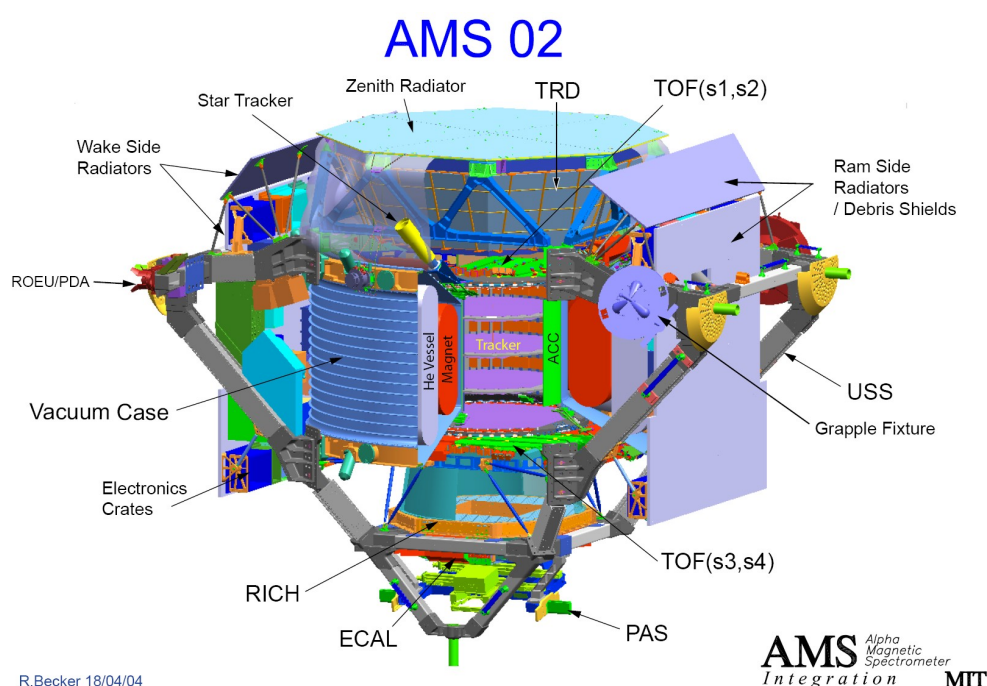


Figure 3.1: A cross section of AMS-02. It shows all subdetectors, the Unique Support Structure (USS) to mount AMS-02 to the ISS, thermal radiators, debris shields and electronic crates.

The Alpha Magnetic Spectrometer-02 (AMS-02) is a multipurpose particle detector foreseen to be mounted to the International Space Station (ISS) to measure primary cosmic rays for at least three years. The experiment can measure leptons and hadrons as well as ions up to $Z \leq 26$ with energies up to the TeV range and γ -rays up to hundreds of GeV. It consists of seven sub detector units, a silicon tracker (Tracker), a Ring Imaging Cherenkov detector (RICH), a Time-of-Flight detector (TOF), a Amica Star Tracker (AST), an AntiCoincidence Counter (ACC) and a Transition Radiation Detector (TRD) which are visible in the technical drawing 3.1. The AMS-02 detector will be mounted to the ISS via the Unique Support Structure (USS). This structure again is the direct mechanical support for all subdetector units except the AST and the ACC, which are mounted to the vacuum tank of the Tracker. If not stated different, the figures of this chapter are taken from reference [AMS09].

3.1 Physical motivations for AMS-02

During a three years flight in Space AMS-02 will perform an accurate, high statistics, long duration measurement of the charged cosmic rays and γ -rays. In contrast to ground based air shower experiments the directly measured primary cosmic ray data of AMS-02 will have much smaller uncertainties for energies up to 1 TeV. Unfortunately its design life time is limited by the amount of superfluid helium for the cooling of the superconducting magnet to about 3 years. Because the Space Shuttle program would be presumably stopped before the end of the mission and a return to earth thus impossible, AMS-02 will continue the data taking without the momentum resolution of the Tracker. This allows to determine the absolute charge of cosmic ray particles, but no discrimination between particles and antiparticles. Thus γ -rays and also nuclei can still be measured.

The three major research topics of AMS-02 are: the search for antimatter, the determination of the age of cosmic rays and of the density of the interstellar material and the indirect search for dark matter.

3.1.1 Search for antimatter

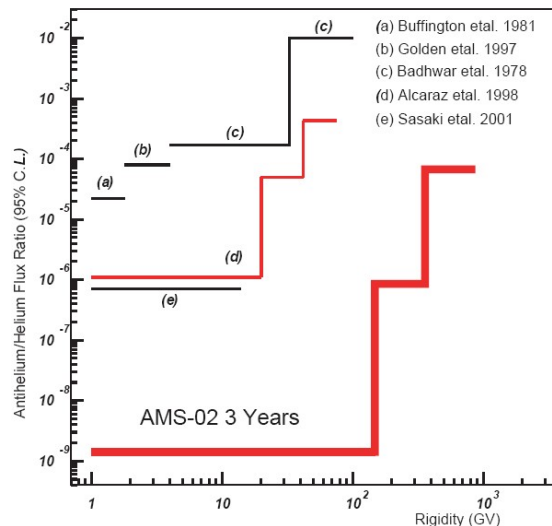


Figure 3.2: Projected AMS-02 limits on the $\bar{H}e/He$ ratio compared to previous measurements.

Recent measurements of the Cosmic Microwave Background by COBE and WMAP show [Spe03], that our universe was in early stages close to thermal equilibrium and thus kT was large in respect to the hadron masses. The standard model of particle physics tells us that in at this stage the reversible annihilation and production of hadron anti-hadron pairs should have taken place. With further expansion of the universe these processes stopped and should have relieved an equal amount of matter and antimatter. It is evident that our solar system mainly consist of matter and measurements of primary cosmic rays show a paucity of antimatter in our galaxy and even on large scale no evidence for intense γ -rays from matter antimatter annihilations are found. There of course exists a large number of antiprotons, but these are secondaries from

cosmic ray interactions. The only distinct evidence for antimatter domains can be proven by the existence of anti-nuclei with $Z > 1$ in the cosmic rays, because those need to be created in thermonuclear processes of anti-stars. A three years flight of AMS-02 will obtain a \overline{He}/He limit in the order of 10^{-9} for rigidities up to 130-140GV/c. The search for antimatter will benefit from the large acceptance of $0.5 \text{ m}^2\text{sr}$ and the low background due to the low detector density. Fig 3.2 shows the expected sensitivity on the \overline{He}/He flux ratio.

The provide information is extracted from the references [AMS09], [dB94] and [Orb03].

3.1.2 The age of cosmic rays and the density of the interstellar material

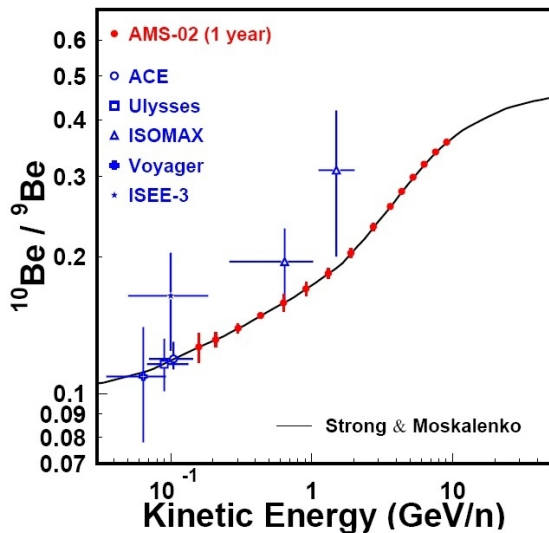


Figure 3.3: Projected AMS-02 measurement of the $^{10}\text{Be}/^9\text{Be}$ ratio.

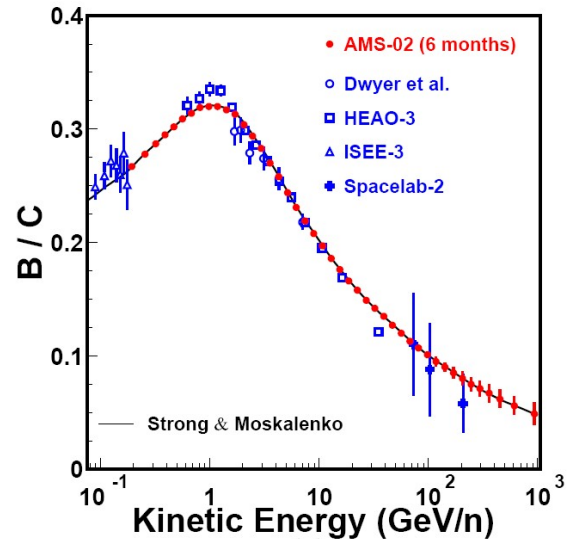


Figure 3.4: Projected AMS-02 measurement of the B/C ratio.

The excellent velocity resolution of the AMS-02-RICH allows to measure the flux of radioactive ^{10}Be in respect to its stable neighbor isotope ^9Be . Due to ^{10}Be half-life of $1.6 \cdot 10^6$ y it serves as a cosmic clock, because the start time $^{10}\text{Be}/^9\text{Be}$ ratios inside cosmic rays shrink during their propagation through the universe and therefore let determine their age. A projected one year measurement of this ratio with AMS-02 is shown in Fig 3.3. Beryllium is a secondary constituent of cosmic rays as well as lithium and boron. All of them are produce by spallation in interactions of heavier primary cosmic ray nuclei with the interstellar material of our galaxy. By comparing stable secondaries to primary ratios of cosmic rays for a given propagation model, it is possible to determine the mean density of interstellar material traversed by this cosmic rays. Fig 3.4 shows the projected B/C ratio for a six month flight of AMS-02; in this case boron (B) is a secondary product created from a primary carbon (C) nuclei.

Detailed information can be found in the references [AMS09], [Ham01] and [Ham04].

3.1.3 Indirect search for dark matter

A first hint for the existence of dark matter (DM) was observed by Fritz Zwicky in 1933, as he found galaxies in the Coma cluster moving faster than the gravitational force of the visible matter allows. In 1960 Vera Rubin discovered from observations of star velocities in spiral galaxies, that they also move faster than expected from their amount of visible matter and the Newtonian dynamics for spiral galaxy discs:

$$\frac{mv^2}{R} = G \frac{mM}{R^2} \rightarrow v = \sqrt{\frac{GM}{R}} \quad (3.1)$$

Inside the bulge of spiral galaxies the mass distribution is $M \propto r^3$, which results in $v \propto r$. Outside the bulge the mass is approximately constant and therefore a velocity distribution $v \propto r^{-1/2}$ is expected. But the observed spiral galaxies showed a close to constant disc velocity. This fact leads to the assumption, that the majority of the galactic mass (80–90%) is distributed in a halo around the bulge and disk as a kind of dark matter. Since we do not see a kind of matter, though it must be widely distributed, it can just interact weakly. The clustering of galaxies hints that the particles of these matter are non-relativistic, thus cold and massive, and therefore are called Weakly Interacting Massive Particle (WIMP). An interpretation in this direction concludes with recent measurements by WMAP¹. The measurements tell us that only 5% of the present energy density of the universe is visible matter, 23% dark matter and 72% dark energy (DE). This leads to the Λ CDM model² model of the universe, where Einstein's cosmological constant is added to the FLRW³ metric. In this case the large fraction of dark energy is explained by the cosmological constant (1917), which Einstein introduced to achieve a stable universe in his cosmological model. A model by Eric Lindner and Robert Caldwell replaces Einstein's constant by the fluctuating scalar quintessence field, which than also allows structure formation of the universe. But the dark energy can also originate from the total amount of vacuum fluctuations in the universe. Last but not least modified Newtonian dynamics on large scales (MOND) according to the hypothesis of Mordehai Milgrom might be able to solve the galaxy rotation velocity problem.

Though the MOND hypothesis is not excluded today, strong evidence was found for the DM WIMP interpretation by de Boer et. al in 2005 [dBSZ⁺05]. The WIMP signature showed up in a renewed analysis of old γ -ray data taken by the Energetic Ray Emission Telescope (EGRET) experiment from 1991 to 2000. EGRET was one of four instruments on the Compton Gamma Ray Observatory. The EGRET data showed an excess of γ -rays above the conventional γ -ray model spectra, that mainly base on γ -ray production in cosmic ray proton proton interactions. In contrast to charged particles, which scatter on interstellar magnetic fields and matter, γ -rays directly point to their emitting source. But all tested conventional models could not describe the shape of spectra in all sky directions. Fig 3.5 shows the best fit of the conventional model contribution together with signals from Dark Matter Annihilation (DMA) and free normalization of the spectrum towards the galactic center. The model spectra were gained from simulations with GALPROP including WIMP's of 65 GeV mass, that generates γ -rays by hadronization of mono-energetic quarks. As normalization was used the low energies part of the spectrum were

¹WMAP, Wilkinson Microwave Anisotropy Probe.

² Λ CDM, Lambda Cold Dark Matter model, referred as concordance model of big bang cosmology.

³FLRW, Friedman Lemaître Robinson Walker. The metric includes the Friedman equations and the cosmological equations of state.

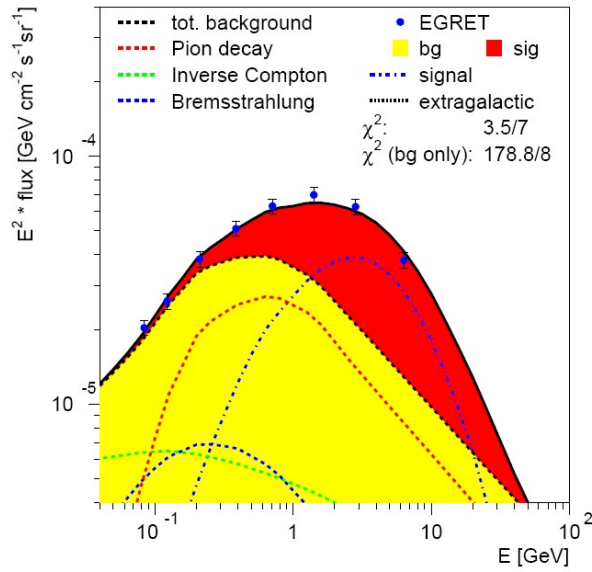


Figure 3.5: The gamma ray excess measured by EGRET. It can be explained by adding a signal of DMA and fitting the complete output between 0.1 GeV and 0.5 GeV to the data [dBSZ⁺05].

only the conventional model contributes. Cold dark matter froze out at some early stage of the universe as soon as its annihilation rate became less than the expansion rate of the universe:

$$N\langle\sigma v\rangle \leq H, \quad (3.2)$$

with an expansion rate given by the Hubble parameter H at freeze out time, the WIMP number density N , the relative annihilation partner velocity v and σ the annihilation cross section. This results in a thermally averaged annihilation cross section:

$$\langle\sigma v\rangle = 2 \cdot 10^{-26} \text{ cm}^3/\text{s}, \quad (3.3)$$

corresponding to a typical weak cross section. The intensity distribution of the EGRET excess leads to halo profiles, shown in Fig 3.6 and 3.7, and to a DMA normalization factor (boost factor) between 20 and 100, since the DMA cross section is proportional to the DM density squared. By fitting the γ -ray distribution in 180 sky directions the DM distribution in the sky was obtained from the boost factor needed for each fit. A common galaxy model with a flat DM density profile in the center and a $1/r^2$ profile was in agreement with the EGRET data outside the galactic disc, but not inside. Here a substructure of two doughnut like rings at distances of 13 kpc and 4 kpc needed to be added. Surprisingly there exists a ring of stars at 13 kpc discovered in 2003 and a ring of atomic hydrogen at 4 kpc and the velocity curve of our galaxy was described with all its features by this model, as visible in Fig 3.8. Additionally a DM ring at 13 kpc the first time allowed to correctly described the shape of the gas flaring of our galaxy. This analysis pushes the need for a precise measurement of all kinds of cosmic rays up to 1 TeV, which will be done by the AMS-02 experiment. In this manner AMS-02 will do an indirect search of dark matter particles, because it will only measure stable DMA end products, but will do this for all kinds of end products.

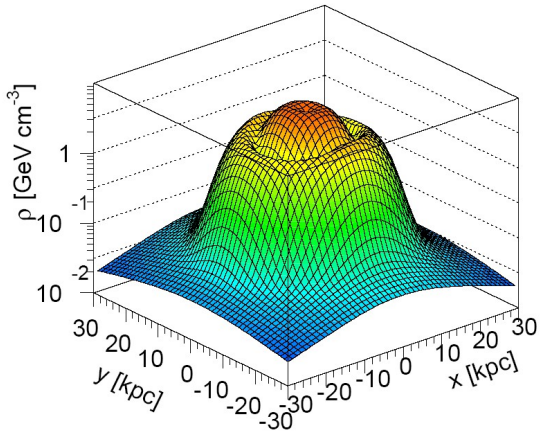


Figure 3.6: Halo profile in the xy -plane of the galactic disc [dBSZ⁺05].

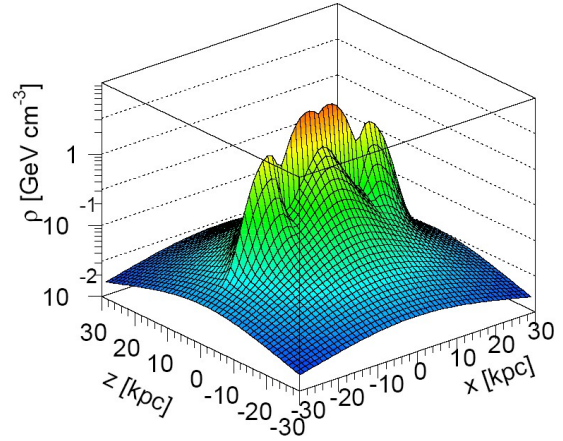


Figure 3.7: Halo profile in the xz -plane of the galactic disc [dBSZ⁺05].

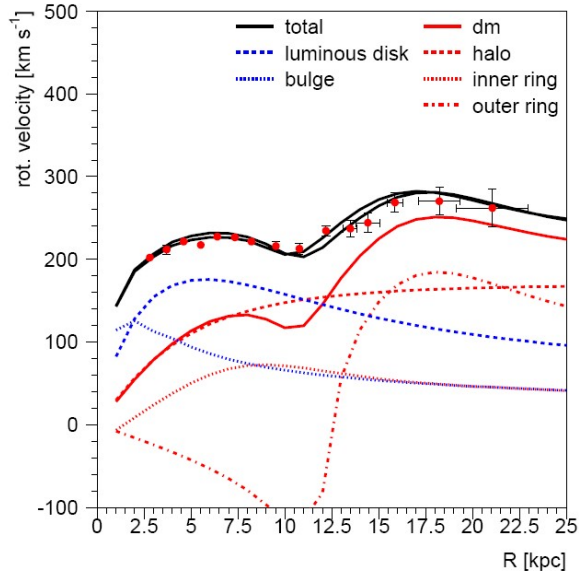


Figure 3.8: Rotation velocity with contributions from the inner and outer DM ring [dBSZ⁺05].

So far no assumption about the nature of WIMP's had been made, but there is a possible candidate predicted by the Minimal Supersymmetric Standard Model (MSSM). This model extends the Standard Model of particle physics (SM) by adding to each elementary boson a fermion and vice versa. The mass scale of MSSM particles is much higher than for SM and the decay into SM particles is forbidden by a new quantum number the R-parity (SM $R=1$, MSSM $R=-1$). MSSM adds soft breaking terms to the supersymmetric Lagrangian, that leads to symmetry breaking at a certain energy scale. In the mSUGRA model analyzed by the de Boer group at the IEKP, Karlsruhe, this symmetry breaking happens through gravitational interactions and reduces the 120 MSSM parameters to five free parameters. By including parameter constraints given by known data there exists an allowed parameter space, where the lightest supersymmetric particle (LSP) is the weak interacting neutralino χ_0 with a mass of 50-

100 GeV. Stable end products of the DMA are $p\bar{p}$ and e^+e^- pairs resulting from hadronization of DMA products and $\gamma\gamma$ pairs. In this case the plotting of the $e^+/e^+ + e^-$ fraction or the \bar{p} flux versus the energy an access will show up above the conventional models. New data from the ROSAT satellite [Eve08] have shown, that in our galaxy exist strong galactic winds leading to an anisotropic propagation of particle fluxes compared to the isotropic propagation model of GALPROP. This difference in the propagation effectively changes the measured charge particle spectra [dB08].

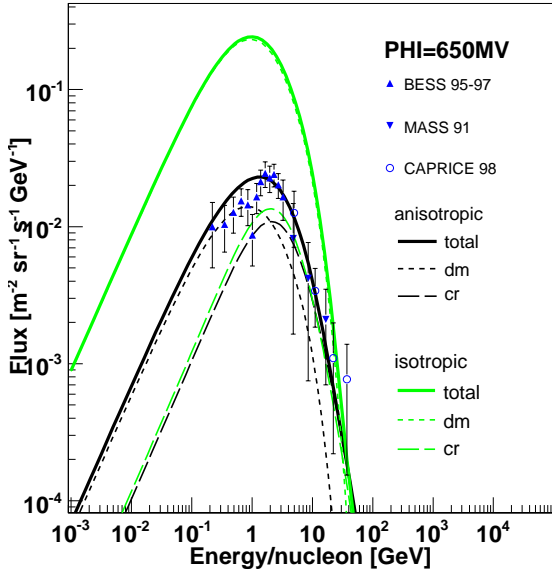


Figure 3.9: Simulated \bar{p} flux with DMA contribution for isotropic and anisotropic propagation compared to data [dB08].

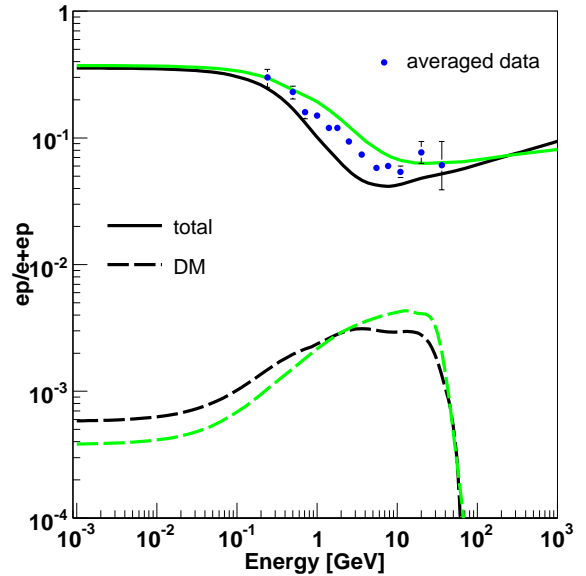


Figure 3.10: Simulated $e^+/e^+ + e^-$ fraction with DMA contribution for anisotropic propagation and averaged data.[dB08].

Fig 3.9 shows a conventional cosmic ray (cr) spectrum of antiprotons with a DM contribution (dm) added as it was simulated for isotropic and anisotropic propagation. The result is compared to data taken by the CAPRICE¹, the MASS and the BESS² balloon experiments. Fig 3.10 shows the simulated electron positron fraction with DM contributions for anisotropic propagation and the averaged existing data values.

One difficulty of the e^+ detection is the $10^4 - 10^5$ times larger p -flux in the cosmic rays. Thus p -rejection factors greater than 10^5 are necessary to detect pure e^+ samples. AMS-02 achieves this rejection as a combination of the TRD with $>10^2$ and the ECAL with $10^3 - 10^4$. A similar situation appears for the \bar{p} detection. In this case the e^- flux is $10^2 - 10^3$ times larger and again the TRD and the ECAL will do the selection. Unfortunately the new e^- and e^+ flux simulations including anisotropic propagation result in error bars for measurable positron fractions much larger than earlier assumed. Thus a DMA search in this fraction may be excluded. Nevertheless precise measurements of the positron fraction are needed to confirm visible signatures in the \bar{p} and γ -ray spectra.

The given information can be found in the references [dB03], [dB94], [dBHSZ04] and [dBSZ⁺05].

¹CAPRICE : Cosmic AntiParticle Ring Imaging Cherenkov Experiment.

²BEES: Balloon-borne Experiment with a Superconducting Spectrometer.

3.2 Subdetectors of AMS-02

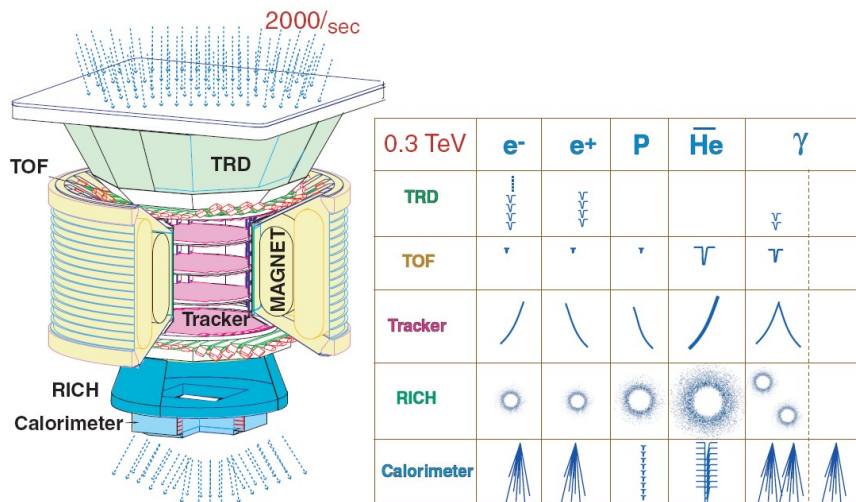


Figure 3.11: AMS-02 and the detectable particle signatures with its subdetectors.

The fast trigger (FT) of AMS-02 detector is given by the TOF system and provided to all other sub-detector read out systems. Additionally TOF delivers a flag for charges greater one providing a proton suppression on trigger level. Particle charges are measured with the Tracker, RICH and TOF detectors and particle velocities with the TOF, TRD and RICH detectors. Identification of leptons and hadrons can be done with the TRD and the ECAL and that of nuclei with the RICH and the TOF. The TRD provides a p/e^+ -separation above 10^2 up to 250 GeV. Momenta of particles are derived from their trajectories in the magnetic field of the Tracker. Its high rigidity resolution of $\sim 2\%$ at 50 GV/c is achieved by a superconducting dipole magnet with a flux density of 0.86 T. To assure a measurement of all particle observable, only trajectories from top (TRD) to the bottom (ECAL) in the opening angle of the TRD will be allowed. The rest is vetoed by a coincidence of the TOF on top and bottom of the Tracker and the ACC surrounding the Tracker. An ECAL sized hole in the center of the RICH assures, that particles just shower off in the ECAL. The ECAL is a three dimensional sampling calorimeter with a radiation length of $17 X_0$. This allows shower shape analysis and lead to a p/e^+ -separation on the level of $10^3 - 10^4$ up to 500 GeV. It also provides a very efficient stand alone γ -trigger with energies down to 2 GeV.

3.2.1 Time of flight detector (TOF)

The AMS-02 TOF detector allows measurements of particles velocities and discrimination between upwards and downwards particle directions with a time resolution of 120 ps and a rejection factor for upwards flying particles of 10^9 . TOF has a geometrical acceptance of $0.4 \text{ m}^2 \text{ sr}$ and consequently also AMS-02, since TOF provides the trigger to the sub-detector units. As soon as a passing particle is detected by the four TOF planes and no veto is given by the ACC, a trigger is send by the trigger electronics. This detector allows to distinguish nuclei

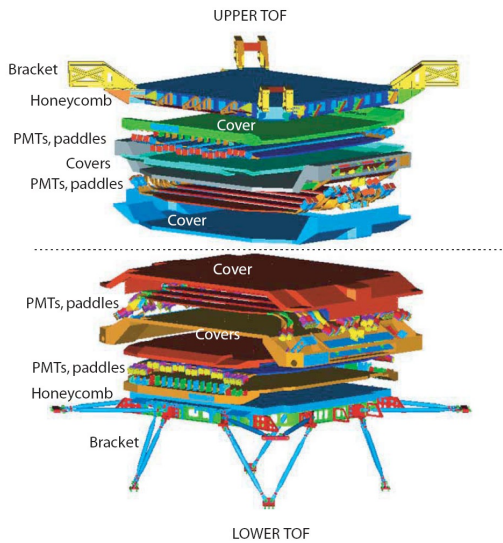


Figure 3.12: Drawing of the Time Of Flight detector.

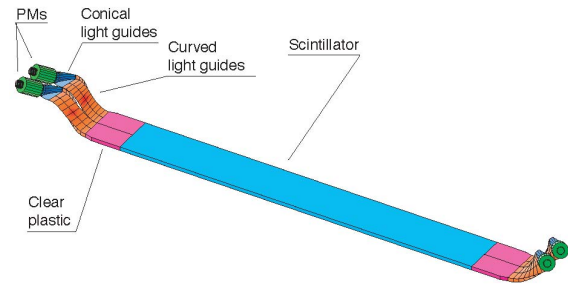


Figure 3.13: Drawing of the Time Of Flight detector paddle.

with charges up to $Z \sim 20$ by their energy deposition. Fig 3.14 shows the time resolution of the TOF and Fig 3.15 a combined charge measurement of TOF and RICH.

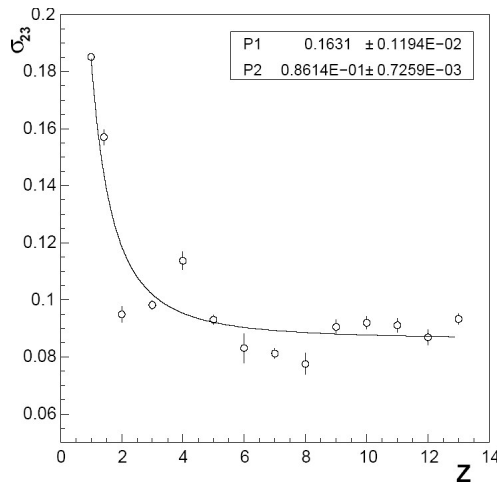


Figure 3.14: Time resolution of the TOF (in [ns]) taken with two counters during a beamtest in 2003.

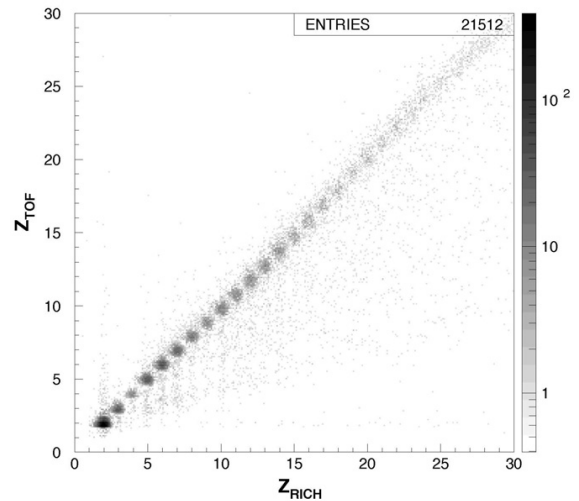


Figure 3.15: Combined charge measurement of TOF and RICH taken with a beamtest in 2002.

The upper and lower TOF are located on top and bottom of the Tracker and both consist of two perpendicular to each other oriented planes with eight or ten plastic scintillator paddles (ELJEN EJ-200 sized: $12 \times 1 \times 117$ -134 cm). Each scintillator paddle is read out by two photomultiplier tubes (HAMAMATSU R5946), like visible in Fig 3.13. Due to a residual magnetic field of up to 3 kG, the PMTs are connected via light guides to the scintillator and aligned in 45° to the field for best performance. The TOF System including all electronics operates from -20°C to

+50°C, weights 280 kg, consumes 170 W electric power and will be mounted via brackets to the USS.

All presented information is retrieved from reference [AMS09] and [Cas03].

3.2.2 Anti Coincidence Counter (ACC)

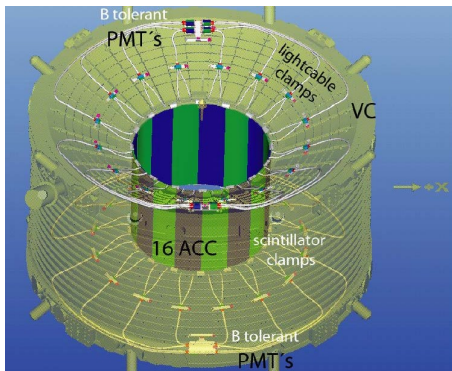


Figure 3.16: Drawing of the ACC. The light is guided in fibers to PMTs on the vacuum case [Doe07].

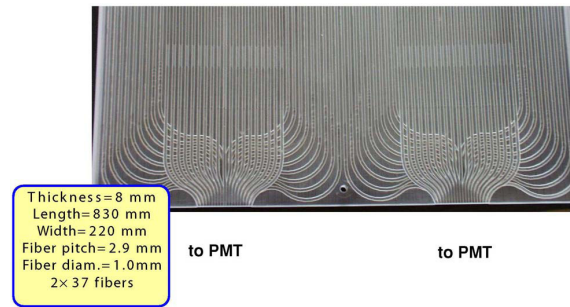


Figure 3.17: One of the 16 ACC scintillator panels with grooves for wavelength shifting fibers.

The AMS-02 ACC is used to veto events producing a trigger, but having trajectories passing into the vacuum tank. ACC surrounds the Tracker with 16 scintillator panels (Bicron, BC414) of 8 mm thickness. The scintillation light is collected with wavelength shifting fibers (Kuraray Y-11(200)M, $d=1$ mm) embedded in groves inside the scintillator panels. On both ends of the panels two output ports with 37 fibers are linked to transition connectors on the upper and lower conical flanges of the magnet vacuum case. From these connectors clear fibers guide the light to photomultiplier tubes (HAMAMATSU R5946) mounted to the vacuum case. To reduce the effect of the residual magnetic field of up to 1.2 kG the PMTs are mounted with there axes parallel to the stray field. For a minimum ionizing particle (MIP) the output charge of the PMTs is approximately 13 pC.

3.2.3 Transition Radiation Detector (TRD)

The AMS-02 TRD separates between particles with same momentum but different mass. Transition radiation (TR) is generated when highly relativistic particles traverse media interfaces (2.1.7). For example emit electrons with momenta above, but protons with momenta below 300 GeV/c do not. For the TRD was measured a p/e^- rejection factor of $10^2 - 10^3$ with a 20 layer prototype beamtest in 2000. Further details on the TRD rejection power and the beamtest can be found in 5.1. To enhance the TR yield the TRD uses polypropylene/polyethylene fleece (LRP-375 BK, PP/PE = 85/15, 0.06 g/cm³) of 20 mm thickness stacked in 20 layers, as illustrated in Fig 3.19. This material is also used for the ATLAS Transition Radiation Tracker (TRT) and the ATLAS collaboration showed, that this material decreases the TR yield just by 10–15% compared to a regular foil stack.

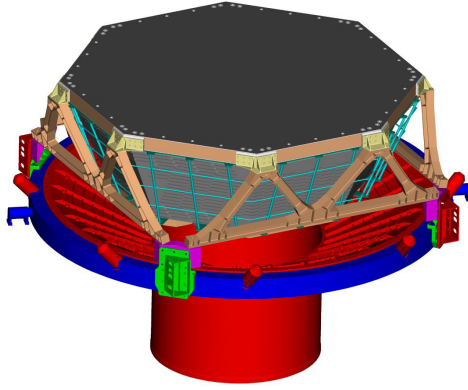


Figure 3.18: Drawing of the TRD. The TRD is supported by an M shaped structure. Inside it carries 328 sandwiches of straw modules and fleece radiator.

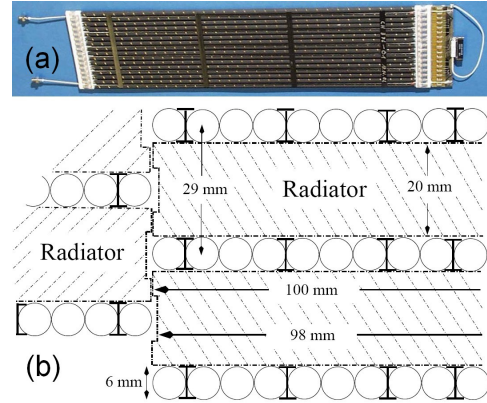


Figure 3.19: (a) Short prototype straw tube module. (b) Sandwich of fleece radiators and straw modules. The TRD layers show alternating shifts.

The TR is detected with proportional straw tube modules at the bottom of each fleece layer. A small prototype of such a module is shown by the picture 3.19. On one side of the straw modules steel gas in/outlets are glued, on the other side the TRD Front end board (UTE), that decouple the signals from the high voltage capacitively.

Each module is made of 16 straw tubes with a central high voltage wire, which will be filled with Xe/CO₂ (80/20) gas mixture. A straw works as proportional counter tube, with +1600 V applied to the central wire. Crossing photons or charged particles generate electrons and ions in the gas by the processes described in chapter 2. The ions are attracted to the tube walls and the electrons to the wire. Due to the $\frac{1}{r}$ dependency of the electric field inside a straw an avalanche ionization starts, when the electrons come close to the wire ($\sim 20 \mu\text{m}$), and the collected charge on the wire is amplified. For the X-ray TR detection Xenon gas with a large atomic charge number ($Z=54$) was chosen to achieve a high total cross section of the photo effect, as mentioned in 2.2. The mentioned proportional amplification is reached by diminishing the avalanche effect in the gas with CO₂ as stopping gas.

The whole TRD is made of a total of 328 modules and in total 5248 straws. Four top module layers are oriented in the x-direction, the central twelve in the y-direction and the four bottom layers again in the x-direction. Thus the TRD also provides a 3D spacial resolution. To avoid module spacings as well as to ensure the mechanical stability of the octagon, the modules of each layer are shifted alternatingly by about 1,5 cm in their height, as visible in Fig 3.19. Due to this shift and the shape of the detector at most two modules have the same length, which varies in a range from 86 cm to 202 cm. Since the TRD is the front detector of AMS-02, a low average density ($\sim 0.06 \text{ g/cm}^3$ without support) was realized to reduce its radiation length effecting the Tracker and ECAL performance. This came along with the necessity to avoid TR absorptions in the straw walls. Therefore the walls



Figure 3.20: Cross section of the straw tube walls.

are build of $72 \mu\text{m}$ thin foils with a substructure of carbon polyimide, aluminum, Kapton and polyurethan, as illustrated by drawing 3.20, and assure the gas tightness, electric strength and mechanical stability.

Since CO_2 leaks much stronger then Xe, the CO_2 leak of the straws is a critical issue for the operation of the TRD. Thus each single tube was leak tested with He at 2.8 bar for five minutes. After gluing the 16 straws of a module to the end caps working as gas manifolds, each module went through a pressure drop test at 1.7 bar in a vacuum vessel. Altogether the total leak rate of all modules is now of the order of 287 l per three years. AMS-02 will presumably carry 19 kg Xe and 4.5 kg CO_2 , corresponding to 8420 l of Xe and 2530 l of CO_2 at standard conditions and a safety factor of 8.8 with respect to the maximum CO_2 leak per year.

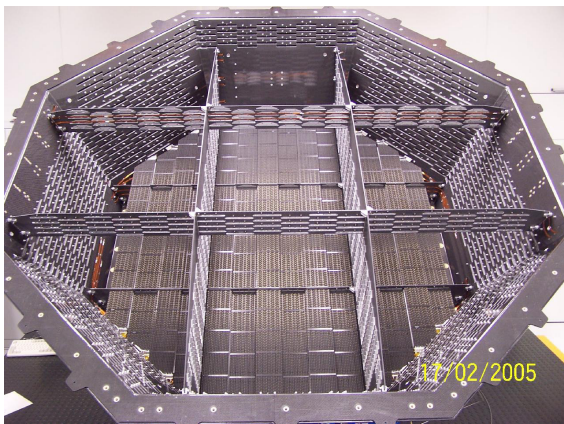


Figure 3.21: The TRD octagon support structure during module assembly. The large amount of module slots in the walls is still visible.

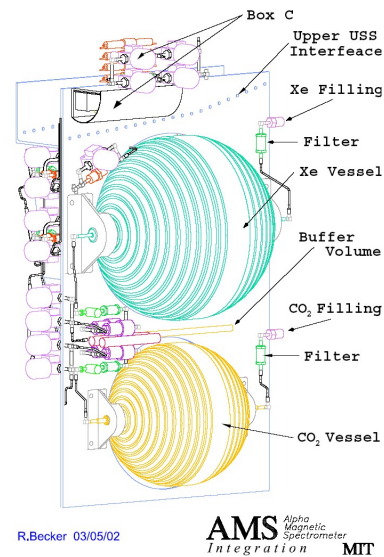


Figure 3.22: TRD gas supply system. Box S consists of a Xenon and a CO_2 vessel. Vessel D is on the back and cannot be seen.

In the center of each straw tube a $30 \mu\text{m}$ gold plated tungsten wire is spanned with a 1 N tension. Due to the $\frac{1}{r}$ dependency of the electric field in the tubes the homogeneity of the gas amplification is strongly affected by the alignment of the wires. Therefore each wire tension was electrically stimulated in a magnetic field and the tension was derived by measuring the resonance frequency. Afterwards the signal homogeneity was tested with different particle sources placed at various points along the tubes and a direct alignment measurement by computer tomography was made.

The support structure of the TRD modules, shown in picture 3.21, is a conical octagon with a width of 1.5 m at the bottom and 2.2 m at the top. It is made of aluminum honeycomb with carbon-fiber skins. Each module slot in the structure is machined with a precision of $100 \mu\text{m}$. The octagon itself is supported by an aluminum "M" structure, which is mounted to the USS.

As mentioned above CO_2 leaks much stronger than Xe, therefore the TRD needs a circulating gas system which stores, mixes and distributes the gas through the TRD modules. The full

system is built of a supply box (Box-S), a circulating box (Box-C) and manifolds, as visible in the drawing 3.22. Box-S stores the Xe and CO₂ in separate Leak-before-burst vessels, that ensure overpressure safety. All valves have a two-fold redundancy. The gas is mixed in a vessel (Vessel D) by measuring the partial pressure and then released into Box-C. Box-C contains redundant pumps to circulate the gas and a CO₂ analyzer. To prevent pressure losses due to a valve or pump failure the pumps and CO₂ sensors are mounted in a gastight vessel. During flight the gas will be mixed once per day. The gas flow through the modules is split into separate circuits by computer controlled input and output manifolds. Large leaks can be detected by pressure sensors in the manifolds and then are closed automatically by the slow control computer. The complete TRD including gas system and electronics weighs 500 kg.

All information in this section is summarized from the references [Sie02], [Gen03], [Fop04], [KS04], [Kir04] and [Mon03].

3.2.4 Silicon Tracker System (Tracker)

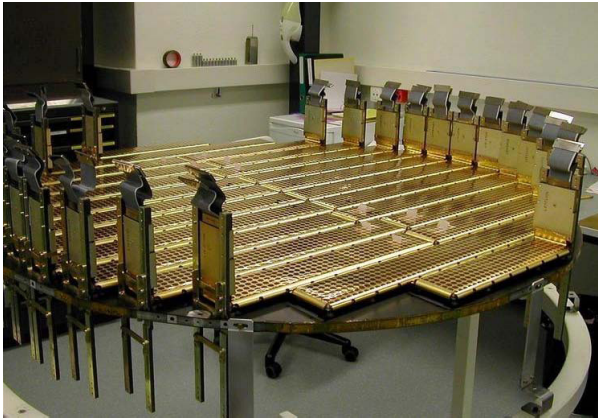


Figure 3.23: Tracker layer 2 completely equipped with ladders. A ladder is composed of double-sided silicon strip sensors

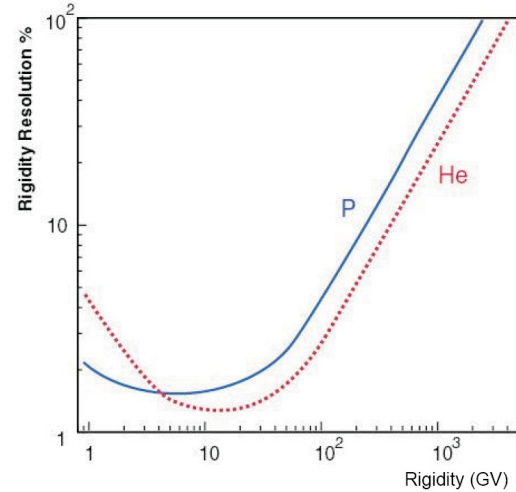


Figure 3.24: Tracker rigidity resolution for protons and helium [Bat02].

The AMS-02 Tracker measures a particle momentum p by detecting its trajectory in a magnetic field of $B = 0.86$ T provided by a superconducting magnet. Due to the Lorentz force the trajectory is bent on a circle with radius R .

$$F_c = mv^2/R = ZevB = F_L \quad (3.4)$$

Equation 3.4 relates the radius to the particle momentum with charge Z and leads to the magnetic rigidity $R \cdot B$ of a particle:

$$RB = \frac{p}{Ze} \quad (3.5)$$

Thus the momentum calculates from the charge and the rigidity. The charge is obtained from the sign of the rigidity and from the detected energy loss of the particle in the silicon sensor of the Tracker using the Bethe Bloch dependency $dE/dx \propto Z^2$, as described in 2.1.1. For

100 GV/c the momentum resolution dp/p of the Tracker is still about 3%, as can be derived from the rigidity resolution in 3.24.

The Tracker consists of close to 2500 double sided 300 μm silicon strip sensors assembled on 192 ladders and mounted to eight circular layers transverse to the magnet axis. Each ladder has 1024 channels summing up to a total of 196608 channels and 6.4 m^2 of silicon. As sensor material a high resistive ($>6 \text{ k}\Omega\text{cm}$) n-type silicon is used, which is on one side implanted with n^{++} strips of 104 μm pitch and 208 μm read out pitch and on the other with p^{++} strips of 27.5 μm pitch and 110 μm read out pitch. The p strips with finer pitch measure the bending coordinate with 10 μm precision and the orthogonal n strips the non-bending coordinate with 30 μm precision. During operation the sensors are reversed biased and fully depleted. Its drift times are in the order of 8 ns for electrons and 25 ns for holes. The signals are decoupled capacitively and connected to the front end hybrids with 50 μm metalized Upilex films glued on the n- and p-side. As support a 5 mm Airex foam is glued the Upilex films of the n-side, then a 100 μm carbon fiber to the foam and afterwards small a aluminum frame to the carbon. At the end all frames are screwed to the Tracker planes, like it is visible in picture 3.23. For electromagnetic shielding these ladders are covered with a double side metalized Upilex film. All ladders are arranged without overlap to simplify the construction and the alignment has a precision of $<5 \mu\text{m}$. The planes are made of a sandwich of aluminum honeycomb and carbon fiber.

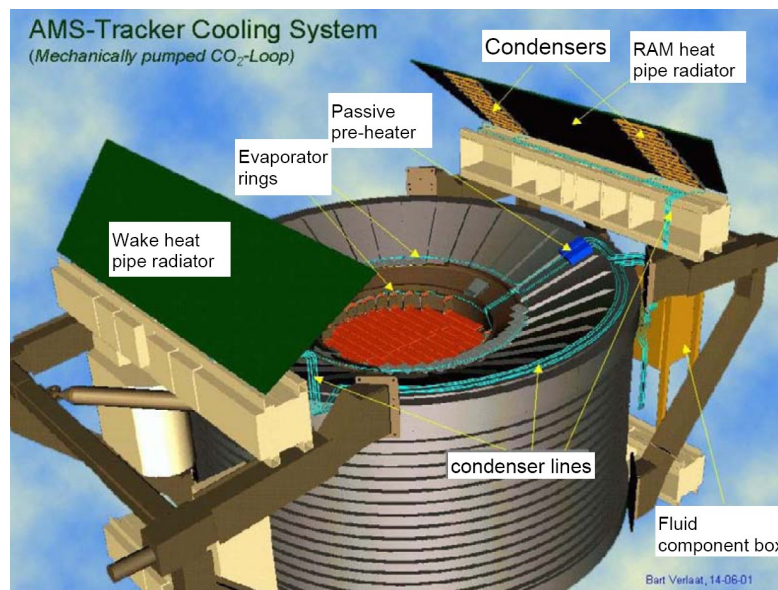


Figure 3.25: Drawing of the Tracker Thermal Control System (TTCS). Thermal bars conduct heat from the readout hybrids to evaporator rings, where some CO_2 evaporates. The liquid/vapour mixture is pumped to the wake and ram radiator to be cooled below the boiling point.

Since the front end electronics on the ladder hybrids generate a lot of heat the Tracker needs a Thermal Control System (TTCS) built as a heat pump system with CO_2 as cooling liquid at 80 bar. Fig 3.25 illustrates the main components of the TTCS. The CO_2 is preheated just below the boiling point to reach the largest heat transfer when the CO_2 passes the hybrids in series. At the end 30% of the liquid is vaporized and then cooled down again in the following condensers

on the Wake and Ram Radiators. The system will run uncontrolled, since it is self-adjusting. The complete Tracker system weighs 186 kg and consumes 734 W electric power.

To ensure the space resolution of $10 \mu\text{m}$ after the shuttle flight and during varying thermal conditions in space the Tracker uses a laser Alignment System (TAS). The complete TAS with all its components is shown in Fig 3.26. A laser beam with a divergence of less than 1 mrad is

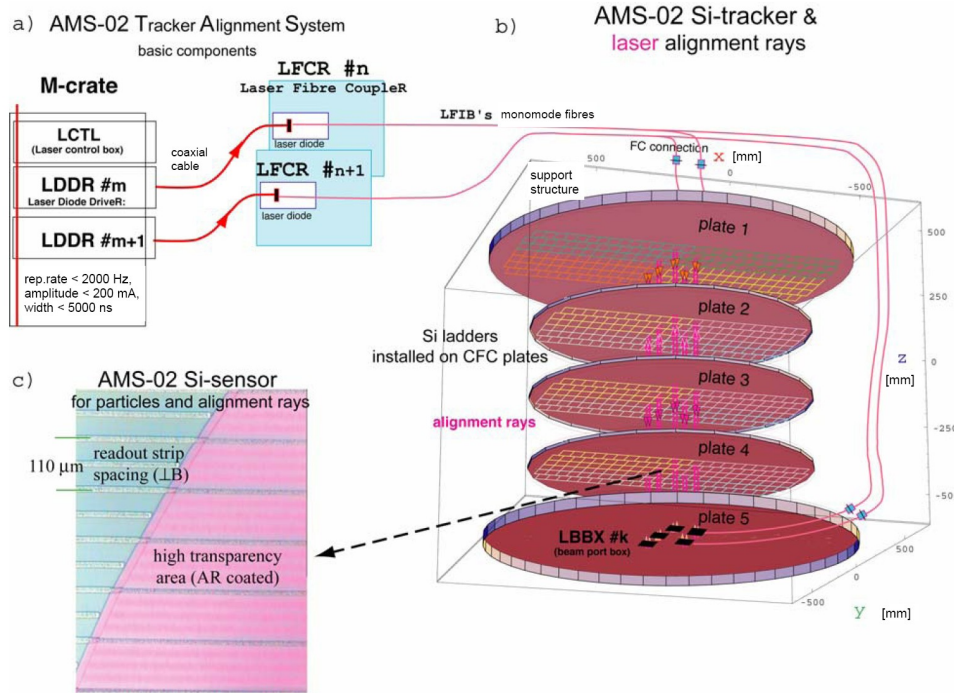


Figure 3.26: Tracker laser Alignment System. (a) TAS components in the M-Crate. (b) The laser beams are injected on the upper and lower Tracker plate by two times five beamport boxes. (c) Micrograph of Anti Reflex (AR) area.

produced by DBR (Distributed Bragg Reflector) laser diodes. The light of $1082 \mu\text{m}$ is guided by mono-mode optical fibers to 2×5 beamport boxes mounted to the outer face of the outer Tracker planes and traverses through all eight silicon layers. A special anti-reflex coating and reduced metallization ($10 \mu\text{m}$) on the laser penetrated sensors ensures a light intensity of 0.8% in the last layer. Together with this system the Tracker alignment reaches an accuracy of less than $5 \mu\text{m}$ in distance and $2 \mu\text{rad}$ in angular direction during the data taking. TAS weighs 3 kg and consumes 1 mW electric power.

The given information is extracted from the references [Cor03], [Cec03], [Cec04] and [Haa04].

An essential part of the Tracker is the superconducting magnet. Two dipole coils generate the field on the inside and on the outside twelve smaller racetrack coils guide the field and increase it. This leads to a central magnetic flux of $B = 0.86 \text{ T}$ and a negligibly small outer dipole field to avoid torques caused by interaction with the earth magnetic field. Fig 3.28 shows the field configuration in detail. All magnet coils are wound of the NbTi/Cu wires (3360 turns dipole, 1457 turns racetrack). They are embedded in a high purity aluminum stabilizer, since the pure

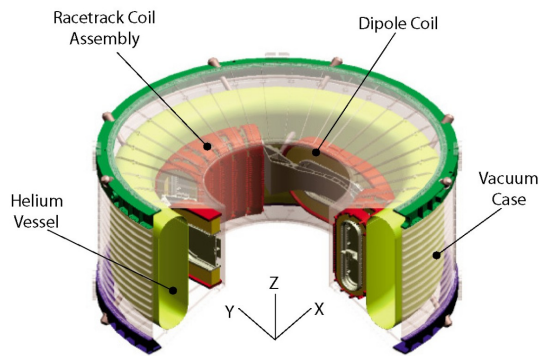


Figure 3.27: AMS-02 superconducting magnet together with the helium tank inside the vacuum case.

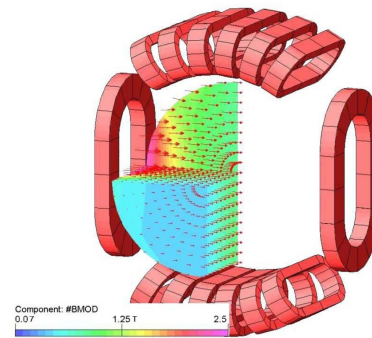


Figure 3.28: Field configuration of the AMS-02 magnet.

type-II superconductor NbTi tends to be unstable due to its low thermal conductivity. The coil cross-section in Fig 3.29 depicts the embedding and the dimensions. All 14 coils are connected in series. In case of a quench in one coil heaters are powered to quench all coils simultaneously and thus distribute the stored energy between all of them. As shown in Fig 3.27 the magnet and the helium vessel for the cooling are housed in a vacuum case, that is mounted to the USS. The magnet has a mass of 2000 kg and is supported by the vacuum case. To hold the magnet inside the tank against the strong loads appearing during launch special straps were designed with high stiffness and low thermal conductivity leaking 3 mW during operation. Fig 3.30 illustrates how the straps are feed through tubes inside the helium vessel to avoid thermal contact with the vessel. Helium has a boiling point of 4.7 K. When cooling it to the lambda point $T = 2.17$ K

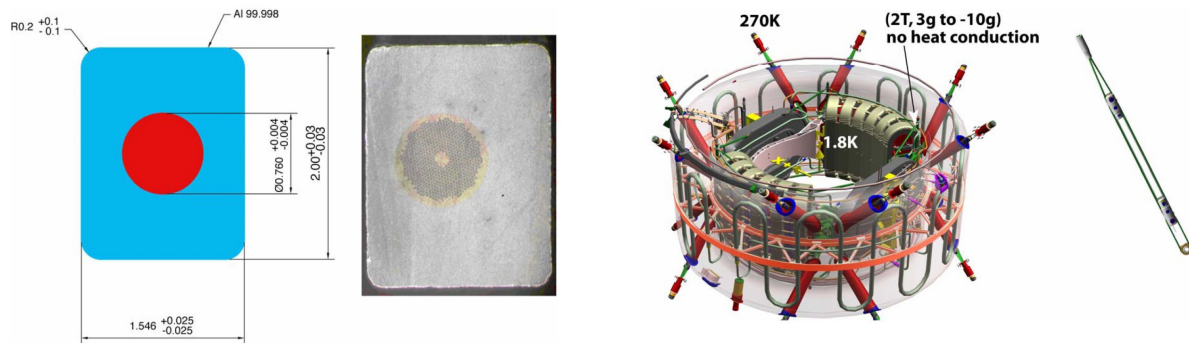


Figure 3.29: Cross-section of a magnet coil.

Figure 3.30: Mechanics of the magnet supporting straps.

it shows two phases, a normal viscous liquid Helium-I and a superfluid liquid with no friction Helium-II. The specific latent heat and the density of Helium-II is higher than for Helium-I. Therefore Helium-II was chosen to gain more cooling power in the limited space of the helium vessel. Since in zero gravity the cooling of Helium cannot be achieved by pumping away the gas phase on top, a special technique taken over from the SHOOT experiment is used. Due to the thermo-mechanical-effect of superfluid liquids the Helium-II flows from a cold to a warm reservoir. By using a porous plug of sintered steel mounted to the helium vessel Helium leaks to the vacuum on the open side of the plug, like illustrated by the drawing 3.31. In vacuum the

Helium evaporates and cools down this side. As consequence a fraction of Helium-I cools to Helium-II again and Helium-II flows back to the warmer vessel. Before the vaporized Helium-I is spilled to the space it flows in tubes and cools four concentric shields surrounding the magnet and the helium vessel. Additional four Stirling cycle coolers connected to the outer vapor shield remove 12 W of heat by consuming 100 W electric power each. Since superfluid helium has a higher thermal conductivity, the present Helium mass in the vessel is measured by the time difference between the injection of a small heat pulse to the Helium and its detection with a precise thermometer in some distance.

The magnet coils are cooled indirect with a thermal bus bar filled with Helium-II. This features a lower heat transfer during a magnet quench, since the Helium-II goes to Helium-I with a lower thermal conductivity. The magnet is only charged during operation on the ISS by a power supply outside the vacuum tank. Once it is charged the power supply will be disconnected by a persistent switch, that forms a superconductive link after closing. All leads that supply the current to the magnet are quite thin to minimize the heat leak. But therefore the mentioned thermo-mechanical-pump becomes necessary to generate a cooling flux of Helium-II at the leads during charging.

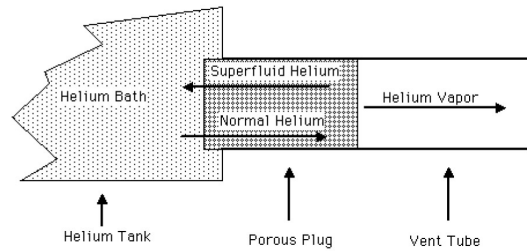


Figure 3.31: Schematic drawing of the phase separation done by the porous plug. [NAS05]

The provided information is summarized from the references [AMS09], [Bla00], [Bla02], [Bla04].

3.2.5 Ring Imaging Cherenkov Detector (RICH)

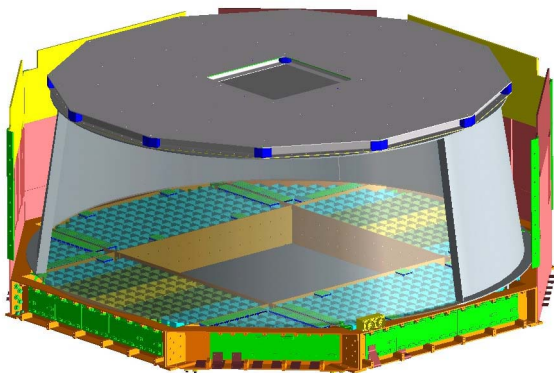


Figure 3.32: Drawing of the RICH detector.

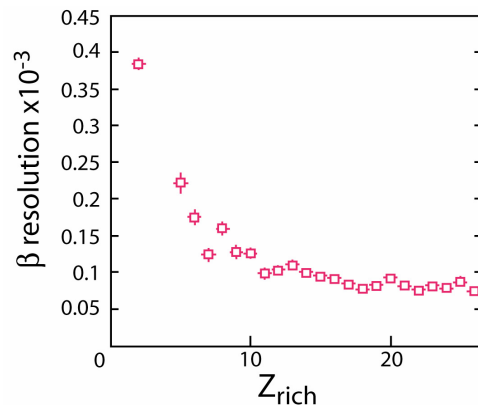


Figure 3.33: Velocity resolution of the RICH.

The AMS-02 RICH, shown in drawing 3.32, allows to determine the velocities of charged particles with a relative accuracy of 1 per mil. Its velocity resolution is plotted in Fig 3.33. In principle RICH needs to determine the opening angle of the Cherenkov cones generated by particles penetrated through a radiator material, a process described in 2.1.6. In fact the RICH PMTs on bottom just detect 2-d projected rings of the radiation from the Cherenkov radiator

on top, as plotted in Fig 3.34. Fig 3.35 depicts the particle charge resolution of the RICH gained from the number of radiated photons.

The conical shaped RICH has a 60 cm upper and 67 cm lower radius and 47 cm height and is

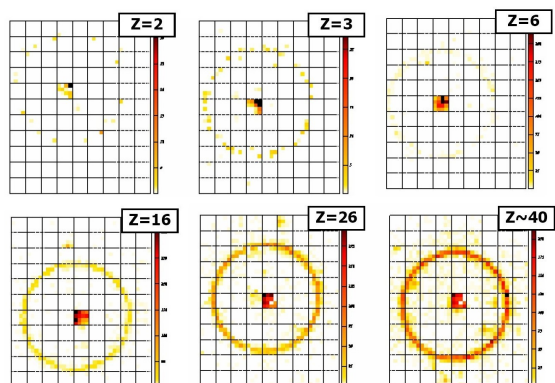


Figure 3.34: Cherenkov rings plotted for single $A/Z=2$ ion events.

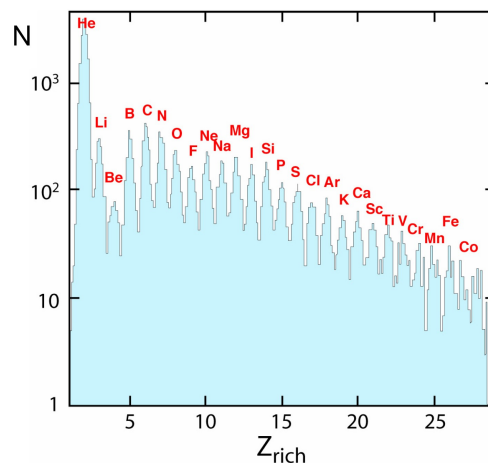


Figure 3.35: Charge distribution for $Z > 1$ measured during a beamtest in 2002 with a $n=1.03$ radiator.

mounted between the lower TOF and the ECAL. A supporting plane on top holds a 3 cm thick radiator build of NaF with $n=1.336$ in the center and a silica aerogel ($m(\text{SiO}_2) + 2m(\text{H}_2\text{O})$) with $1.025 < n < 1.075$ in the outer part. This design increases the efficiency for particles traversing the central hole of the detection plane, since larger n give a wider cone. All in all 80 rectangular blocks of aerogel sized $11.5 \times 11.5 \times 3 \text{ cm}^3$ and 16 of NaF sized $8.5 \times 8.5 \times 0.5 \text{ cm}^3$ are used. Most of the light is directly detected by the photomultipliers of the lower plane, but about 30% point to the detector outside. To collect also the outside light a conical mirror reflects it into the sensitive detector area. This effectively increases the active size of the RICH. The reflective side of the mirror is coated with 100 nm aluminum and 300 nm of SiO_2 and the mirror has a lower diameter of 134 cm and an upper of 114 cm. The coating provides a reflectivity of $>85\%$ at 420 nm wavelength. Because the residual magnetic field at the lower plane is still around 300 G, specially shielded photomultipliers are required. The chosen HAMAMATSU R7600-00-M16 fulfill this need and additionally serve a reduced size and a fast response at the low operational voltage (800 V).

The given information is derived from reference [Bu03] and [AMS09].

3.2.6 Electromagnetic Calorimeter (ECAL)

The AMS-02 ECAL is placed at the end of the detector and provides a precise three-dimensional imaging of the longitudinal and lateral shower development. Charge particles and photons lead to secondary production in the lead and the fibers of the ECAL. As long as the secondary energy is higher than a critical energy E_c they also produce particles and an electromagnetic shower emerges. A parametrization of the longitudinal shower profile is given by:

$$\frac{dE}{dt} = \frac{E_0 \cdot f^{g+1} \cdot t^g e^{-ft}}{\Gamma(g+1)}, \quad \Gamma(g) = \int_0^\infty e^{-x} x^{g-1} dx \quad (3.6)$$

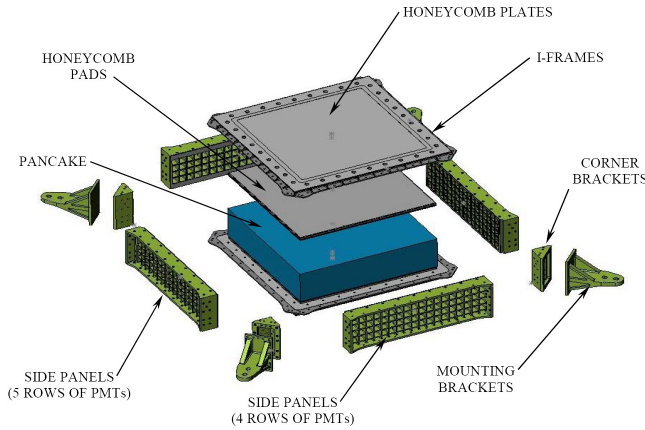


Figure 3.36: Mechanical layout of the ECAL. The active detector is labeled pancake. PMTs are mounted to the side panels. ECAL is fixed to the USS with corner brackets

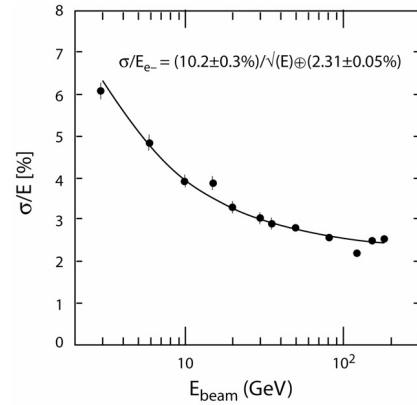


Figure 3.37: Energy resolution of the ECAL. The resolution is parameterized by the formula given in the plot.

with the Gamma function $\Gamma(g)$, $t = x/X_0$ the shower depth in units of the Radiation length $X_0=17$, g and f as fit parameters and E_0 the primary energy. The shower first grows with t^g and then start to decrease with e^{-ft} after the shower maximum

$$t_{max} = \frac{g}{f} = \ln\left(\frac{E_0}{E_c}\right) + k \quad (3.7)$$

with $k = 0.5$ for γ -cascades and $k = -0.5$ for e^- -cascades. A lateral shower size can be approximated by the lateral size of a homogenous calorimeter, the Molière radius:

$$R_m = \frac{21 \text{ MeV}}{E_c} X_0 \text{ [g/cm}^2\text{]}. \quad (3.8)$$

Typical electromagnetic shower profiles are plotted in Fig 3.38.

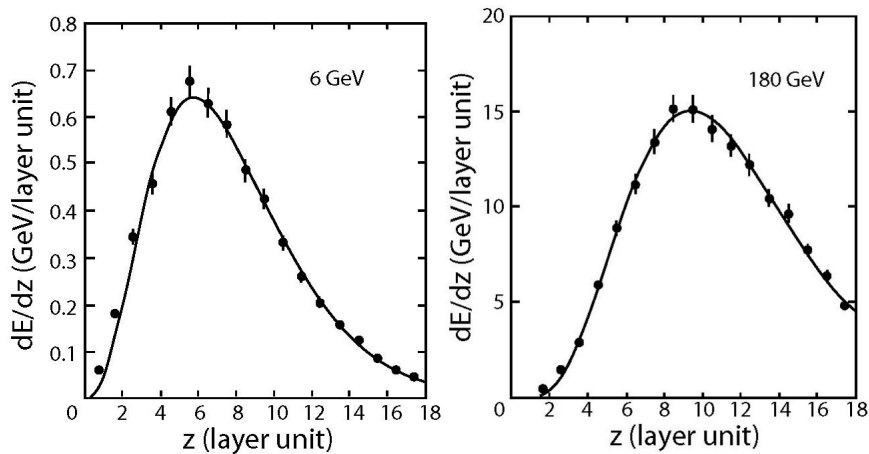


Figure 3.38: ECAL longitudinal shower profiles for 6 GeV and 180 GeV electrons.

The ECAL consists of a sandwich of lead and scintillating fiber with an active area of $648 \times 648 \text{ mm}^2$ and a thickness of 166.5 mm. It has a substructure of 9 superlayers 18.5 mm thick, made of eleven 1 mm thick lead foils interleaved with 1 mm diameter fibers fitted into grooves in the lead and glued with epoxy. The superlayers are stacked together toggling the fiber direction each time by 90° thus four layers are parallel and five perpendicular to the x-axis. Photo 3.39 visualizes the out coming fibers and their orientation.

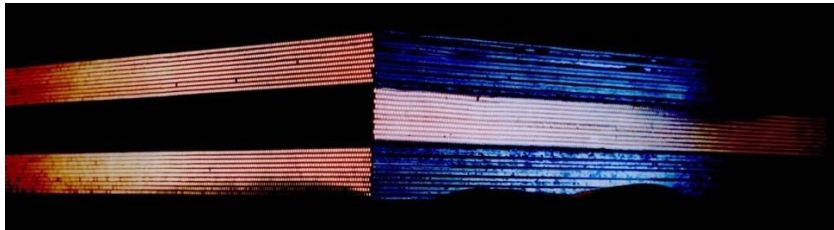


Figure 3.39: One edge of three ECAL layers. Red dots are out coming fibers.

With its average density of $6.9 \pm 0.2 \text{ g/cm}^3$ the ECAL weights 496 kg in total. As support a frame of aluminum alloy is used. It is assembled out of four panels, which house the photomultipliers, as depicted in drawing 3.36. At the top and bottom honeycomb plates are mounted and the hole structure is fixed via brackets to the USS.

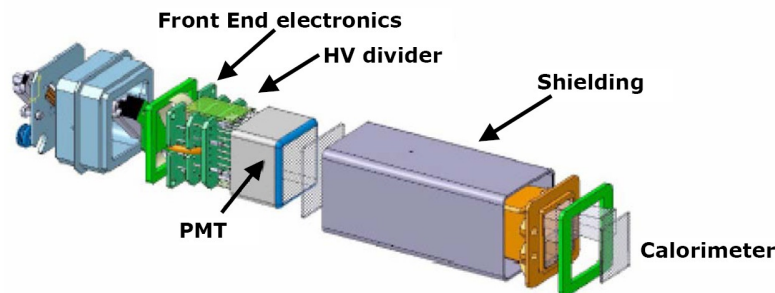


Figure 3.40: Light collection system of the ECAL. A magnetic shielding covers the light guides, the HV divider and the front end electronics.

The scintillating fibers are read out by 324 four-anode HAMAMATSU R7600-00-M4 photomultipliers (PMT), shown in Fig 3.40. This results in a total of 1296 active cells. Each anode covers an active area of $9 \times 9 \text{ mm}^2$ connected with 35 fibers. The 36 PMTs of a superlayer are connected alternately to opposite ends. Due to a residual magnetic field of 20 G the PMTs, the light guides, the HV divider and the front end electronics are housed in a 1 mm thick magnetic shielding made of a soft iron square tube 30.5 mm wide and 74 mm long. Additional to the TOF trigger ECAL provides a stand alone γ -trigger. This trigger is activated in two steps. The first fast decision within 180 ns comes from a threshold on the PMTs of the six central layers. The second provided before $1 \mu\text{s}$ is obtained from a fast reconstruction of the particle direction. Only particles with inclination smaller 20° are accepted and ensured that they have passed all other subdetectors. An efficiency of 90% is expected at 2 GeV and more than 99% at larger than 10 GeV. As soon as the trigger decision has been taken, it is delivered to the AMS-02 global trigger.

All provide information can be found in reference [Cad02] and [AMS09].

3.2.7 AMICA Star Tracker and GPS System

The AMICA¹ Star Tracker is a pair of optical telescopes with CCD-cameras² to measure the AMS-02 orientation by comparing the image with sky maps. This system determines the pointing direction with arc-sec precision. An overview of the system components and its position on the AMS-02 detector is given by Fig 3.41.

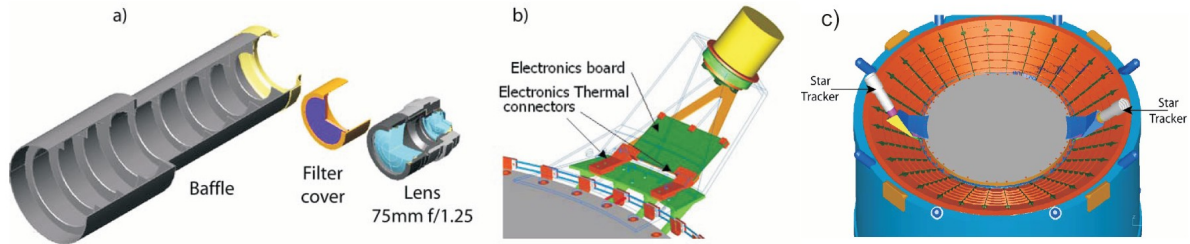


Figure 3.41: AST, AMICA Star Tracker system. (a) AST optics. (b) AST support and readout structure. (c) AST position on AMS-02.

Both CCD-cameras have a frame rate of 30 Hz using a 512×512 pixels CCD chip with $16 \times 16 \mu\text{m}^2$ pixel size. Their lenses has a focal length of 75 mm and f/1.25 with 6 mm aperture. Band pass filters (475 nm to 850 nm) reduce the noise, as well as prevent saturation and protect from infrared and ultraviolet light. The 369 mm long baffles suppress emitted or reflected light from the space station. Both support structures are made of reinforced carbon fiber with zero thermal expansion to ensure mechanical stability. The AST orientations are chosen such, that no object like solar panels, radiators, etc. reach into the field of vision. The electronics consist of a controller unit, separate program, data and image memories and a housekeeping board measuring voltages, currents and temperatures. An additional photo-detector delivers the sky background intensity and in case of too high background the CCD intensifier is switch off. Only Stars with a magnitude lower than 7th are acquired in a field of $6.25^\circ \times 6.25^\circ$.

The AMS-02 GPS has a precision of a few microseconds, thus the AMS-02 data can be correlated with other experiments in the electromagnetic spectrum. As GPS system was chosen the ALCATEL Topstar 3000D, which is connected to two antennas mounted in different directions to ensure sufficient satellite signal reception. The gathered time information will be included in the event data together with the local timer of the trigger system.

The provided details are included in reference [Car05] and [AMS09].

¹AMICA, Astro Mapper for Instrument Check of Attitude.

²CCD, Charged Coupled Device.

Chapter 4

The AMS-02 TRD data acquisition electronics

The development of the AMS-02 electronics required large efforts to cope with the requirements of power consumption, radiation and vacuum stability, weight, schedule and money. All AMS-02 data acquisition and power supply electronics are housed in crates or boxes that are screwed to the Wake or Ram radiators at the sides of AMS-02, which radiate the heat produced by the electronics. The cost of the Data Acquisition (DAQ) system was reduced by avoiding as far as possible the assembly of space qualified components. Instead high graded commercial parts were tested for bit flips and latch up in heavy ion beam tests to verify the functionality under ~ 1 kRad/year radiation in space. To prevent any loss of detector parts due to electronics part failure, most of electronic boards have a two fold redundancy. Board and crate level Environmental Stress Screenings (ESS) and Thermo Vacuum Tests (TVT) assured the mechanical stability during launch and the operation under extreme temperatures in the space vacuum. All AMS-02 electronics fulfill the NASA requirements of electromagnetic compatibility, proven by EMI-tests. This chapter gives a brief introduction to the general AMS-02 DAQ-system, but concentrates on the development and test of the TRD DAQ-system, which is one topic of this thesis.

4.1 The AMS-02 DAQ-system

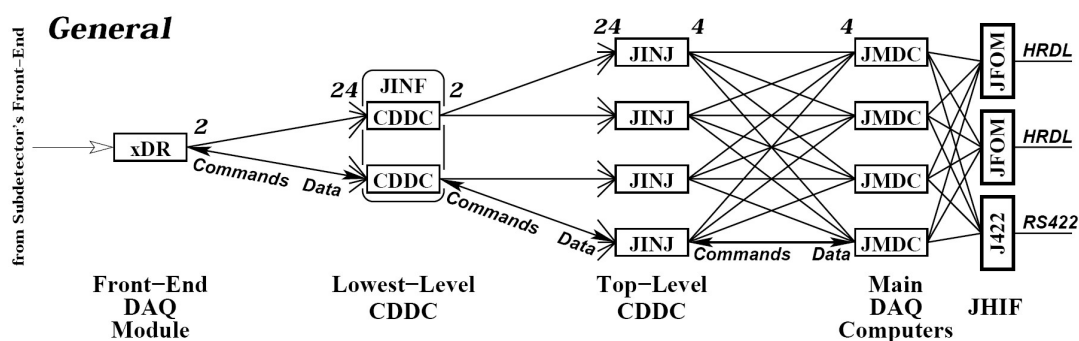


Figure 4.1: AMS-02 DAQ structure. First the detector data is reduced in *xDR* nodes and then gather and buffered by *JINF*s in the subdetector crates. On request it is send send to *JINJ* and from there to the *JMDC*. It least the data is linked to the *HRDL* and from there via *RS422* to the ISS data infrastructure. All links are bidirectional. [AMS09]

The AMS-02 DAQ system has a unified design, that reduced the development time and enhances the system reliability. The unification is reached by a Common Digital Part (CDP) in all subdetector DAQ nodes (xDR) and a slightly modified Command Distributor and Data Concentrator (CDDC) to collect the data in the higher level DAQ. A schematic drawing of this infrastructure is depicted in Fig 4.1. As soon as a trigger arrives, all detector signals are preamplified, shaped, sampled, digitized and multiplexed in the subdetector front ends and read into a gate array buffer memory of the subdetector CDPs. Then the raw data is reduced to detector hit data and stored in a buffer memory. On request this data is sent from the CDDC inside the subdetector electronics via point to point AMSWire links to the top level CDDCs and reaches the main computers linked to the ISS data Infrastructure.

The 120 V power arriving from the ISS solar panels is converted by the AMS-02 Power Distribution System (PDS) into 28 V. From there it is distributed to the subdetector power supply boxes, which convert the incoming voltage to the specific subdetector needs by DC/DC converters.

The CDDCs inside the subdetector electronics also operate as LeCroy protocol master for slow control commands, that control the digital functionality of the subdetector slave boards as sketched in Fig 4.2.

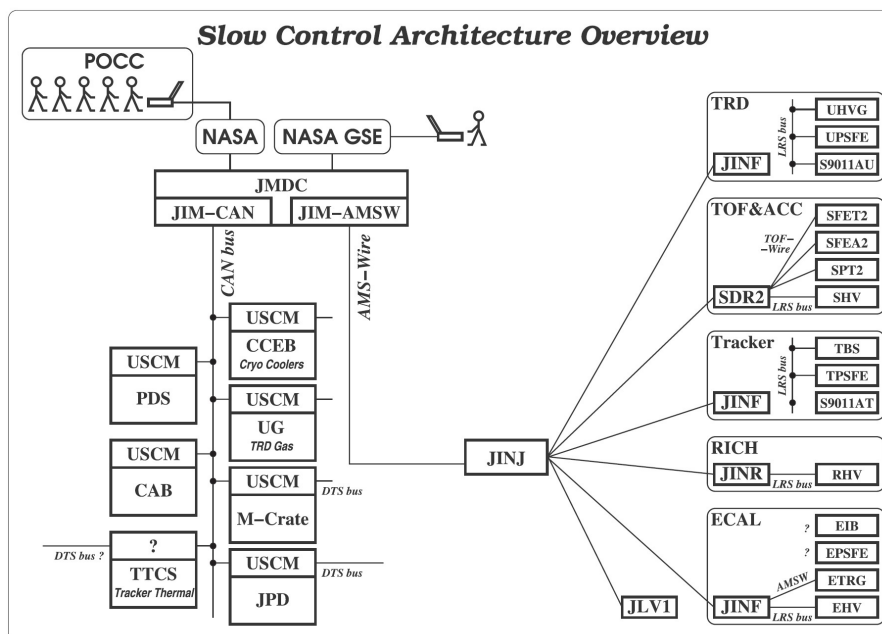


Figure 4.2: Slow control commands are transmitted on two different paths. The TOF, TRD, Tracker, ECAL, RICH subdetectors receive LeCroy commands by AMSWire links, all other subsystems are controlled via CAN-Bus. [AMS09]

4.1.1 Interfaces to the International Space Station

Two power feeds are connected to the ISS solar arrays, which provide between 109 and 126 V. AMS-02 is designed to consume 2000 W. The PDS fulfills the NASA requirements of isolation,

grounding and inrush currents. A thermal interlock powers PDS heaters when AMS-02 is switch on. The PDS converts the ISS power with >90% efficiency and switches the supply voltages of the subsystem power boxes. It is controlled and monitored with a pair of Universal Slow Control Boards (USCM).

Telemetry and commanding data are sent via the Low Rate Data Link (LRDL) based on the MIL-STD 1553B dual serial bus. This link is split to each of the four AMS-02 Main DAQ Computers (JMDC), which include an IBM PowerPC 750 microprocessor with RISC architecture and 200 GB flash memory as data buffer. The LRDL uses the ISS Ku-Band and S-Band data path to prevent single-point failures of the bus splitting. On the outside AMS-02 has two link splitters, that can be swapped during Extra Vehicular Activity (EVA). About 20% of the LRDL are allocated by AMS-02 with a duty cycle of 70%. Ten byte of critical health data are transmitted with a close to 100% duty cycle.

Data is transferred through the High Rate Data Link (HRDL) based on fiber optics communication. On the ISS the HRDL is connected to the Ku-Band radio downlink, which supports 43 MBit/s. All four JMDCs are connected to HRDL in redundancy and allocate 2 MBit/s of the link. As well as for LRDL also the HRDL cable can be swaped during an EVA.

4.1.2 DAQ electronics communication (AMSWire/Can-/LeCroy-bus)

The AMS-02 DAQ electronics uses three communication standards for bidirectional command and data transmission: the point to point link AMSWire, the CAN-bus and the LeCroy-bus.

AMSWire is based on the ESA SpaceWire standard with Data-Strobe (DS) encoding. The data rate is 100 MBit/s in both directions. In AMS-02 this link sends data from the subdetector DAQ to the higher DAQ and slow control commands in opposite direction. Signals are transmitted as Low Voltage Differential Signals (LVDS) on two wire pairs in each direction. One pair transmits the data, the other the Strobe, which changes its state whenever the next data bit value is the same as the present. This coding includes the transmission clock and improves the skew tolerance to almost 1-bit time as compared to of 0.5-bit time for data clock encoding. AMSWire is a Master-Slave protocol, that means a slave does not reply until the master requests it. Advantages of the LVDS transmission are insensitivity to potential differences of driver and receiver and noise suppression as well as low electromagnetic interference due to the low opposite currents. Wire connections are done by a micro-miniature-d type connector with eight signal contacts and a screen termination contact. The link can be terminated with 100 Ω resistors.

The serial CAN-bus was developed by BOSCH in the 1980s with a new specification v2.0 in 1991. In AMS-02 this bus transmits commands for and replies of the subdetector control electronics and the PDS. It consists of two lines, CAN-H and CAN-L, with differential signals. The dominant bit, two opposite levels on CAN-H and CAN-L, are referred as "0", the recessive bit with identical levels are referred to as "1". Electrical damages due to signal collisions on the bus are avoided by open-collector outputs. The CAN-bus needs to be terminated by 120 Ω resistors at each end. On a 40 m bus length a data rate up to 1 MBit/s can be reached. As a multi-master bus CAN allows the communication in redundant systems independent of a failure in one node, which are switched off. A receiver is not addressed directly, rather the nodes are contacted by a message identifier. The transmitter includes a Cyclic Redundancy Check (CRC) in the message. In case of an inconsistent check by the receivers, the transmitter is asked to restart the communication immediately by receiving an acknowledge error.

The LeCroy-bus was designed by the LeCroy Corporation for the digital interface of the high voltage Chip MHV100, used for the High Voltage Generator Board (UHVG) of the TRD electronics. In AMS-02 this bus is used for communication on the lowest level of the slow-control system. Signals are transmitted using LVDS on two wire pairs one for data and one for clock. The communication is initiated by the bus master (e.g. JINFv2). In the first 32 bit of the communication a command is transmitted to the slave, in the second 32 bit the slave sends an echo or a reply in case of a read request.

4.1.3 Common parts of the DAQ electronics (CDP/CDDC)

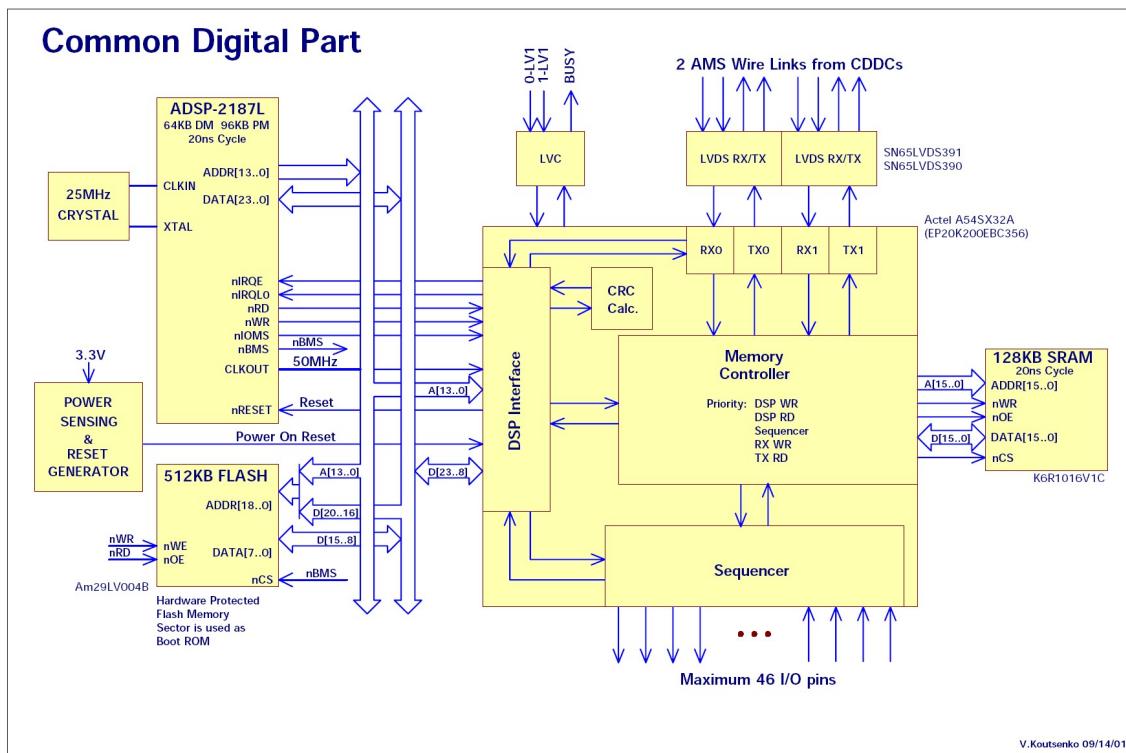


Figure 4.3: The Common Digital Part consists of an Analog Device Digital Signal Processor (ADSP), a flash memory, an SRAM, LVDS driver/receiver and a Field Programmable Gate Array (FPGA).

The Common Digital Part (CDP) contains the DAQ logics of each AMS-02 DAQ board. It consists of an Analog Device Digital Signal Processor DSP 2187L, a 512 kB AMD AM29LV004B Flash memory, and 128 kB Samsung Static Random Access Memory (SRAM) K6R1016V1C and a Field Programmable Gate Array (FPGA) Actel A54SX32A. During the FPGA program development a reprogrammable Altera Apex EP20K200EBC356 was used and then exchanged with the radiation hard single programmable Actel FPGA including the final program. With an arriving LV1 trigger at a CDP node the FPGA sequencer starts the reading of digitized data from the detector front ends to the SRAM. If the DSP recognizes a raw event it processes the event and stores the reduced event in the output buffer of the SRAM. In case the CDP receives AMSWire commands, it stores them in the SRAM and the DSP reads and processes them.

After an event request the data is transmitted from the SRAM to the requesting AMSWire transmitter. A layout of the CDP is depicted in Fig 4.3.

The DSP is a single-chip micro processor with build in 32 k of 24-bit program memory and 32 k of 16-bit data memory clocked with 25 MHz. It is power with 3.3 V consumes 168 mW at full speed. In an additional low power state it consumes 32 mW or 12 mW with reduced internal clock until an interrupt occurs. One instruction is executed in a single cycle, yielding 50 MIPS¹ processing power. Up to eleven interrupts are available, four are external. Internally five buses are used a programm memory address-, a program memory data-, a data memory address-, a data memory data- and a result bus. Externally the two address buses share a 14-bit address bus, which allows together with the 24-bit data bus to access the off-chip flash memory and the SRAM via the gate array DSP interface. Its three computational units ALU, MAC and shifter are connected by the data-, the program- and the result-bus.

The CMOS flash memory has a size of 4 MBit segmented in 512×8 bit and is powered by 3.3 V. Its data sheet guarantees 1000000 write cycles per sector and 20 years data retention at 125°C. The DSP boots from the flash memory. The first three memory sectors are hardware protected and contain a bootstrap code, a boot loader and three identical copies of a ROM Monitor. The ROM Monitor is the base program, that serves AMSWire request and allows to load programs from the flash memory. During boot the bootstrap code is loaded and by its execution is loaded the boot loader. The boot loader does a CRC² of the three ROM monitor versions and loads the first intact one. If all three versions are corrupted, it is reconstructed by majority logics out of the corrupted ones. Remaining eight sectors of this memory allow to store data or detector specific programs.

The SRAM with 64K×16 bit is powered by 3.3 V and has a standby power dissipation of 5 mA and 93 mA in operation. In general SRAMs require large memory cells and thus large packagings, which make them expensive. But otherwise this allows to feed all address lines inside and makes them fast, since all address bits can be applied at the same time. The CDP accesses the SRAM with 20 ns.

An FPGA houses a large amount of logic gates, that can be interconnected volatile or nonvolatile by programming tools depending on the chip type. Afterwards the gate network represent a program, that is executed in a single clock cycle. Thus a processing power comparable to CPUs is achieved, while the power consumption is much less due to lower clock rates. The AMS-02 CDP and CDDC FPGAs contain common logic parts like AMSWire links, a CRC calculation, a DSP interface and a memory controller. The CDP FPGA houses a sequencer including sequences specific for each subdetector to start the multiplexing of analog signals to the ADC and to read digitized data. The CDDC FPGA the space for four additional AMSWire protocols to connect up to four master and 24 slaves. All FPGA firmware parts were developed using VHDL³. The common firmware parts were programmed by MIT and the specific parts by the subdetector groups. During the development phase the programs were directly loaded to a volatile SRAM of an Altera Apex FPGA or from a nonvolatile boot memory (EPCT32 flash EEPROM⁴). Since the firmware in a SRAM can be damaged by radiation, the final software version was programmed to the Actel Antifuse FPGAs. Both FPGAs types have the same supply voltage of 2.5 V and a clock of 50 MHz provided by the DSP. The Actel Antifuse

¹MIPS, Million Instructions per Second.

²CRC, Cyclic Redundancy Check.

³Very High speed integrated circuit Hardware Description Language.

⁴Electrical Erasable Programable Read Only Memory

FPGA has metal-to-metal antifuse interconnections between logical gates and the gates are interconnected by electrical by burning appropriate connections.

4.2 The TRD DAQ-system design and development

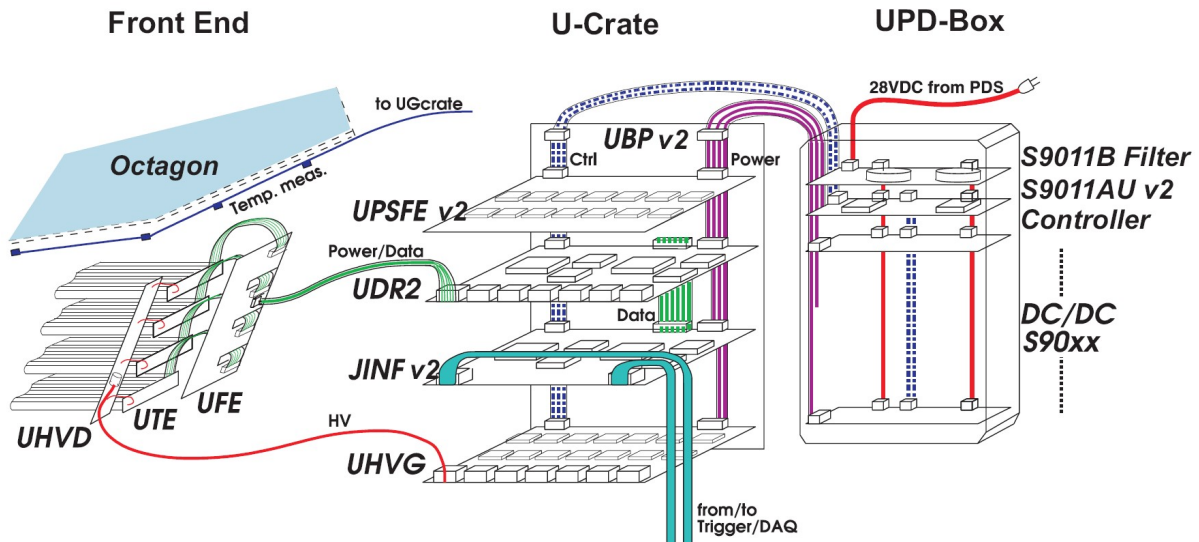


Figure 4.4: Schematic drawing of the TRD DAQ system. The system consists of front end electronics, two U-Crates and two UPD-Boxes. The front end electronics are mounted to the detector, close to groups of always four straw modules. A U-Crate and a UPD-Box build a fully functional readout set. One of the two sets is mounted to the wake the other one on the ram radiator.

The TRD DAQ system consists of front-end electronics attached to the detector side, data acquisition and high voltage electronics housed in two Crates (U-Crate) and DC/DC converters with slow control electronics inside two power distribution boxes (UPD). Drawing 4.4 illustrates an overview of the system. The U in the following acronyms stands for the German word *Übergangsstrahlung* meaning *transition radiation* in English. The detector and the front-end electronics have been built by the RWTH Aachen and the responsibility for the electronics development and production have been taken by the University of Karlsruhe.

The AMS-02 TRD electronics development and production was done in four steps. In the Engineering Model (EM) phase all electronics circuits and the FPGA firmware were designed, built and tested for their functionality. For the level 1 Qualification Model step (QM1) the TRD electronic boards with final functionality were built in Europe. Then this boards underwent a laboratory and a beam test to verify full functionality and the design DAQ rate. Since the production of space qualified electronics is quite expensive most of the AMS-02 electronics production was assigned to the NASA certified facilities of the Chungshan Institute of Science and Technology (CSIST) in Taiwan, which already did the design and production of the Main DAQ Computer (JMDC). The concentration on one company also assured the same production standards and less qualification control overhead, but required a knowledge transfer to CSIST

in a level 2 Qualification Model (QM2) production. Only minor design changes were applied during this step. The QM2 production included board quantities for one complete U-CRATE as well as UPD and was space qualified by extensive board and a crate level tests. Afterwards the Flight Model (FM) production was started with quantities of 2 U-Crates and UPDs and 1 Flight Spare (FS) U-Crate and UPD. This final production then went through AMS-02 acceptance tests.

4.2.1 TRD front-end electronics (UFE/UTE/UHVD)

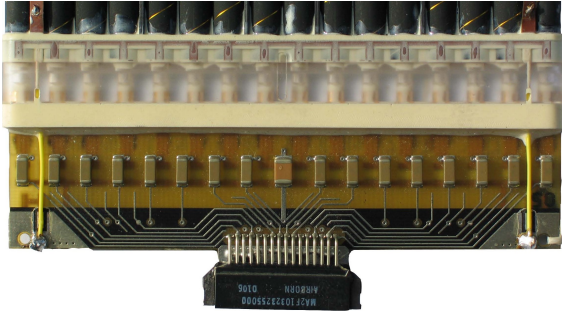


Figure 4.5: Photo of the UTE mounted to the end of a straw module.



Figure 4.6: Photo of the UHVD board.

The TRD Tube End boards (UTE) are mounted to each detector module, as visible in photo 4.5. They supply the 16 wires of a module with high voltage via $2\text{ M}\Omega$ resistors and decouple the signals from the high voltage with a 150 pF capacitor.

Fig 4.6 shows the High Voltage Distributer (UHVD), a simple wire board with HV-connector. It is mounted to the octagon walls and splits the high voltage of a U-Crate HV-channel into separate lines for a group of four modules. All modules of a group are connected to one Front-

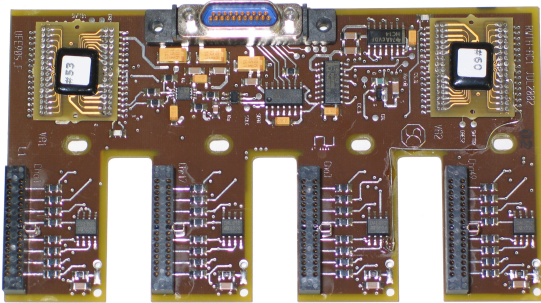


Figure 4.7: Picture of the UFE.

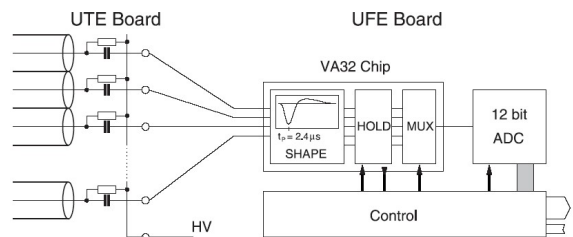


Figure 4.8: Scheme of the TRD front end electronics.

End board (UFE), which is mounted to the TRD octagon walls and shown in Fig 4.7 and 4.8. The analog signals of all 64 channels are amplified by two IDEAS VA32HDR12 chips on the UFE. Each chip contains 32 preamplifiers, CR-RC shapers, a sample-and-hold as well as a multiplexer. They have linear dynamic ranges up to 1.5 pC with 1% accuracy and a peaking time of $2.4\ \mu\text{s}$. All multiplexed signals are digitized by a 12-bit serial Analog Device 7476 ADC. An increase of 2 ADCcounts/fC leads to a dynamic range of 3000 ADC counts. Thus for a gas gain of 3000 a MIP corresponds to about 80 ADC counts. The noise is below 2 ADC counts

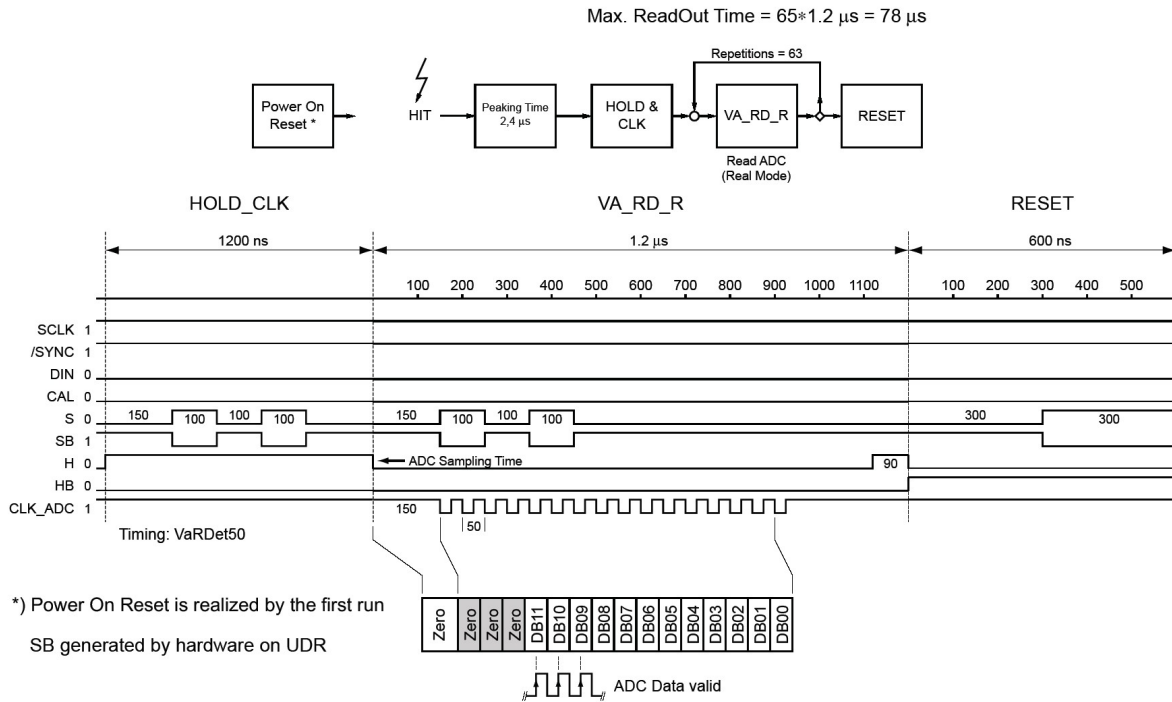


Figure 4.9: Readout sequence defined for the UFE boards.

and the pedestal in range of 400 ADC counts. This allows measurements from 0.3+MIPs up to 33 MIPs or up to 45 MIPs in the full dynamic range. The 82 UFEs of the TRD are supplied, controlled and read out via a cable connection to 12 TRD Data Reduction boards (UDR2) in the U-Crate. The ± 2 V supply lines for the digital and analog electronics are separated to avoid injection of noise coming from the digital side. But these lines were combined inside the U-Crate to reduce the quantities of UPSFEs (UPSFEv2) after a redesign for weight reduction. Shift-in signals activate one of the two parallel connected VA chips. This signals and also the multiplexing clock, the holdVAs to hold signals in the VA, the shinB, the dreset for a VA reset and the teston signals for the test mode are generated by a HCC¹ chip, which receive the UDR2 control sequences. The HCC chip was originally design for the Tracker, that uses 64 channel VA chips. Therefore the multiplexing clock is reduced from 64 to 32 by a JK flip flop on the UFE board. Two main UFE sequences are available, a standard readout and a calibration sequence. A standard sequence read out takes $78 \mu\text{s}$. Before the calibration sequence starts, a DAC value is set. The read back of the DAC pulse in all channels takes 2.6 ms. The first channel is read with a delay ($240 \mu\text{s}$ instead of $30 \mu\text{s}$), as shown in Fig 4.9, to overcome a cross talk problem between the first and second VA channel.

4.2.2 TRD DAQ and supply electronics (U-Crate)

The U-Crate walls are made of single pieces of aluminum 7055, which were anodized at surfaces where no electric and thermal contact is desired and otherwise alodined. All U-Crate drawings

¹HCC, Hybrid Control Circuit.

were made by CGS¹ and the machining and surface treatment was performed by CSIST. The 16 boards inside a crate are U6-sized cards connected via a backplane (UBPv2). A central JINFv2 splits the U-Crate in a high voltage side with 6 UHVGs and low voltage side with three power groups built by one UPSFEv2 and a two UDR2. As inner plane the boards have a copper layer to conduct heat to the sides, where it is contacted to pads with wedge locks screwed on. The wedge locks guide the boards in the U-Crate slits during insertion and achieve mechanical stability as well as thermal contact after fixing. All boards are protected by digital Solid State Fuses (SSF), which disconnect the 3.3 V digital supply line (5 V for UHVG) in case the current is continuously larger than 1.5 to 2 times the nominal value in a latch delay time. The SSFs are also used to switch on/off redundant halves of a board by AMSWire or LeCroy-bus commands. Internal temperatures can be monitored by 84 sensors of the LeCroy MHV100 chip on the 6 UHVGs and read via LeCroy protocol. On the outside DALLAS sensors are placed on the crate walls. They are read by the slow control electronics of the TRD gas system together with about 200 DALLAS sensors inside the TRD octagon.

Backplane (UBPv2)

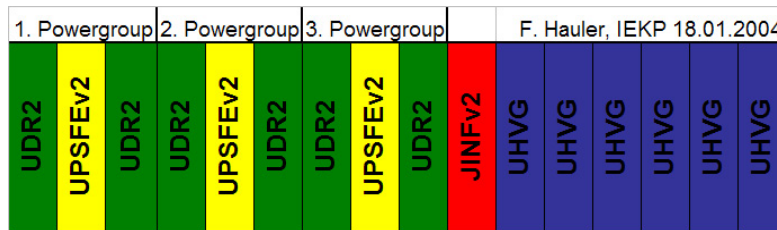


Figure 4.10: Board placement on the UB Pv2.

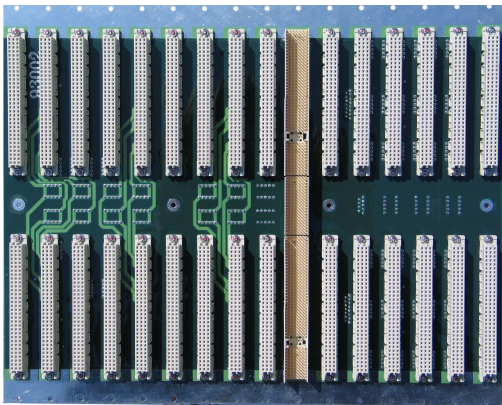


Figure 4.11: Top view on the UB Pv2.

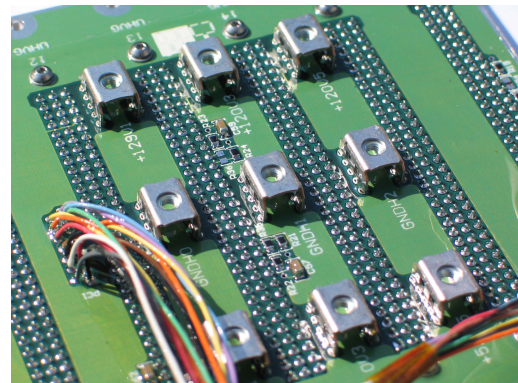


Figure 4.12: Power taps and slow control connector on bottom of the UB Pv2.

The TRD backplane (UBPv2) connects the U-Crate boards to the power supply and between each other by 15 slots with 2×96 VME connectors and a JINFv2 slot with a 525 pin cPCI connector. A photo of the backplane is shown in Fig 4.11. It was developed in a collaboration of MIT and the University of Karlsruhe. On one side of a JINFv2 six UHVGs are placed and

¹CGS, Carlo Gavazzi Space, Milan, Italy

the other side is split into three power groups, each with two UDR2s and one UPSFEv2, as sketched in Fig 4.10. The seven currents from one UPSFEv2 flow via the backplane and two UDR2s into 14 UFEs connected to this UDR2s front panels. All redundant ± 2 V line regulator outputs of a UPSFEv2 are connected together on the backplane. The power connections to the UPD are realized by a cable screwed with ring lugs to 39 power tabs on the backside of the UBPv2, as shown in the photo 4.12. For the slow control interconnection to the UPD a 15-pin micro-d pigtail connector is soldered to the backside. The TRD grounding scheme tries to reduce the impact of digital noise by separating the DC/DC converter grounds in the UPD and connecting the high voltage (120 V, 5 V) and low voltage (± 2.8 V) grounds as well as the shield only on the octagon and the digital ground (3.3 V) only to shield (*dirty ground*) on the backplane.

Main computer interface board (JINFv2)

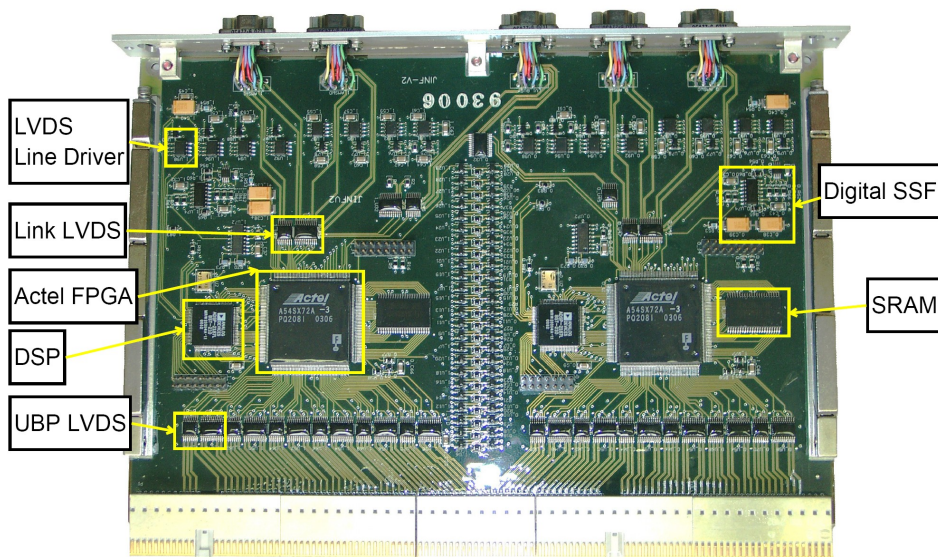


Figure 4.13: Front side of a JINFv2 board. Two CDDCs feature a two fold redundancy.

The JINFv2, visible in Fig 4.13, acts as the U-Crate interface to the higher level DAQ and is build of two redundant CDDCs. It has five 9 pin micro-d front panel connectors, four are AMSWire links and one a trigger/busy link. Two AMSWire links belong to a redundant half of the JINFv2 and allow an additional wire redundancy for each half. After an AMS-02 weight optimization this wire redundancy is planned to be omitted. Just half of the 24 addressable AMSWire links of a JINFv2 CDDC are used by the six U-Crate UDRv2s. The slow control of the three UPSFEv2, six UHVG and the S9011AUv2 inside the UPD is done with eight LeCroy-buses. Due to the amount of connections for all communication lines JINFv2 has a cPCI connector to the backplane. After power up both JINFv2 CDDCs are on, but under nominal conditions one is switch off to reduce the power consumption. JINFv2 was developed by MIT.

Data reduction board (UDR2)

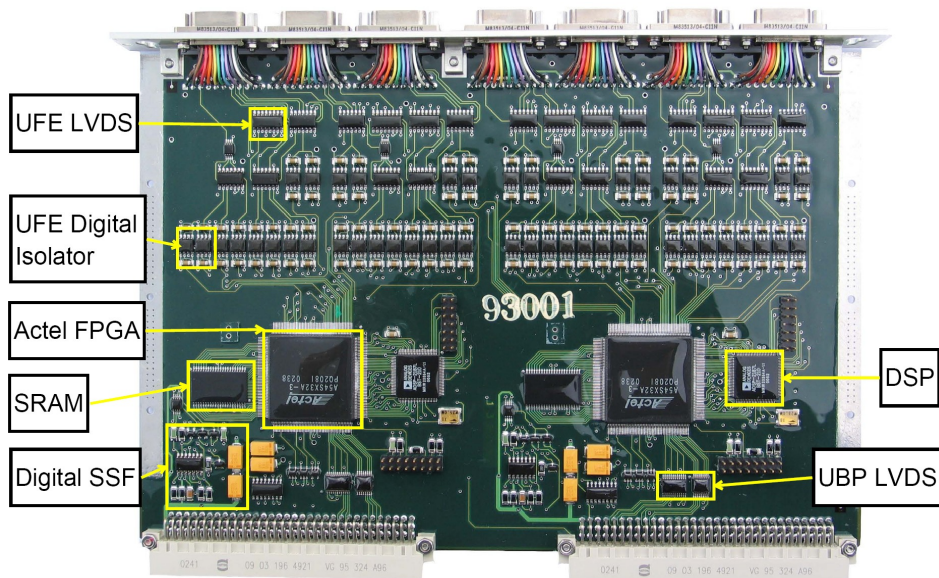


Figure 4.14: Front side of a UDR2 board. Two CDPs feature a two fold redundancy.

The UDR2, shown in Fig 4.14, acquires data by sending sequence signals to the UFE. Afterwards it reduces the data by zero suppression and stores the processed data until the JINFv2 board collects it. At a trigger rate of 2 kHz the raw data of the TRD is approximately 20 MByte/s and is reduced by the UDR2s to 78 kByte/s for single track events. The UDR2 contains two redundant CDPs powered with 3.3 V and a Detector Dependent Part (DDP) powered with ± 2 V. Only one CDP can be active on the UDR2. A SWAP/OFF signal (high/low) changes between the redundant parts. The DDP distributes the power from the UPSFEv2 to seven connected UFEs and transfers all signals between the UFEs and the CDP. Power line 1/2, 3/4 and 5/6 are merged and line 7 of the two power group UDR2s are merged on the backplane. Each of this merges is supplied by its own ± 2 V UPSFEv2 channel in one power group. To avoid digital noise injection to the UFEs, the 3.3 V CDP signals are decoupled with an Analog Device high speed digital isolator from the ± 2 V of the DDP. The UDR2 was developed in cooperation of CAEN¹, MIT, INFN, RWTH Aachen and University of Karlsruhe.

Power Supply for Front-ends board (UPSFEv2)

The UPSFEv2, depicted in Fig 4.15, houses 14 linear regulators with ± 2 V output supplying 14 UFEs. Two double redundant Actel antifuse FPGAs control and monitor the status of the 14 linear regulators as well as the solid state fuses of the UHVGs and UDR2s. The FPGAs are accessed by LeCroy protocol on separate buses. Since the three UPSFEv2s on the UBPv2 use the same buses, the boards have a 5 bit geometric address set by jumpers on the backplane. This address corresponds to the slot number on the backplane. By splitting the 14 linear

¹CAEN, a company in Viareggio, Italy, which is specialized on high energy physics and aerospace electronics as well as microelectronics.

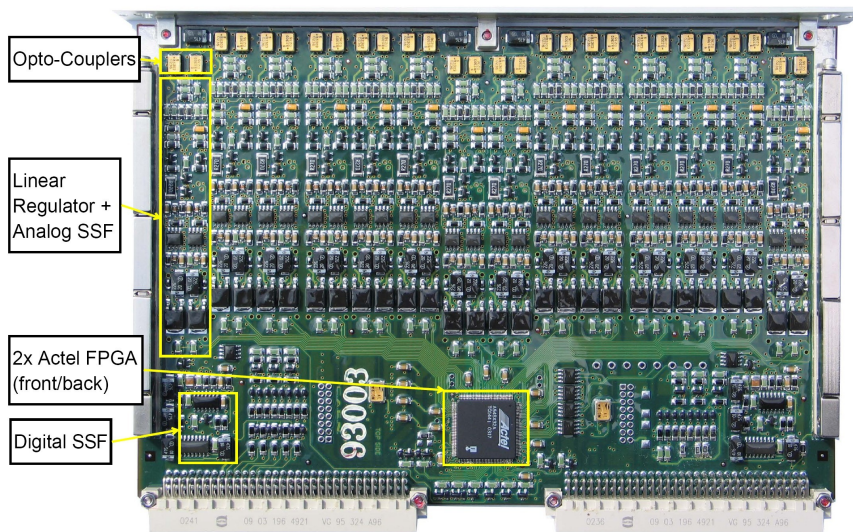


Figure 4.15: Front side of a UPSFEv2 board. The board houses two times 7 linear regulators and two Actel FPGAs on the front and back side to achieves a two fold redundancy.

regulators into seven primary and secondaries a redundancy is achieved. Each regulator of the first half is interconnected in parallel to one of the second half and has its own output to the backplane connector. Output diodes prevent flow back currents between the regulators. The two halves are supplied by independent ± 2.8 V, which allows to switch off one half and save power by *cold* redundancy in nominal condition.

The digital 3.3 V control and status feedback signals are coupled with optocouplers to the analog 2.8 V side. Analog SSF circuits for each regulator channel prevent overcurrents, that might force a UPD DC/DC-converter to stay in permanent overcurrent protection. In case of a latch-up the outputs are switch off and recover after 250 ms.

The linear regulator circuit provides a ± 2.8 V to ± 2.0 V conversion efficiency of 71%. On each redundant half a DALLAS DS18S20 temperature sensor is mounted, that reads temperatures between -55°C to 125°C with a digital resolution of 9-bit and a conversion time of 750 ms. They need to be powered by 5 V and read by the DALLAS 1-wire bus. After the loss of a U-crate USCM due to a required weight reduction, there is no circuitry providing a readout from the inside and this sensors are unused.

High Voltage Generator board (UHVG)

The UHVG, visible in Fig 4.16, consists of 14 Cockcroft Walton high voltage elevators. Always two elevators are interconnected by diodes, which achieves cold double redundancy. Thus seven high voltage channels are available per UHVG and supply 7×4 TRD straw modules via the UHVD boards. One elevator is built of 16 diode/capacitor stages and rises the primary 120 V up to a maximum of 1750 V. The oscillating input voltage for an elevator is controlled by a LeCroy MHV100 chip. Each UHVG half is supplied by separate 120 V for the elevators and 5 V for the LeCroy chip and connected to a different LeCroy bus. For a LeCroy protocol access to all MHV100 chips three bits of the address are set on the boards and the other two on the

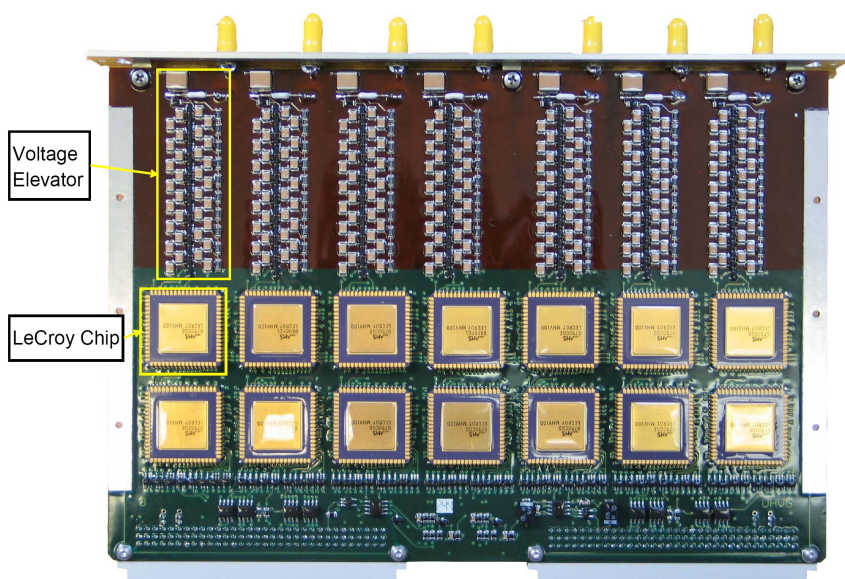


Figure 4.16: Front side of a UHVG board. The board houses two times 7 linear Cockcroft Walton high voltage elevators controlled by LeCroy MHV100 chips to feature a two fold redundancy.

backplane to define the slot. The MHV100 chip houses several DACs, an ADC and the power control logics. The different DACs set the output voltage and the overcurrent and overvoltage limit and the ADC digitizes the temperature, the HV current and the HV feedback voltage. Additionally a previous DAC can be read by the ADC. To reach a necessary ± 5 V accuracy off all HV channels, each channel has to be calibrated. One unprotected unique 3.3 V line supplies the LVDS chips for the LeCroy bus on the both halves. Due to a UHVG communication loss during the QM1 TVT at -20°C the MHV100 supply voltage was risen to $+5.2$ V, which now enables the operation down to -25°C .

4.2.3 Power distribution box (UPD)

The UPD-Box houses seven DC/DC-converters that convert the incoming 28 V from PDS to the needed voltages of the U-crate. All UPD boards have a dimension of 16×15 cm and a full redundancy split on two halves of the boards. The incoming 28 V is filtered by the S9011B board and given via wire connection to terminal blocks, that split the filtered supply to wires soldered on the DC/DC-converter input pins. The S9011B is placed between the three low voltage converters S9048U (± 2.8 V). On right side three high voltage supply converters S9056 (120 V/5.2 V) are mounted and on the left the digital control board S9011AUv2 board together with the digital supply S9053U (3.4 V), as sketched in Fig 4.17. Upon power-up all halves of the DC/DC-converters are powered and enabled. Under nominal operation just one half of the converters is enabled to save power. The UPD is controlled by LeCroy communication on a slow control cable from the UBPv2 to a 15-pin micro-d receptacle at the left UPD main wall, which is connected with the S9011AU.

As shown by the power distribution scheme Fig 4.18 one half of the S9056 supplies one redun-



Figure 4.19: Photo of the UPD box. Visible is the right main wall with the 28 V supply and the HV as well as digital 3.3 V output connectors.

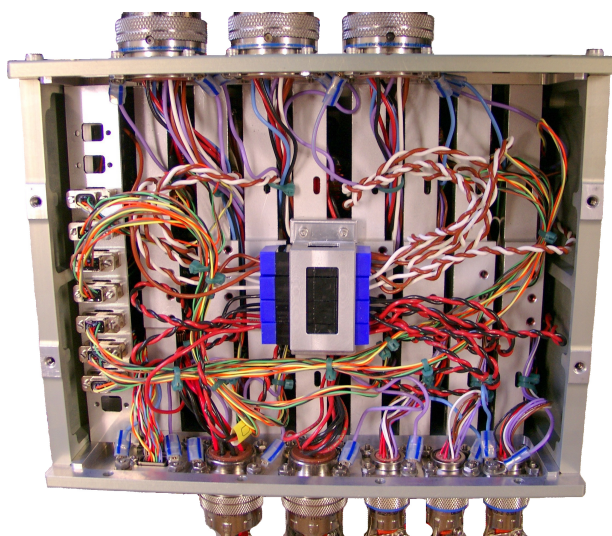


Figure 4.20: Top view of an open UPD box. Visible are the four terminal blocks in the center, all input and output connectors and the huge amount of cabling.

piece of aluminum 6061 T651 and the UPD walls of a single piece of aluminum 7075 T7351. The aluminum was anodized¹ at surfaces where no electric and thermal contact is desired and otherwise alodined², thus providing a conducting surface necessary for shielding. All UPD flight mechanics were designed by CGS³ and produced as well as surface treated by CSIST. To hold the terminal blocks in place a fixture plate and bracket was designed and produced in Karlsruhe with surface treatment by CSIST. It is now used in all subdetector power distribution boxes. All screwing onto aluminum parts is protected by self-locking Helicoils and all applied torques to the FM/FS production are recorded and included in a Acceptance Data Package (ADP) for the NASA. The QM2 UPD assembly was done in Karlsruhe and the flight assembly at CSIST guided by a UPD assembly documentation prepared in Karlsruhe. This assembly documentation belongs to this thesis and gives further information [Sch07].

General layout an features of the DC/DC-converters

The UPD DC/DC-converters are switching mode power supplies, that hack an input DC current and sends it to a transformer primary coil. After rectification of the secondary coils outputs the DC voltage is higher or lower as the 28 V input voltage. Since the maximum transferable power in a transformer is proportional to the input frequency, the core mass of the transformer can be reduced and the conversion efficiency improves by using a hacking frequency above non hearable 150 kHz. This principle is carried on until the transformer is made of single wire inductances (air coil), which feature no coil saturation in strong magnetic fields, but lead to high electromagnetic emissions and a low EMI tolerance. The used UPD converters have a magnetic field tolerance of 500 G, obtained by ferrite core transformers of about 3 cm diameter times 1

¹According to MIL-A-8625 Type II Class 1.

²According to MIL-C-5541 Class 3.

³Carlo Gavazzi Space, SPA, Milano, Italy

cm height. This section gives only a brief description of the UPD DC/DC-converter electronics layout, since the schematics are confidential intellectual property of the CAEN company and cannot be shown. Fig 4.21 depicts the block diagram of the S9056 DC/DC-converter. The input

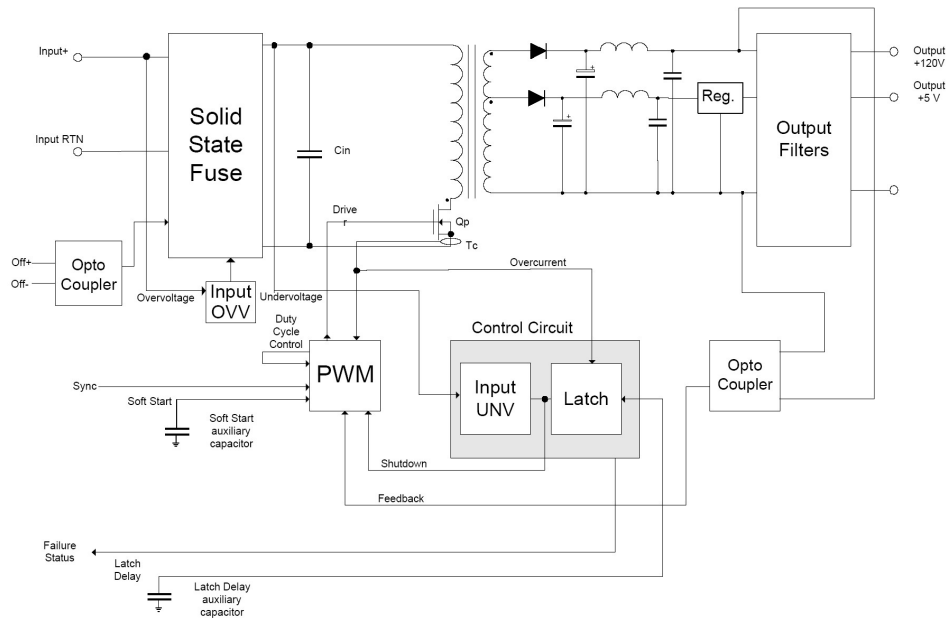


Figure 4.21: Block diagram of the S9056 DC/DC-converter. The diagram of other converters only differ in the part from the secondary transformer up to the outputs [CAE03].

current first runs through a filter built of different capacitances and an impedance. Then it enters a Solid State Fuse (SSF) circuit, that ramps the voltage on its output by 5 V/ms to limit the charging current of the input filter capacitances. It also turns off the board for temperatures above 82°C and recovers operation below 75°C measured by a temperature sensor AD590KF. The SSF is controlled by an optocoupler working as on/off switch of the board and by an overvoltage protection circuit, that becomes active above 31.5 V. After applying 2.5–50 V at the optocoupler diode the UPD converters switch off and on again for 0–0.8 V. In addition the output voltage is slowly ramped by the power manager circuit inside a Soft Start Time (SST) between 13 ms and 16 ms (adjustable by an auxiliary capacitance). This feature limits the charging currents of the output filter capacitances and of any device connected to the outputs. In case of an input undervoltage of less than 26 V or overvoltage of greater than 31.5 V the converter is switch off and recovers with a soft start sequence. For an output overcurrent, dependent on the maximum applicable load, a control circuit shuts down the power manager circuit and an off/on cycle has to be performed. Any active protection enduring longer than a Latch Delay Time (LDT) of about 100 ms (adjustable by an auxiliary capacitance) switches the SSF off and leads to a failure status.

The failure status is given by an open collector circuit and can be read by applying up to 30 V to the collector with reference to the input return line. An auxiliary coil on the primary transformer side senses the induction to the core and activates the failure status in absence of induction, which causes a SSF switch off. The power manager circuit includes a current mode PWM controller TI UC2843A and provides a clock (up to 500 kHz) to a MOSFET transistor.

This transistor hacks the input current to the primary transformer coil coming from the SSF. The clock frequency is given by an active circuit, that sets a reference timing capacitance and resistance at the PWM controller RT/CT input. This circuit also allows a synchronization of different DC/DC-converter start ups, but is not used for the UPD. A small current sense transformer in the primary current line connected to the PWM controller Isense input achieves a pulse-by-pulse controlled overload and short circuit protection. The output voltages are monitored in front of the output filters by a feedback given to the PWM controller. In this feedback circuit an optocoupler is used, which obtains the galvanic decoupling between the input and output side of the converters. Further details can be found in [CAE03],[Sch07].

All DC/DC-converter data sheets quote a radiation tolerance of 30 kRad. To satisfy the vibration stress tolerance all transformers and large capacitances are glued to the boards. The 8 layer polyamide PCBs have a height of about 2 cm. All on/off and error status signals of a converter are joined by soldering a cable with a 9-pin micro-d pigtail connector to three of the six control signal pads on each board half. The power in/outputs and shield connections are made by wires soldered to pins of the converters.

Digital power supply DC/DC-converter (S9053U)

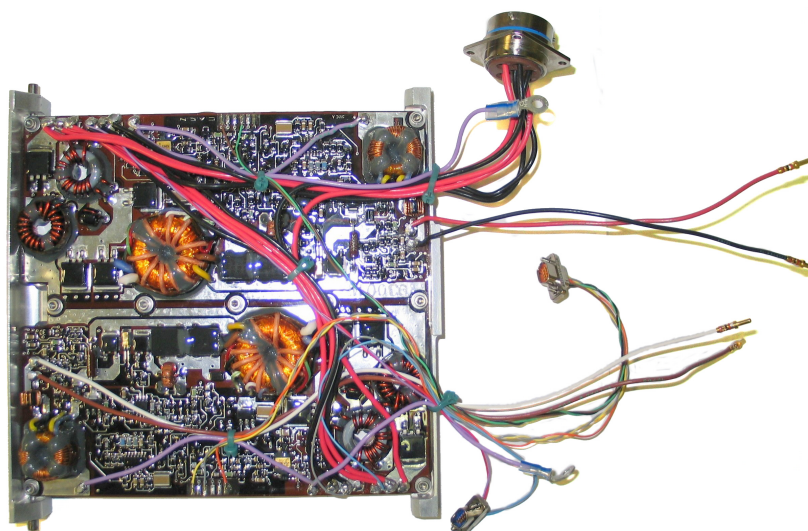


Figure 4.22: Top view of a S9053U DC/DC-converter on its I-Frame. All cabling to the output connectors and the terminal blocks is shown.

The S9053U DC/DC-converter, depicted in Fig 4.22, supplies the 3.3 V power for all digital parts of the U-Crate electronics. Since the S9053U provides also the power to the UPD control board S9011AU and it is a single supply this converter starts in hot redundancy (both halves on). Thus the S9011AU will be powered again after a loss of the nominal S9053U half by performing a power cycle. Therefore each S9053U output has a diode to prevent flow back currents between the interconnected halves. This leads to an acceptable small loss of the maximum power conversion efficiency from $\geq 78.2\%$ given by the data sheet to 72% measured during tests. In reality the S9053U generates 3.4 V, which is slightly dropped to about 3.3 V

on the cable to the U-Crate. Its input current is limit by the SSF to 2.2 A and the output power to 29 W. One S9053U board weighs 340 g.

Front-end supply DC/DC-converter (S9048)

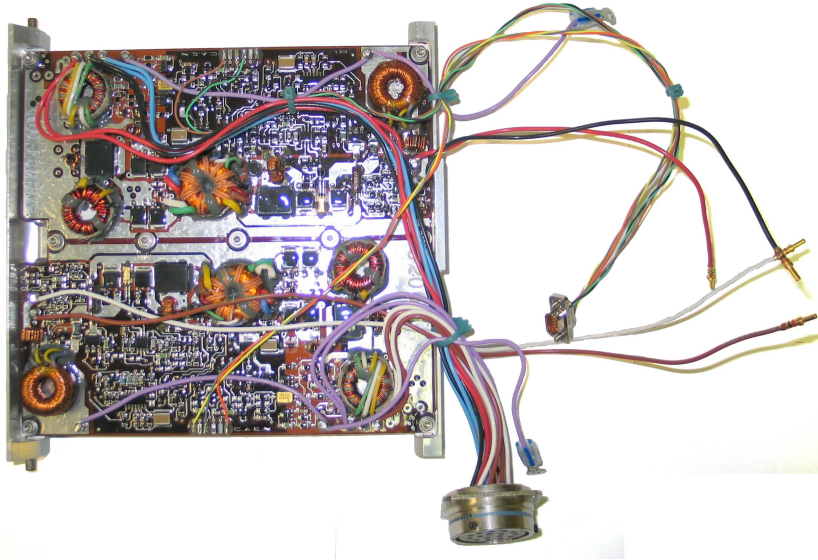


Figure 4.23: Top view of a S9048 DC/DC-converter on its I-Frame. All cabling to the output connectors and the terminal blocks is shown.

The S9048 DC/DC-converter, depicted in Fig 4.23, provides the ± 2.8 V low voltages for the line regulators of the UPSFE. Unfortunately it was found during functional tests of the UPSFE that the regulators cannot work with supply voltage levels below ± 2.5 V. Due the fact that the UPSFE drives about a factor of 2 larger current on the negative than on the positive supply line the ± 2.8 V of the S9048 are shifted by 1 V. All this and an additional voltage drop on the cabling made it necessary to rise the S9048 output voltage between the QM1 and FM phase from original ± 2.5 V to ± 2.8 V. This change was only possible by exchanging the transformer. The S9048 has a measured maximum power conversion efficiency of 78%, which is in agreement with the data sheet. The S9048 input current is limit by the SSF to 1.75 A and the output power to 16.6 W. One S9048 board weighs 273 g.

High Voltage supply DC/DC-converter (S9056)

The S9056 DC/DC-converter, depicted in Fig 4.24, provides 120 V to the Cockcroft Walton high voltage elevators of the UHVG and the 5.2 V supply to the UHVG LeCroy chips. To assure stable operation of the UHVG LeCroy chips below 20°C the original 5 V output of the S9056 was risen to 5.2 V. This change was easy applicable, since its transformer generates 6 V, which are then regulated to 5.2 V on the board. The S9056 has a measured maximum power conversion efficiency of 65%, which is in agreement with the data sheet. The S9056 input current is limited by the SSF to 1.75 A and the output power to 6 W. One S9056 board weighs 256 g.

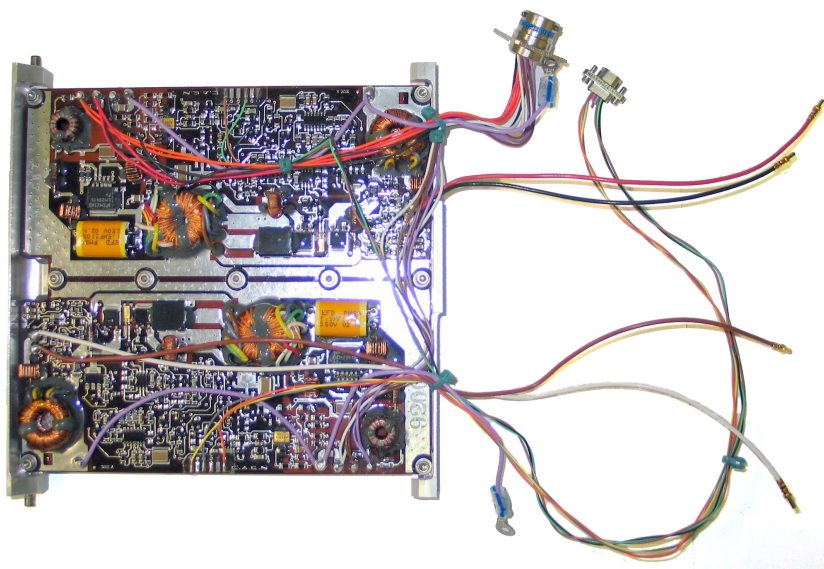


Figure 4.24: Top view of a S9056 DC/DC-converter on its I-Frame. All cabling to the output connectors and the terminal blocks is shown.

UPD controller Board (S9011AU)

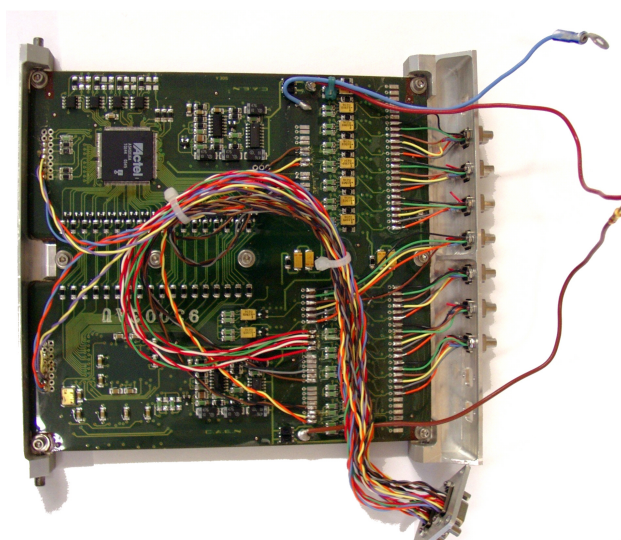


Figure 4.25: Top view of a S9011AU control board on its I-Frame. Visible are the DC/DC-converter control connections on the I-Frame, the two LeCroy connections on the panel and the voltage supply wires to the terminal blocks.

The S9011AU, depicted in Fig 4.25, is designed under contract with the CAEN company. It controls and monitors the seven UPD DC/DC-converters by a logic program burnt to two Actel A54SX32TQ144 FPGAs. This logic includes the LeCroy protocol for the communication with the U-Crate JINF. A cable connection from the U-Crate Backplane to the UPD achieves

the LeCroy communication and the 3.3 V power supply of the board. As protection of the digital 3.3 V line each half has a solid state fuse, which switches the board off when the current exceeds a limit of 230 mA. Like for the UPSFEv2 the S9011AU has two DALLAS DS18S20 temperature sensors, that are connected to the backplane (UBP) cable but are unused after a weight reduction requirement (see section 4.2.2). To save power each Actel of a redundant S9011AU half can switch of the other one via the SSF. After power up both are on. To control the DC/DC-converter this board has nine groups of 3 solder pads. Two pads of a group are connected to the on/off signal pads of a DC/DC-converter half and apply the digital 3.3 V to switch the half off. The remaining pad applies 28 V via an optocoupler diode to the error status open collector circuit of this converter half. The 28 V lines on the S9011AU are directly connected to the 28 V outputs of the S9011B filter by cables soldered to a pin of each S9011AU half. To connect one DC/DC-converter always two pad groups are joined by soldering a 9-pin micro-d receptacle cable to them. The in total seven receptacles are mounted on the S9011AU controller frame and are connected to the seven control cables coming from the DC/DC-converters.

Power input Filter (S9011B)

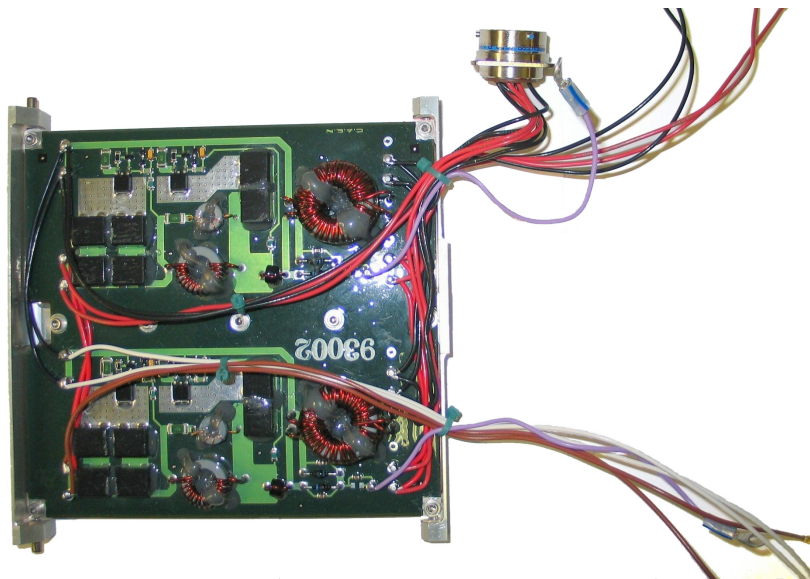


Figure 4.26: Top view of a S9011B filter board on its I-Frame. All cabling to the input connectors and the terminal blocks is shown.

The S9011B, depicted in Fig 4.26, is designed under contract with the CAEN company. It reduces the amount of noise conducted through the 28 V line into the UPD called conducted susceptibility and coming out of the UPD called conducted emission. Fig 4.27 and Fig 4.28 show the filter capabilities of the S9011B against this two noise types. The layout of the S9011B is based on RC and RL high and low pass filters with a large RL low pass filter coil at the output side of the board. On the input sides wires are soldered to the four pins of each redundant board halve and are then fed to a connector mounted to one of the UPD side walls. On the output side wires are soldered to the board for connection to the power distributing terminal

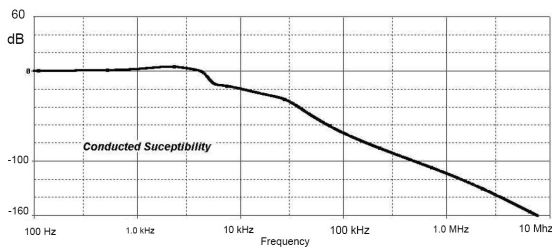


Figure 4.27: Conducted susceptibility of the S9011B filter [CAE04].

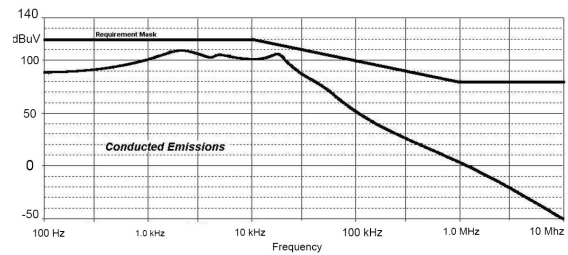


Figure 4.28: Conducted emission of the S9011B and the required limits [CAE04].

blocks of the UPD. To establish a passive redundancy of the S9011B, all related board half outputs are interconnected on the output side.

4.3 The TRD electronics qualification and acceptance tests

Qualification procedure - board level

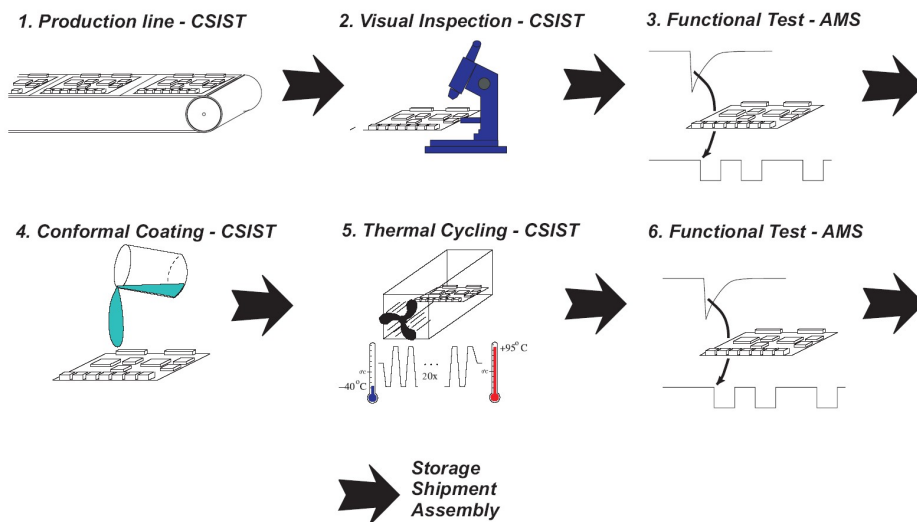


Figure 4.29: Qualification/acceptance procedure for the board level production. [Hau05]

To guarantee the operation of all TRD electronics after a space shuttle flight and under temperatures from -20°C to $+50^{\circ}$ in the vacuum of the space extensive tests were performed. These tests were divided into space qualification tests done in the QM1/QM2 phase and acceptance tests done for the FM electronics. The performed electrical and functional test procedures were identical. However in case of a malfunction during the qualification phase an electronics part replacement or a redesign was allowed, while in case of the FM phase only parts could be replaced. Fig 4.29 illustrates the qualification as well as the acceptance procedure performed for all QM2 and FM/FS TRD boards. Additional tests had been already done during the QM1 phase. They included vibration tests for one piece of each UPD DC/DC-converter type to

assure the fastness of there coils to the PCB and several Thermo Vacuum Test (TVT) cycles for this converters and the UHVG, that proved the heat production and conductance or the high voltage safety under thermal stress in vacuum. The board level space qualification tests at CSIST in Taiwan right after the board assembly included a first functional test, followed by an Environmental Stress Screening (ESS) and a second functional test. For the crate level space qualification the U-CRATE and UPD passed the same procedure followed by an Electromagnetic Magnetic Interference (EMI) test at CSIST and a TVT in Terni, Italy. Due to a change in the grounding scheme after the EMI test problems, it was repeated in Terni. The whole FM production went through the same chain of tests as the QM2 production, but with lower ESS and TVT stress profiles to shrink the total accumulated stress and a skipped EMI test due to the kept design.

For all DC/DC-converters halves efficiency curves were measured, which allows to predict the total AMS-02 power consumption. Furthermore, the QM2 S9048 converter curves helped to estimated a necessary output voltage increase of the FM S9048 to avoid malfunctions of the UPSFE for voltages below 2.5 V, since the S9048 output voltage is load dependent and essentially dropped on the supply cable. Each tested FM/FS DC/DC-converters has a documentation of all tests, its efficiency curves as well as failures and repairs. These document¹ are always carried with the boards or the UPD, in case they are assembled.

The following sections will concentrate on the complete test of the board level UPD electronics and the electrical tests of the QM2 U-Carte boards, which includes the major work done for this thesis. All further performed test up to the final UPDs and U-crates are described in reference [Sab08].

4.3.1 Environmental Stress Screening (ESS)

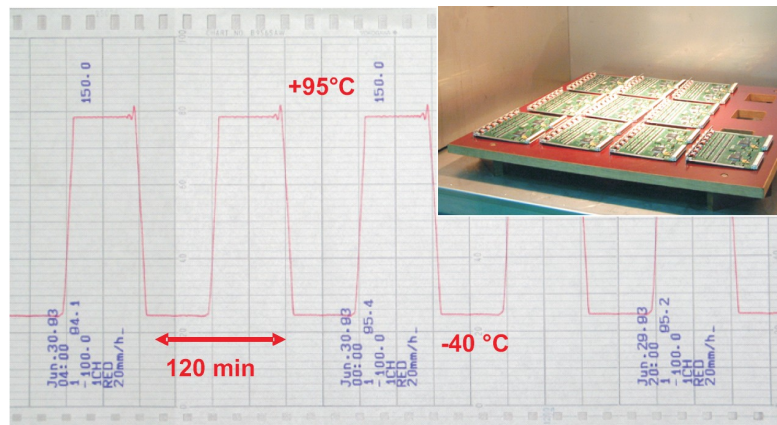


Figure 4.30: Plot of the thermal-cycling profile for the board level tests. Right corner: Photo of boards inside the temperature chamber. [Hau05]

The Environmental Stress Screening included a temperature cycling in a thermo-chamber and an additional vibration test on a vibration table for the the UPD and the U-Carte. For the temperature cycling the devices simply lay on an isolating plate, as depicted in Fig 4.30, since

¹All test documents are also published on the page: <http://www-ekp.physik.uni-karlsruhe.de/amswww/>

the heat was transferred by convection. These tests proved the stability against the heat expansion and the extreme temperature operation. For the vibration test of the UPD and U-Crate the devices were directly screwed to the vibration table at their screw-holes. For the additional vibration tests of QM1 DC/DC-converters at the RWTH Aachen the boards were screwed to their I-Frames, then to aluminum brackets and the brackets to the table. All vibration tests verified the mechanical stability under the strong accelerations expected during the Space Shuttle launch.

AMS-02 Thermal Stress Profile

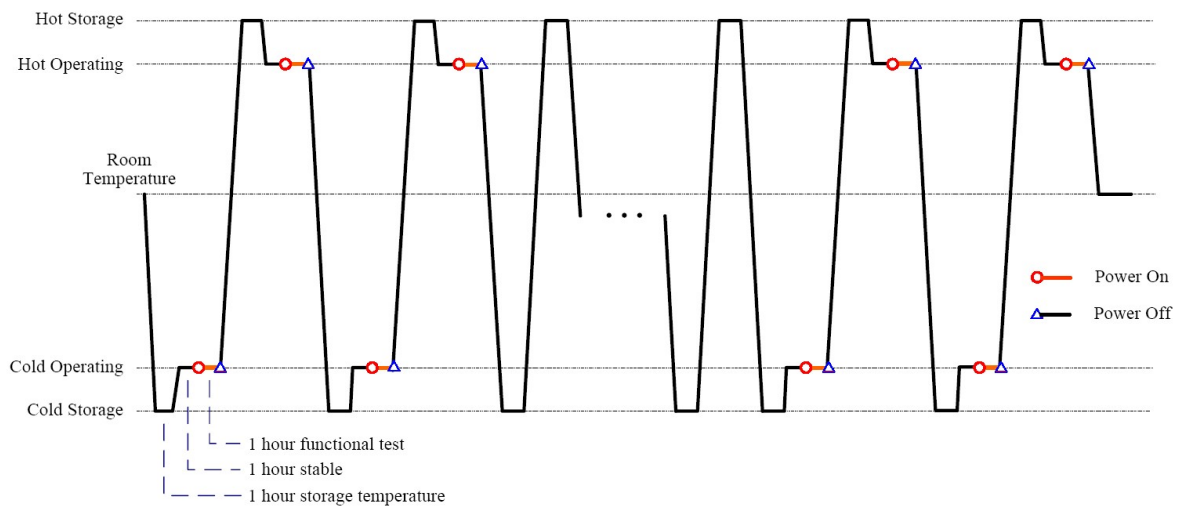


Figure 4.31: Plot of the ESS temperature profile. [Hau05]

During the board level ESS all electronic boards went through a temperature cycling inside a thermo-chamber with 20 cycles from -40°C and $+95^{\circ}\text{C}$. Fig 4.31 shows a generalized temperature screening profile. Only the DC/DC-converters ESS profile had additional cold and hot operation steps at -25°C and $+55^{\circ}\text{C}$ in the first and last cycle. Functional tests during these steps check all protections and measured their conversion efficiency and output voltage stability at different temperatures. Due to a missing UPB at that time a rather complicated to realize control and single operation of the U-Crate boards during the cycling was skipped.

For the Crate level ESS a temperature cycling with ten cycles was performed and functional tests with cold and hot operation steps, like illustrated in Fig 4.30. The profile levels are given by table 4.1. Then followed a vibration test and again five temperature cycles with functional

Table 4.1: Temperature levels for the crate level ESS.

Phase	Hot storage	Hot operation	Cold operation	Cold storage
QM2	$+85^{\circ}\text{C}$	$+55^{\circ}\text{C}$	-25°C	-40°C
FM/FS	$+80^{\circ}\text{C}$	$+50^{\circ}\text{C}$	-20°C	-40°C

tests in the first and the last two cycles. All tests on vibration tables, like the one depicted in

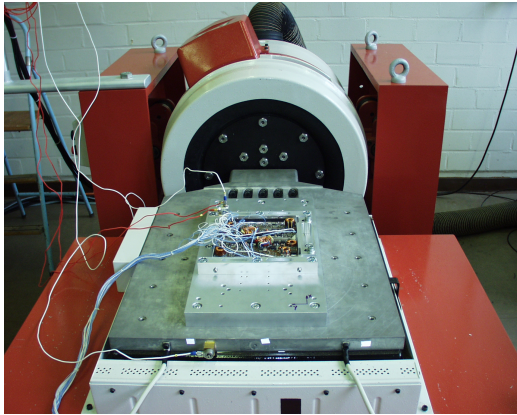


Figure 4.32: *Vibration test of a QM1 DC/DC-converter at the RWTH Aachen.*

AMS-02 Random Vibration Spectrum

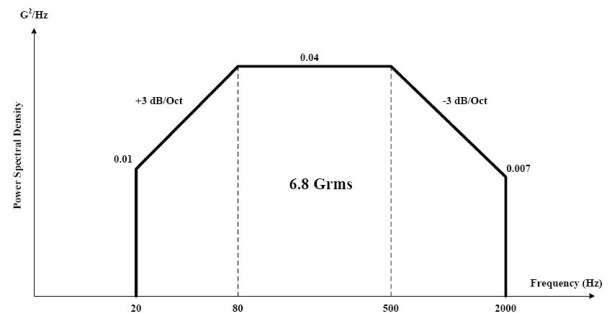


Figure 4.33: *Random vibration spectrum used for vibration tests.*

Fig 4.32, were performed in x-, y- and z-direction and accelerations sensors were mounted to the table, or to the board fixations. A random vibration spectrum was applied and measured with the sensors. For this kind of test the acceleration is given in units of the Earth gravitational acceleration G. The mean square accelerations G^2 for a certain bandwidth was recorded by the sensors and afterwards normalized to the bandwidth as G^2/Hz . In Fig 4.33 G^2/Hz is plotted for different bandwidth frequencies in the entire frequency range. The integral of this plot gives the mean square acceleration over the frequency range and its square root is referred to be the vibrational stress per time G_{rms} . For the applied 6.8 G_{rms} almost all acceleration peaks lie within a 3σ limit of 20.4 G. This stress spectrum was applied for 10 minutes per axis for qualification tests and just 1 minute per axis for the acceptance tests. During all vibration tests the hardware was powered and in case of the UPD and U-Crate also functional readout test were performed to identify latent defects and manufacturing flaws.

4.3.2 Thermo Vacuum Test (TVT)

In contrast to an ESS a Thermo Vacuum Tests (TVT) is performed in evacuated chambers with a heat conducting plate, where a temperature profile can be applied. Such TVTs were used to prove the heat conduction of the crate mechanics and their operation in the space vacuum, since this environment misses convection. Because the heat conduction is difficult to achieve for electronics boards without proper fixation, this kind of test was mainly done for complete crates. Only a single DCDC-converter of each type was tested during the QM1 phase to ensure the necessary heat conduction of the board designs. Additionally a single UHVG board was tested in the QM1 phase at the MPI Garching, but it was provisorily fixed to the plate, since only its high voltage safety was checked. For all other tests the heat flow was guaranteed by screwing the devices to the conducting plate in same way as for the vibration tests. Temperatures at critical points of the mechanics were measured continuously during the tests and the data was used to verify the thermal analytical model of the mechanics and the electronics. After the chamber reached less then 10^{-5} mbar a temperature profile with four cycles and four temperature levels: hot and cold storage and hot and cold operation, as

AMS-02 Thermal Vacuum Test Profile

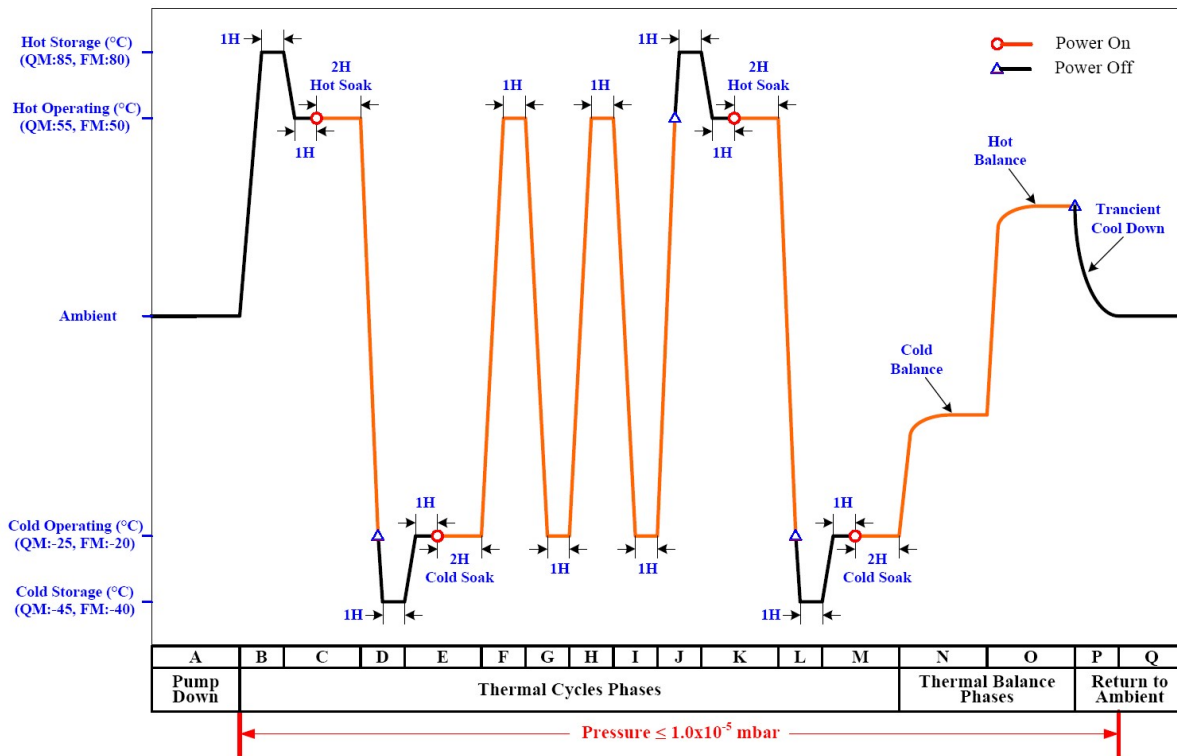


Figure 4.34: Plot of the TVT temperature profile. [Hau05]

shown in Fig 4.34, was applied. The stress profile had the same levels as the one of the crate level ESS (table 4.1). All QM1 TVT profiles were equal to the QM2 one, except the one for DC/DC-converters tested at the RWTH Aachen, that had only cold and hot operation levels of -40°C and $+80^{\circ}\text{C}$. At all operation temperatures the electronics were powered and from time to time, explicitly at the hot and cold soak period, were performed functional tests.

4.3.3 Test devices

During the EM and QM1 phase the U-Crate backplane (UPD) was not built, and the production of an EM and a QM1 test backplane¹ became necessary to allow an immediate start of tests after board delivery. This solution then also offered the opportunity to implement additional test points and electrical test circuits. Further a UPSFE test backplane² was developed for an extensive test of the analog Solid State Fuses (SFF) inside the 14 UPSFE linear regulators. This is important, because a loss of one of this protections would force a S9048 DC/DC-converter to stay in constant overcurrent protection and thus would cause the loss of 14×4 TRD modules. For the DC/DC-converter a manual test setup was developed and in prospect of the large FM/FS production also an automatic load system, that checked the device functionality

¹The test backplanes were designed by M. Brückel, F. Hauler and L. Jungermann, IEKP, [Brü03]

²The UPSFE test backplanes was designed by R. Eggert, F. Hauler and L. Jungermann, IEKP, [Egg04]

and measured the conversion efficiencies of each DC/DC-converter half. All FM/FS DC/DC-converters were tested together with the Tracker production¹ including two batches of 20 and 52 boards, 25 belonged to the TRD and the rest to the Tracker. In total it summed up to about 3000 efficiency points.

The UDR and the UPSFE test-backplanes

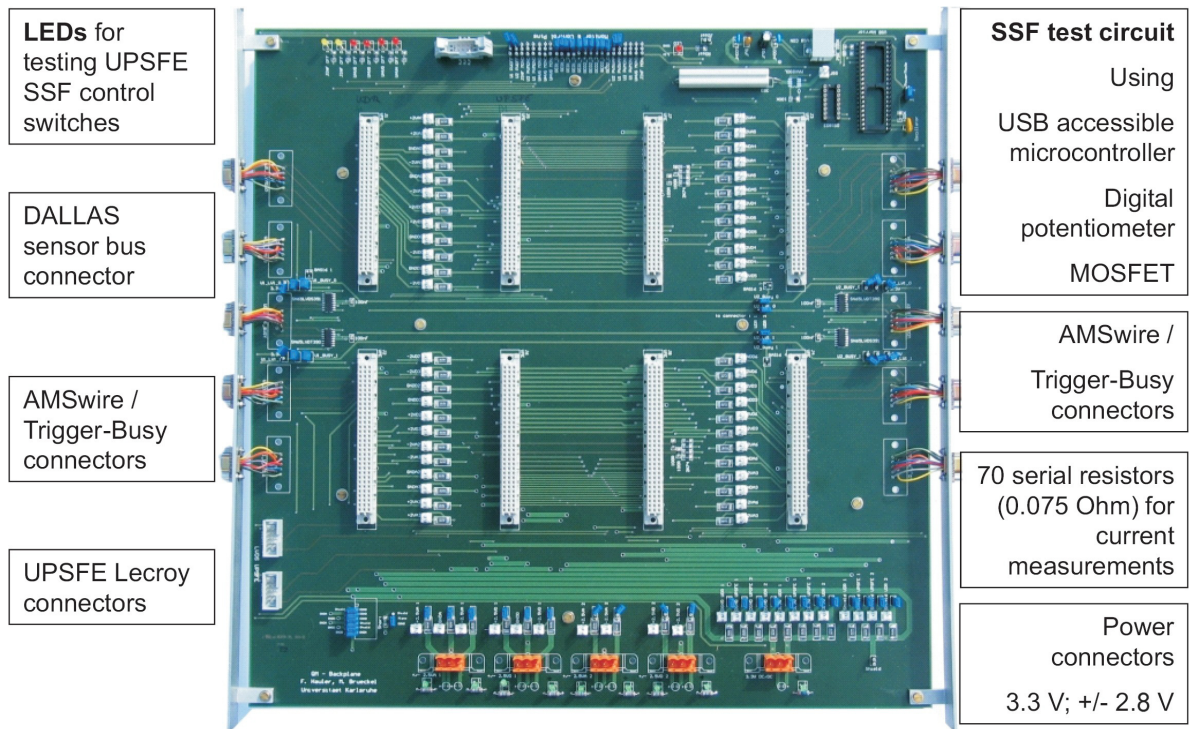


Figure 4.35: Photo of the QM1 test backplane including a feature description. [Hau05]

The EM test backplane allows to test one EM UDR2 and two parallel connected EM UPSFEs. It provides 3.3 V and ± 2.8 V power, four AMSWire links to the UDR2, a trigger/busy connection and a LeCroy bus slow control connection for the UPSFE. Simple LED circuits check the function of all Solid State Fuse (SSF) control signals given by the UPSFE and Jumpers can be attached to set the SSF monitor signal of the UDR2 or to simulate the SSF status signals give to the UPSFE. Each power supply line, the shield line and the 14 times ± 2 V lines between UDR2 and UPSFE are equipped with current sense shunt resistor of 0.075Ω with a parallel connected jumper to measure the voltage drop. These current sense points were used to determined the nominal power consumption, the stability of the ± 2 V lines and circuit defects, by local nominal current deviations. The further development of the QM1 test backplane, visible in Fig 4.35, was related to changes on the QM1 boards with a different connector layout, which made the EM backplane incompatible to the QM1 board. All features of the EM backplane were taken over, but additionally the QM1 backplane allows to test a full QM1 power group composed of two UDR2s and two UPSFEs. Therefore eight AMSWire links, four for each UDR, a 1-Wire

¹The FM/FS DC/DC-converters test were performed together with Sandor Blasco, INFN Perugia, Italy.

bus connection for Dallas temperature sensors and two trigger/busy links are available. After an AMS-02 weight optimization one UPSFE of each power group was removed and the linear regulator interconnections changed. Although the QM1 backplane does not support the final power group layout, it was still suitable for the QM2 and the FM/FS production tests of the UDR2 and the UPSFEv2.

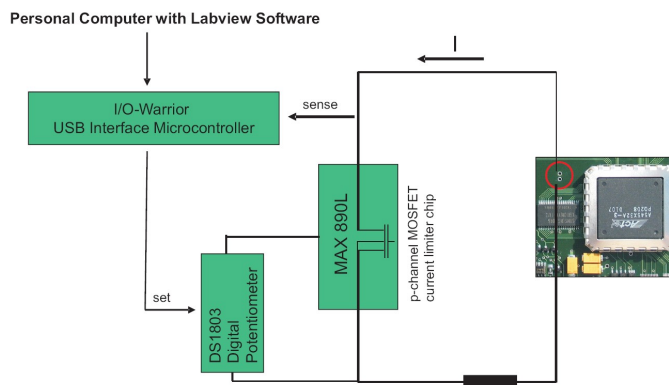


Figure 4.36: Schematic of the digital SSF test circuit. A microcontroller sends sequences to a digital potentiometer, that defines the current through a MAX890L current limiter.

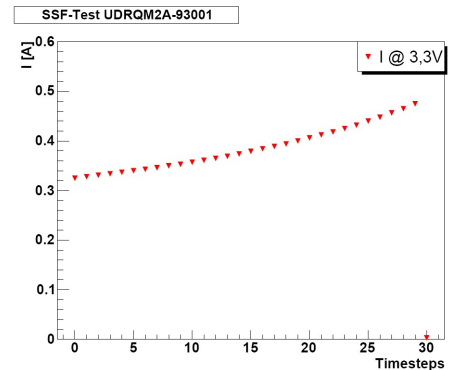


Figure 4.37: Plot of the Solid State Fuse (SSF) tests current versus time. After the SSF is disabled the current drops to zero.

To test the digital supply SSF of all boards the QM1 test backplane offers a circuit shown in Fig 4.36. In this circuit the current runs from the digital SSF through a digital high current switch MOSFET MAX 890L working as current limiter and a load resistor to ground. Its gate is controlled by an 8-bit digital potentiometer DS1803, which is set by a 2-wire serial bus connection with a strobe (SDA) and clock (SCL) line to an I/O-warrior-40 microcontroller¹. The 2-wire serial bus is realized at two of the 40 I/O pins of the microcontroller, which allow a maximum data transfer speed of 30 bit/s. All commands are send from a PC via USB to the microcontroller and are generated by a LabView² program. The I/O warrior is supplied by the 5 V USB power and the digital potentiometer by the digital 3.3 V of the backplane. To obtain the SSF switching status, the 3.3 V SSF output is connected to one I/O pin of the microcontroller. As soon as the current set by the MOSFET is larger than the limit of the board a disabled SSF is sensed as low potential at this pin. A typical output of this measurement is plotted in Fig 4.37. More information about the design can be found in [Brü03].

The UPSFE test backplane, shown in Fig 4.38, provides 3.3 V and the ± 2.8 V, a LeCroy bus slow control connection and a Dallas sensor 1-Wire bus connection to the UPSFE. Like for the QM1 backplane it has LEDs for the control signals and jumpers for the monitor signals of the UPSFE and additional jumper to set the geometric address of the board. All linear regulator SSF test circuits, visible in Fig 4.39, work in the same way as the digital SSF test circuit of the QM1 test backplane. In total 28 MAX890L are used as current limiter for the ± 2 V output lines of a UPSFE. Always two of them are controlled by the two potentiometers inside one DS1803 chip and the 14 DS1803 are set by an I²C-bus³ connection to two I/O warrior microcontrollers.

¹I/O warrior, USB interface microcontroller, Code Mercenaries, Germany.

²LabView, graphical data flow programming language by National Instruments.

³I²C-bus, the bus is patented by Philips Semiconductors, the Netherlands.

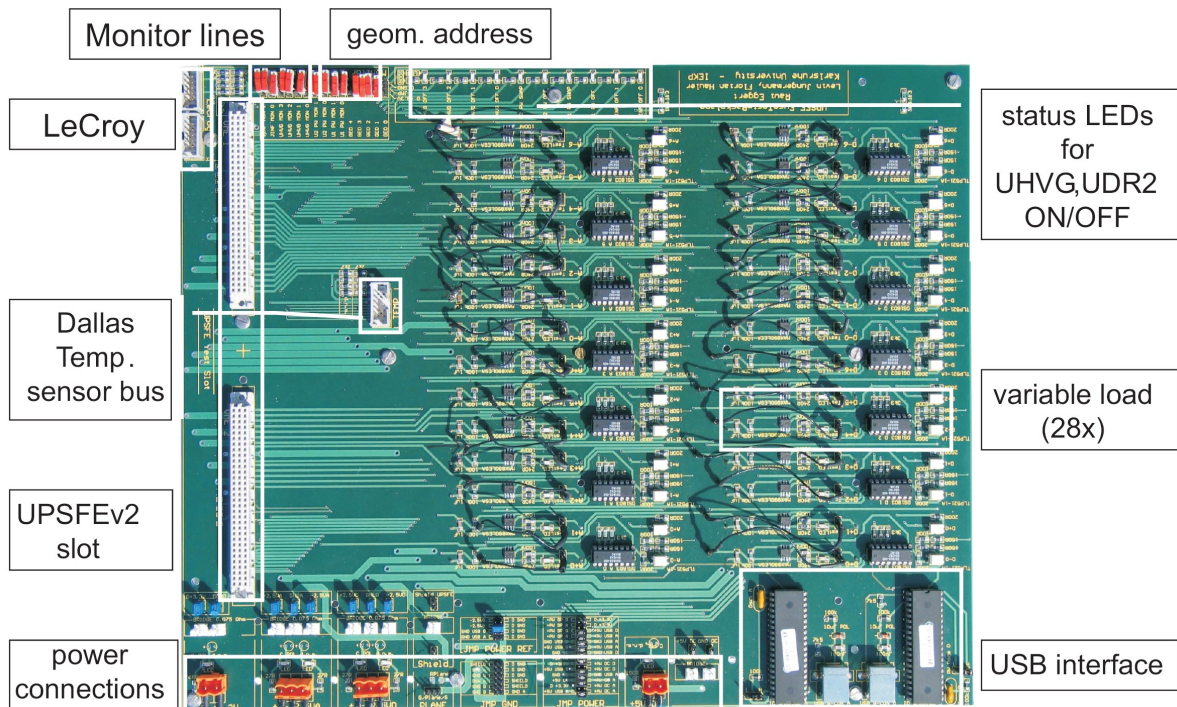


Figure 4.38: Photo of the UPSFE test backplane including a feature description. [Hau05]

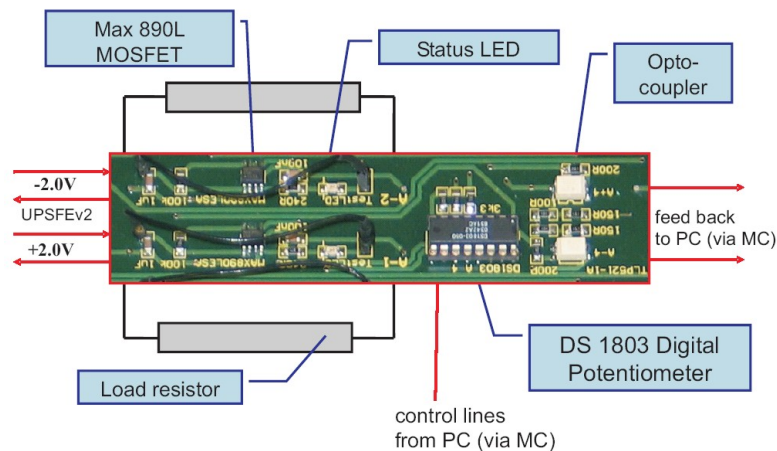


Figure 4.39: Variable load circuit on the UPSFE test backplane. It consists of MAX980L MOSFETs, a digital potentiometer and optocouplers.

The I²C capability of the I/O-warrior-40 was chosen, since the 14 circuits need to be controlled simultaneously. By sending just one I²C command via USB a throughput of 750 bytes/s can be reached. Two microcontroller are needed, because the DS1803 chips has just a 3-bit address and therefore only seven of them can be accessed by one I²C bus. All test circuits of a redundant UPSFE half are always read and controlled by only one of these microcontrollers. Since the DS1803 operates with 3 V or 5 V supply, it is powered together with the I/O-warrior-40 by

a separate 5 V supply of the backplane. To obtain each SSF switching status, each linear regulator output is connected to the diode side of 28 Toshiba TLP521 optocoupler. In case of a disconnected ± 2 V line by the SSFs the optocoupler transistors applies 5 V to an I/O pin of the I/O-warrior-40, because the microcontroller only senses positive 3-5 V levels. Additional 28 status LEDs are connected in parallel to the MOSFETs and light as soon the corresponding UPSFE regulators are powered through the SSF.

Since the MAX 980L MOSFETs used as current limiter are digital switches with non-linear drain currents, that also differ for each MOSFET, a current calibration for each applied ADC value at the DS1803 was necessary. Therefore the current was sensed as voltage drop on the load resistance behind the MOSFETs and the load resistance was determined by four point measurement. Each calibration was parametrized by a fourth order polynomial fit to the data points and achieves a 2 mA precision. In any case the 8-bit DS1803 potentiometers just allow steps of about 10 mA per ADC value, but this was sufficient for all tested SSF current limits of a few hundred milliamperes.

Variable load system for DC/DC-converter tests

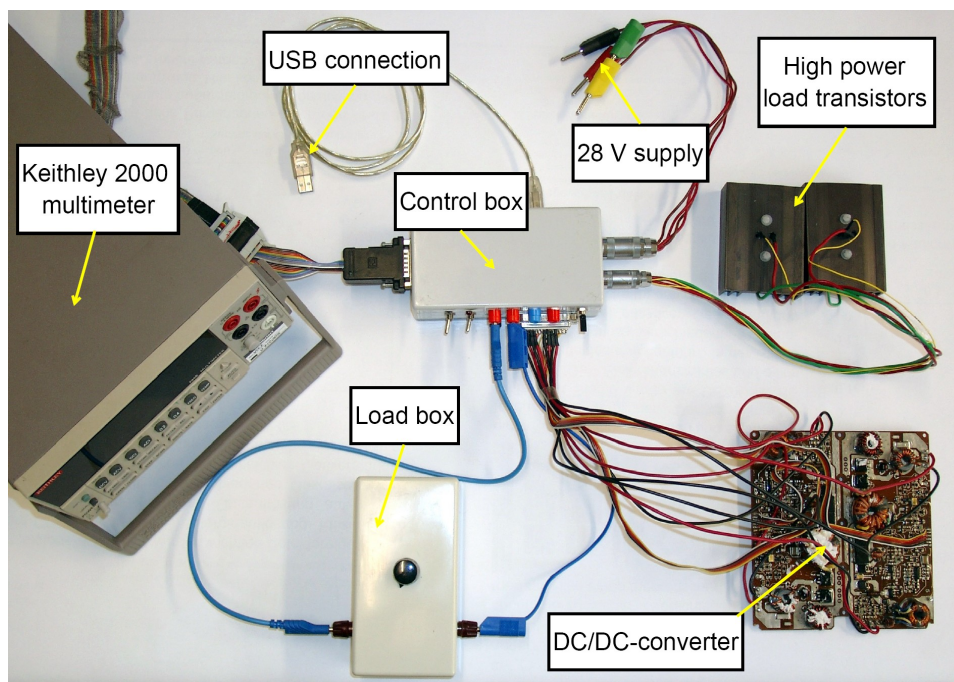


Figure 4.40: Photo of the variable load system for DC/DC-converter test including a component description.

The variable load system, shown in Fig 4.40, consists of a control box, two 2N3792 bipolar PNP high power transistors on cooling bars working as variable loads, a high voltage load box and a Keithley 2000 multi-meter with a 10 channel scanner card.

For test of the S9056 and the S9055¹ DC/DC-converters, their high voltage outputs need to

¹The S9055 DC/DC-converters belong to the AMS-02 Tracker

be connected via the control box to a load box, that houses five load resistors specified for the S9056 and S9055 high voltage. The load resistors are then selected by a multi switch on top of this box.

The configuration of the load system allows to test all types of TRD and Tracker DC/DC-converters by exchanging a single plug. Therefore all in- and outputs as well as control pads of a DC/DC-converter need to be connected by a cable with a female 25 pin sub-D plug to the control box. On the right side of the control box two 6 pin high current Lemo connectors are mounted, that connect the variable loads and the 28 V supply voltage. The opposite side has a 5 V plug to deliver the control and status signals of the converters and a 20 pin sub-D connector to connect the Keithley 2000 scanner card. A switch on the front disconnects the 28 V supply during a converter exchange.

The converters are activated by two switches on the front, that apply a 5 V on/off high to each converter half. Further two LEDs display the halves error status signal. A schematic layout of the DC/DC-converter control circuit is shown by Fig 4.41. The same circuitry was already used for the functional tests of the QM1 and QM2 DC/DC-converters, where it was placed on a small control board.

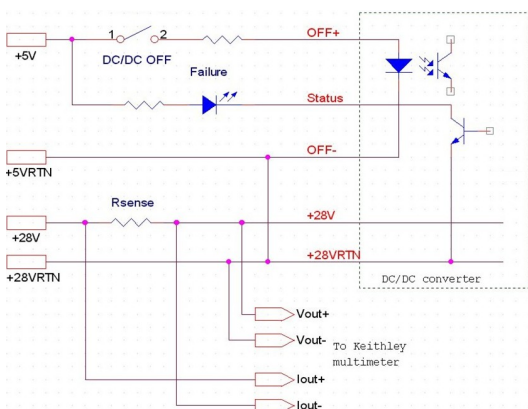


Figure 4.41: Schematic of the control circuit inside the control box.

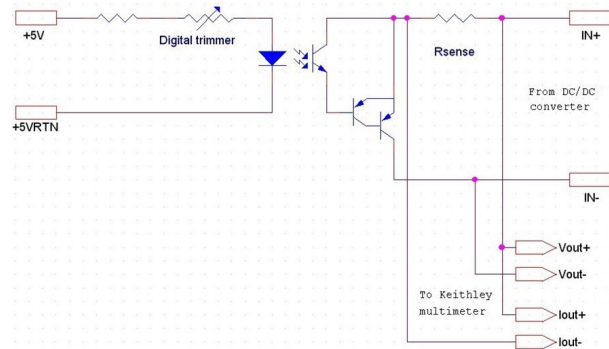


Figure 4.42: Schematic of the variable load circuit. A triple Darlington circuit with a high power transistor as last stage operates as load for a DC/DC-converter.

Inside the control box a board with a I/O-warrior-40 microcontroller is housed, which is commanded via USB and controls a DS1803 digital potentiometer via I²C bus like for the UPSFE test backplane. Both chips are powered by the USB 5 V. The two potentiometers of the DS1803 are used as voltage dividers of the USB 5 V to separately power two Toshiba TLP521 optocoupler diodes. The two NPN optocoupler transistors together with two PNP transistors on the board and the 2N3792 transistors on the outside build two complimentary triple Darlington transistors, which are connected to the DC/DC-converter outputs. Because the collector current of the TLP521 (50 mA) is much to low to drive necessary current of about 7 A on a 2N3792 transistor, the triple Darlington circuit was needed. The decoupling was used to protect the digital side of the control board against the high voltage outputs of a part of the tested DC/DC-converters. With a maximum power rating of 150 W the 2N3792 transistors is a sufficient load for the 29 W maximum output power of the S9053U and also for the 34 W maximum output power of the S9054 converter used by the Tracker. Fig 4.42 shows the layout of the variable load circuit.

All DC/DC-converter output currents run through current sense resistors on the control board and then via the applied loads back to the converters output return. The input current also runs through sense resistors before they enter a converter. A PC running a LabView program sets the low voltage loads applied to the DC/DC-converters via USB. Afterwards all voltages and voltage drops on the sense resistors are measured by the Keithley scanner card, which is controlled by the same LabView program via GPIB commands. The voltage drops on the 0.075Ω sense resistors with 1% precision are recalculated to currents. With the high precision of the sense resistors and the Keithley 2000 an accuracy of about 1% for the power $P = I \cdot U$ and of about 2% for the conversion efficiency $\eta = P_{out}/P_{in}$ measurements is reached.

Originally the system was designed for a fully automatic measurement of the UPD DC/DC-converters by using two high power Darlington transistors and a single DS1803, since this boards have only two outputs. To stay flexible to test S9052 DC/DC-converters with three outputs (former in the UPD) a third V/I-sense circuit with banana plug connection was included. During the first FM/FS production tests it turned out to be also useful for the Tracker converters, that partly have three output and the system was adapted for the tracker as well.

4.3.4 TRD Test Environment

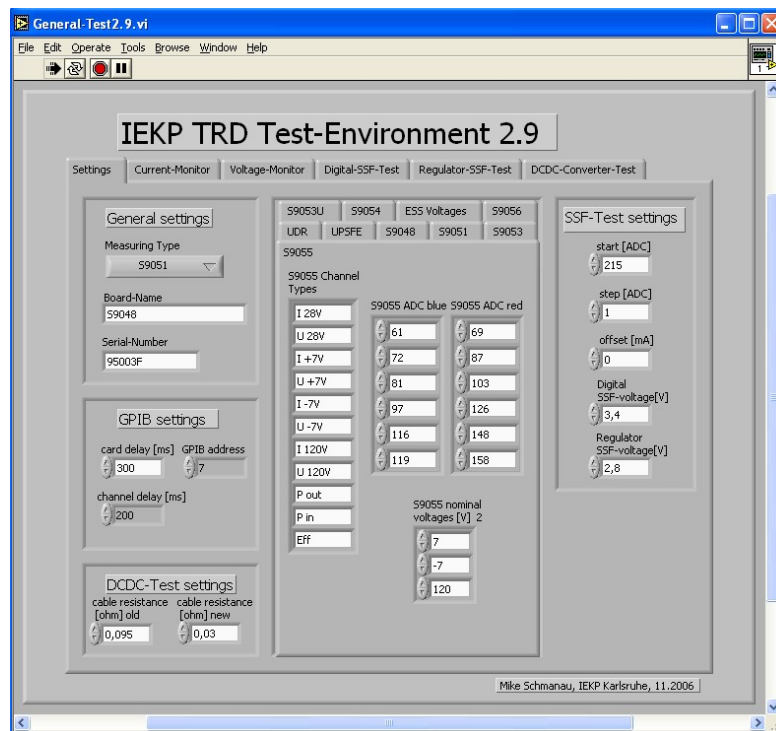


Figure 4.43: Overview of the TRD Test Environment. This software controlled the test devices and log the data of most electrical tests performed for the TRD QM2 and FM/FS board production.

All test equipments for the TRD electronics have many test points and circuits that need to be read or controlled by a PC. Therefore a Labview program called the "TRD Test Environment"

was implemented, that includes procedures to control and read these points or circuits and records all measured data to log files. The Graphical User Interface (GUI) of this software, depicted in Fig 4.43, is split into six tabs.

On the first tab, shown in Fig 4.44, general settings such as the tested devices to initialize the test type, the board name and its serial number can be applied, which are written together with the test date to log files for each board. Further the GPIB address and the readout timing of the Keithley 2000 multimeter can be set. On the bottom left the resistance of the wiring between the DC/DC-converter and the load system control box need to be entered. In the center a tabbing is placed to enter all nominal current and voltage values as well as the load configurations for each DC/DC-converter type. By a control on the right the digital solid state fuse (SSF) input voltage and the UPSFEv2 regulator SSF output volatges can be set, which are used for current calculations. Additionally a start ADC value and an ADC step size can be chosen to speed up the SSF tests.



Figure 4.44: TRD Test Environment settings tab.

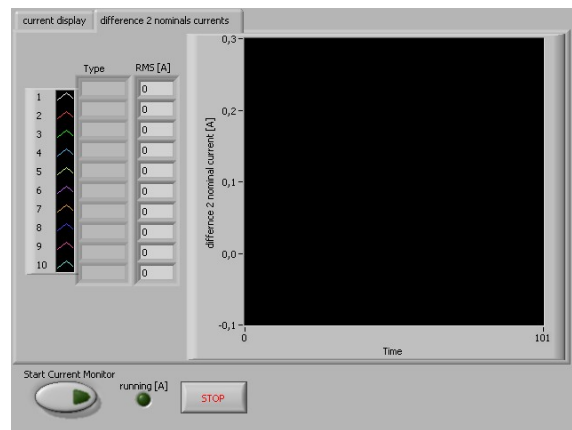


Figure 4.45: TRD Test Environment current monitor tab.

The "Current-" and "Voltage-Monitor" tabs, visible in Fig 4.45 and Fig 4.46, continuously measure the voltages or currents at maximum ten test points. During execution of the test procedure the Keithley 2000 multimeter is commanded via GPIB to scan all the voltages with an internal 10 channel scanner card. Therefore a scanner card cable with ten jumper connectors exists, that can be arbitrarily mounted to the tests points of the backplanes. A further tabbing either visualizes all measured value in a graph together with their actual averages, or the difference between measured and nominal values together with the actual RMS. All currents are calculated from measured voltage drops on the 0.075Ω sense resistors of the test backplanes.

The "Digital-Part-SSF" test on the fourth tab, depicted in Fig 4.47, continuously rises the current through a digital SSF on a TRD electronic and indicates the SSF current as well as the 3.3 V and GND supply lines currents. The supply currents are measured by a Keithley 2000 in the same way as for the "Current-Monitor" and the SSF current is calculated from the applied ADC value and the calibration function mentioned in 4.3.3. To perform this test a special cable need to be attached between the SSF test circuit on the QM1 backplane and the test points of each redundant board half. All boards need to be powered with their digital supply voltage. Commands are send via USB. During execution of the tests procedure the SSF current is ramped in about 10 mA steps until the SSF is disabled. At that moment the still

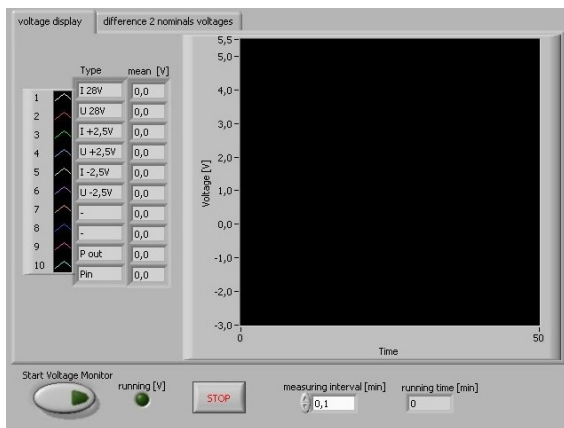


Figure 4.46: TRD Test Environment voltage monitor tab.

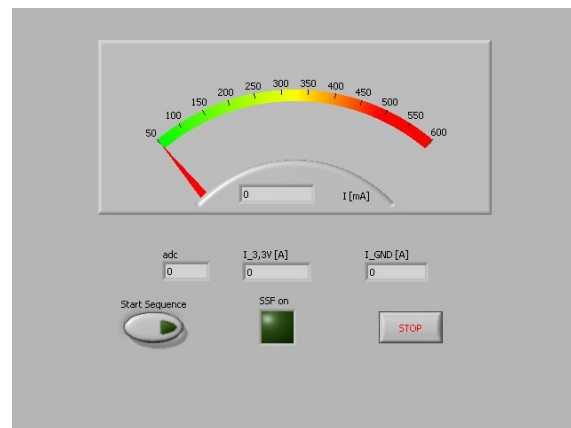


Figure 4.47: TRD Test Environment digital SSF test tab.

supplied board tries to recover, which results in a on/off toggling of the SSF within the latch delay time. As soon the switching is sensed, the maximum current is recorded and the load is set back to its minimum. The GUI on this tab looks simple, but the commanding related to the test circuit design is rather complicated, since each command is send bit by bit through an I/O-warrior-40 to a digital potentiometer.

The "Regulator-SSF" test on the fifth tab, shown in Fig 4.48, automatically tests the functionality of 14 SSF circuits inside 7 regulator circuits of a redundant UPSFEv2 halve. For an UPSFEv2 plugged to the test UPSFE backplane the currents on each negative and afterwards on each positive 2 V output channel is continuously risen. During a test the actual channel number, the polarity as well as the output and supply currents are indicated. The output current is calculated from the applied ADC value and the measured calibration function of the circuit (4.3.3). All currents on the digital 3.3 V and GND lines as well as on the ± 2.8 V supply lines of each redundant half are measured in the same way as for the "Current-Monitor". Commands are send via USB. For different redundant halves needs to toggled between the two USB connections on the UPSFE backplane. During execution of the tests procedure the channel current is ramped in 10 mA steps until the SSF is disabled and starts toggling like for the digital SSF. Then the maximum current is recorded, the load is set back to its minimum and the same procedure is repeated for the next channel up to the last. In addition the number of performed cycles for each channel can be risen by a control of the GUI to check the SSF behavior after heating with overcurrent. The commanding structure of this procedure is quite simple, since for each step only one I²C read/write command is send through the I/O-Warrior-40 to the digital potentiometer.

The "DC/DC-Converter" test on the last tab, visible in Fig 4.49, sends sequences to the variable load system to measure the conversion efficiency of this boards and to check their protection circuits. All actual in- and output voltages and currents are displayed by indicators and all measured efficiencies versus the output power are shown in a graph. Thereby the voltages and currents are measured in the same way as for the "Current-" and "Voltage-Monitor" and the efficiencies are calculated as $\eta = P_{out}/P_{in}$ with the power $P_{in/out} = I_{in/out} \cdot U_{in/out}$. Like for the UPSFE regulator-SSF test the commanding is done by I²C through the I/O-Warrior-40 to the digital potentiometer of the control box and established via USB. The GUI allows to store

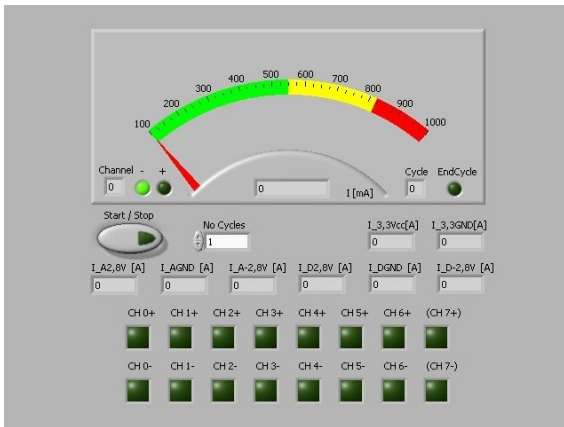


Figure 4.48: TRD Test Environment
UPSFE regulator SSF test tab.

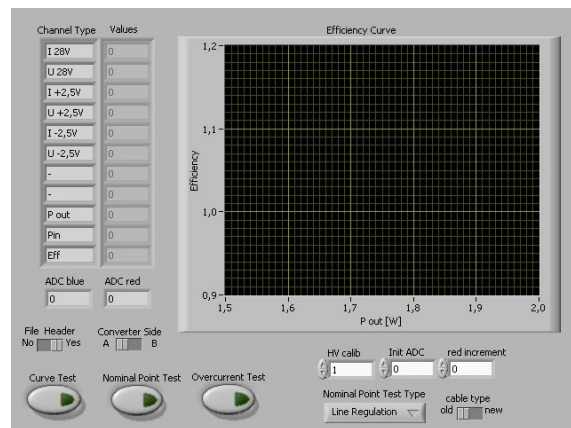


Figure 4.49: TRD Test Environment
DC/DC-converter test tab.

all measurements made for functional tests before and during a board level ESS in a single file. For the first test of a DC/DC-converter the switch "File Header" need to be set to "yes" and a header as well as the table structure of the data are written the log file. For all further runs for the same board the switch should be set to "no" and the previous file is opened by referring to the type and serial number of the board. To specify measurements of redundant halves in the log file the "A/B-side" switch of the GUI needs to be toggled before starting the test of the other side. After attaching a DC/DC-converter to the control box and switching it on, three test procedures can be executed. The first one, the "Curve Test", measures an efficiency curve by applying step by step five different loads and measuring all voltages and currents. A second one, the "Nominal Point Test", measures the conversion efficiency at the U-Crates nominal input power. A specific header for different temperatures or line regulations measurement can be chosen with the "Nominal Point Test Type" ring and is written to the log file by starting with the "A-side". A third procedure, the Overcurrent Test, applies 1.5 times the maximum load at the boards output. This activates the SSF and the converter half replies an error status, which is indicated by one LED of the control box.

4.3.5 Performed test procedures

At the beginning of the tests each board was visually inspected. The followed test procedures included manual and automatic electrical test, slow control tests and Soft Start Time as well as Latch Delay Time tests. All tests of the DAQ functionality are not described in this thesis, but can be found in reference [Hau05].

Slow control tests

For the slow control tests of the UDR2s, the boards were plugged to QM1 test backplane and after power up the redundant sides (FPGA) were switched on/off by the control line jumpers on the backplane.

Instead the UPSFEv2s were mounted to the UPSFE test backplane and their redundant sides as well as all line regulators were switched on/off by LeCroy communication. In the QM2 phase

the commands were sent from a Linux PC via an EPP-CAN box ¹ to a USCM on a miniature backplane ² and the USCM interpreted the CAN-bus commands to LeCroy commands on cable connection to the UPSFE backplane. After delivery of the UBPv2 in the FM/FS phase it was more reliable to use the final way of commanding, established as an AMSWire communication between a EPP-AMSWire box and a JINFv2 on the UBPv2 and a LeCroy communication transmitted on the UBPv2 LeCroy cable to the UPSFE backplane.

The S9011AU was commanded by LeCroy communication established by the USCM in the QM2 phase and the JINFv2 in the FM/FS phase. To test all DC/DC-converter switching and error status reading functionality of the S9011AU, a QM1 DC/DC-converter was connected to each of its nine control pad groups. Thereby the supply voltage and the control signal powering was delivered by cables soldered to each board.

Manual electrical tests of the DC/DC-converter

In the QM1 and QM2 phase the control and status functionality of the DC/DC-converters was tested with a small board including the circuitry shown in Fig 4.41. For further functional tests high power resistor chains on 3 cooling bars were applied as different output loads. A photo of this chains is shown in Fig 4.50. As high voltages output loads resistors inside a box were connected and selected by a multi switch, as mentioned in section 4.3.3. This comfortable solution was applicable, since all tested high voltage outputs drive low power. Five different

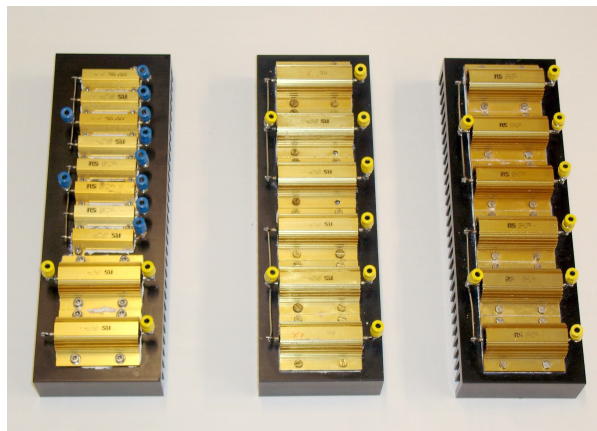


Figure 4.50: Photo of three resistor chains used for manual efficiency measurements of the DC/DC-converters.

load resistors were chosen and all voltages and voltage drops on the outputs were measured manually with a Keithley 2000 multimeter. At the end this resulted in efficiency curves for each board half. In addition to possible power estimates, the curves were useful to detect defects showing up as difference to a reference board. Further the line regulation efficiencies were measured for input voltages of 26.5 V and 30.5 V and an attached nominal load, which is later

¹The EPP-CAN box was designed by Vladimir Koutsenko

²The Universal Slow Control Module (USCM) was the slow control device in the QM2 U-Crate design, which is now done by the JINFv2

applied by the U-Crate. At all ESS operation temperatures only nominal load efficiencies were recorded and the overcurrent protections were checked by applying a very high load ($\leq 1\Omega$).

Automatic electrical tests

Most of the electrical tests of the U-Crate boards and the FM/FS DC/DC-converters were performed with use of the TRD Test Environment, therefore this section refers to its procedures.

The "Current-Monitor" difference display of the TRD test environment was executed before and after the U-Crate board level ESS to detect part defects or variations of redundant parts and weak solders or circuit shorts. In the same period digital supply SFF and linear regulator SSF tests of the UPSFEv2 were done. For this task the UDR2 and UPSFEv2 were powered by the test backplanes and the S9011AU by a cable connection to the 3.3 V supply pads. A further "Voltage-Monitor" scan during the QM2 crate level ESS proved the stability of all UPSFEv2 ± 2 V output channels at different temperatures.

During the DC/DC-converters first functional tests before the ESS were recorded efficiency curves. For each board half of a low voltage converters was simply executed the "Curve Test" procedure. For a S9056 and S9055 converter half was additionally applied a load box resistor to the high voltage output and then the "Curve Test" was performed for the low voltage outputs. This procedure was repeated for all four load box resistors. In addition to possible power estimates, the derived efficiency curves were useful to detect defects showing up as difference to a reference board. At the end of the first tests line regulation efficiencies for input voltages of 26.5 V and 30.5 V were measured by running the "Nominal Point Test" procedure. At all ESS operation temperatures only nominal load efficiencies were recorded with the "Nominal Point Test" procedure and the overcurrent protections were checked with the "Overcurrent Test" procedure.

Soft Start Time and Latch Delay Time tests

The Soft Start Time (SST) of the DC/DC-converter and the Latch Delay Time (LDT) of all SSFs on TRD electronic boards were measured with an oscilloscope. The LDT tests guaranteed the overcurrent protection mechanisms of the UPD and the U-Crate, since a too short LDT duration leads to a not sensed SSF error status by the slow control FPGA on the S9011AU and UPSFEv2. Thus not only a non-operating SSF, but a false LDT timing can cause an electronics part damaged.

To derive the LDT of an U-Crate board an oscilloscope probe was attached to the SFF supply lines and the LDT was measured as the high level time during the SFF off/on oscillations for an applied overcurrent (see section 4.3.4). The DC/DC-converters LDTs were obtained by attaching one probe to a low voltage output, setting a trigger level slightly below the output voltage and applying a high load ($\sim 1\Omega$) to an operating output. The appearing partial voltage drop triggered the scope and the LDT was measured as the time until a complete voltage drop appeared due to a disabled SSF. The DC/DC-converters SST was retrieved by triggering the scope with one probe on a switched on supply line and reading the time until a stable low voltage high appeared with a second probe.

4.3.6 Results of the QM2 U-Crate and UPD S9011AU board level tests

The JINFv2 and the UHVG board level tests were done by Vladimir Koutsenko, MIT. In the QM2 U-Crate ESS time table 4.2 are listed the performed board level tests for the U-Crate electronics.

Table 4.2: Time table of the QM2 U-Crate and UPD S9011AU board level ESS tests at CSIST

Test Date	#	Board Type	Serial Number	Commend	Testers Name
Jun,04	10	UDR2 S9070	93001-93010		F. Hauler, IEKP M. Schmanau, IEKP
Nov,04	9 1	UPSFEv2 S9043 S9011AU	93001-93009 93003		L. Jungermann, IEKP M. Schmanau, IEKP

By visual inspection of the QM2 UDR2 a bad component was detected on the board with serial number 93005, as visible in Fig 4.51. Further problems were found by the "Current-Monitor"

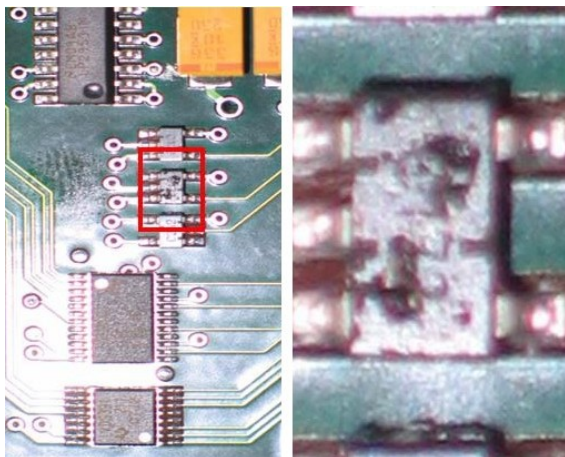


Figure 4.51: Bad component on UDR2 93005 during production. The component failed visual inspection and was replaced before board level functional tests.

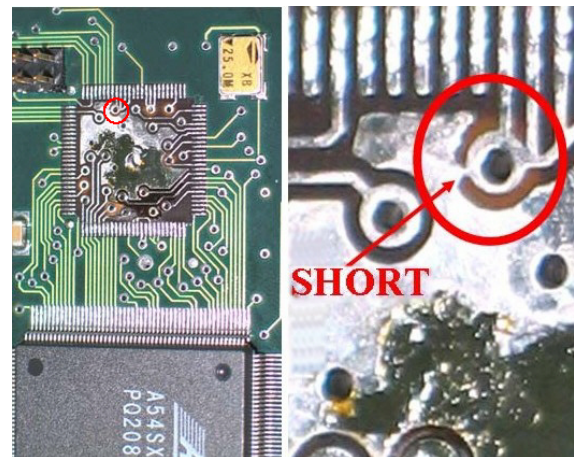


Figure 4.52: DSP solder problem on UDR2 93005, 93006 and 93009 during production. The problem was hard to detect since normally the area is covered by the DSP.

difference display of the TRD test-Environment. Three UDR2 board with serial numbers 93005, 93006, 93008 and 93009 showed a current leak of a few milliamperes to the shield and some of them also SRAM and flash memory problems, but no visual short. By joining these facts together, it was found that a small tin dot shorted a heat conducting shield pad under the DSP chip to a via, as shown in Fig 4.52. It was hardly a production flaw, since the via was simply too close to a shield pad. Therefore it was decided to fill solder stop into the vias to prevent this problem.

During the QM2 tests of the UPSFE a non-working overcurrent protection of the fourth positive regulator channel on the redundant B-side of board 93004 was found. The failure was repaired by replacing the error status optocoupler and the operational amplifier LM258D in

the overcurrent feedback circuit of this channel. A similar failure was found after the UPSFE FM/FS ESS for the board 95005F, where the opamps LM258D and LM6142AIM of the first B-side channel were replaced. All other QM2 UPSFEs showed no problem.

Since QM2 S9011AU for the UPD is a slow control board, with similar circuitry and components as the U-crate boards, it was produced together with these boards and thus also tested with them and showed no problems.

At the end the tests were a success with an electronics yield more than enough to fill a complete QM2 U-Crate.

4.3.7 Results of the QM1/2 and FM/FS UPD board-level tests

Time table 4.3 lists all vibration tests and TVTs performed for the QM1 DC/DC-converters and the later produced QM2 S9053U converter. All TVTs showed a good heat dissipation of the boards and negligible small deviations of their conversion efficiencies at different temperatures. For the vibration test a random spectrum (see section 4.33) and harmonic frequencies in x-,y- and z-direction were applied. None of the heavy coils on the boards were teared off and the harmonic vibration derived only Eigenfrequencies above the 50 Hz limit specified by the NASA.

Table 4.3: Time table of the DC/DC-converter vibration and TVT tests

Test Date	#	Production phase	Board Type	Test type	Test place
Jun,03	1	QM1	S9053	Vibration	RWTH Aachen
Nov,03	1	QM1	S9056	Vibration	RWTH Aachen
Nov,03	1	QM1	S9053	TVT	MPI Garching
Apr,04	1	QM1	S9054	Vibration	RWTH Aachen
Aug,04	1	QM2	S9053U	Vibration	RWTH Aachen
Aug,04	1	QM2	S9053U	TVT	RWTH Aachen
	1	QM2	S9053		

Time table 4.4 shows all performed ESS tests for the QM2 DC/DC-converters. Some of the DC/DC-converters tested before the ESS had missing components, but none of them are UPD boards. Just one QM2 S9048 DC/DC-converter had a broken wire of the auxiliary coil on the primary transformer side, which caused a loss of the overload protection. The transformer was replaced and the board went through the tests. At the end all QM2 DC/DC-converter showed stable efficiencies and full functionality.

All performed final FM/FS ESS tests are listed in the time table 4.5. Examples of the measured efficiency curves for each DC/DC-converter type including the nominal efficiencies at different ESS temperatures are plotted in Fig 4.53. During the first functional tests of all FM/FS S9048 wrong output voltages were measured. A wire of the output filter (storage) inductor was soldered to the wrong pad on all redundant halves and the error was found to originate from the assembly procedure document provided by CAEN. After soldering all wires to the right pads the outputs of S9048 boards operated fine. One of these board, the serial number 94005F,

Table 4.4: Time table of the QM2 DC/DC-converter ESS tests at CSIST

Test Date	#	Board Type	Serial Number	Commend	Testers Name
Nov,03	4	S9048	92001-92004		M. Menichelli, INFN
	4	S9051	92001-92004	labeled qm1-4	M. Schmanau, IEKP
	4	S9053	92001-92005		
Jan,04	7	S9054	92001-92007		E. Fiori, INFN
	4	S9056	92001-92004		M. Schmanau, IEKP
Nov,04	1	S9048	93001		L. Jungermann, IEKP
	1	S9053U	93001		M. Schmanau, IEKP

Table 4.5: Time table of the FM/FS DC/DC-converter ESS tests at CSIST

Test Date	#	Board Type	Serial Number	Commend	Testers Name
Mar,06	10	S9054	94001F-94010F		M. Schmanau, IEKP
	10	S9056	94001F-94011F	except 94005F	S. Blasko, INFN
May,06	8	S9048	94001F-94009F	except 94005F	M. Schmanau, IEKP S. Blasko, INFN
	4	S9053U	94001F-94004F		
	21	S9053	94001F-94022F	except 94019F	
	18	S9055	94001F-94018F		
	1	S9056	94005F	after repair	
Sep,06	1	S9048	94005F	after repair	S. Blasko, INFN

also had a non-working overcurrent protection on the A-side. The reason was a broken wire of the auxiliary coil on the primary transformer side. After replacement of the transformer the protection operated fine. A third error was found on the B-side of the S9056 board serial number 94005F. Its outputs did not operate due to a broken temperature sensor AD590KF disabling the SFF. The board was repaired by replacing the sensor.

At the end all FM/FS UPD DC/DC-converters went successfully through the ESS tests.

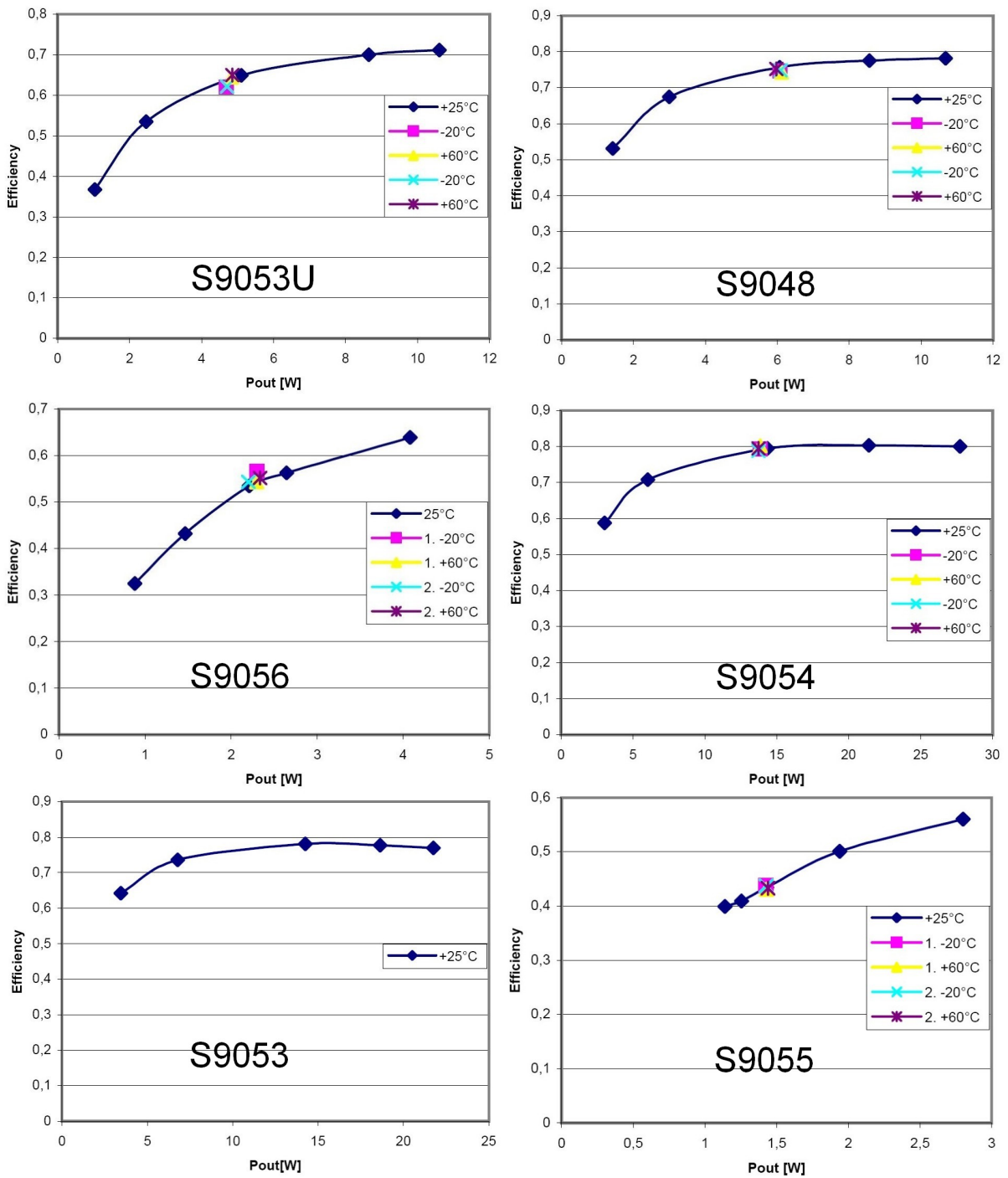


Figure 4.53: Efficiency curves for each tested FM/FS DC/DC-converter type with nominal efficiencies measured during ESS. The S9054, S9053, S9055 belong to the TRD Gas System and the Tracker. The ESS of the S9053 was done separate from the UPD production one.

Chapter 5

The AMS-02 TRD Monte-Carlo simulation

Monte Carlo simulation (MC) of HEP experiment detectors are performed to estimate the detector efficiencies and can be used to develop analysis codes before measured data is available. In general these simulations treat particle interactions as a probability for an observable to initiate or result out of a physical process. The relation between a probability and an observable are called probability density functions (pdf) and are known by measurements or theoretical calculations. An interaction is simulated by generating observables as random numbers obeying the pdfs. In case of MC simulations this is realized by generating random points inside the probability versus observable space and choosing only random observable from points below the pdf. Thus the simulation works like a gambling shooter step by step integrating a normalized pdf to one. In reality the procedure is more complicated due to many involved interactions and the necessity to fulfill all conservation laws.

The following chapter describes a GEANT4¹ MC simulation of the AMS-02 TRD developed as possible replacement for an existing GEANT3² version included in the present AMS-02 detector simulation. The new implementation was motivated by an analysis of beamtest data taken with a TRD prototype in the year 2000, that showed a strong deviation between the proton rejection factors derived from the data and the GEANT3 simulations. Here the rejection factor $R = N_{total}/N_{mis}$ was defined as the total particle number of a sample N_{total} divided by the misidentified ones N_{mis} of this sample. To exclude as origin a poor beam purity, a second beamtest with a much higher beam purity was performed. But the recorded data gave the same result and the facts suggested a problem in the detector simulation. To overcome the problem a diffractive process was introduced into the simulation. Such a process was motivated, since diffraction typically generates additional particles along the beam direction, that are not spatially resolved by the TRD. Thus protons may look like electrons generating TR due to additional energy depositions. But the parametrization of the introduced process was just adjusted to cancel the observed deviation and not physically motivated. Therefore it was worthwhile to test the GEANT4 capabilities for a TRD simulation, because this framework includes new hadronic physics implementation including diffractive processes and is continuously developed, supported and tested due to its wide use, for example for the LHC detectors.

The analysis code of the presented data was written in C++ with help of the today widely used ROOT³ classes. All methods, cuts and constants were kept the same as for the earlier GEANT3 analysis, in order to be able to compare with the former results.

¹GEANT4 is a C++ based MC detector simulation framework today used to simulate the CERN LHC detectors.

²GEANT3 is a FORTRAN based MC detector simulation framework used to simulate the CERN LEP detectors.

³ROOT, an object oriented data analysis framework developed at CERN

Unfortunately, the analysis of the GEANT4 simulation lead to the same deviation as GEANT3, independent of the used hadronic physics implementation provided by GEANT4. Thus some aspects of the diffraction theory were studied, that lead to a physical motivation for the cross section used by the former parameterized process. The derived cross sections were then taken for a diffractive background estimation, obtained by a PYTHIA¹ simulation, whose results strongly hint at a diffractive origin of the deviating p -rejection factors.

5.1 Beamtests with the TRD prototype

Table 5.1: Event numbers recorded for the beamtest in 2000. Suffix k denotes $\times 1000$

E_{beam}	X7				E_{beam}	X7	H6
[GeV]	$\#e^-$	$\#\mu^-$	$\#\pi^-$	$\#p^+$	[GeV]	$\#p^+$	$\#p^+$
5.0	120k				120.0	30k	215k
10.0	160k		20k		140.0	30k	
15.0				45k	160.0	40k	290k
20.0	150k		20k	30k	180.0	40k	
40.0	160k		20k	60k	200.0	80k	155k
60.0	180k	190k	20k	20k	250.0	65k	
80.0	120k	170k	20k	20k			
100.0	200k	110k	50k	150k			

In summer 2000 two beamtest with a TRD prototype² were performed, that already had straw modules and fleece radiators of the final TRD design. These beamtests were accomplished at the X7- and the H6-beamline of the CERN Super Proton Synchrotron (SPS). During the first beamtest data were taken for e^- , μ^- , π^- and p^+ at energies ranging from 5 to 250 GeV. The later H6 beamtest should provide a clean proton data sample by suppressing beam contaminations with the H6 CEDAR³, because a p -rejection problem was discovered. An overview on the recorded data is given by table 5.1.

All given information and shown figures in this section are extracted from reference [Orb03].

5.1.1 Beam test setup

The X7 beam is produced by SPS protons, that can be scattered on one or eventual two targets and thus provides primary, secondary or tertiary hadrons and leptons with energies between 5 GeV and 250 GeV. In either case beams with an intrinsic momentum resolution of $\Delta p/p = \pm 0.8\%$ can be generated by using deflections and focusing magnets and collimators. The beamline is equipped with two threshold cherenkov counters. One of them is operated with He the other with N_2 gas. These counters were used for the proton runs to reject all other particles by discarding the readout trigger for any signal from the counters. By combining

¹PYTHIA, a FORTRAN based Monte Carlo event generator for particle physics

²The prototype was built by the RWTH Aachen. And the Aachen group also performed the beamtests.

³Cherenkov Differential counter with Achromatic Ring focus.

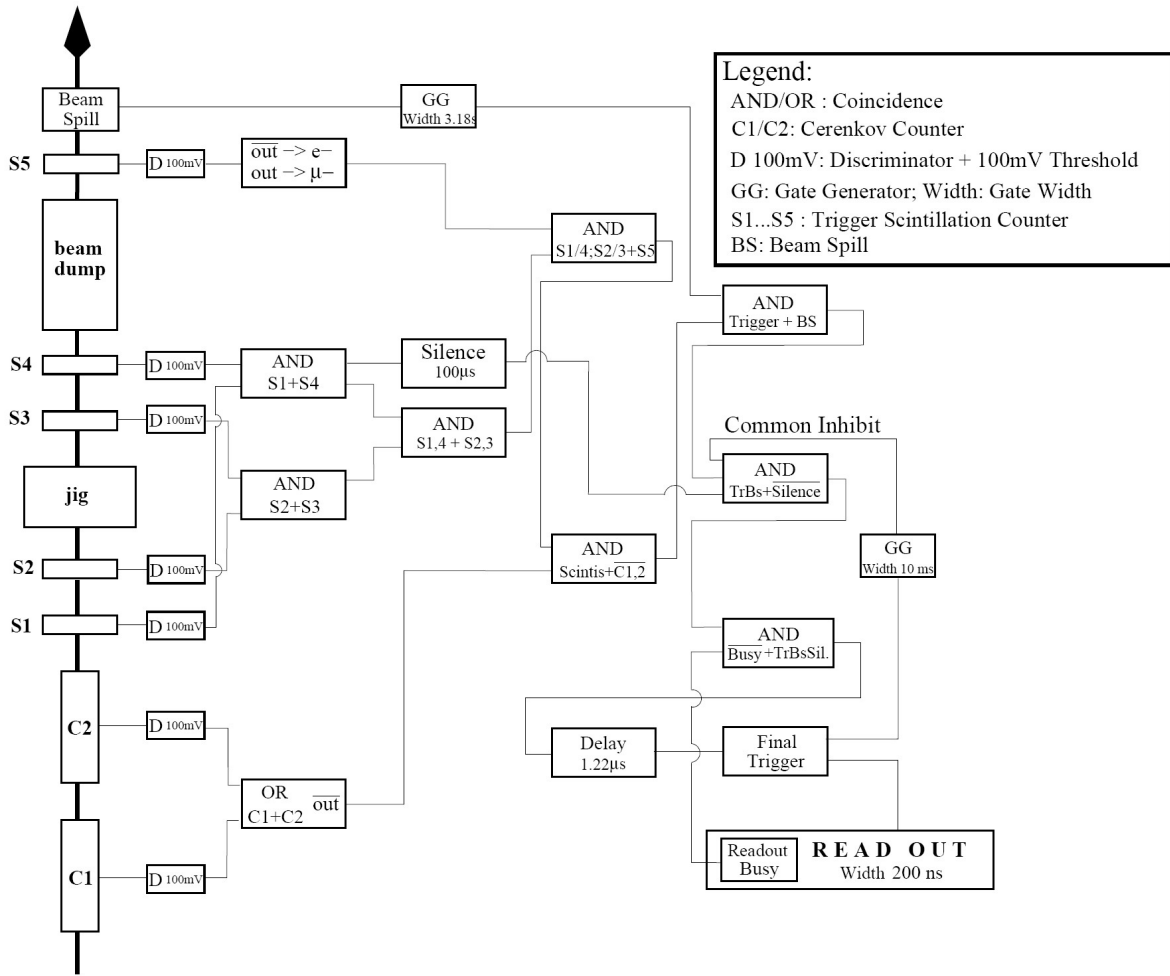


Figure 5.1: Beamtest setup and trigger logic used at the X7 beamline. [Orb03]

both counters the detection inefficiency was 1.15%. The X7 beamtest setup, drawn in Fig 5.1, included five scintillation counters. Two inner counters sized $10 \times 15 \times 1$ cm and $18 \times 10 \times 1$ cm were shiftable attached to the jig, two outer sized $18 \times 10 \times 1$ cm in about 2 m distance in the front and back of the jig. The fifth counter was placed behind the 2 m long beam dump to trigger or reject μ^- . A readout trigger was given for a coincidence of the inner and outer counters together with a count or none veto of the fifth scintillator. This trigger was again inhibited by a readout busy and a silence veto of $100 \mu\text{s}$ given by a coincidence of the outer counters. The taken data has events of high particle purity, since the trigger strongly discriminated against lighter particles.

A detailed description of the H6 beamline setup will be omitted, since the data seems to got lost and thus could not be used for the analysis in this chapter. It just need to be mentioned, that differential CEDAR Cherenkov counter drastically reduced the uncertainties of the contamination. Since the lighter particles were clearly separated by the used CEDAR setup compared to the X7 case [Orb03], [Bov82], the contamination was about a factor 10-100 times smaller. However the TRD rejection power derived from the H6 beamtest data showed the same deviation, and this would correspond to a contamination of the proton samples of the order of 1.‰.

5.1.2 The TRD prototype

The TRD prototype used for the beamtest in 2000 was the fourth prototype during the design evaluation studies for the TRD. It already had 20 layers of straw tube modules interleaved with 20 mm fleece radiator, but the modules had an equal length of 40 cm. One layer included two modules and in contrast to the later TRD design, 16 layers were oriented in y-direction and the 3rd and 4th as well as the 16th and 17th layers in x-direction. During production each module underwent the same tests as the later TRD modules. They were mounted inside an aluminum jig, as depicted in Fig 5.2, that also supported the gas tubing, the readout electronics and the high voltage dividers.

Like in the final TRD the two modules of a layer were shifted against each other in z-direction. Thus the modules build a two tower like structure, where the one closer to the beam was called N-Tower the other P-Tower. A detailed drawing of the internal geometry is shown in Fig 5.13. For both towers mainly ATLAS fleece material was used, as described in 3.2.3. Only the central 3 sets of 4 successive layers were equipped with different types of radiators for radiator evaluation studies. But the analysis in all following sections is just carried out for data, where the beam ran through ATLAS type radiator. The gas supply system attached to the jig had 6 gas chains. All gas parameters necessary for later gas gain calculations were retrieved from a flowmeter set to 1.2 l/h and differential pressure sensors, while the absolute pressure was measured at the gas exhaust and the temperature inside the jig. The beam angle could be adjusted by a turntable on which the detector was mounted. Two beam windows of 20×20 cm size on the front and back of the jig were closed with 5 mm acrylic panes, which then corresponded to the same amount of material as the honeycomb plates on top of the final TRD.

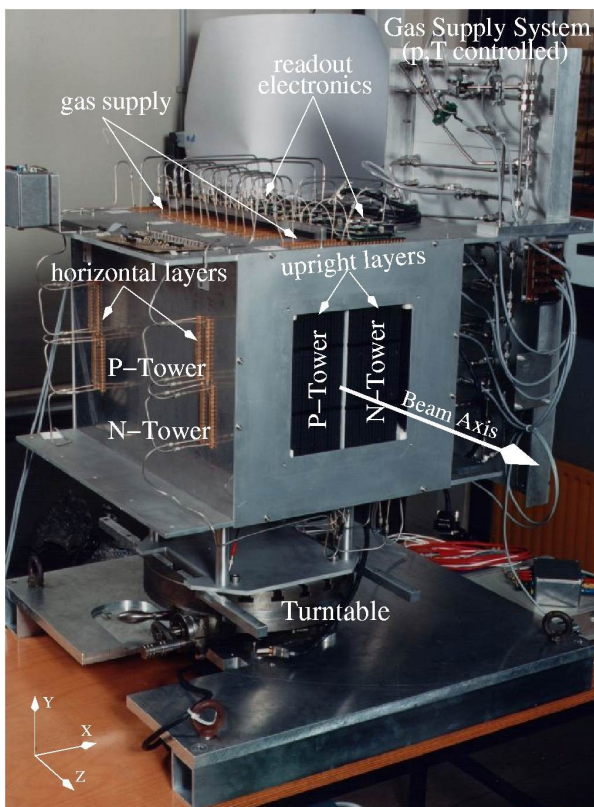


Figure 5.2: Photo of the 20-layer TRD prototype. [Orb03]

Since the final readout front ends were not available at that time, the readout was done with separate boards each carrying three 12bit ADCs, which serially received the analog signals from the front-end electronics (VA-chips). Two of this boards with each time 8 VA-chips were connected to the vertical modules and 2 smaller ones with 3 VA-chips read out the horizontal modules, the trigger scintillator PMs and the Cherenkov counters of the Beam test setup. In general the readout front ends were equal to the TRD UFE design. But as considerable difference they hosted VA32HDR2 chips instead of the VA32HDR12, since the UFE chips were later made as costum design for the AMS collaboration. The VA32HDR2 chips just have a dynamic range of 1100 fC compared to 2000 fC for the UFE chips and the linear range was

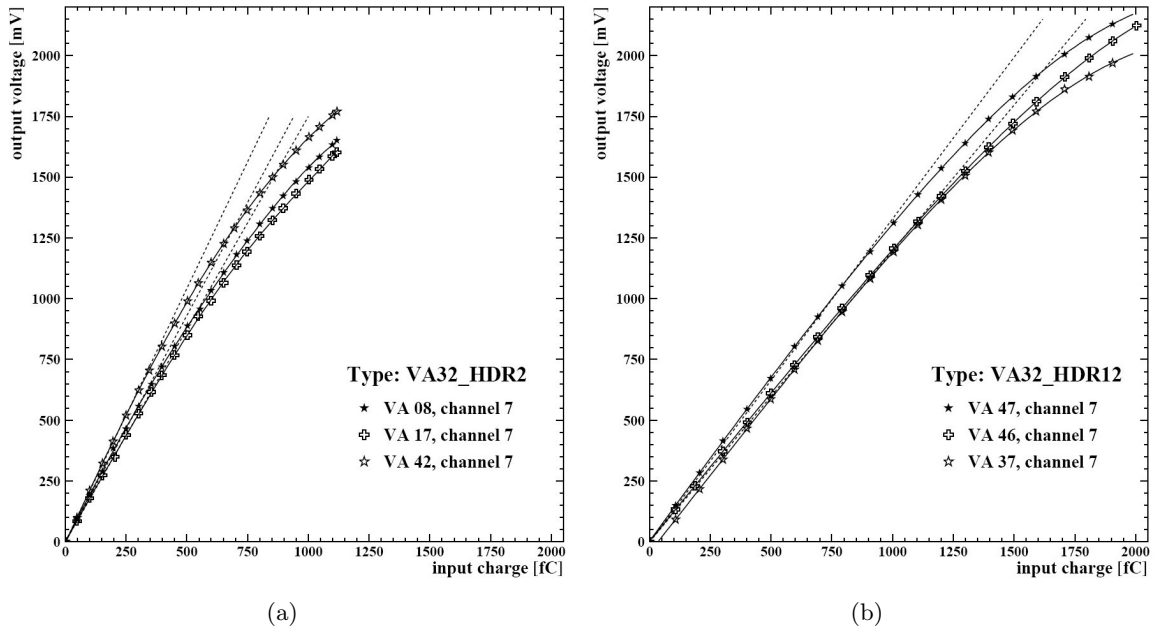


Figure 5.3: (a) Gain linearity of the VA32HDR2 used for the prototype. (b) Gain linearity of the VA32HDR12 used for the final TRD. [Orb03]

about a factor three smaller as shown in Fig 5.3. Since for a VA32HDR2 a signal of ~ 160 fC corresponds to an energy deposition of 5 keV or 4 MIPs, all energy depositions spectra show an early cut off at about 35 keV, depending on the pedestals.

5.1.3 Raw data analysis of the X7 beamtest

The data used for all analysis and comparisons to GEANT4 simulations in section 5.4 were in form of preprocessed raw data stored in Hbook files. To give an estimate of any error resulting from the preprocessing as well as to explain some of the track reconstruction parameters, this section summarizes the raw data analysis methods.

The energy calibration was done with a randomly triggered ^{55}Fe source (max. peak energy of 5.9 keV) throughout the beamtests. All measured energy depositions were fitted by a Fermi function (non relativistic form). These fits retrieved the edges of the degenerated spectra, caused by the random trigger and the resulting shift in the integration time. At the end an overall energy calibration factor of:

$$ecf = (9.09 \pm 0.05) \text{ eV/ADC count} \quad (5.1)$$

was obtained.

All energy depositions of the stored data were corrected according to the VA chip non linearities and the pedestal was subtracted, which reduced the dynamic range on average by 25%. The electronic pedestals ranged from 800 to 1400 ADC counts with a pedestal width (noise) between 2 and 6 ADC counts, as shown in Fig 5.4. A broad vertical N-Tower pedestal probably

originated from a bad readout cable and a multiplexer timing problem. The common-mode noise was already subtracted by the common-mode correction built into the VA-chips.

VA- and gas gain changes, caused by the finite mechanical accuracy and the gas flowing from the first to the last module, were corrected by a channel by channel inter-calibration. Therefore a Landau fit to the energy depositions of the muon runs in a range up to 600 ADC counts was performed and all resulting MOP (Most Probable) values were equalized by multiplying an inter-calibration factor. These factors were stored and used for all other particle runs as well. The error of this method was retrieved from the fit errors and stayed inside a 1% level.

Since the data was taken over days with different temperature and pressure conditions, a further gas gain correction was necessary. Averaged MOP values for each muon run were calculated and plotted as relative changes of the average gas gain versus the appropriate gas densities and then fitted by a straight line. This method showed, that an increase of the gas density by 1% leads to a decrease of the gas gain of 5.24%. All later gas gain correction factors were calculated from the gas densities during the data taking and the slope of this fit.

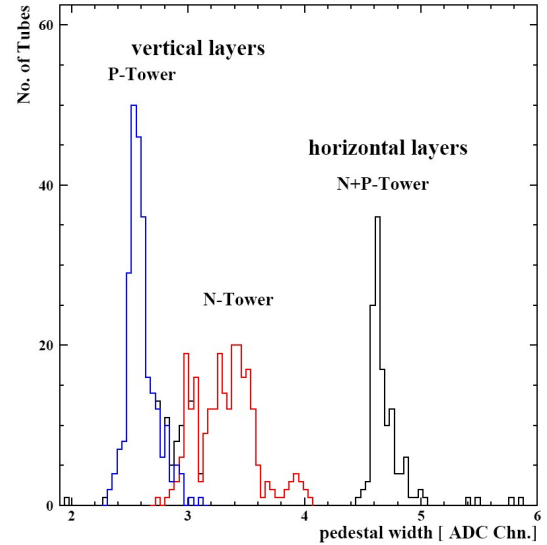


Figure 5.4: Pedestal width distribution of all 640 channels. [Orb03]

5.2 Rejection power analysis

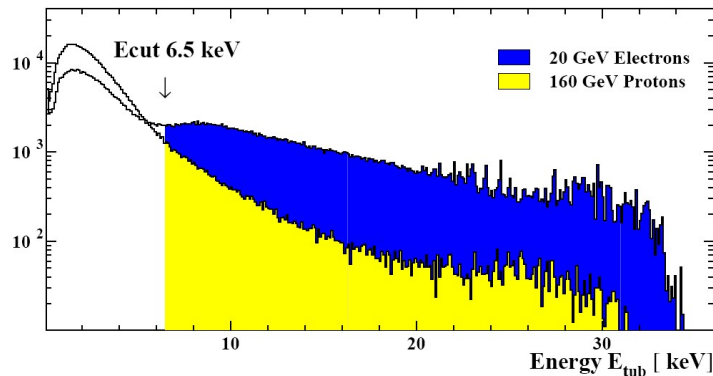


Figure 5.5: Overlay of the accumulated energy deposition distribution for e^- and p . All single track event hits of a sample are accumulated in one histogram. [Orb03]

As mentioned in the introduction and explained in detail in section 3.1.3, the identification of positrons depends on the TRD rejection power of protons. Fig 5.5 shows, that protons can be rejected by a cut on single track energy spectra. But this method has a quite small rejection

power or a worse positron efficiency, dependent on the applied cut. By the previous beam test analysis p -rejection factors were derived with four different methods, a cluster counting method and three likelihood methods. All of them showed a p -rejection power mismatch between the data and the GEANT3 simulation. To determine the p -rejection factor for the e^+ detection its enough to use electrons available at the X7 beamline instead of positrons, since the result does not change in absence of magnetic fields.

5.2.1 Likelihood method

The three proven likelihood methods differed in the way to calculate the likelihood value L_e for an event to be electron like. For the first one the geometric means of hit probabilities for electrons and protons were built separately. The second one directly calculated the probability quotient for each hit and gained L_e as arithmetic mean for all hits. And the third method tested the standard likelihood definition combining summation and multiplication of integral probabilities.

Since the geometric mean method showed the best performance for the previous data analysis, only this method is described in detail and was used for the complete rejection power analysis in this thesis. Details of all other tested rejection analysis methods can be found in reference [Orb03]. As rejection factor definition the quotient $R = N_{total}/N_{mis}$ is used, where N_{total} is the total particle number in a background sample and N_{mis} the misidentified one .

Likelihood methods make use of the full information contained in the energy spectra. Each spectra is normalized to an integral of one and used as probability density distributions. All p as well as e^+ probabilities are separate multiplied of all and a geometric mean:

$$P_{e,p}^{mean} = \sqrt[n]{\prod_{k=1}^n P_{e,p}^k(E_{dep})} \quad (5.2)$$

is calculated out of the products, where n is the number of hits. The likelihood value L_e for an event to be positron-like is then derived as:

$$L_e = \frac{P_e^{mean}}{P_e^{mean} + P_p^{mean}}. \quad (5.3)$$

This calculation needs to be done for a complete p and e^+ sample and the $-\ln L_e$ are then filled to separate histograms. Fig 5.6 shows this distributions gained for 160 GeV protons by the previous analysis and also indicates the likelihood cut (LH-Cut). The electron distribution peaks a factor of 2 lower than the one for protons. The LH-Cut is defined as the L_e value of the electron

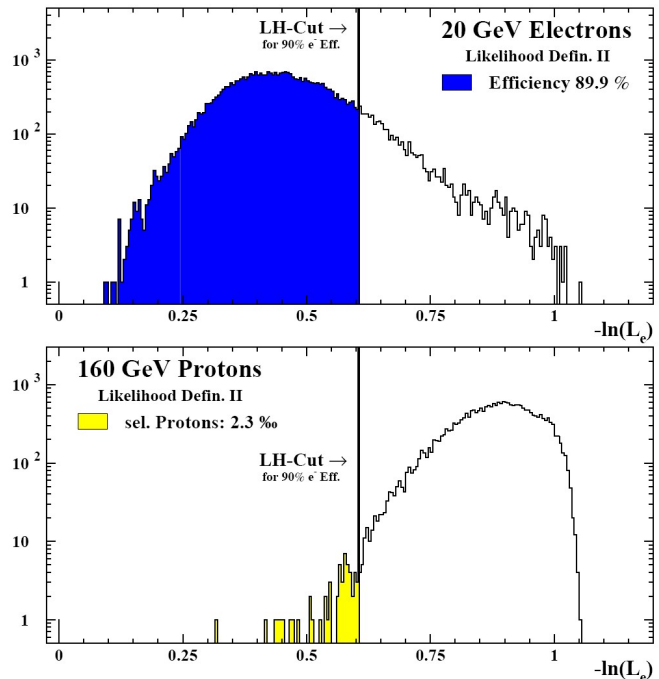


Figure 5.6: Likelihood distributions, for 20 GeV electrons and 160 GeV proton samples. [Orb03]

distribution yielding an integral from zero of 90% of the total distribution. By applying this cut to the proton distribution the integral below the cut gives the number of misidentified protons for an electron efficiency of 90%. The rejection factor for the example case in Fig 5.6 calculates as fraction of the total proton event number $N_{p,tot}$ and the misidentified ones $N_{p,miss}$ to $N_{p,tot}/N_{p,miss} = 435 \pm 57$.

5.2.2 Cluster counting method

The Cluster counting counted so called "TR-clusters". In this case "TR-clusters" were defined as track clusters with energy depositions above 6.5 keV, a value where additional TR starts to be visible in the spectra. About 90% of the electron tracks have a "TR-cluster" number of 6 or larger. Thus this threshold was used to select electron like events in the data of the mono energetic proton and electron beams. The distributions of the cluster counts show a Poisson shape with an expectation of 8 counts for electrons ($E > 20$ GeV) and about 2 for protons, dependent on the proton energy.

5.2.3 Rejection power mismatch between data and GEANT3

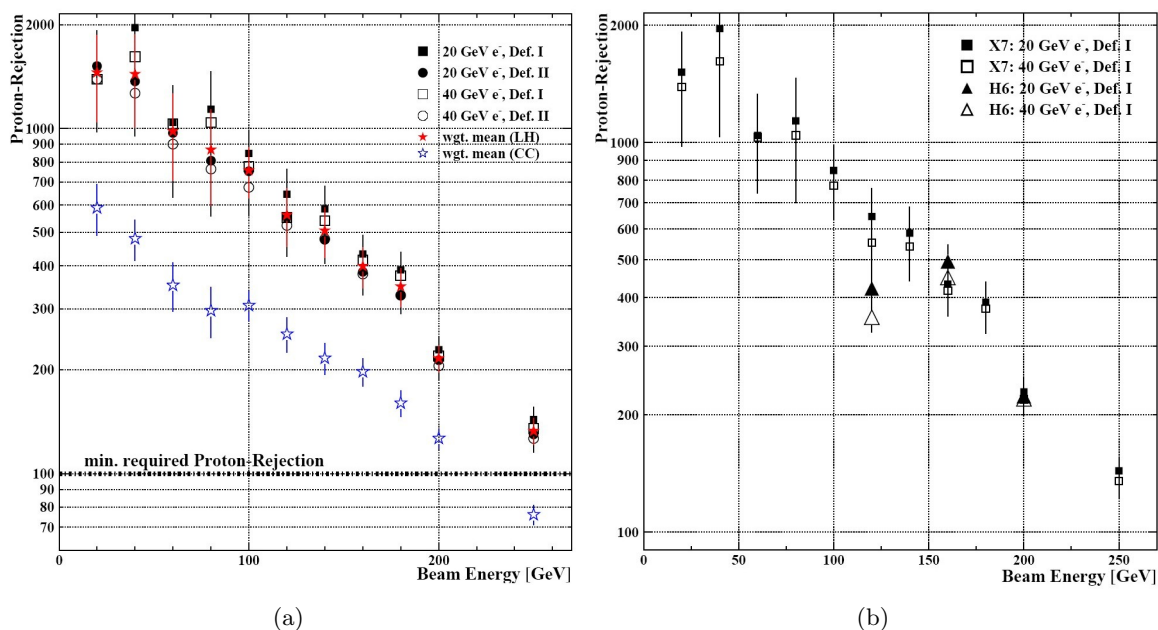


Figure 5.7: (a) Rejections factors versus p^+ energies by 3 methods: cluster counting (blank stars), geometric mean (Def.I) and arithmetic mean (Def.II) likelihoods. (b) Comparison of likelihood rejections versus p^+ energies derived with the X7- and H6-beamline data. [Orb03]

After a track reconstruction only single track events were selected to ensure background free data samples for the rejection power analysis and comparison to Monte Carlo simulations (MC). Details of this reconstruction and selection can be found in section 5.5.2. Fig 5.5 shows an accumulation of all hit energy deposition in a single histogram for e^- and p for single track

events. It is visible, that protons deposit energy just by ionization and electrons also by TR resulting in a much stronger distribution tail. Cutting above the TR threshold of 6.5 keV can already reject protons, but results in a low rejection power and a bad electron (positron) efficiency. In Fig 5.7 (a) different rejection factors are plotted against all proton beam energies derived for electrons samples with 20 GeV and 40 GeV. It includes the cluster counting method (blue stars), the geometric means likelihood method (Def.I) and the arithmetic means method (Def.II). A second beamtest at the H6-beamline with much higher beam purity lead to the same results for rejection factors gained by method Def. I, as it is visible in Fig 5.7 (b).

The conclusion for the tested p -rejection method was, that the cluster counting failed the needed rejection factor limit of $> 10^2$ and that the geometric mean likelihood method seemed to be the best performing method.

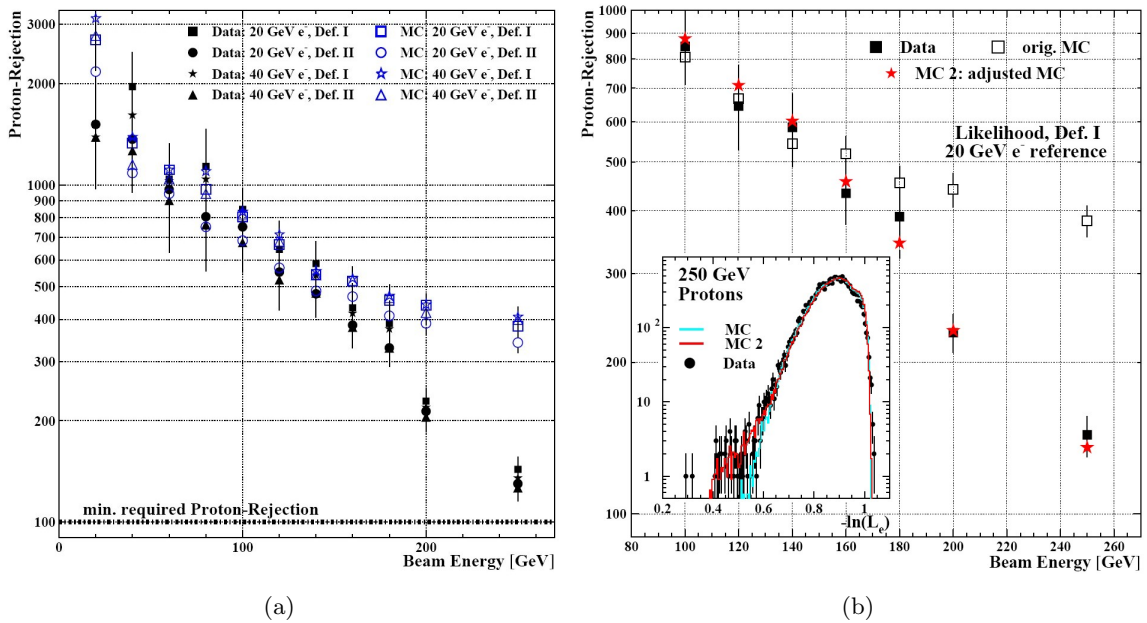


Figure 5.8: (a) Rejection factors versus the p^+ energies for the data and the GEANT3 MC gained by different methods and electrons energies of 20 GeV and 40 GeV. (b) Likelihood rejection factors versus p^+ energies above 100 GeV for the X7 data, the original (MC) and the adjusted GEANT3 MC (MC2). Inserted are the likelihood distributions for Def. I. [Orb03]

As mentioned of this chapter a rejection power deviation between the data and the GEANT3 simulation was found. The deviation starts above a proton energy of about 100 GeV independent of the used electron energy and the analysis method, as depicted in Fig 5.8 (a). It hardly results from an energy calibration error, since on the one hand this would lead to a global shift of the rejection factors and on the other hand the used likelihood methods are only sensitive to relative alignments and shapes of distributions. An error of the gas gain calibration can also be excluded, because the gain factors are distributed between 0.95 and 1.01 on the whole energy range, but the analysis still results in smooth rejection factor curves. Thus the problem could not be solved by changes of the analysis and detailed studies of the misidentified data events showed no significant systematics suitable for a further selection. The problematic events just

showed additional three TR-clusters compared to the Poisson expectation of the proton cluster distribution (5.24) and have a total event energy deposition of about two times the mean value for all protons events. They are selected as electrons, since they only carry typical electron signatures, as retrievable from Fig 5.23, and thus they also were indistinguishable in an assumed to be unknown data sample.

To overcome the deviation the assumption was made, that the misidentified events include diffractive scattering of protons with the detector producing pion pairs along the beam direction. Since these pion pairs add additional on track ionization depositions seen as TR-clusters by the TRD, such events look like electrons. Thus the GEANT3 simulation was extended by a parameterized diffractive process. If the assumption is valid and the extension appropriate will be discussed in section 5.3 and 5.6. In Fig 5.8 (b) rejection factors derived for the data are compared with the extended (adjusted) and the original GEANT3 simulation. The inserted proton likelihood distributions for 250 GeV protons shows, that only the adjusted MC simulation agrees with the data for small $-\ln(L_e)$ values.

5.3 Diffractive background cross section in the TRD

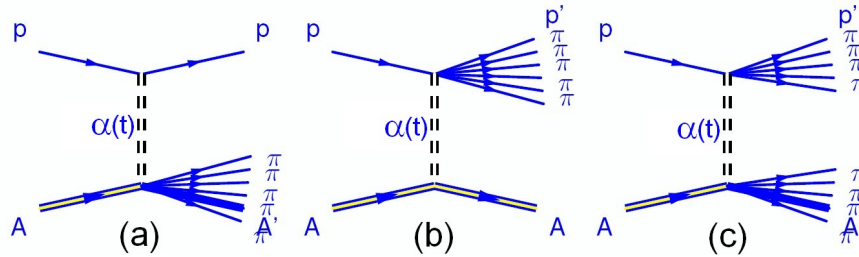


Figure 5.9: Feynman graphs for coherent single and double diffraction. (a) Target single diffraction, (b) projectile single diffraction, (c) double diffraction. [Sch83]

In the previous section it is mentioned, that the data of the TRD prototype beamtest might include a background not described by a standard GEANT3 simulation. Therefore the hypothesis was made, that the background originates from diffractive scattering inside the detector. In the following a process was implemented by assuming a beam proton scattering on the mainly organic material (^{12}C) of the TRD as $p + C \rightarrow p + C + \pi^+ + \pi^-$. This process generates pion pairs of tens of MeV running in the beam direction with an effective maximum cross section of $\sigma_{eff} \approx 15$ mb. It starts to produce pairs randomly distributed along the tracks above a threshold 100 GeV and just for protons. Unfortunately available cross section data for proton diffraction on carbon covering the beamtest energies could not be found and in reference [FGS00] is mentioned, that it is quite rare. Thus a direct confirmation or exclusion of the diffraction hypothesis by known cross sections was not possible and the necessary cross sections were derived from theoretical predictions of the dependencies between the $p + p$ and the $p + C$ case. As introduction to the diffraction theory some of its aspects and problems are summarized from the references [Bor05] and [Gou95]. In the following some available data for proton scattering on nuclei is shown, which is then related to a theoretical prediction for diffractive scattering on nuclei.

The name "diffraction" originates from concepts in optics and related to the description of nuclear high energy scattering physics introduced in the Fifties by Landau, Pomeranchuk, Feinberg et al. [VB02]. In the Born approximation the same equation for the elastic scattering amplitude can be derived from the scattering of a plane wave passing through and around an absorbing disk, which results in a "diffraction" pattern for hadron-hadron scattering. By the Good and Walker picture diffractively produced systems of dissociated particles were predicted to have the same quantum numbers as the initial beam particle. This means that only the quantum numbers of the vacuum are exchanged in diffractive interactions. For dissociation of the beam particles one can distinguish between different classes of diffractive events in hadron-hadron scattering: elastic scattering, where both particles stay intact; single diffractive dissociation of the projectile or the target (SD), where one particle dissociates; double diffractive dissociation (DD), where both particles dissociate. Double pomeron exchange (DPE) occurs for much higher energies than discussed in this thesis. In Fig 5.9 Feynman graphs are drawn for the single and double diffractive cases.

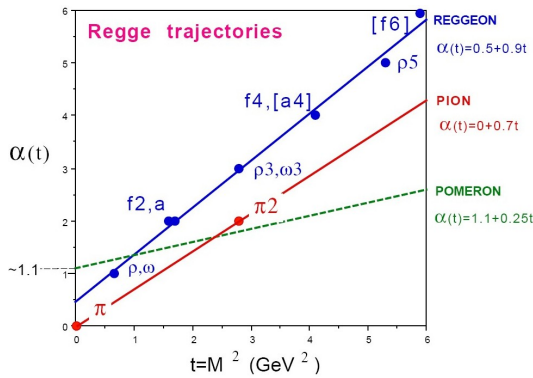


Figure 5.10: The parameterization of the most important Regge trajectories: pion (π), reggeon (\mathbb{R}) and pomeron (\mathbb{P}). [Bor05]

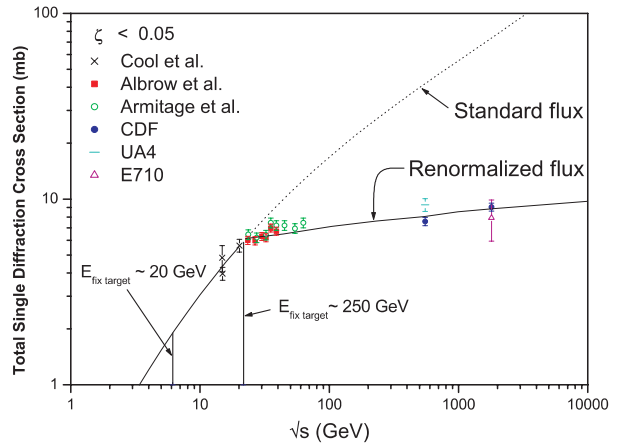


Figure 5.11: Measured total SD cross section in pp and $\bar{p}p$ scattering as function of \sqrt{s} compared to standard (dashed) and renormalized predictions from Regge theory. [Bor05]

In the 1960s Tullio Regge discovered a linear correlation between the squared masses of strong interacting particles or hadrons and their spins, as shown in Fig 5.10. In the Regge theory this correlation is described in the complex angular momentum plane by linear Regge trajectories: $\alpha(t) = \alpha(0) + \alpha' \cdot t$. These trajectories are exchanged between the beam particles as illustrated in the diagrams in Fig 5.9. For this phenomenology diffraction corresponds to the exchange of a Regge trajectory, that has the quantum numbers of the vacuum. The total cross section dependence on the center of mass energy \sqrt{s} , is determined by the intercept of the trajectory $\sim s^{\alpha(0)-1}$. Furthermore the elastic and diffractive cross sections are expected to increase with s as $\sim s^{2\alpha(0)-1}$, such that the ratio to the total cross section rises with s . To describe the rising behavior of the total cross section the pomeron trajectory was postulated with an intercept of $\alpha_{\mathbb{P}}(0) = 1$. In contrast to all other trajectories no particle has been identified on the pomeron trajectory. As the pomeron trajectory has the largest intercept of all Regge trajectories, pomeron trajectory exchanges dominate at high energies and its parameters have been derived from fits to the data of soft diffractive interactions. Fig 5.11 visualizes arising compli-

cations, when applying these parameterizations to even higher energies, where the predictions overestimate considerably the measurements. Different approaches have been developed, for instance by taking into account multiple pomeron trajectory exchanges or by renormalization of the diffractive cross section parametrization. Since they are needed for energies higher than the ones of the TRD prototype beamtests a further description shall be omitted. For future cosmic ray measurements pomeron exchange might play a role for protons above 250 GeV. Then the decrease of the TRD performance due to proton TR contributions may be reinforced by diffractive backgrounds with slowly rising cross section, but increasing forward momenta of generated pion pairs.

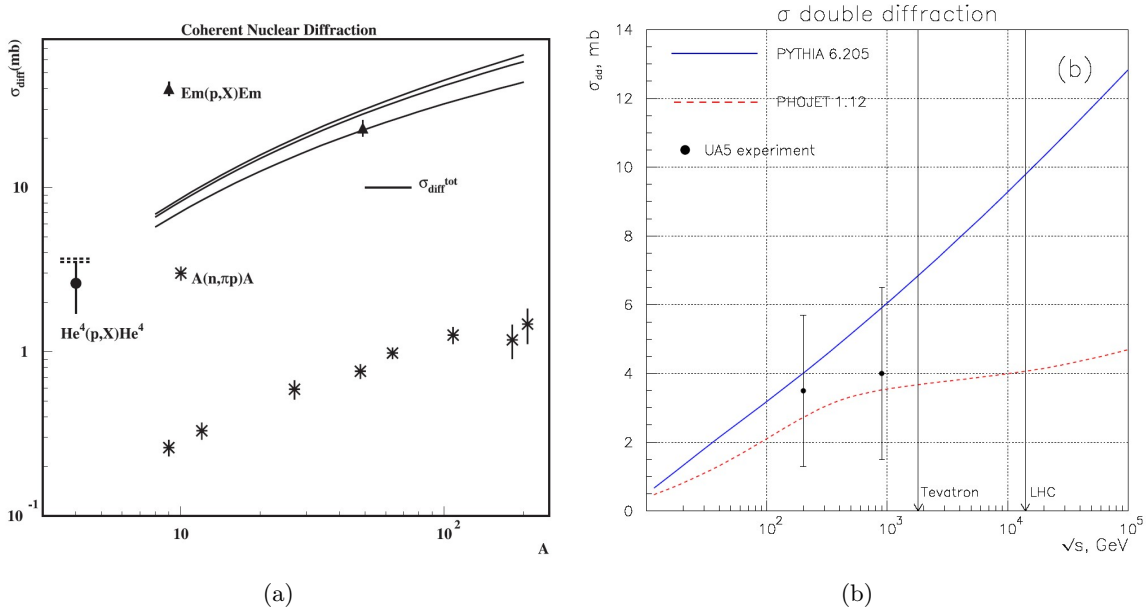


Figure 5.12: (a) Coherent diffraction cross section of protons and neutrons on nuclei versus the atomic number A . Data points: $n + A \rightarrow p + \pi^- + A$ (stars), emulsion targets (triangles), $A = 4$ (${}^4\text{He}$) (circle), theoretical prediction for ${}^4\text{He}$ (broken line). [FGS00] (b) Double diffraction cross section measured by UA5 compared to the cross section used by the MC particle event generators PYTHIA and PHOJET. [FS04]

Table A.1 included in Appendix A lists measured invariant cross sections for 100 GeV/c protons scattering elastically and diffractively on protons and nuclei for small transversal momentum of the secondary proton. The cross sections of different nuclei with atomic number A scale for large momentum transfers as about $\sim A^{0.8}$. Due to stronger contribution from elastic scattering, which scales with the atomic charge number Z as Z^2 , the factor drops with shrinking momentum transfers. For the discussed fix target energies up to 250 GeV the proton nuclei interactions hardly resolve nucleon constituents and therefore a diffraction is mainly coherent. A theoretical formulation of the cross section A -dependency for coherent diffraction is given by Frankfurt, Guzey and Strikman in reference [FGS00]. Fig 5.12 (a) shows the resulting dependencies for exclusive processes together with different measurements. For light nuclei ($A < 16$) this theory also predicts a scaling of the diffractive cross section as $A^{0.8}$. This seems to be reasonable, because the predicted dependency is only slightly larger than the simple disc approximation $A^{2/3}$ of a nucleus. Thus the lack of available cross sections data can be bypassed by scaling the

amount of data available for the $p + p$ case to the $p + C$ one.

The TRD prototype beamtest covered an energy range between 20 GeV and 250 GeV, which corresponds to total $p+p$ single diffraction cross sections of 1.9 mb – 6.1 mb (projectile+target) derived from the interpolated data, as depicted in Fig 5.11), and a small double diffraction contribution of about 0.4 mb – 1.8 mb from the PYTHIA 6.234 parametrization shown in Fig 5.12(b). With a scaling factor of $12^{0.8} \approx 7.3$ the inclusive diffractive cross section (single+double) for carbon nuclei then ranges from ~ 17 mb for 20 GeV protons to ~ 58 mb for 250 GeV. Taking into account, that only a fraction of diffractive background events generated with this cross sections will be selected as electrons, as discussed in 5.6.2, the assumption of a background production cross sections up to 15 mb made for the parameterized GEANT3 process is quite possible.

An alternative inelastic origin of the background was excluded by an analysis of the misidentified proton single track events showing no significant high p_t -trajectories, since the expectations for such interactions are large transversal momenta as well as large multiplicities. It needs to be mentioned, that the narrow configuration of the used prototype lead to a moderate xy-resolution of transversal tracks and further the y-resolution suffered from the only two times two straw modules with a large gap (~ 45 cm).

5.4 GEANT4 simulation of the prototype beamtest

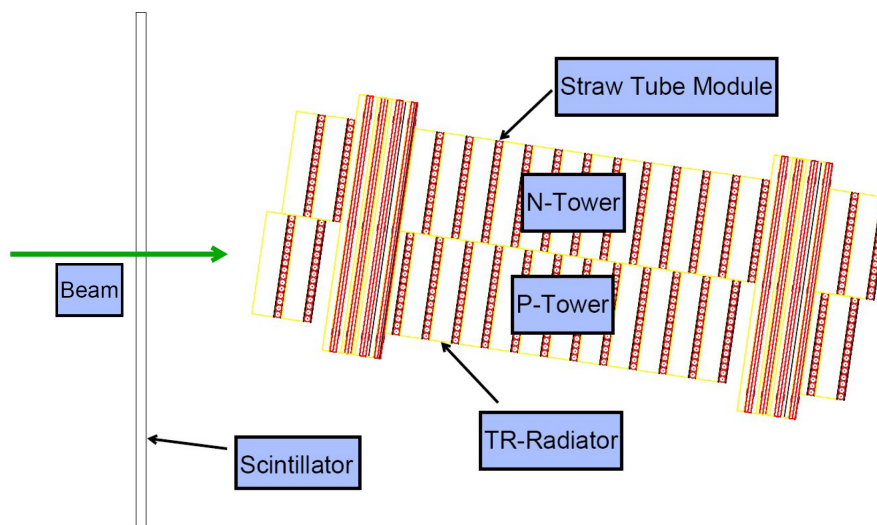


Figure 5.13: Drawing of the TRD prototype geometry and one of the front scintillators as it is used inside the GEANT4 simulation. This drawing was generated for detector to beam angle of 7.5° .

As mentioned in beginning of this chapter the observed deviation between the proton rejection powers derived from the data and the GEANT3 simulation was suggested to be a problem of the simulation. Therefore a GEANT4 simulation of TRD prototype beamtest was implemented, since the GEANT4 framework offers a description of energy loss in gases by the

Photo-Absorption-Ionization, various transition radiation processes and especially several new hadronic physics implementations including diffractive processes.

A common structure of a Geant4 simulation includes a primary particle generator (PrimaryGeneratorAction.cc/.hh), a geometry definition (DetectorConstruction.cc/.hh), a sensitive detector part readout (here named TubeSD.cc/.hh), a physics list (PhysicsList.cc/.hh) including all necessary processes and an event readout part (EventAction.cc/.hh).

All physical processes used for the GEANT4 TRD simulation are called in a modular physics-list object, that separately registers electromagnetic and hadronic physics lists. The simulation of the 20 layers TRD prototype beamtest includes TR radiator volumes and TRD modules. The straw tube walls are built of an averaged material mixture of the substructure and the same is done for the gold plated tungsten wire. Each module also includes the same number and geometry of carbon fiber stiffeners. A drawing of the TRD prototype used for the simulation is shown in Fig 5.13. The flight modules already mounted to the TRD octagon have a different geometry, which is also included in the code. All layer orientations, positions and length are read from a file, thus the flight TRD geometry can be generated by exchanging this file and the module definitions.

To allow a fast start up of the simulation a slight change of the TR process code was necessary¹. Thus the TR process code is additionally included in the files AMSGammaXTRadiator.cc/.hh and AMSVXTRenergyLoss.cc/.hh. A further change was necessary for the electromagnetic standard physics list, which is extended by the TR process and the Photo Absorption Ionization (PAI) process inside the AMSEmStandardPhysics.cc/.hh.

5.4.1 Beam profile adjustment

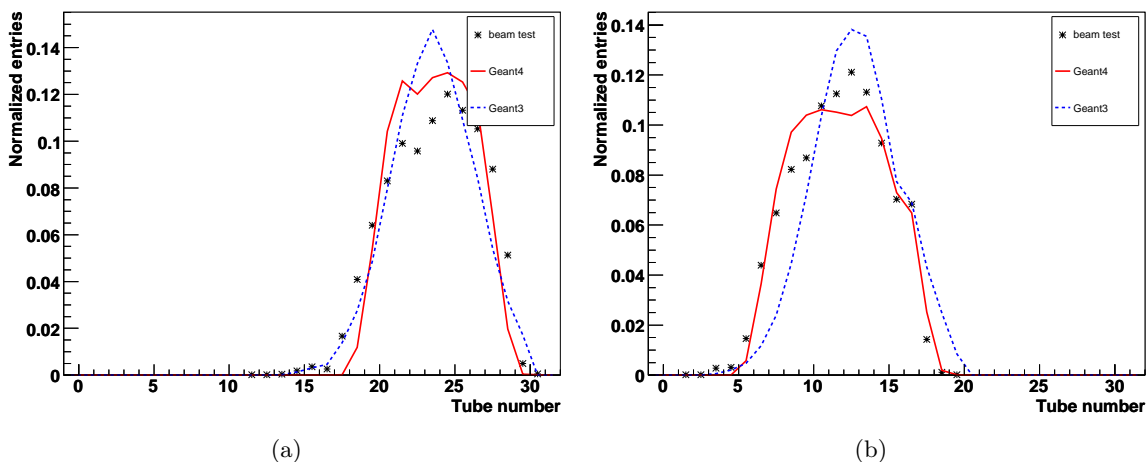


Figure 5.14: Data and simulation ($G3, G4$) beam profiles inside the first (a) and the last (b) prototype layer for proton energies of 200 GeV and a detector to beam angle of 7.5° .

Fig 5.14 shows a data to simulation comparison of the first and last layer beam profiles for 200 GeV protons. The good alignment and moderate shape agreement to the data was achieved

¹The modification was confirmed by the developer Vladimir Grichine, GEANT4, CERN

by a Geant4 general particle source with a diameter of 2 cm at a distance of 2.5 m similar to the geometry of a beam pipe. This agreement was necessary to achieve the same tail shape of the energy deposition distribution as for the data. Due to different pedestals and intercalibration factors, the dynamic ranges of each electronic readout channel varied significantly for the beamtest. Thus each energy deposition distribution of a channel has a different electronic cutoff showing up in the tails. These cutoffs were calculated from each pedestal and intercalibration factor and applied to the simulation during analysis. But the use of wrong channel cutoffs needed to be avoided by achieving similar beam profiles.

An agreement of the tails is especially important for the likelihood rejection analysis presented in this chapter. For this analysis energy distributions accumulated for the whole detector were used to profit from higher statistics. Inside the distributions the electronic cutoffs show up as a tail region of about 10 keV and accumulated significant more energy depositions than the expected Landau tail in this region. Thus the likelihood probability of a proton energy deposition in this range is exaggerated and a proton may be identified as electron. Unfortunately the effect was intensified by an electronics readout system with half of the dynamic range of the final TRD leading to cutoffs ranges at already 30 keV. But luckily showed a likelihood analysis with a fixed cut below all cutoff regions no significant difference for the absolute rejection power. Even worse it led to stronger fluctuations of the rejection factor due to changed distributions and therefore the electronic cutoffs were kept.

Slight deviations between the data and simulation cutoffs were already found by the previous analysis, but rather result from the beam profiles than from the errors on the pedestals and the intercalibration factors. Especially for the intercalibration the errors of the Landau fit for channels at the beam profile edges were affected by the intrinsically low statistics.

5.4.2 Simulation of gas-ionization

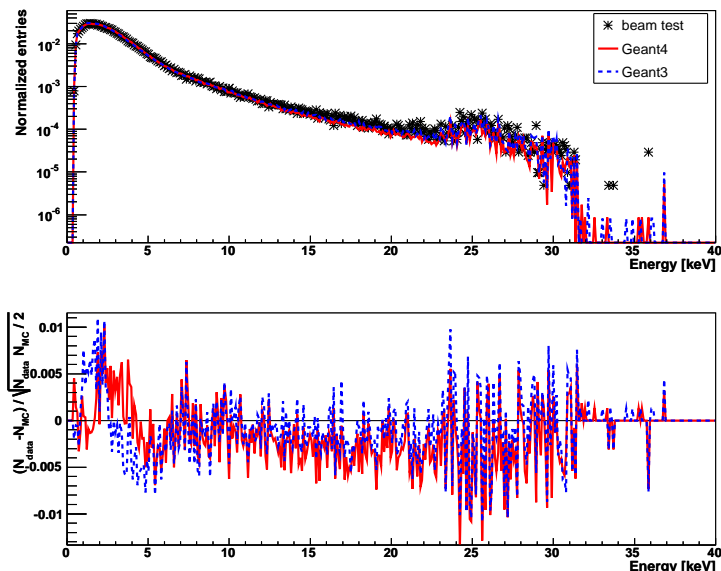


Figure 5.15: (top) Data and simulation energy depositions of 160 GeV protons accumulated for the whole prototype. (bottom) Differences between the simulations and the data.

As mentioned in chapter 2 the gas ionization cannot be simulated by using the Bethe-Bloch formular as done inside the GEANT4 standard ionization process. Instead the fluctuations of energy depositions in thin media need to be simulated as photon exchange by the GEANT4 PAI process (G4PAIModel).

Histogramming energy depositions of ionizing protons with energies in the beamtest range results in Landau distributions. By accumulating the energy depositions to 20 histograms for each related prototype layer and to a single histogram for the completed detector, one retrieves layer and detector distributions with much higher statistics. In case of the TRD prototype beamtest these statistics are necessary to tune the Landau tails of the simulated spectra to the data, since the data files include $2 \cdot 10^4 - 4 \cdot 10^4$ events with typically 19 on track hits spread over about 300 channels. Fig 5.15 depicts a data to MC comparison of the energy depositions accumulated for the whole detector and a proton energy of 160 GeV. The lower panel show shows the difference between data and MC simulations.

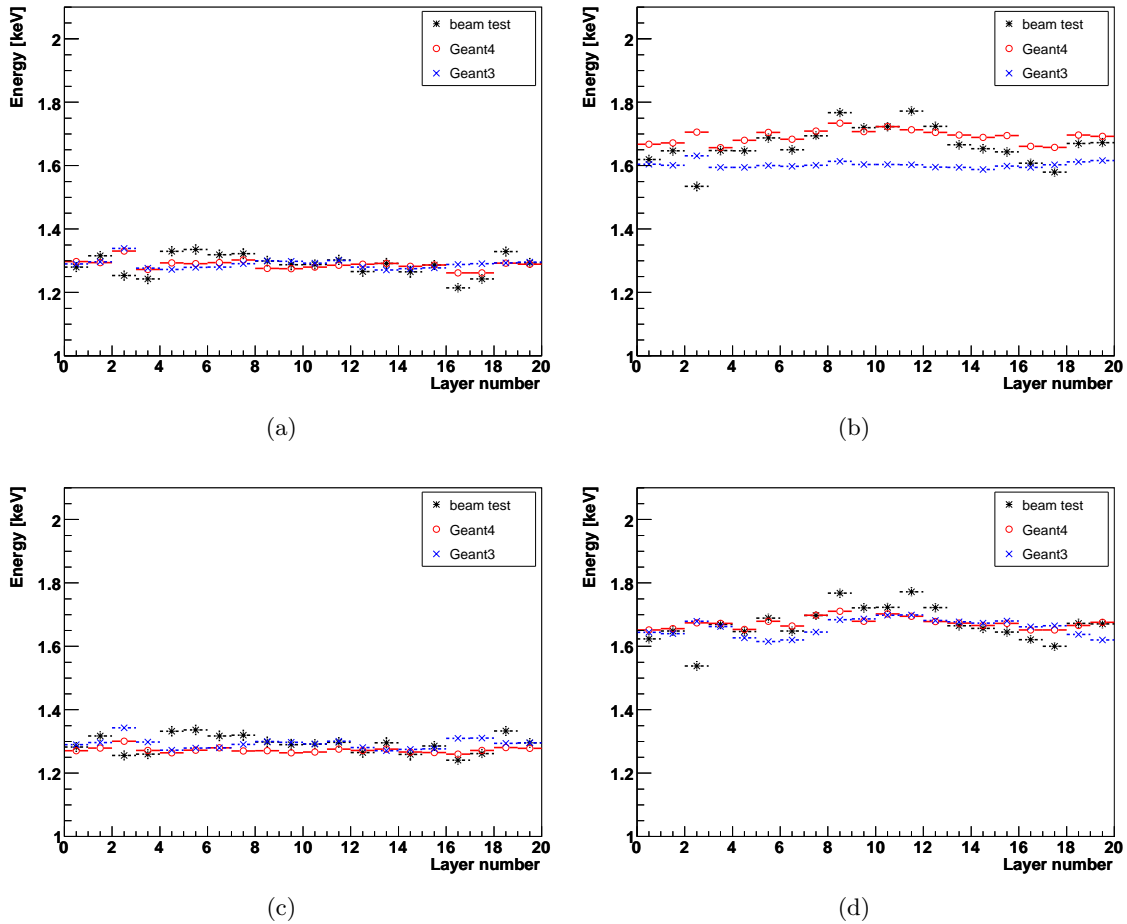


Figure 5.16: Data and simulation MOP values of a Landau fit to the accumulated layer energy depositions of protons. They are plotted for a GEANT4 Xe/CO₂ density of 4.78 mg/cm³ and 20 GeV (a) as well as 250 GeV (b) (slightly overestimated) protons, and for a density of 4.72 mg/cm³ and 20 GeV (c) (slightly underestimated) as well as 250 GeV (d).

The visible agreement between the data and the GEANT4 simulation was reached by tuning the gas density as a free parameter of the ionization process. Therefore different simulation outputs were generated with a density ranging from 4.2 mg/cm^3 – 5.0 mg/cm^3 in steps of 0.1 mg/cm^3 . First the gas density for all channels was adjusted to the low energy data range from 20 to 80 GeV to avoid any spectral changes from starting proton TR contributions. But slight disagreements with the high energy range required a retuning for an intermediate energy range between 100 and 160 GeV, which then was taken for the further analysis and comparison. Since the GEANT3 simulation was adjusted to 160 GeV protons [Orb03], this choice seems to be reliable. As estimators were used the MOP values of the Landau fits (0.6 keV-10 keV) to all detector and layer spectra. Examples of the resulting MOP values for the data and simulations tuned to the low energy range and the intermediate range are plotted in Fig 5.16. For the low energy range the best fit was achieved for a Xe/CO₂ density of 4.78 mg/cm^3 , which makes a difference of 7.2% with respect to the density of 4.46 mg/cm^3 used for the beam test and of 4.4% in respect to 4.58 mg/cm^3 used for the GEANT3 simulation. For the intermediate energy range the density resulted in 4.72 mg/cm^3 and a difference of 5.8% to the data. The origin of

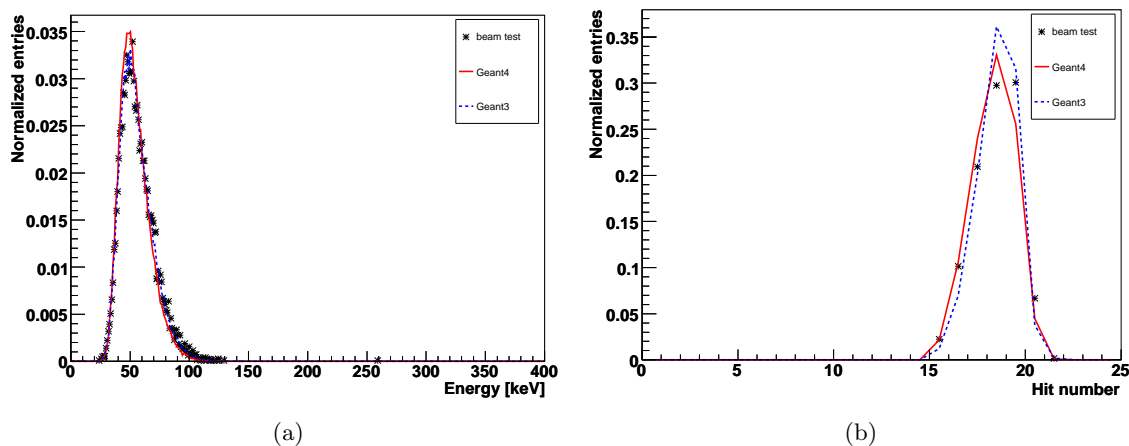


Figure 5.17: Data and simulation ($G3, G4$) total event energy depositions on track (a) and hit number on track per event (b) for 80 GeV protons.

the density difference to the data could not be solved. But the adjusted GEANT4 simulation agrees well with all data energy depositions as well as the total event energy depositions and the hit numbers found on track, visible in Fig 5.17. Even the deviation between the different energy ranges turned out to be negligible, because the followed rejection power analysis showed no significant differences for a densities of 4.78 mg/cm^3 or 4.72 mg/cm^3 . Further comparison plots for the tuned densities and all energies can be found in appendix C.

5.4.3 Simulation of transition radiation (TR)

The GEANT4 simulation Framework includes several TR processes, while for GEANT3 a FORTRAN code written by members of the HERA-B was used [Orb03]. The available GEANT4 TR processes are suitable for regular radiators, like foils stacks, and irregular ones, like foams or fiber fleeces. Since the AMS-02 TRD uses fleece radiators, the irregular process class called

”G4GammaXTRadiator.hh” was chosen. Unfortunately this class needed a slight modification to the ”AMSGammaXTRadiator”, because the standard code generates TR photon number and energy tables by referring to a pointer of each radiator object. Since most AMS-02 TRD radiators have different length they are different objects and get a table built for each particle. This leads to unacceptable startup times of about one hour, although these tables are independent of the radiator length. Therefore the TR process was modified to build tables for each particle once and to call the tables on the object name.

In general the processes simulate an irregular radiator as a kind of foil stack with foil-thicknesses varied by the gamma-distribution. A description of the underlying formalism is given in 2.1.7. Input parameters for this process are properties like the material, a foil- and a gap-thickness as well as a total number of foils, which altogether represent the fiber fleece. Since the density and size of the TRD radiators is known, the gap thickness and the number of foils result from a given foil thickness. Thus just the foil-thickness and the two further parameters ”GammaGas” and ”GammaGap” describing the foil and gap fluctuations for a fleece like radiator need to be adjusted.

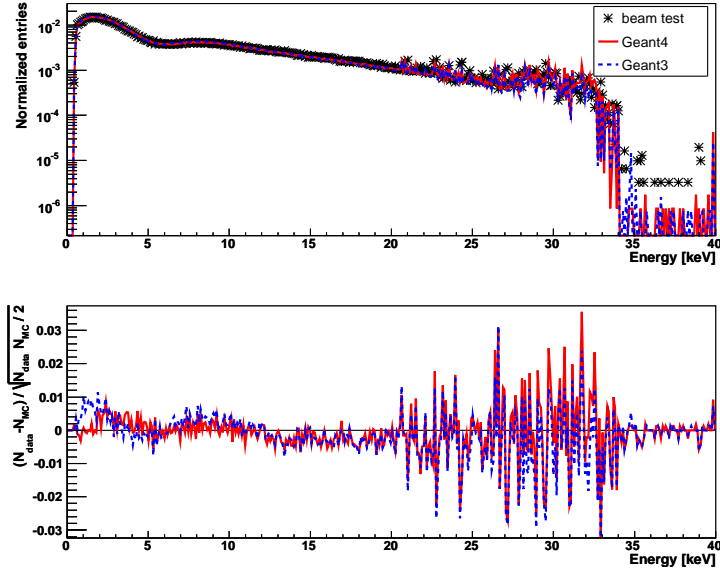


Figure 5.18: (top) Data and simulation energy deposition of 20 GeV electrons accumulated for the whole prototype. (bottom) Differences between the simulations and the data.

Fortunately the foil-thickness can be estimated by taking into account that the radiators are a stack of thinner fleeces with fibers mostly oriented along the radiator (by combing). Therefore the fibers are close to parallel and perpendicular to the traversing particles and the effective distance between the radiating surfaces (corresponding to the foil-thickness) is close to the mean penetration length $d = \pi r_{\text{fiber}}^2 / 2r_{\text{fiber}} = 7.8 \mu\text{m}$ through a single fiber. With this estimate, the TR process was tuned by producing several outputs for electrons of 20 GeV and foil thicknesses in range of $7.4 \mu\text{m}$ to $8.6 \mu\text{m}$ ($0.2 \mu\text{m}$ steps). As fluctuation parameters various combinations were proven in two steps. In the first step the parameters were varied on an exponential scale between 1 and 1000, to derive a region of rough agreement, and for the second precise iteration a linear range between 1 and 20 was chosen. With a χ^2 -test between all detector and layer distributions of the data and the simulation, a best fit was found for a foil-thickness of $7.8 \mu\text{m}$

and fluctuation parameters of $\text{GammaGas}=2$ and $\text{GammaGap}=2$.

The data and simulation in Fig 5.18 include all detector hits accumulated in a single histogram. Since all of them are later used as likelihood distributions, the simulated distributions need a good overall agreement to the data to obtain the same rejection power. Important deviations between data and simulation are visualized by plotting the distributions on logarithmic scale and by plotting the relative differences. Fig 5.19 depicts the same for the accumulated de-

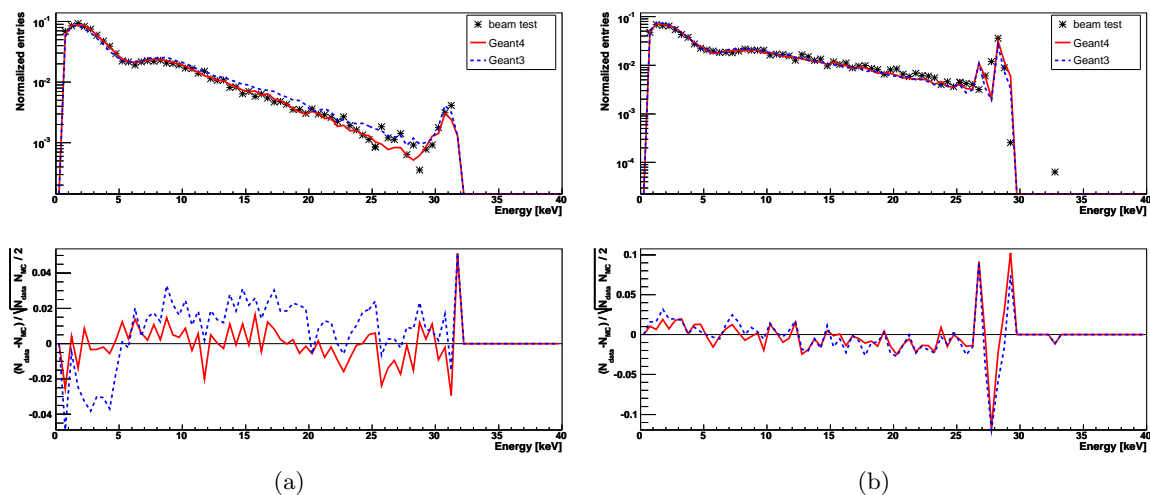


Figure 5.19: (top) Data and simulation ($G3, G4$) energy depositions of 20 GeV electrons accumulated for the first (a) and the last layer (b). (bottom) Differences between the simulation and the data.

positions of the first and the last detector layer. In this case an agreement indicates a good description of the non-absorbed TR contribution, which rises with each past layer and thus also the distribution tails.

5.4.4 Hadronic physics approaches in GEANT4

For hadronic interactions GEANT4 provides a complete physics list including suitable processes for specific needs. In this list all thresholds and overlaps for the processes are set by the developers and thus multiple counting of any contribution or any kinds of interferences can be avoided. Chooseable are the LHEP physics lists, based on a parameterized modeling of hadronic interactions for low and high energies, the string model based lists (QGS) using a quark gluon string model for interactions and the FRITIOF model (FTF) based lists applying the Lund string model above energies of 5 GeV. The ones extensively tested for a GEANT4 simulation of the TRD prototype are listed in table 5.2.

The parameterized models are improved versions of the GHEISHA model (GEANT3). In the LHEP list are combined the high and the low energy parameterized models (HEP/LEP) describing inelastic interactions for all hadrons as well as elastic scattering off a nucleus and the capture of negative stopped particles and neutrons with cross sections based on the GHEISHA

Table 5.2: List of tested GEANT4 hadronic physics models suitable for an energy range of 20 GeV – 250 GeV including their features and the GEANT3 GHEISHA model.

hadron physics	interaction model	de-excitation model	diffraction
GHEISHA	parametrization	-	no
LHEP	parametrization	-	no
FTFP	FRITIOF (Lund) >5 GeV	precompound	projectile+target
FTFC	FRITIOF (Lund) >5 GeV	CHIPS	projectile+target
QGSP	Quark Gluon String >25 GeV	precompound	target
QGSC	Quark Gluon String >25 GeV	CHIPS	target

parameterizations. Inside the parameterized hadron physics model of the LHEP list as well as for the GHEISHA model diffractive scattering is neglected.

The string model lists use the parameterized model (LEP) for interactions of projectile particles with energies below 25 GeV. Nuclear capture of negative particles and neutrons is simulated by using the Chiral Invariant Phase Space (CHIPS) model. Proton and neutron coherent elastic scattering uses the CHIPS parameterization. Compared to LHEP physics lists, they use improved cross sections for hadronic inelastic interactions of pions based on a tabulation by Barachenko and of protons and neutrons based on parameterizations by the Axen and Wellisch. Selectable physics lists are QGSP, QGSC with possible further name extensions, which apply the quark gluon string model for protons, neutrons, pions, Kaons and nuclei. The QGS model includes only target diffraction. In GEANT4 9.1 an experimental stage QGSP_DIF physics list is available offering a single projectile diffraction flag. But a short try of this flag within the TRD physics list lead to an immediate crash of the simulation and the problem has been unsolved.

In contrast the FTF lists use a description based on the FRITIOF string excitation and fragmentation (LUND model). They also use the parameterized model (LEP) for low energy interactions, but only for projectile particles with energies below 5 GeV. The selectable physics lists are FTFP and FTFC with possible further name extensions. All FTF based lists include diffractive scattering for single target, single projectile and double diffraction.

The "P" inside all lists names announces, that the nuclear de-excitation is modeled by the precompound model, while for the ones including a "C" the CHIPS model is used. There exist additional lists using some parametrization to gain cpu performance or cascade models serving a better description of hadronic interactions for primary energies below 10 GeV. Since they were not suitable for the prototype simulation details about them will be omitted.

For the AMS-02 TRD simulation the interest lies in a reasonable good description of elastic and inelastic scattering to generate backgrounds shrinking the detector performance and to reach an agreement in the event selection efficiencies between the data and the simulation MC. Of special interest is the simulation of single target and projectile and of double diffractive scattering to achieve a background reducing the TRD rejection power to the measured one for higher energies. At the moment only the FTF physics includes all this diffraction processes, though the result doesn't differ for the TRD prototype simulation compared to the other solutions.

A more detailed description and tests of the GEANT4 hadron physics processes can be found in the references [Fol07] and [AFG⁺07].

5.5 Analysis of data and simulations

The beamtest data files include two flags from the former analysis storing information about events found to have a single track and about the hits on track. Since this is not true for the simulations, a track reconstruction needed to be implemented. Unfortunately the data includes a cross talk to neighbor tubes, which was not fully suppress by using the flags. Therefore the whole reconstruction was repeated with a new C⁺⁺ based code using the ROOT classes. All shown GEANT3 distributions and plots are analyzed from existing simulation output files for the different particles and energies¹. To avoid deviations between the beamtest data and the simulation originating from different algorithms or numerics, the complete analysis was done with the same code and methods and only the data files were exchanged. If not stated differently, the shown plots only include hits on single tracks.

5.5.1 Readout system parametrization for the simulations

As only difference between treatment of data and simulations a simple parametrization of the electronics readout system was added during the read-in of the simulation outputs. The distributions shown in Fig 5.15 and 5.18 have cut-off regions in their high energy tails, originating from different dynamic ranges of each readout channel. This reduced dynamic ranges can be calculated as the difference between the maximum dynamic range of 4096 ADC counts and the channel pedestals. To generate the same cutoffs for the simulation, the beamtest pedestals are read as ADC values from a given file. Than they are converted to an energy deposition equivalent by scaling with the energy calibration factor and are further multiplied with the intercalibration factors read from a file, to include the different VA-gains of the readout front ends and their bad channels. At the end they are multiplied with the gas gain correction factor to account for the correct gas density during data taking. Thus the resulting cutoffs vary for each proton data files due to the gas gains and the different beam angles.

5.5.2 Track-reconstruction and event selection cuts

All performed analysis used hits above a cut of 50 ADC counts plus 3 times the noise of the appropriate channel. Further only hits with distances closer than $d = 3.1 \cdot (1 + 2 \tan \alpha_B)$ to the track were defined as on track, where α_B is the angle to the beam. The analyzed beamtest data include a cross talk of about 10%-15% to direct neighbor tubes with a lower numbering, which was suppressed by skipping hits with an energy deposition less than 15% compared to the related neighbor tube.

To retrieve background free beam particles the implemented track reconstruction combined with the event selection selected single track events, which was easily achieved by weighted linear regressions in x and y direction in two iterations. The first iteration suppressed all multiple hits in a prototype layer by weighting them with the maximum distance d_{max} of hits in a layer.

¹The data and GEANT3 files were provided by the the RWTH Aachen, Physics Institute Ib

The weight was set to $w = 1/d_{max}$ for $d_{max} > 0$ and to the pitch error of $w = 6.2/\sqrt{12}$ mm for $d_{max} = 0$. Thus neighbor tube hits were softly suppressed to account for single tracks that cross two tubes of a layer. In the second iteration only hits with the smallest first fit residuals were regressed, selected as 15 hits for the y direction and 6 for the x-direction. Checks with different or additional weights for the second fit showed either a stronger fluctuation of the rejection power or an overall drop of the selection efficiency ($\sim 10\%$). Therefore they were excluded, since the performance of the TRD depends on the highest achievable proton rejection power as well as on the highest electron (positron) selection efficiency.

For the event selection two approaches were tried. The first applied a global event cut on the estimator $\sigma = \sqrt{\sum residual^2/(n-2)}$ of the second fit. By just selecting clean single track events with a fit estimator smaller then the pitch (6.2 mm) the rejection power of the data rose in the whole energy range, but comparatively stronger for energies above 160 GeV. In this case the rejection power deviation between data and simulations was slightly decreased, but for a cut range between 3-1 times the pitch also the selection efficiency for all particle types was reduced by 5-15%. Thus this selection led to a similar result as a smaller electron efficiency cut in the likelihood analysis and was excluded. But the result indicates, that the problematic events for the energies above 160 GeV show a different hit pattern inside the prototype. The second selection approach applied the set of cuts listed in table 5.3. These cuts were already

Table 5.3: List of cuts applied for the event selection.

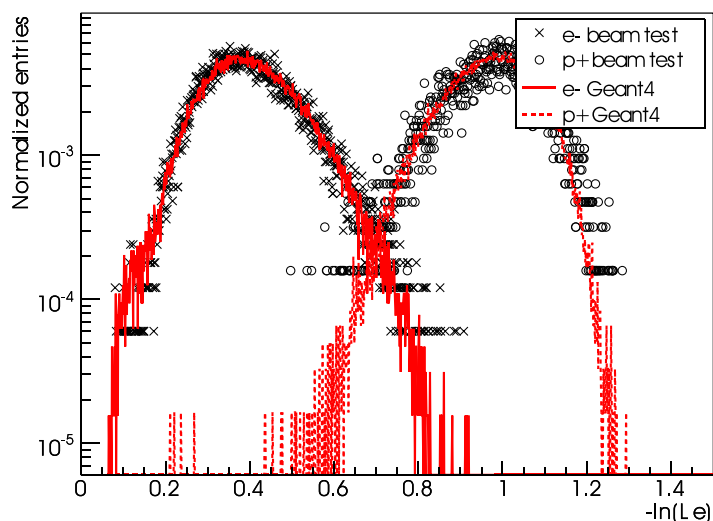
Cut Parameter	limit
# hits on XY-track	≥ 15
# hits on "road"	< 4
# hits off "road"	≤ 4
# "TR-Cluster" off track	≤ 1
# layers with more than one hit	≤ 5
$E_{onTrack}/E_{total}$ [%]	≥ 75
# Y-layers with hits on track	≥ 12
X-hit o. tr. Z-distance ("xspan")	≥ 14

used for the previous data analysis and set limits on the hit number found on track as well as in- and outside a road distance to the track chosen as 3 times the pitch. They further allowed at maximum one off track hit above 6.5 keV taken as TR cluster as well as a total on track energy deposition larger 75% and at least of one hit in the first two and the last two layers for the y-direction (Fscan). The Fscan cut assured a well reconstructed track in y-direction, which was detected by only 4 straw tube layers.

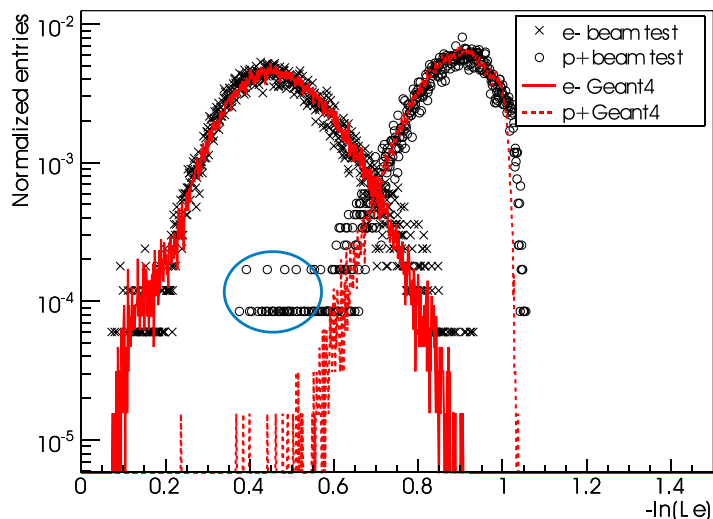
5.5.3 Rejection power comparison between data and simulations

All shown results in this section were obtained with the geometric mean likelihood method and the LH-Cut definition of the previous analysis (see section 5.2.1). As likelihood distributions were used the energy spectra accumulated for the complete prototype. The probabilities were derived by the graph evaluation function of ROOT, which interpolated between the bin values.

In addition was tested a method, that retrieved $-\ln L_e$ for each layer hit separately from the 20 layer distributions. But the resulting rejection factors showed strong fluctuations due to low statistics in the layer distributions and their different cut-off ranges. Nevertheless the analysis of future TRD data may profit from this method, because it accounts for the non-absorbed TR contribution rising with the traversed layer number and thus should be more sensitive. In this case the observed fluctuations caused by different cut-off ranges should vanish due to the larger dynamic range and the smaller pedestals shifts between different TRD modules.



(a)



(b)

Figure 5.20: Data and GEANT4 simulation likelihood distributions for 20 GeV electrons and 20 GeV protons (a) as well as 250 GeV protons (b).

Fig 5.20 shows the $-\ln L_e$ distributions for 20 GeV electrons together with the the ones of 20 GeV and 250 GeV protons. In the highlighted area (blue circle) of the data distribution for

250 GeV protons a strong left side tail reaching into the electron distribution is visible. This tail includes the problematic background events of interest in this chapter. The discrete steps in the tail show up due to the logarithmic scale of the normalized histogram with only about 20000 entries and include single or double entries in one of the 800 bins.

The comparison between the data and the GEANT4 simulation rejection factors and also the selection efficiencies were carried out for all GEANT4 LHEP, FTP and QGS physics lists suitable for the energy range of the TRD prototype beamtest. Fig 5.21 shows the rejection factors retrieved for the data, the standard (GHEISHA) and adjusted GEANT3 simulation (+ diffractive process) and the GEANT4 simulation. The rejection factor for different GEANT4

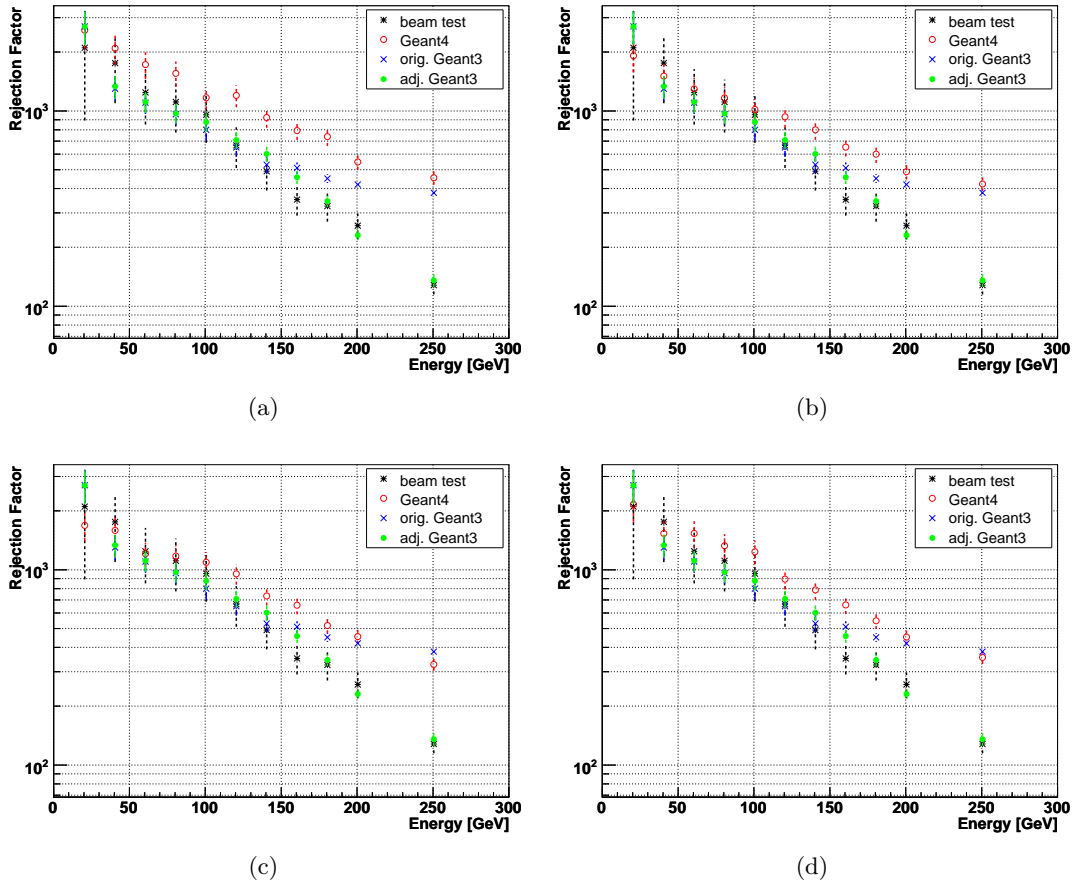


Figure 5.21: Energy dependence of the rejections factors for the data the standard and adjusted GEANT3 simulation and the GENAT4 simulation. The different plots are derived for the GEANT4 hadron physics approaches: (a) no hadron physics, (b) LHEP, (c) QGSC and (d) FTFP.

hadronic physics approaches are separately plotted for the cases: no hadronic physics (a), LHEP (b), QGSC (c) and FTFP (d). Accounting for the included errors bars just displaying the statistical error, a significant difference is only visible without hadronic physics. All hadronic physics list result in a visible rejection power deviation to the data above 160 GeV, though it is only expected for the LHEP case, since it misses diffractive interactions at all. The similarity

between the QGS and FTF physics behavior is also unexpected, since the QGS physics only includes single target diffraction.

Another deviation to the data was found for the event selection efficiency of the analyzed samples. As shown in Fig 5.22 the number of selected events is much higher without hadronic

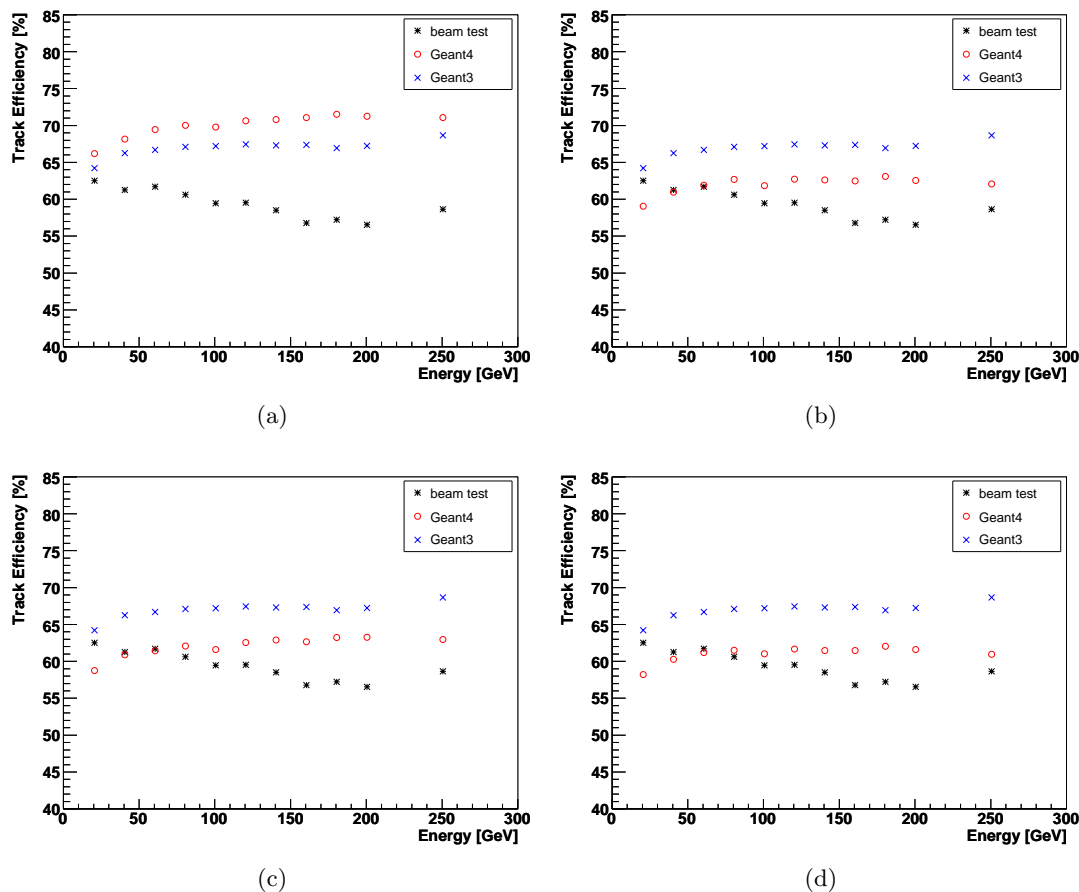


Figure 5.22: Energy dependence of the selection efficiencies for the data the standard and adjusted GEANT3 simulation and the GEANT4 simulation. The different plots are derived for the GEANT4 hadron physics approaches: (a) no hadron physics, (b) LHEP, (c) QGSC and (d) FTFP.

physics (a). This agrees with the expectations, since the detector induced background is much smaller for neglected elastic and inelastic hadronic interactions. For all physics lists approaches (b,c,d) the efficiencies are of the order of the ones for the beamtest data. But in contrast to the data efficiencies they rise instead of dropping with higher beam energies and the maximum difference of about 5% makes up a quite large event number in relation to an average data sample size of 2×10^5 events. On the other hand GEANT4 describes the detector induced background better than the GEANT3 simulation including GEISHA physics, since the derived GEANT3 selection efficiencies are well above the beamtest data.

Summarizing, the so far available physics implementation in GEANT4 is insufficient to describe thin TR detectors with a permil sensitivity between proton and positron (electron) signatures.

This conclusion is confirmed by a study of diffractive backgrounds inside the TRD prototype generated with PYTHIA and presented in the following section.

5.6 PYTHIA study of a possible TRD background

Since the GEANT4 simulation of the TRD prototype also showed deviating proton rejection powers, the possibility of an invisible diffractive TRD background was proven by a further analysis. This analysis was written in FORTRAN and includes PYTHIA 6.234 to generate the kinematics and particle multiplicities of diffractive events. Since PYTHIA simulates interaction only up to nucleons and the TRD mainly consist of carbon, the events were simulated as $p + p \rightarrow p + X$ diffraction and the result was scaled with the nucleon number dependency of coherent diffraction cross section to the $p + C \rightarrow p + X$ and $p + C \rightarrow C + X$ case. This method can serve as a good approximation, because the necessary diffractive interactions in the energy range of the prototype beamtest should be mainly coherent. The kinematic range of generated particles was set to a minimum center of mass energy of 10 MeV and a minimum stable particle range of 1 m. As diffraction process settings either the standard parameters were used or a set of parameters found to give the best agreement to available data by a MC study presented in reference [FS04]. But inside the error bars both settings lead to the same diffractive background.

After the event generation all particles were tracked to detector hits, then tracks were reconstructed from the hits and selected with the same set of cuts as for the beamtest data. All events passing the selection are then taken as a background, that is indistinguishable from single track events in the prototype and thus diminishes the rejection power. This background is extracted for the two front scintillators and the prototype itself. The procedure of tracking, reconstruction and event selection seems to be rather complicated to estimate the diffractive background, but in reality it was a simple way to get rid of uncertainties arising from the treatment of escaping trajectories to the sides of the TRD prototype. For example a simple selection of trajectories with a small angle to the beam ($\alpha = \arctan(\text{tube diameter}/\text{detector length})$) suffered from overestimated backgrounds due to neglected escaping trajectories or from underestimated backgrounds by regarding their occurrence as multiple track events.

5.6.1 Generation of a prototype hit pattern

The particle tracking inside the TRD prototype geometry is parameterized by generating 5000 pure diffractive (single+double) events for each layer, used as interactions in the center of the prototype layers. The code starts producing interactions in the center of the first layer, and after 5000 events it steps to the next one. Also the two front scintillators are included by generating 5000 events at each of their distances. All primary trajectories run orthogonal to the detector layers without any beam angle. The hit positions of charged particle trajectories are calculated by the particles momenta and the concerning layer distance to the interaction point. Instead of performing a full fast-simulation to generate energy depositions from distributions, each crossed straw tube is taken as a hit for the track reconstruction.

Many diffractive proton-proton interactions generate charged and neutral pions. The π^0 immediately decays as $\pi^0 \rightarrow \gamma\gamma$ and the decay photons are partly converted to e^+e^- -pairs in the detector material. For the background extraction this pair production is neglected and only

considered for the event selection, since the generated photons with energies greater 67 MeV in general pass the detector and just shrink the selection efficiency due to a few off-track hits of produced pairs. A prototype layer with a thickness $d = 2.9$ cm is mainly built of Carbon with an average density of $\rho = 60$ mg/cm³, while the Xenon gas of each layer can be approximated as a box with a thickness of $d = 6$ mm and a density of $\rho = 4.7$ mg/cm³. For off-track photon hits the attenuations for Carbon and Xenon can be approximated by their constant values above 1 GeV, which results for Carbon in $\sigma \sim 1.8 \cdot 10^{-2}$ cm²/g and for Xenon in $\sigma \sim 9 \cdot 10^2$ cm⁻²/g ([NIS]). With these parameters the pair production probability in a prototype layer can be estimated as $P = 1 - e^{-\rho\sigma d} = 3.12 \cdot 10^{-3}$ and in the Xenon gas of a layer as $P = 0.25 \cdot 10^{-3}$. Thus the off-track photon tracking in the TRD prototype could be simplified by adding for each photon that crosses a tube a constant pair production probability of $P = 3.12 \cdot 10^{-2}$ to the respective on-road or off-road hit count values (see section 5.5.2). The used probability was multiplied by a safety factor of 10 compared to the estimated one for a single layer. This was necessary, since the method of distributing a pair production probability along the photon trajectory does not reflect the real statistics of the pair production process. In reality off-track pairs are instantaneously produced and due to the additional tracks in the detector the event is rejected. With this factor only one π^0 decay with close to parallel photon trajectories is needed to generate one off-track TR-cluster, without at least six decays are needed. Nevertheless this factor diminishes the resulting diffractive background by less than 5%.

5.6.2 Background extraction from the prototype hit pattern

The first step of the background extraction reconstructed a track at the tube center positions of the hit pattern. In a second step only single track events related to the track were selected. For both steps the methods were identical to the ones described in 5.5.2. But instead of setting an energy deposition threshold, a TR-cluster in reality resulting from a proton and a X-ray TR hit of the same tube was defined as a multiple charge particle hit. It was taken into account the total on track energy deposition in with a median of about 60 keV and the number of hits on track with a median of about 18.5 for 80 GeV protons (see section 5.4.2). Thus a mean single hit energy deposition can be approximated as ~ 3.2 keV and the deposition of two or more charge particles is then equal or greater than a TR cluster cut of 6.5 keV. In detail multiple charge particles hits greater than 2 were approximated as 1.5 clusters to account for the higher energy deposition, since such a proton cluster is more likely identified as electron.

An analysis of misidentified proton events in the beamtest data showed considerable more events with an average of 6 TR-cluster, defined as energy deposition of ≥ 6.5 keV in the TRD prototype. This originates from an already high probability of electron events with 6 TR-clusters, as visible in the cluster count distribution in Fig 5.23. Therefore the threshold of 6 clusters could be used as a valid indicator to extract electron like events, as it was done for the cluster count analysis, mentioned in 5.2.3. Fig 5.24 shows the Poisson fit expectations of the proton cluster count distributions against all beamtest energies. This count values mainly originate from pure ionization in the detector gas (Landau tails). The proton and the electron cluster count expectations of the GEANT4 simulation are about 0.2 clusters lower then the data ones (GEANT3 as well). In the proton case it results from a slightly larger number of events without clusters. But the small difference is spread on the whole energy range and existent for electrons and protons. Therefore it hardly affects the rejection power for higher beam energy.

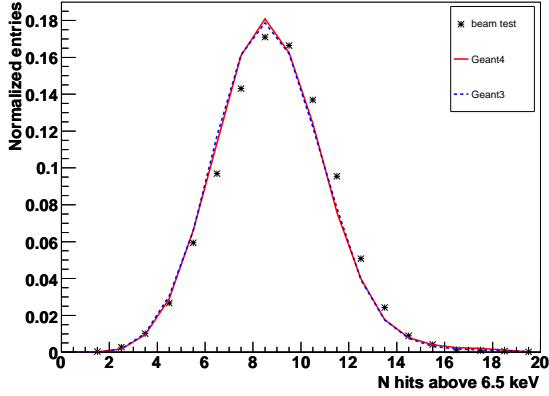


Figure 5.23: TR-cluster count distribution of 20 GeV electrons for a TR-cluster cut of 6.5 keV on the energy depositions on track.

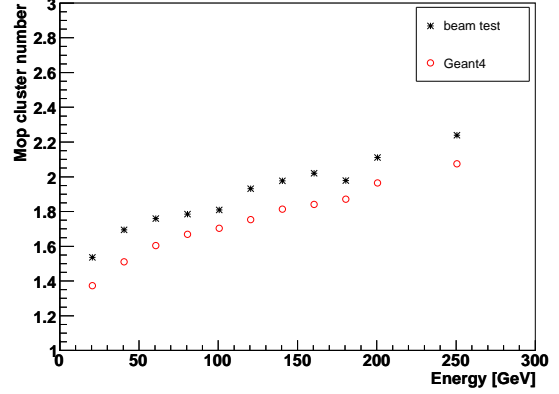


Figure 5.24: Expectations of a Poisson fit to the cluster count distribution of protons for all tested beam energies and TR-cluster cut of 6.5 keV.

For the background extraction the Poisson expectations of the proton data are taken as initial cluster counts and are added to the ones resulting from diffraction. Thus the none negligible energy dependency of the ionization contributions is included, which partly shifts the cluster count numbers for higher energies above the chosen threshold. Proton events with cluster numbers ≥ 6 (5), are counted as the number of still selected diffractive events $N_{0,back}$ inside the totally simulated pure diffractive events N_0 . The detector background N_{back} inside one event is then calculated as:

$$N_{back} = \frac{N_{0,back}}{N_0} e^{-l\rho_{target}\sigma_{pC}} \quad (5.4)$$

with the inclusive diffractive $p + C$ cross section σ_{pC} , the prototype length $l = 59$ cm and its mean nuclei density $\rho_{target} = N_A/A \cdot \rho_{det} = 3.011 \cdot 10^{21}$ 1/cm³. The nuclei density results from the mean detector density $\rho_{det} = 0.06$ g/cm³, the Avogadro number $N_A = 6.022 \cdot 10^{23}$ and the nucleon number $A = 12$. The $p + C$ cross section was derived by scaling the $p + p$ cross section with the nucleon number dependency for coherent diffraction of light nuclei ($A < 16$):

$$\sigma_{pC} = A^{0.8} \cdot \sigma_{pp} \sim 7.3 \cdot \sigma_{pp}, \quad (5.5)$$

which is in agreement with theoretical predictions and existing data in the concerning energy as mentioned in section 5.3.

The inclusive single diffraction cross sections of the PHYTIA parametrization led to overestimated backgrounds for lower energies, caused by a too flat slope of this parametrization compared to the data depicted in Fig 5.11. Therefore these cross sections were derived from a cubic fit to the available data points. But in case of the double diffraction the PHYTIA parametrization was used, since the available data has too few points and large error bars. Scaling the sum of both inclusive $p + p$ cross sections to the $p + C$ diffraction case, results in a range from 17 mb for 20 GeV to 58 mb for 250 GeV, as discussed in 5.3. By regarding that only about 30% of the generated PHYTIA events are selected, an "exclusive" background cross section range between 5 mb to 17 mb can be estimated, which is in reasonable agreement with the range used for the diffractive GEANT3 process (see section 5.2.3).

In Fig 5.25 the resulting backgrounds, including the counts for the prototype and the two scintillators, are compared to the needed ones to discard the rejection power deviation. The needed backgrounds N_{back} are calculated from the difference between the GEANT4 (R_{G4}) and the data (R_{data}) rejection factors as $N_{back} = 1/R_{data} - 1/R_{G4}$. Fig 5.25 (a) displays the

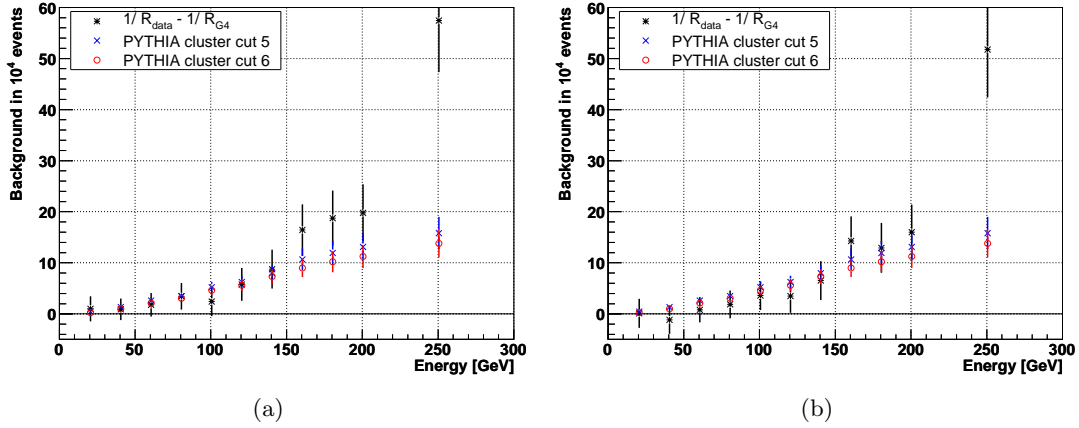


Figure 5.25: Selected TRD prototype backgrounds from a PHYTIA diffraction with a TR-cluster cut of 5 and 6. They are compared to the ones needed to describe the rejection power deviation between the data and a GEANT4 simulation without hadronic physics (a) and with FTFP physics (b).

background for R_{G4} simulated without hadronic physics, while Fig 5.25 (b) does the same for the FTFP physics included. Both show the PYTHIA result for a cluster thresholds of 5 and 6. The close scintillator contributes with 15% and the one in 2 m distance still with 10% and the ratios stay constant for all projectile energies.

The strong deviation of the 250 GeV point did not vanish with different settings and methods of the analysis. For example, one method accounted for additional TR from high energy pions, but was rejected since it adds maximum 1% to the background. Thus it may result from a less pure beam, since the 250 GeV data was taken with a secondary target. But this argument is weak, since the data point seems to fit the exponential slope of the rejection power curve. Especially the fact, that the modified GEANT3 simulation describes the background well by generating two pions along the beam direction with about the same cross sections, makes a lack of the approximated $p + C$ kinematics for higher beam energies more likely.

Fig 5.26 depicts the counted multiplicities N for the selected 250 GeV events plotted together with a chosen particle ID. It has a strong peak for charged pions (ID=2) with a multiplicity of two, and close to no contributions from electrons and positrons (ID=4) as well as muons (ID=5). Many events also include π^0 's, which immediately decay to photons (ID=3), the reason why the photons mostly have even multiplicities. After a diffractive interaction of PHYTIA about 20% of the selected events have lost their projectile proton (ID=1), because they were converted to neutrons. For the analysis these neutrons can be neglected, since all of them carry energies above 10 GeV and would not decay inside the prototype. Thus the assumption of a background dominated by two pions maybe a valid approximation, but in reality the signature of such events is more complicated as it is parameterized by the GEANT3 process. Further the pion pairs in diffractive PHYHIA events selected carry energies of tens of GeV, as visible

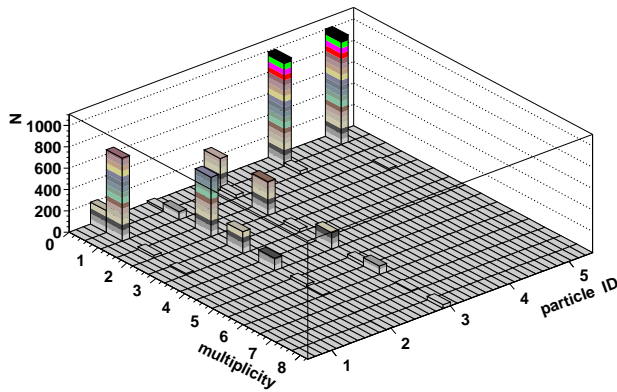


Figure 5.26: Multiplicity distribution of a certain particle inside the selected diffractive PYTHIA events. Particle ID: 1= p , 2= π^+/π^- , 3= γ , 4= e^-/e^+ , 5= μ^-/μ^+ .

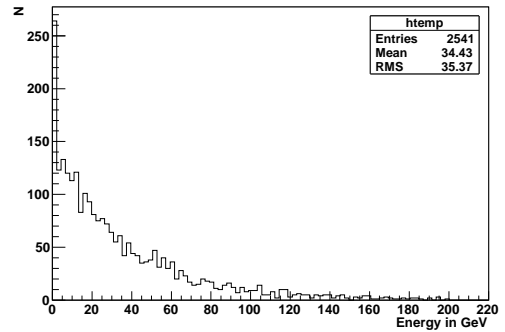


Figure 5.27: Energy distribution of all on track pions inside the selected diffractive PHYTIA events with a primary proton energy of 250 GeV.

in Fig 5.27, and not a few MeV as assumed for the GEANT3 process. About 10% of the total events lay in the peaking bin for energies below 5 GeV.

5.7 Conclusion of the GEANT4 and PYTHIA background simulation

The TRD background study with diffractive PYTHIA showed, that up to 200 GeV the picture of an additional diffractive pion background agrees with the results. However above 250 GeV beam energy the results cannot be attributed to diffractive processes.

Though GEANT4 seems to behave better as the GEISHA parametrization of GEANT3 for hadronic backgrounds, the available version still shows the observed rejection power deviation between the TRD prototype beamtest data and the simulations (see section 5.5.3). A solution similar to the one for the GEANT3 simulation, by implementing a diffractive process with parameterized kinematics and multiplicities derived from a PYTHIA simulation, was not pursued, because of missing confirmation of a diffractive origin of the deviation. Furthermore this solution would be a stand alone fix just available for AMS-02 and needed to be updated for future GEANT4 version changes. Therefore the results of the presented analysis were transmitted to the GEANT4 collaboration and a possible solution was promised. If no solution will be provided, the mentioned parametrization should be considered, since later analysis developments tuned with help of GEANT4 simulations, like the powerful likelihood methods or neural networks, would suffer from the overestimated rejection power.

Fortunately AMS-02 is a multipurpose detector, which should resolve signatures of diffractive backgrounds or other origin generated in the TRD. This can be done either with a planned testbeam of the complete AMS-02 detector or with cosmics in space, by exploiting the event identification power of the Tracker combined with the RICH and ECAL detectors.

Chapter 6

The Mimosa-V Detector for the REGINS imaging project

The REGINS project within the European Community Initiative INTERREG III C is financed under the European Regional Development Fund. Its objectives are to enhance and support inter-regional and strategic co-operation between the participating partner regions from Austria, Germany, Italy and Hungary. Sub-projects are approved with the help of three calls for a proposal. For the presented sub-project the collaborators were: the Institut für Experimentelle Kernphysik at the University of Karlsruhe (TH), the Department of Physics and Mathematics at the University Insubria in COMO, Italy and the Department of Functional and Structural Biology at the University Insubria in COMO. As research topic the development of a silicon imaging device for autoradiography of microarrays was proposed. This device was intended to replace the film and the phosphor plate imaging used up to now. Films have a poor detection efficiency, while phosphor plates in general have a low spatial resolution, and both generate extra costs.

The MIMOSA-V CMOS pixel detector was developed as an alternative to CCD detectors by the SUCIMA collaboration, pioneered by the LEPSI/IREs teams in Strasbourg. Like MIMOSA-V most CMOS detectors are Active Pixel Sensor (APS), which feature a sensitive element, either a photodiode or a photogate, a first amplification stage plus a reset transistor and a selection switch in each pixel cell. Fig 6.1 shows a schematic drawing of the pixel read out. The basic scheme was first implemented in the MIMOSA-I chip and later transferred with minor modifications to all further developed chips. Since different applications often ask for a sensitivity to very low energetic sources, a back-thinned version of the MIMOSA-V with very thin dead layer was built. In the detector design minor radiation hardness approaches are considered, which lead to a radiation hardness for ionizing particles of > 3.5 MRad. However its hardness ($< 10^{12}$ n/cm²) for nonionizing radiation cannot compete with silicon strip and hybrid pixel sensor [Jun05].

6.1 CMOS pixel sensors as particle detector

Complementary Metal Oxide Semiconductor circuits (CMOS) have logical gates built of NMOS and PMOS transistors. Due to the complementary logic the current flows only during switching and therefore the power consumption is reduced.

The concept of CMOS pixel arrays originates from the industry as detectors for visible light. They are produced in a standard process and compete with the well known CCD¹ technique. Since standard processes for commercial applications are constantly optimized, the device design need to be adapted for each new iteration. Thereby the detectors benefit from new processes parameters like smaller pitches, but is also affected by unwanted changes like thinner epitaxial layer, that reduce the signal.

In general the detection principle of solid state particle detectors is based on collecting charges from electromagnetic interactions inside the detector material, which are either generated by ionization or by photo-effect, Compton-effect, and pair production. All these processes are described in chapter 2. Inside a depleted diode the generated electrons drift to the positively biased side and the holes vice versa . A major difference of CMOS sensors compared to other solid state particle detector is shown by the schematic in Fig 6.2. Only a small part of the

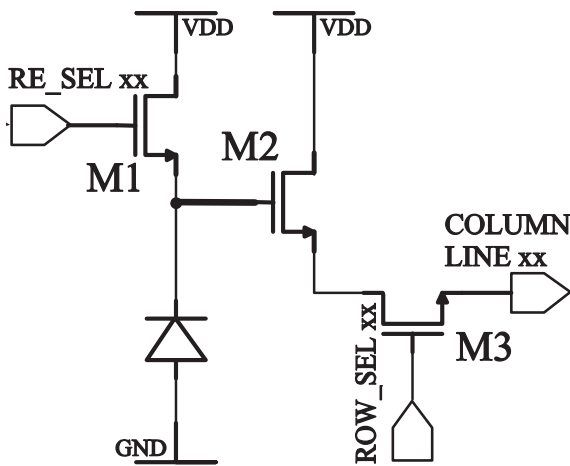


Figure 6.1: Schematic drawing of a CMOS pixel read out. M1 is the reset transistor, M2 one part of the source follower of the amplifier and M3 the select switch. [Dep04]

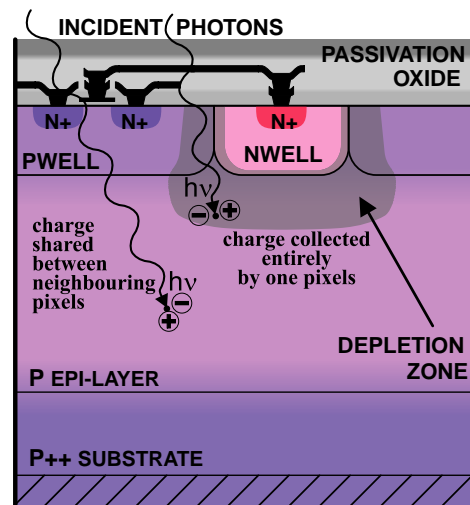


Figure 6.2: Schematic cross-section through of a CMOS pixel with the electronics (top), the collecting diode (top and middle), the epitaxial layer (middle) and the substrate (bottom). [Dul05]

low doped epitaxial layer is depleted by the low transistor source-drain voltage. But CMOS detectors still have a high detection efficiency, since the electrons generated in the epitaxial layer have a long lifetime and drift towards the signal collecting diode. Thus CMOS detectors achieve a fill factor of 100% and a tracking resolution of 1.5 μm . Although the amount of generated charges in a micrometer thick sensitive layer is very low, such a pixel reaches a signal to noise ratio of >30 due to the incorporated first amplification stage and the very small capacitance.

As an example of a CMOS pixel readout the MIMOSA design, shown in Fig 6.1, shall be taken. It consists of three transistors and therefore is called the "3T-approach". An enabled reset switch (transistor M1) connects the charge collecting diode to the reverse bias and the accumulated electrons are removed. The source follower (transistor M2) does the first stage of

¹CCD, Charge Coupled Device

signal amplification. A further enabled row select switch (transistor M3) connects the output of transistor M2 to the source follower. The column select switch and the current source of the source follower are located on the outside and are shared between many pixels. Between two reset operations the charge in a pixel is continuously integrated. Thus the frame readout can be repeated until the detector diodes reach their charge saturation point. Taking the previous frame integral as pedestal of the current, each frame can be reconstructed. The described technique is well known as "Correlated Double Sampling" (CDS) and removes the switching noise, but slightly increases the white noise. With CDS readout frequencies up to 40 MHz could be achieved for the MIMOSA-V. The increase of the noise is negligible compared to the dominating kTC noise, which originates from thermodynamic fluctuations caught by a pixel reset duration insufficient to reach the equilibrium. Fortunately the kTC noise is removed by applying CDS. Another noise, called the shot noise, is added by integrating the leakage current of the diode.

As drawback of CMOS detectors a high particle penetration depth through the electronics layer is required, which strongly increases the low energy threshold of detectable β -particles. To overcome this problem, the SUCIMA collaboration developed a back-thinned MIMOSA-V chip without substrate, which is radiated from the backside. Further information is given in 6.1.2.

All provided information given in this section can be found in the references [Dep02], [Dep04], [Dul05] and [Jun05].

6.1.1 The MIMOSA-V sensor

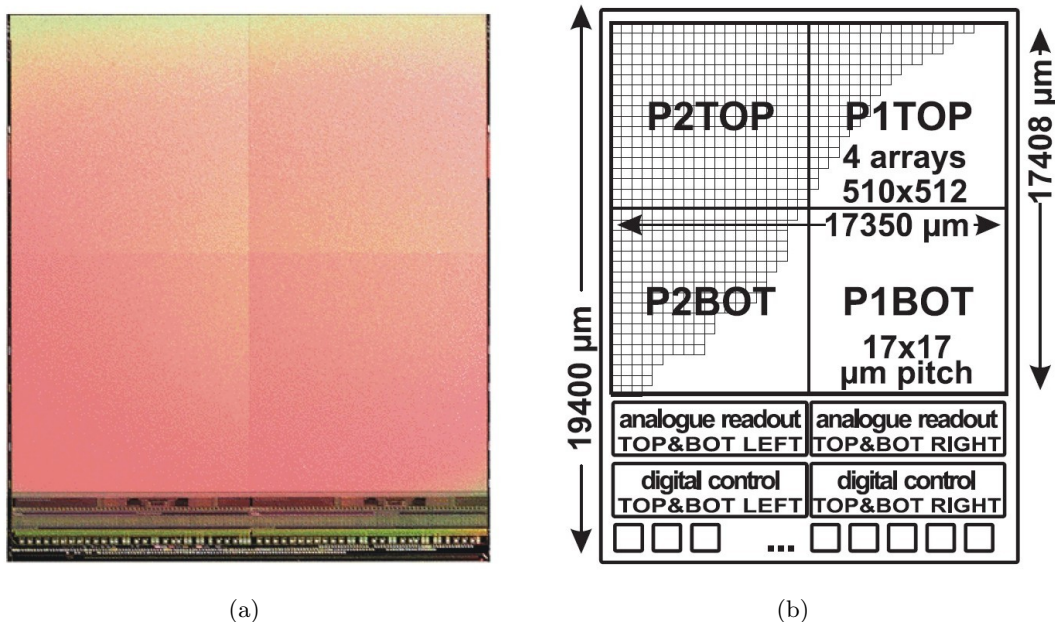


Figure 6.3: (a) Picture of a MIMOSA-V detector. [Jun05] (b) Sensor electronics schematic depicting the sub-matrices and the analog and digital read out parts. [Dep04]

The SUCIMA project developed a variety of silicon detectors for the use in different medical applications and HEP experiments. Among these detectors is the MIMOSA-V chip, which was originally designed as a detector prototype for a possible linear collider experiment.

A picture of the MIMOSA-V chip and a schematic overview is shown in Fig 6.3. The MIMOSA-V sensor was produced in a $0.6\ \mu\text{m}$ technology and has a surface of $19400 \times 17350\ \mu\text{m}^2$ segmented into 4 different sectors each with its own analog output. A sector sub-matrices consist of 510×512 pixels with a pitch of $17\ \mu\text{m}$. The digital part of the chip and the output buffers are all located on one side of the detector. Each pixel has n-well/p-epi charge collection diode with a dimension of either $3.1 \times 3.1\ \mu\text{m}^2$ or $4.9 \times 4.9\ \mu\text{m}^2$ depending on the sub-matrix. The readout electronic on top of the sensor was already mentioned as an example in 6.1 and allows a readout clock frequency up to 40MHz.

Furthermore the chip offers a set of different operation modes: the standard mode, a rolling shutter mode and a fast scan mode. The fast scan mode reads only every ninth pixel (column and row) and the signal from interleaved pixels can also be summed.

6.1.2 The back-thinned MIMOSA-V sensor

An important step made by the SUCIMA collaboration was to test the process of back-thinning a MIMOSA-V on wafer basis. This process was applied for the first time for this kind of chip and reduced the lowest energy of detectable particles significantly. In silicon sensors this threshold is defined by the thickness of the dead layer above the sensitive volume and the characteristic stopping power of the particle. The dead layer of CMOS sensors together with the top metallization has a typically thickness of a few μm corresponding to an energy threshold of tens of keV for electrons. Thus a standard CMOS detector cannot reach a sensitivity below a spectral expectation values for tritium of $\sim 5.9\ \text{keV}$ and is also just in range of the one for ^{14}C of $53.5\ \text{keV}$.

Therefore the idea was born to flip the sensor, etch away the substrate down to the sensitive volume and than to radiate the sensor from the back side. This back-thinning process was performed in several steps:

- Starting with the standard CMOS pixel sensor, Fig 6.4 (a), in a first step all inhomogeneities on the top coming from the interconnection layers and the bond pads need to be filled up.
- After this the sensor wafer is plane enough and the handle wafer can be glued on it, as depicted in Fig 6.4 (b). Then the bulk material of the sensor wafer is etched away by a process, that stops as soon as it reaches the surface of the epitaxial layer. Unfortunately this process is kept as corporate secret by Atmel and cannot be presented.
- In a next step, a passivation layer of a 100-300 nm silicon oxide is grown on the new surface. This layer, together with the depth of a very flat doping to restore the potential increase towards the edge, then defines the new dead layer, which leads to an energy threshold of a few keV.
- A serious problem occurs for the bonding of the chip, since the bond pads are still on top. To connect them, holes were drilled through the epitaxial layer up to (down to) the metal layer, as visible in Fig 6.4(c) These holes need to have steep edges to keep the distance

to the sensitive volume and therefore the bonding need to be done with very thin needles and bond wires.

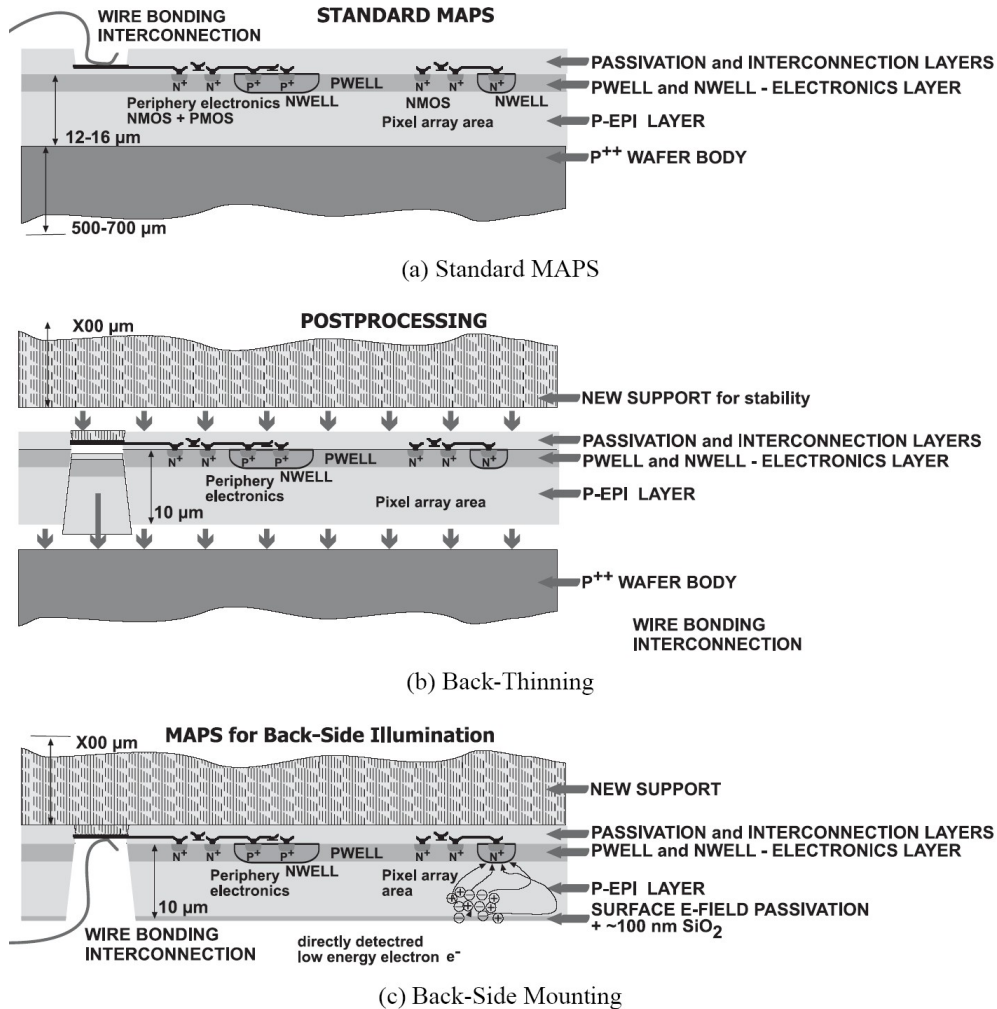


Figure 6.4: Illustrations of the back-thinning process used on the MIMOSA-V. (a) The CMOS pixel sensor in its standard configuration. (b) The process of smoothing the surface, glueing the handle wafer, removing of the bulk material and drilling access holes to the bond pads. (c) The resulting CMOS sensor with a very thin dead layer. [Jun05]

Fig 7.3 shows a back-thinned MIMOSA-V on a standard hybrid. With the resulting detector measurements in an HPD¹ [Dul05] and an autoradiography with a tritium source [Dep04] were performed, where the sensor showed the expected sensitivity.

¹HPD, Hybrid Photo Detector - a PMT like photon detection system photo cathode is replaced by a silicon detector is used for the read out instead of a standard cathode

6.2 Radiation Damage in Silicon Sensors

Semiconductor devices, that detect radiation like the one used by the REGINS project, are affected by detector performance losses due to radiation damages. In general three types of radiation damages are distinguished: displacement of atoms in the lattice, transient and long term charges from ionization in insulator layers and formation of interface defects. The displacement of atoms primarily happens in the bulk material of the detector, since it is the thickest part of the sensor, and therefore is called "bulk damage". The generation of localized charges by ionization and of interface defects are treated under the term "surface damage". Both effects shrink the signal to noise performance of a device by decreasing the signal height and increasing the noise and the leakage current. Thus trapped charge carriers and interface defects lead to an aging effect of electronic devices used in radiation environments.

The following sections summarize considerations for the design of radiation hard silicon detectors, as they are presented in reference [Jun05].

6.2.1 Bulk Damage

Silicon atoms are displaced in the lattice by a minimum recoil energy of approximate 15 eV, originating from elastic scattering of charged or neutral particles. In reality this threshold is smeared out, since the recoil energy depends on the direction to the lattice. A recoil energy up to 2 keV creates isolated point defects, while for higher energies up to 12 keV clusters of about 100 point defects with a diameter of about 5 nm are formed. Since the momentum transfer depends on the mass of the projectile particle, electrons start to generate point defects for energies of at least 260 keV and clusters for 4.6 MeV, while neutrons need only 190 eV for a point defect and 15 keV for a cluster. Most of the defects are annealed due to remigration of the atoms. The persisting $\sim 2\%$ of the defects introduce additional energy levels in the band structure of the semiconductor, which can act as acceptors, donators or charge traps. Thus changed capture, generation and recombination rates of non-equilibrium charge carriers affect the bulk electrical field as well as the capacitance and the resistivity of the material and can even lead to a type inversion of the detector. Dark currents, that originate from introduced levels close to the center of the band gap, can be significantly reduced by cooling. For traps, that decrease the Charge Collection Efficiency (CCE) by capturing charges and releasing them after the readout time, higher temperatures are preferred to reduce the trapping time.

6.2.2 Surface damage

Ionization by charged particles or photons creates e-h pairs. Due to a high number of traps ($10^9 - 10^{10} \text{ cm}^{-2}$) in the interface of two different materials (e.g. Si/SiO₂) originating from lattice mismatch and dangling bonds, this charges often concentrated around the interface. The number of interface states strongly depends on the production process parameters (e.g. oxidation temperature) and is additionally risen due to broken chemical bonds by radiation. Incoming particles also generate e-h pairs in the SiO₂ layers on top of the bulk material. Not all of these pairs recombine and the remaining electrons and holes are separated by the electric field across the oxide. Thereby the recombination strongly depends on the quality of the oxide and ranges from a total recombination for radiation hard oxide to a few percent for standard oxide.

As the electron mobility in the oxide is several orders of magnitude higher than that of holes and due to a much smaller trapping cross-section in n-MOS transistors, most of the electrons are collected by the positively biased gate contact. The holes drift via a hopping transport towards the Si–SiO₂ interface, stuck in the existing traps and change the electrical properties of the interface, which affects the functionality of the device. A cross-section through a n-MOS transistor and an illustration of the charge trapping in the gate oxide - silicon interface for a positive gate voltage is shown in 6.5. The resulting effect is measured as an increase of the

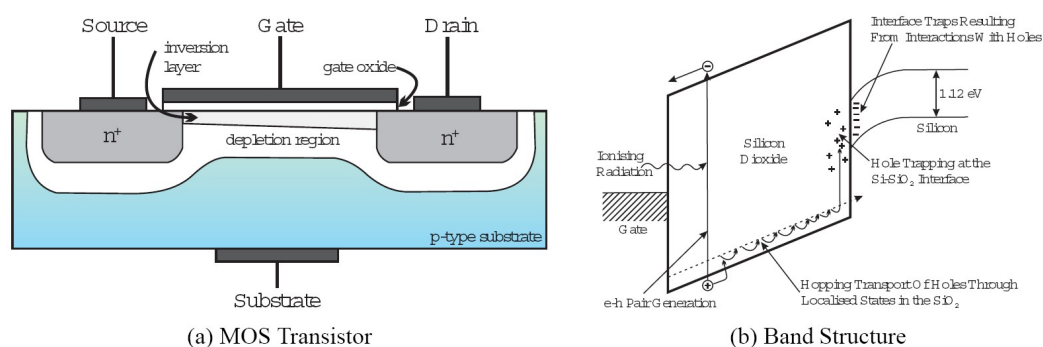


Figure 6.5: (a) A cross-section of a n-MOS transistor, with a positive gate voltage applied. (b) The band structure in the MOS contact for a positive gate voltage. It illustrates the hole capturing in the Si-SiO₂ interface. Taken from *reflevin*

leakage current and limits the radiation hardness of most of the common read out electronics. For n-MOS transistors the oxide charge-up can reach a concentration, that inhibits a complete switch off of the transistor. Primarily, the charge up leads to a shift of the threshold voltage V_{th} for n-MOS and p-MOS transistors. This threshold is related as $V_{th} \propto t_{ox}^n$ to the oxide thickness t_{ox} and the production process factor n and results from a rising tunneling probability of recombination electrons with thinner oxides. Thus production processes using thinner oxides, like the deep sub-micron technologies, are more radiation hard.

Another effect of accumulated positive charges in the oxide is the formation of parasitic charge transfer paths by creating inversion layers between n-wells in the p-type substrate, which lead to a decreasing signal to noise ratio or even to short circuits. An approach to overcome this issue is the "enclosed transistor" design. In this layout a circular gate contact encloses either the source or the drain of a transistor and prevents the formation of parasitic charge transfer paths to neighboring transistors. Devices built with the enclosed transistor design and the deep sub-micron process are the APV25 and the Beetle front-end chips used for the LHC experiments.

Chapter 7

The Mimosa-V longterm Data Acquisition

The milestone of having developed a detector like the back-thinned MIMOSA-V sensitive enough for tritium autoradiography was only one step to the imaging of protein localizations on microarrays. Due to the extremely low activities of the ^3H standard probes (8 nCi/mg – 489.1 nCi/mg, later used 0.1 nCi/mg – 109 nCi/mg), the number of expected decays inside a single frame ($4 \times 510 \times 512$ pixel) readout time of 25 ms (software triggered) is quite low and an information contained in typically 10^5 to 10^6 frames is required for a significant images. Thus the second step in success was a sparsification at the earliest possible point in the data acquisition chain to optimize the mass data storage and the frame rate. For an unaffected efficiency, a weak real time selection was applied on the cluster seed candidates, tagged and saved together with the nearest 24 neighbors.

The frames were grabbed from the sensor by the SUCIMA DAQ System connected via USB2 to a PC, which allowed a maximum transmission of about 20 MB/s or roughly 10 frames/s after a slight modification of the PC driver. A MIMOSA-V DAQ software specially written for this readout task acquired the data by exploiting the maximum USB transmission rate and simultaneously reduce it. After a one day run the DAQ software already displayed sharp images of the measured standards, as discussed in 8.3.

7.1 SUCIMA Data Acquisition System

The SUCIMA DAQ system was designed and built by the collaborating Krakow group. Its modular design allows to read all detector types used in SUCIMA: CMOS, SOI and silicon micro-strip detectors and it consists of a data acquisition board called "SUCIMA Imager", a special repeater board for the CMOS sensors and a hybrid.

7.1.1 The Data Acquisition Board "SUCIMA Imager"

The SUCIMA Imager digitizes the incoming signals, stores them in a memory, does some data processing like an on board CDS (6.1) and then shifts the result to the IO FIFO for the USB2 transmission. Therefore the board hosts a Field Programmable Gate Array (FPGA, Xilinx Virtex II), four 12 bit ADCs (Analog Devices, AD9226), four SRAM chips (ISSI, IS61LV25616) and a Cypress USB2 interface chip (CY7C68013 EZ-USB FX2) for the IO. A picture of the PCB is shown in Fig 7.1.

The FPGA provides the digital control and clock signals for the ADCs, controls the memory and handles the communication with the computer. It has 1 million system gates running at

an internal clock rate of 420 MHz and its IO pins are grouped in 8 banks. Bank 0 and 1 communicate with the ADCs, bank 2, 3, 6 and 7 are the interfaces to the 4 SRAM chips storing the data for processing and transfer and bank 4 and 5 communicate with the FIFO and the IO chip. For each of the 4 input channels one ADC converts the analog data from the sensors with a maximum rate of 65 MHz in parallel and the output is stored in the appropriate SRAM chip serving a capacity of 256 k 32 bit words. The USB transmission is established in synchronous mode allowing transfer rate up to 480 Mbit/s. In reality it is reduced by the transmission overhead, which leads to a maximum achieved data rate of 240 Mbit/s.

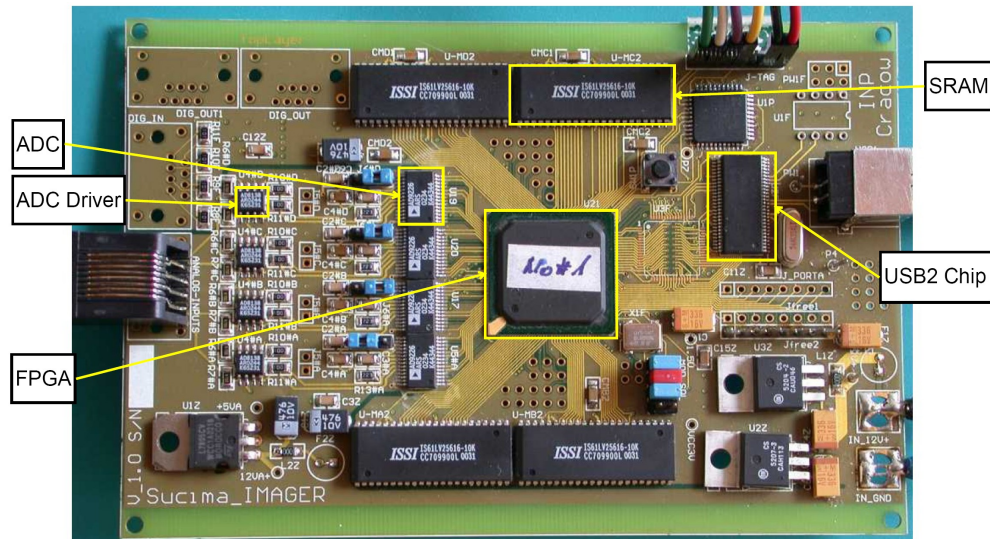


Figure 7.1: The SUCIMA Imager card houses a FPGA that reads analog data via 4 ADCs, generates the digital signals for the sensor and has a USB interface chip for data transmission to and communication with a PC.

The FPGA firmware is stored in an EEPROM and loaded to the FPGA during power-up. To adapt the firmware for each detector type, it can be reprogrammed via a JTAG¹ interface. In principle this offers the opportunity to implement a sparsification for the large amount of data from the MIMOSA-V. Such a code needs a lot of gates for the noise, pedestal, bad pixel calculation and especially the cluster search and therefore would not fit into the FPGA. Even if it fits, the DAQ board would not provide enough memory to store all necessary matrixes. But at the moment there is a work ongoing to implement the sparsification on the next iteration of readout board, that hosts an Altera FPGA with minor mathematical processing features and much more memory. Though up to now the sparsification need to be done with a realtime LabView Software, which also serves as the source of algorithms implemented in the next step FPGA firmware.

The interested reader can find more details about the DAQ system in reference [Cze01].

¹JTAG: Joint Test Action Group of the IEEE

7.1.2 The repeater and the hybrid

The repeater, visible in Fig 7.2, works as an interface between the SUCIMA Imager and the hybrid. It is mounted onto the DAQ board and supplies the hybrid and the DAQ with power, generates the reference voltages for the amplifiers on the sensor and amplifies the analog signals coming from the hybrid. For the MIMOSA readout the repeater and the DAQ card are supplied

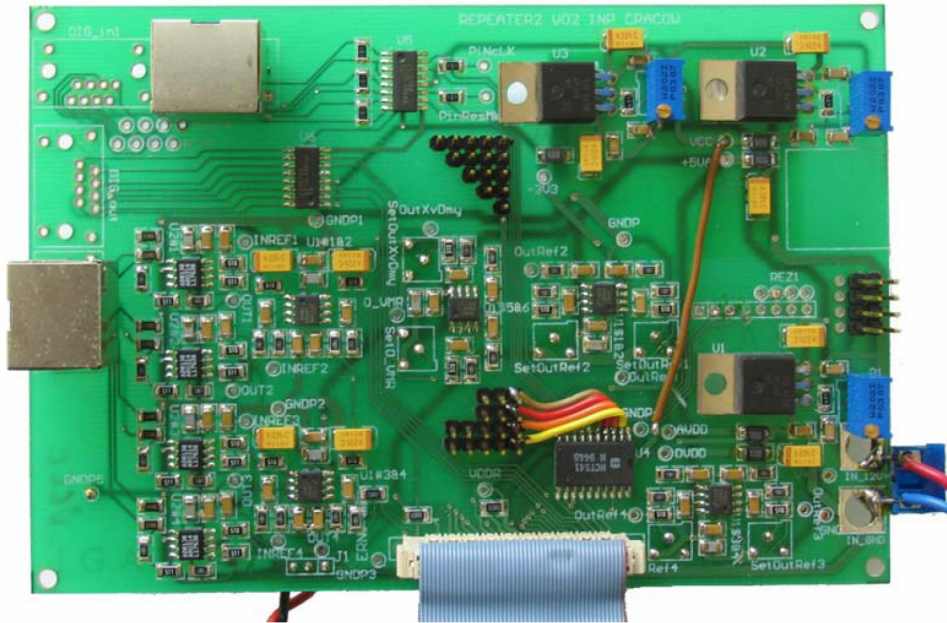


Figure 7.2: The repeater for the SUCIMA Imager. On the top and left side it has two connectors for fast analogue and digital signals, at the bottom a ribbon cable to connect the hybrid and on the right the power input. The digital control signals and the power lines are connected by interconnection pins.

by one 8.5 V line, that is regulated by LM317 ICs to all internal voltages separately on both board. The reference voltages for the amplifiers on the sensor can be set for each of the four output channels by potentiometers at the input of operational amplifiers. The power supply to and the digital control transmission from the DAQ card are achieved by a piggy back connection with standard pin connectors. The digital clock and reset signals to and the analog data signals from the sensor are transmitted via short twisted pair CAT5e cables with RJ45 connectors. The hybrid is connected via a 50pin ribbon cable to the repeater, which carries all supply and reference voltages, as well as all digital and analog signals.

Fig 7.3 shows the hybrid with a MIMOSA-V mounted. On top the hybrid supports the sensor mechanically and on bottom it carries the first external stage of signal amplification and a set of RC filters for the supply voltages. With a gain of one the amplifier acts as line drivers to the repeater.

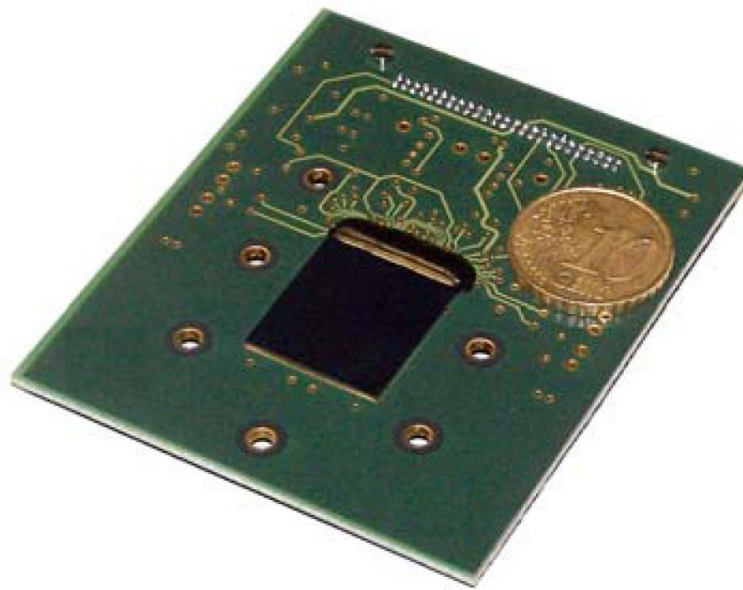


Figure 7.3: The MIMOSA-V hybrid with a back-thinned sensor mounted on top.

7.2 The MIMOSA-V DAQ software for realtime sparsification

Low activity measurements with the back-thinned Mimosa-V sensor require a realtime sparsification, meaning a data acquisition and instant reduction during a long term run (e.g. one day). All measurements for the REGINS project were performed at room temperature allowing about 4 CDS frames before the pixels are saturated. Additional cooling of the sensor offers the use of up to 40 CDS frames due to low noise and leakage currents. For the REGINS measurements only the 3rd and 4th acquired CDS frame was used to exclude some additional reset noise in the 1st and 2nd frame. In an exposure time of 25 ms/frame this leads to an effective frame rate of 10 s^{-1} corresponding to a raw data stream of $\sim 20 \text{ MB/s}$ or $\sim 1.7 \text{ TB/day}$. A data reduction to manageable sizes for single images was only possible inside the DAQ software according to missing mathematical processing features of the DAQ system and its too small memory. This LabView based (Version 7.2) MIMOSA-V DAQ software includes a fast data acquisition and data reduction executed in parallel. A snapshot of its front panel is shown in Fig 7.4. The data reduction just records hit clusters with a mean energy above a "Cluster Mean" cut (T_{mean}) and a cluster seed energy above an "Event Threshold" cut (T_{event}). These cuts are easily adjustable during data taking on the bottom left of the front panel.

The general structure of the MIMOSA-V software was taken from an existing SUCCESSOR DAQ software ¹, which is suitable to readout SUCCESSOR chips, a chip generation of SUCIMA with maximum 112×112 pixel, and has capabilities to read MIMOSA chips. But soon turned out, that its incorporated algorithms are much too slow to even read data streams of 20 MB/s from a MIMOSA-V detector and the memory exhausting initial noise and pedestal calibration algorithms required a lot of hard disc swapping. Therefore all algorithms behind the panels have been exchanged by more sophisticated but pure LabView algorithms.

¹SUCCESSOR DAQ-software by Levin Jungerman, IEKP, U. Karlsruhe

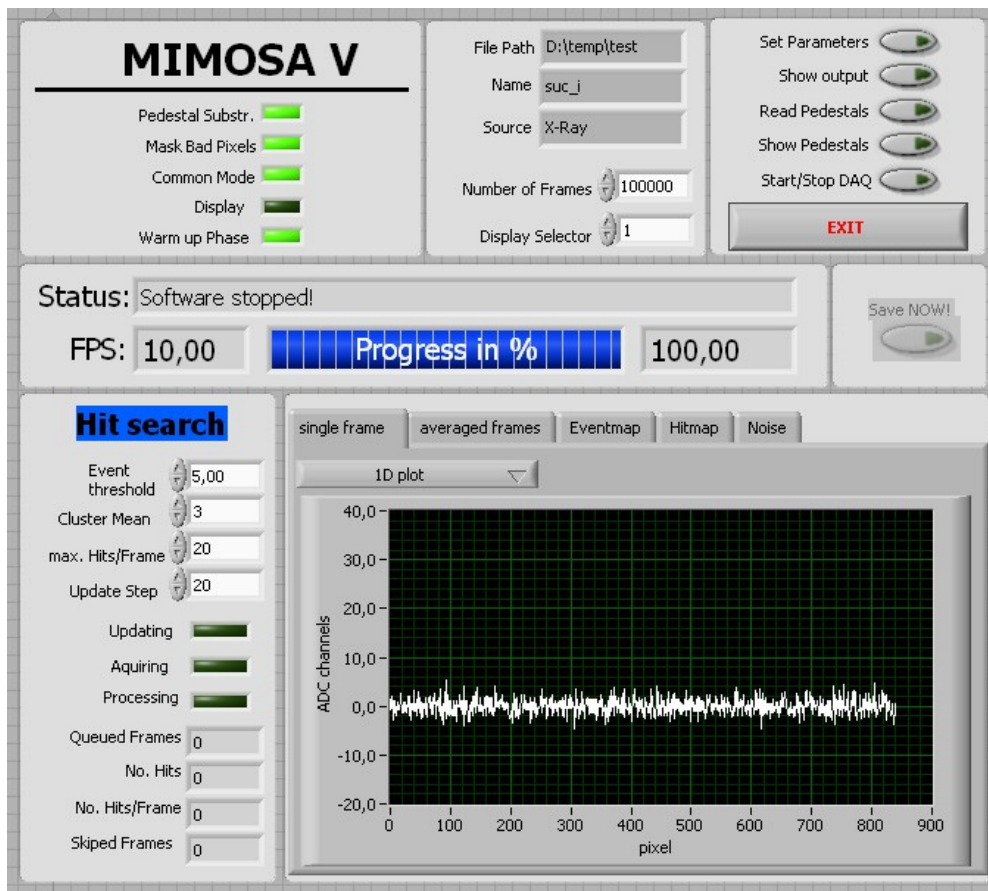


Figure 7.4: The frontpanel of the MIMOSA-V DAQ software with displays for the recorded Hitmap (integrated clusters), the Eventmap (single event hits), the actual noise and further frame dependent images. On the lower left can be entered some often adjusted data reduction settings, while on top a part of the analysis algorithms can be switch on/off, the data size and file path can be set and the initialization of analysis and sensors setting as well the pedestal and the noise can be performed.

The implemented software not only records data, it also integrates all pixel hits as a "Hitmap" matrix, stores all pixel ADC value up to the next event in a "Eventmap" matrix, and updates the noise, pedestal, and bad pixel matrix. Further all the resulting images or distributions can be continuously displayed on the front panel.

7.2.1 Software settings inside "Set Parameters"

After pushing the "Set Parameters" button a further panel appears, as depicted in Fig 7.5. Seven tabs of this panel allow to apply settings for different sensor types, the readout system, the pedestal calibration, the data output and the data reduction. After choosing a sensor type (MIMOSA I-V or SUCCESSOR I-V) the row and column pixel numbers and some further settings are automatically adjusted to used default values. All defaults can be edited, but shall be done with care, because it changes the readout sequences. Additionally the sensor read out

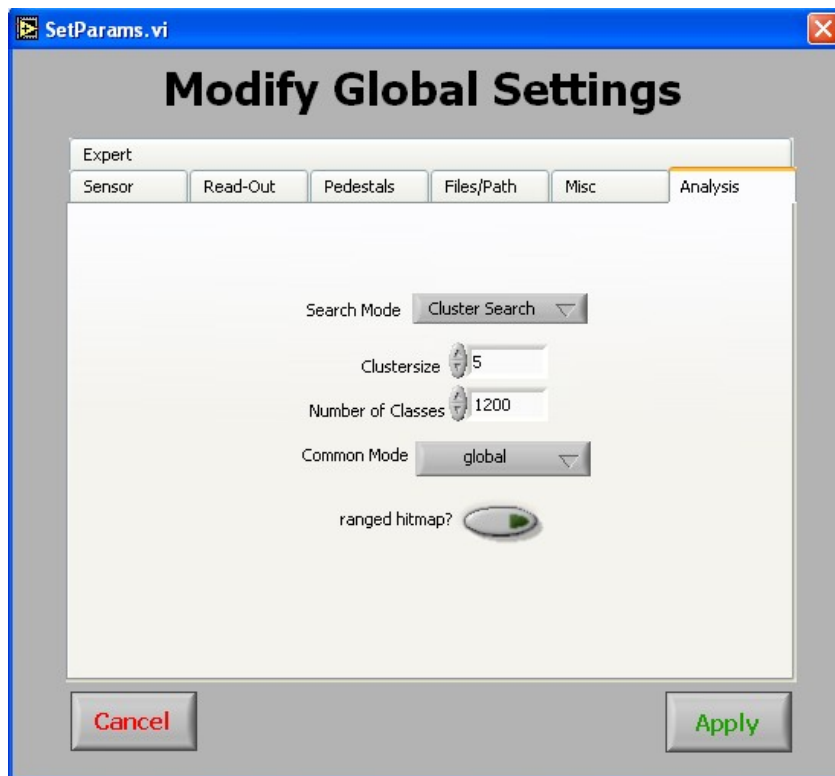


Figure 7.5: The settings panel of the MIMOSA-V DAQ software. The different applicable settings are ordered on separate tabs reflecting their functionality.

clock ≤ 10 MHz (5 MHz default), the read-out mode "raw data", "CDS" and the read sensor channel "1-4, all (default)" can be set, which automatically switches the read and displayed pixel number. For the pedestal and noise initialization a data sample size ("acquired frame number", N_f) need to be entered and for the bad pixel masking a "noisy pixel threshold" (T_{noisy}). Various combinations of flags allow to selected output files for the final and initial noise and pedestal, the common mode noise, the reduced and raw data as well as the Hitmap and the settings itself. They are partly available as binary or text files. Two data reduction mode are selectable. One is a "cluster search" method, that records only hit clusters, and the other a "threshold scan", that records only hit above a threshold. In case of the cluster search also the expected "cluster size" of a detected particle type need to be entered.

All applied settings are stored in a file and loaded during software start, thus they need not to be modified for repeated measurement.

7.2.2 Initialization and raw data processing

Pushing the "Read Pedestals" button on the upper right of the front panel invokes the pedestals and noise initialization. At the beginning the pedestals P_{ij} are derived from the pixel ADC

values $E_{f,ij}$ for an accumulated frame number N_f by a gaussian mean algorithm like:

$$P_{ij} = \frac{1}{N_f} \sum_f^{N_f} E_{f,ij} \quad , \quad (7.1)$$

together with a first noise estimate $\sigma_{est,ij}$ as gaussian variance:

$$\sigma_{est,ij} = \frac{1}{N_f - 1} \sqrt{\sum_f^{N_f} (E_{f,ij} - P_{ij})^2}. \quad (7.2)$$

Afterwards a cumulative noise algorithm is executed using an independent data set with the same frame number as for the pedestal. At first the common mode noise σ_{CM} of each frame is calculated as the gaussian mean of all pedestal subtracted pixel values below the bad pixel threshold T_{bad} :

$$\sigma_{f,CM} = \frac{1}{N_{ij} - N_{bad}} \sum_{ij \neq bad}^{N_{ij} - N_{bad}} E_{ij} - P_{ij}; \quad E_{ij} < T_{bad} = T_{noisy} \cdot \sigma_{est,ij} \quad . \quad (7.3)$$

Then the initial pixel noise σ_{ij} is gained as gaussian variance:

$$\sigma_{ij} = \frac{1}{N_f - 1} \sqrt{\sum_f^{N_f} ((E_{f,ij} - \sigma_{f,CM}) - P_{ij})^2} \quad . \quad (7.4)$$

At the end the initial bad pixel mask is evaluated as a matrix with "0" entries for pixels values above T_{bad} and otherwise "1". The splitting of the pedestal and noise statistics was necessary to avoid the storing and transfer of a very large data set (~ 500 MB), which caused a memory overflow for the original algorithms. Since fast but less robust gaussian algorithms are used, high activities sources need to be removed before an initialization to avoid signals in the pedestal distribution changing the results. But for used the fast software trigger the initialization is not effected by typical low activity particle sources used for autoradiography. During data acquisition the bad pixel mask is multiplied with the frames and bad pixels are set to zero ADC. Then the pedestal matrix and the common mode noise are subtracted, while the common mode noise is derived by the same algorithm as for the initialization, but with $T_{bad} = T_{noisy} \cdot \sigma_{ij}$. Afterwards hits or clusters are selected for pixel values above a threshold, defined as $T_{select,ij} = T_{event} \cdot \sigma_{ij}$. Each pedestal, noise and bad pixel matrix is continuously updated during the acquisition, as described in 7.2.3.

7.2.3 Sophisticated LabView algorithms

Commonly the data flow programming language LabView is used for slow control commanding and monitoring or single data value readouts. In contrast the MIMOSA-V DAQ software grabs a megapixel frame within 100 ms and furthermore subtracts the pixel pedestals and the common mode noise, discards bad pixels and searches all hit clusters in the matrix with pure LabView algorithms. In this sense LabView acts as a fast data acquisition framework with intrinsic GUI. The code inside the MIMOSA-V DAQ software makes use of a parallelized data acquisition and analysis, skipping of distorted frames and an uninterrupted data flow. Further it minimizes statistical calculations for large data samples (noise, pedestal), uses simple but effective algorithms and avoids non-necessary data displays.

Running mode pedestal and noise calculation

To account for changes of the pedestals and noise and the bad pixel mask during a long term run, their values are continuously updated after a certain frame number. On the lower left of the front panel can be found a switch to set an "Update Step" size of several frames. For each update step the data is written to the hard disc and the previous pedestals and noise and the bad pixel mask are recalculated by using running mode algorithms for the gaussian mean:

$$P_{f,ij} = \frac{N_{f-1} \cdot P_{f-1,ij} + E_{f,ij}}{N_f} \quad (7.5)$$

and variance:

$$\sigma_{f,ij} = \frac{\sqrt{((N_{f-1} - 1) \cdot \sigma_{f-1,ij})^2 + ((E_{f,ij} - \sigma_{CM}) - P_{f,ij})^2}}{N_f - 1} \quad (7.6)$$

and the initialization algorithm for the bad pixels. The skipping of intermediate frames takes into account the statistical independence of the noise and pedestal fluctuations on short enough time scales. But of course a too large interim would make the algorithm useless. Rising the update step inside a reasonable range of 0-20 frames increases the total speed of the processing, but the overall gain of acquisition performance is only of the order of 10%.

Parallel data acquisition and reduction

For large data streams in range of the maximum USB2 transmission rate the acquisition performance increases more than a factor of two by parallelizing the raw data acquisition and the processing. In LabView all structures without interconnection are execute in parallel, except they are explicitly called in sequence frames. Raw data source are in general interconnected with followed processing algorithms, as typical for data flow languages. To disconnect such incoming and outgoing data streams LabView offers the "queue" Vi, acting similar as a first in first out buffer addressed by a reference. In the MIMOSA-V DAQ Software such a "queue" Vi buffer is used to exchange data between the acquisition and the processing. This avoids a DAQ waiting for the processing and wise versa. During processing the USB2 transmission operates on its maximum by continuously reading data and pushing it to the queue and because this operations runs nearly independent from the CPU, the processing also runs with maximum CPU performance.

During data taking the parallel approach can be balanced by choosing the DAQ software update step such, that the number of queued frames, indicated on the lower left of the front panel, reaches a constant below the maximum queue size. Though the necessity of this procedure is not strongly motivated, since it just leads to a moderate shorter update cycles for the noise and pedestal. Thus in general it should be enough to chose the update step as large, that an empty queue is indicated.

Online display reduction

A rather large performance gain of about 20% to 30 % can be reach by avoiding online data displays, since all the additional calculations for the large images cost allot of cpu performance. Therefore all online displays on the front panel of the MIMOSA-V Software can be deactivate by a switch placed on the top left of the front panel as long as they are not needed.

Cluster search and threshold scan reduction

The data reduction is performed by just storing the information of particle hit clusters of fixed size reaching a compression factor of a about 10^5 or all hits above a threshold with a factor of 10^4 .

Clusters are searched by their central seed contained as maximum ADC values inside the acquired frame hits above the selection threshold $T_{select} = T_{event} \cdot \sigma_{ij}$. For a found cluster the seed and its surrounding pixel values are discarded from the matrix and stored in case the mean cluster value is above the adjusted "Cluster Mean" threshold. This procedure is repeated until no further seed is found. All REGINS measurements of tritium and ^{14}C beta-particle used a cluster size of 5×5 pixel. In case of the used fixed cluster size the energy depositions of particle with flat angles to sensor surface are underestimated, which seems to be none negligible, since the source distances was still in range of few hundred micrometer and flat angle tracks were quit probable. On the other hand, a recursive cluster size scan fixing this problem was not applicable, due to the large computation overhead. Thus the implemented method just makes a compromise. Nevertheless, the resulting β -spectra of tritium and ^{14}C gained with a fixed cluster size still show the expected 3-body decay shape and correct endpoint ratios, as shown in Fig 8.7.

The included threshold scan reduction only selects pixel hits above a threshold adjusted as T_{select} . This method achieves an overall performance 30% faster then the cluster search, but leads to a smaller reduction. This originates from a necessary low hit threshold to record all surrounding cluster pixels, which rises the recorded noise. The low threshold also makes the threshold scan less robust against seldom bias supply instabilities or pickup signals causing distorted frames and thus the "Hitmap" on the software displays often vanishes in a noise background.

Skipping of distorted frames

The first measurements with the simple threshold scan reduction sometimes showed a none flat common mode noise distributions in the frames. Therefore a cut was implemented setting an expected limit on the hits inside a frame. It is adjustable on the lower right of the front panel ("max. hits/frames") and needs to be set appropriate to the measured activity. Frames with hits above this limit are simply skipped. With this algorithm the acquisition and the frame rate stabilizes strongly, since events including thousands of hits due to a none flat common mode or pick up noise are not processed. Thus this cut was also essential for the later used cluster search reduction.

Uninterrupted data flow

One performance loss often unknown to LabView programmers is caused by the use of many wire bifurcations and frame transfers transmitting large data amounts. In this case the data flow is interrupted by LabView creating copies of the data for a bifurcation or transfer. All this is also true for subVis, but they additionally induce a calling overhead. Therefore such an implementation style should be avoided as much as possible in time critical parts as event loops by using shift registers or queues and a single Vi without subVis. In the MIMOSA-V

DAQ software case all large arrays storing the noise, pedestal, bad pixels, displayed images and further are transferred to a following cycle by shift registers. The processing speeds up enormous, if all operations on large arrays are performed with LabView provided Vis (summation, subtraction...) and not in loops, since a single C-code is called.

Chapter 8

The Mimosa V back-thinned for microarray imaging

The research topic for the REGINS project was to develop an electronic imaging device for labeled molecules on bio-chips, which are also called microarrays. The bio-chips technology arose in the 90's, but was established very fast in pharmacy, medicine, biochemistry, genetics and microbiology, since high amount of tests can be performed on short timescales even automatically and only small probes are necessary. For the techniques used today molecules are bound on glass or polymer substrates.

One of the current used methods for microarray imaging is the radioisotope labeling or autoradiography. The available autoradiography methods have problems like detection inefficiencies, low spatial resolutions, or high costs for films. The presented measurements in this section show, that these problems can be solved by using CMOS detectors of special design like the back-thinned MIMOSA-V. A picture of the used experimental setup is shown in Fig 8.1. The

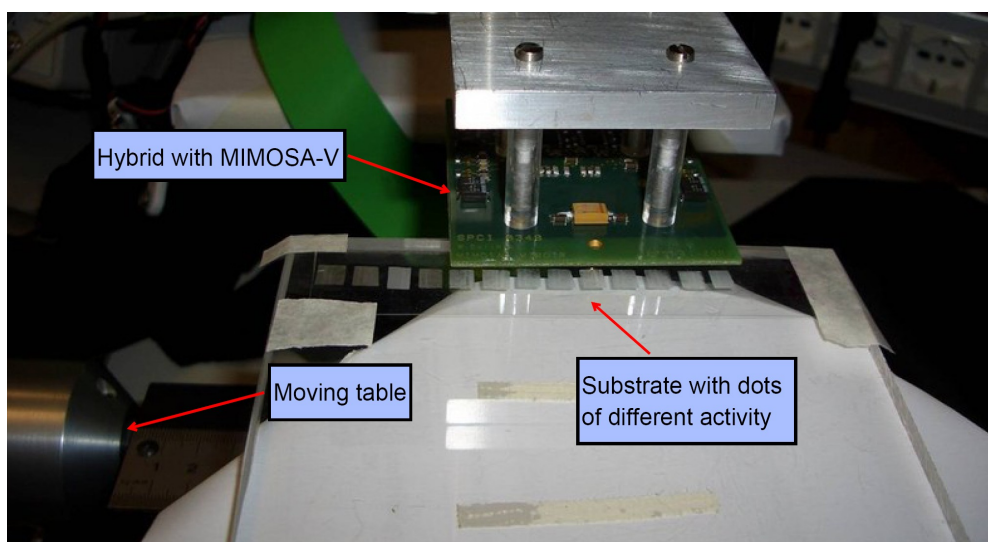


Figure 8.1: Experimental setup used for the low activity measurements with the back-thinned MIMOSA-V.

back-thinned MIMOSA-V reaches the sensitivity to sharply resolve ^{14}C and tritium (^3H) labeled molecules on pixels with dimensions of 1 mm^2 or even smaller, which forces a granularity

at the level of 20-25 μm . Furthermore the sensor features the sensitivity to measure the spectrum of emitted particles with an accuracy allowing a differential imaging between ^{14}C and tritium labels. Therefore the signal needs to be strongly discriminated against dark counting rates, to stay sensitive for the extremely weak specific activity of typical measured samples ($\sim 1 \text{ kBq/mg} = 27 \text{ nCi/mg}$). This dark counting rates include a stochastic component, related to electronics noise and to the cosmic ray flux, and a non-stochastic component, related to bad pixels (e.g. high leakage currents) and distorted events with an abnormal occupancy, due to bias supply instabilities or pickup signals. In general the field of applications for autoradiography is limited by the short ranges of β -particles and their arbitrary momentum directions, that forces detector-source distances of at most a few hundred μm .

8.1 Imaging constraints for ^{14}C and ^3H spectra

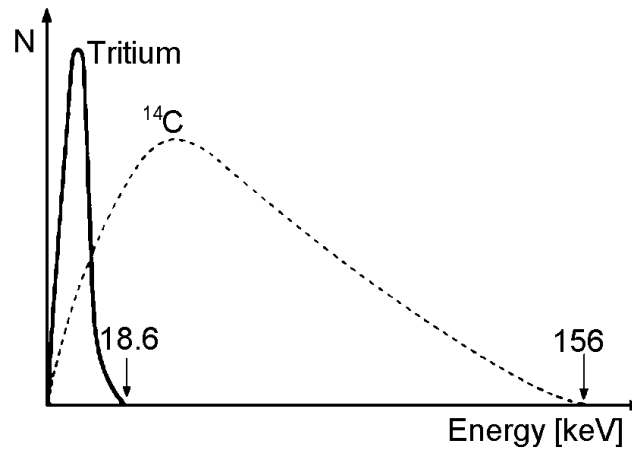


Figure 8.2: Illustration of the ^3H and the ^{14}C β -spectra with marked endpoint energies.

The prospect of imaging β -emitters such as ^3H and ^{14}C , it is necessary to ensure the sensitivity of the used detector. In case of the MIMOSA-V this could be accomplished by a back-thinning process described in 6.1.2. For imaging purposes the low energy threshold of a sensor should be below the spectral expectation of the source to reach a high detection efficiency. For spectral analysis this threshold even needs to be far below the expectation to derive the full spectrum.

In single β^- decays a neutron decays into an electron, a proton and an electron antineutrino. This 3-body decay conserves the momentum for a proton staying at rest and lead Wolfgang Pauli to the postulation of the neutrino (1930) long before its discovery (1956). But due to the 3-body decay of ^{14}C and ^3H , the energies of their decay electrons are distributed in broad spectra as illustrated by Fig 8.2. The resulting electron intensity $I(p_E)$ for a momentum p_E can be analytically calculated as:

$$I(p_E)dp_E = p_E^2(E_0 - E)^2 F(Z, E)dp_E \quad (8.1)$$

The formula just depends on the end point E_0 of the electron energy spectrum, which can be approximated by the decay energy due to the small mass of the electron antineutrino ($<$

2.2 eV) staying at rest for maximum electron momentum. The rather complicated Fermi function $F(Z, E)$ in the formula describes relativistic Coulomb corrections and has various approximation with different accuracies. In the non relativistic case $E < m_0c^2 = 511$ keV and low atomic charge numbers Z it can be approximated by $F(Z, E) = 1 + \pi\alpha ZE/p_E$ with the fine structure constant $\alpha \approx 1/137$ [VGB⁺84]. By using the relativistic relation $p_E^2 = E^2 + (m_0c^2)^2$ and $p_E dp_E = E dE$ the spectrum can be written as:

$$f(E)dE = \sqrt{E^2 - (m_0c^2)^2} E (E_0 - E)^2 \left(1 + \frac{\pi\alpha ZE}{\sqrt{E^2 - (m_0c^2)^2}}\right) dE. \quad (8.2)$$

And in terms of the kinetic energy $E_k = E - mc^2$ with $dE = dE_k$ follows:

$$f(E_k)dE_k = \sqrt{E_k^2 - 2m_0c^2E_k} (E_k + mc^2) (E_{k0} - E_k)^2 \left(1 + \frac{\pi\alpha Z(E_k + mc^2)}{\sqrt{E_k^2 - 2m_0c^2E_k}}\right) dE_k. \quad (8.3)$$

For this analytical derived spectrum the expectation can be calculate as:

$$\langle E_k \rangle = \frac{\int E_k f(E_k) dE_k}{\int f(E_k) dE_k}. \quad (8.4)$$

In case of a tritium spectrum with $Z=1$ and $E_{k0,H3} = 18.6$ keV it results in $\langle E_{k,H3} \rangle \sim 5.9$ keV and for ^{14}C with $Z=6$ and $E_{k0,C14} = 156$ keV in $\langle E_{k,C14} \rangle \sim 53.5$ keV. Electrons with energies in range of the tritium expectation have a CSDA range in silicon of about 500 nm (extrapolated NIST data [NIS]). Therefore the only 100 nm thick passivation layer of the back-thinned MIMOSA-V allows to achieve an energy detection threshold far below the tritium expectation and makes also spectral analysis possible.

8.2 Imaging constraints for microarrays

The today available microarray designs can either detect DNA-fragments or proteins. DNA-microarrays already allow to analyze 100,000 known genes in samples of patient tissues. Each pixel is covered with single stranded DNA fragments and detects relative changes of gene expressions. The fragments are labeled with fluorescence pigments of different color and the intensity and wavelength of the color mixture are detected by a laser camera. In 1994 the first commercial "HIV Gene Chip" was sold by the company Affymetrix. Protein-microarrays can be used in clinical diagnostics, in research, and in food and environmental analysis. In diagnostics they help to identify tumor-markers as well as autoimmune and infection disease. In research they can find substrates for kinases, ligands of receptors or protein interactions. Transferase (kinase, polymerase, etc..) activities of proteins can be measured by using radioactive functional groups. Thereby a transferase replaces functional groups with the radioactive ones, in case the protein is a substrate for the transferase. The binding and retention on protein arrays is mediated via a thermodynamically driven binding mechanism dependent on their folding. Thus the detection of proteins can be considerably more complex, when their specific folding is changed by labeling with fluorescence pigments. But replacing hydrogen with tritium does not harm the folding and autoradiography is possible.

An example for kinase activity measurements by autoradiography of microarrays is shown in Fig 8.3. The Fig illustrates a microarray production flow and a detected image, as it is presented in

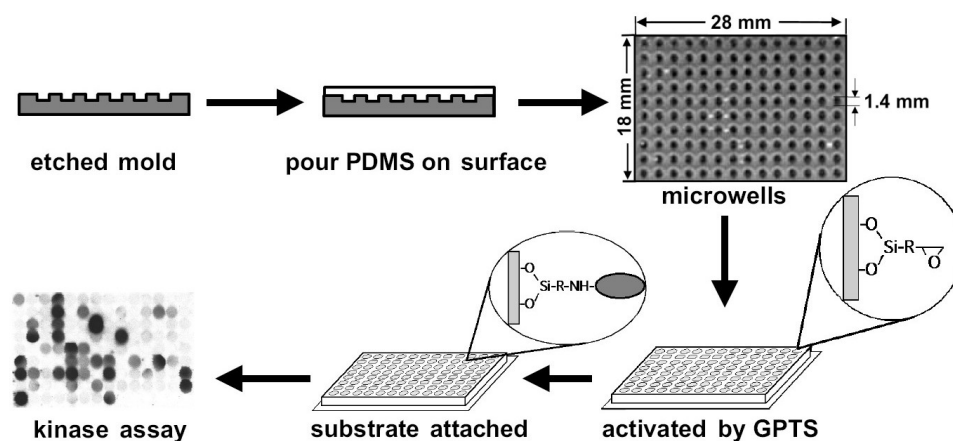


Figure 8.3: Illustration of a protein chip production flow and a detected image, including the substrate and pixel dimensions. [ZKC⁺00]

reference [ZKC⁺00]. In this case a substrate with microwells was produced by pouring PDMS (polydimethylsiloxan) on a mold and peeling the substrate away after curing. In a next step the substrate surface was modified by GPTS (3-glycidoxypropyltrimethoxysilane) and then different test proteins were covalently bound to the wells. These wells were blocked with 1% BSA (bovine serum albumin) to saturate the pixels with unspecific protein interactions. Then the kinase was added together with $^{33}\text{P}\gamma\text{-ATP}$. During 30 min incubation at 30°C the kinase displaced BSA from the test proteins and attached the radio labeled ATP to the proteins, in case the proteins are substrates for kinase. By extensive washing the unbound $\gamma\text{-ATP}$ and the BSA was removed. Then the microarray was exposed to an X-ray film, that typically has resolutions of a few μm , and a phosphor-imager, which had a resolution of 50 μm and was quantitative due to low detectable density rates.

For the commercially available phosphor-plate-imager BAS 5000 Fujifilm a granularity down to 25 μm and a minimum detectable density rate for ^{14}C of $\sim 9 \cdot 10^{-1}$ dpm/mm² (dpm: decomposition per minute) is claimed. The device costs about 70000 Euro and an image plate about 1000 Euro, while the plate for tritium autoradiography is recommended for single use. In comparison the backthinned MIMOSA-V provides a granularity of 17 μm and the measurements presented in the following sections derived a minimum density rate for ^{14}C of $\sim 3 \cdot 10^{-1}$ dpm/mm² at 20°C and of $\sim 1.4 \cdot 10^{-2}$ dpm/mm² at 4°C. So the sensor allows tritium autoradiography without additional costs and the prices of possible imaging devices will unlikely exceed the ones of phosphor-plate-imager.

8.3 Images of ^{14}C and ^3H standards for different activities

Within the REGINS project two batches of measurements for tritium standard dots with activities from 8 nCi/mg to 489.1 nCi/mg and ^{14}C standard dots with activities from 18.4 nCi/mg to 220 nCi/mg were performed. These dots were measured within exposure times of about one day at room temperature. Envisaged was the direct displays of recorded images to enable an immediate analysis of microarray pixel patterns. All raw data of the first batch was reduced

with the threshold scan method, which was fast to implement in the DAQ software. But this method was less robust against bias supply instabilities or pickup signals and the final image often disappeared on the software displays as mentioned in 7.2.

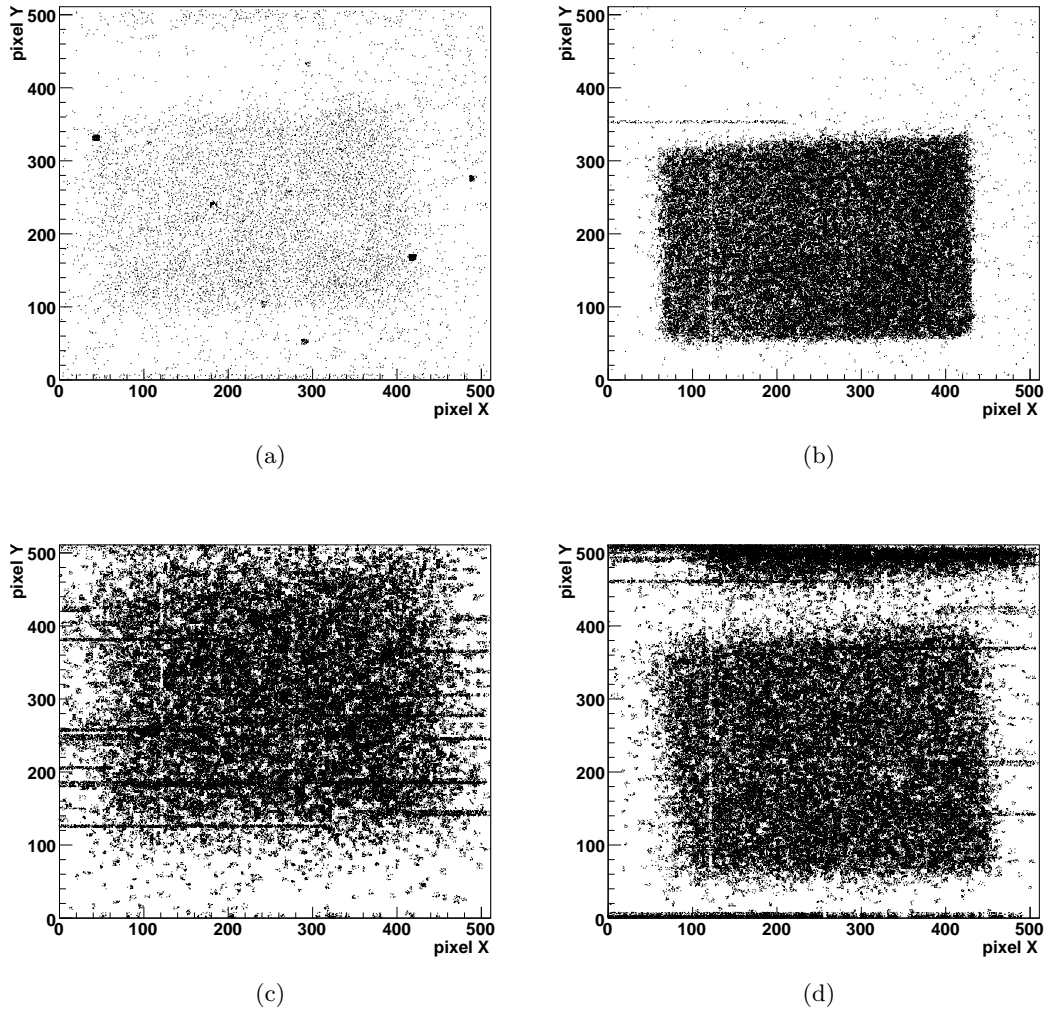


Figure 8.4: Off line analysis image of ^3H dots with 8 nCi/mg (a) and 489.1 nCi/mg (b) and sizes of $\sim 6 \times 4 \text{ mm}^2$ as well as of ^{14}C dots with 18 nCi/mg (c) and 220 nCi/mg (d) and sizes of $\sim 6 \times 5 \text{ mm}^2$.

Nevertheless the images were recovered by an off-line analysis of the recorded data. All algorithms of this analysis code were implemented in C++ with help of ROOT classes. The code searches all clusters in the acquired frames with a seed threshold of 5 ADC counts, an pixel threshold of 3 ADC counts and a cluster size of 5×5 pixels. Examples images of the lowest and highest activity tritium and ^{14}C dots, as they resulted after post processing, are shown in Fig 8.4. An area covered by 3×3 pixels of the protein chip in Fig 8.3 reflects the size of the dots.

To avoid the post processing a cluster search reduction and a rejection of frames with abnormal occupancy (cluster number $> 50-100$) was implemented to the DAQ software. After this changes

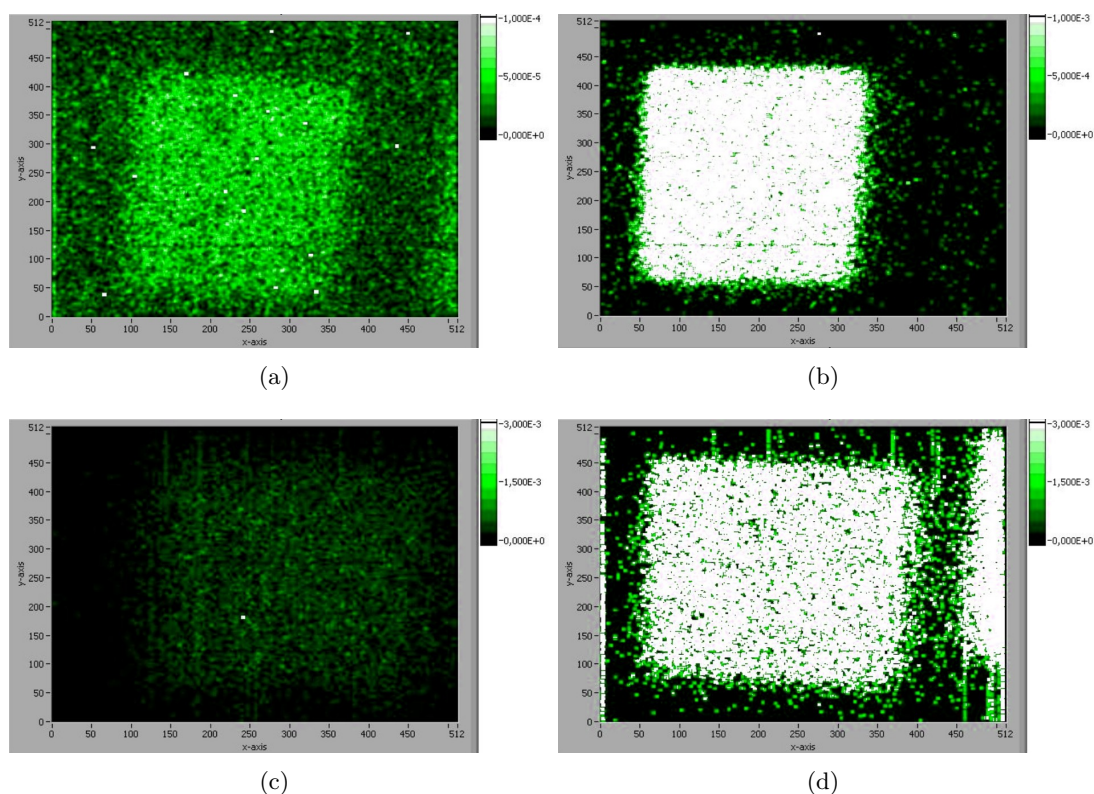


Figure 8.5: Images of ^3H dots with 8 nCi/mg (a) and 489.1 nCi/mg (b) and sizes of $\sim 6 \times 4$ mm² as well as of ^{14}C dots with 18 nCi/mg (c) and 220 nCi/mg (d) and sizes of $\sim 6 \times 5$ mm² captured from the DAQ software display.

all images were directly visible on the software displays, as shown by the captured example images of ^{14}C and ^3H dots with different activities in Fig 8.5.

A complete impression of the backthinned MIMOSA-V sensitivity is given by the images of ^3H dots visible in Fig 8.6. They were recorded with the cluster search reduction of the DAQ software in an exposure time of only 2 hours, while the sensor was cooled to 4°C. The cooling led to a density rate of $\sim 1.4 \cdot 10^{-2}$ dpm/mm² and reduced the masked bad pixel and rejected frame number by a factor of 3 compared to measurements at room temperature.

8.4 Differential imaging of nCi probes

An approach, offered by the fully analog readout of the MIMOSA-V, is the differential imaging of molecules labeled with different isotopes like ^{14}C and ^3H . This method is widely used for the fluorescence technique already mentioned for the DNA analysis, since further information is retrieved simultaneously. For ^{14}C and ^3H labels it becomes possible due to clearly separated β -spectra and applicable, since the back-thinned MIMOSA-V reaches a detection threshold far below the spectral expectations. The cluster energy spectra measured with the back-thinned MIMOSA-V, visible in Fig 8.7, show a nice 3-body decay shape with distinct separated peak

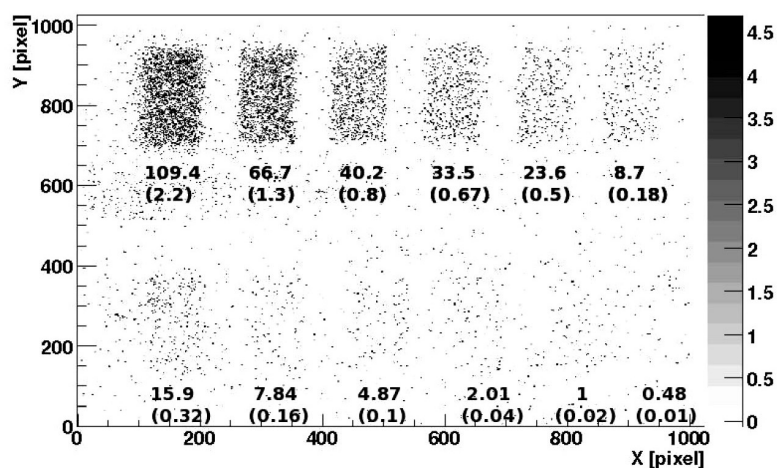


Figure 8.6: Images of RPA506 and RPA507 standards with activities from 0.48 nCi/mg to 109.4 nCi/mg recorded at 4° C. [Cac07]

positions. Because an energy calibration was missing, the spectra are only plotted against the

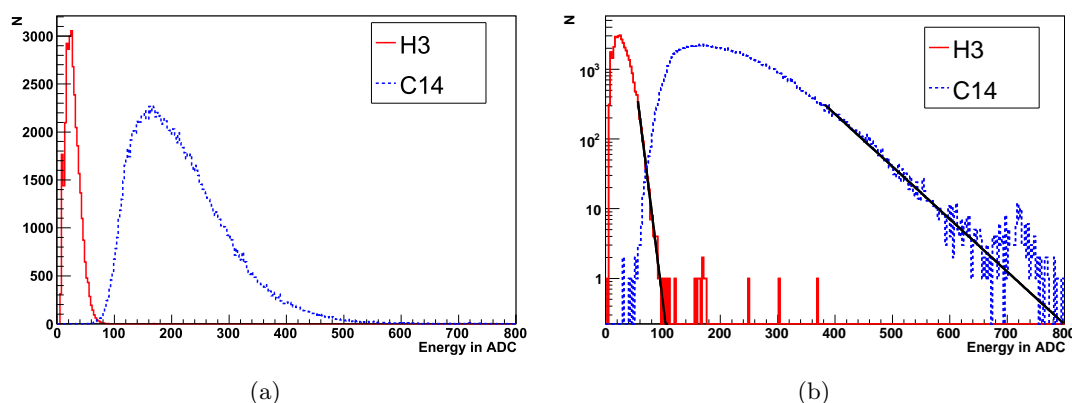


Figure 8.7: (a) Measured tritium and ^{14}C energy spectra of the standard dots, derived by the off line analysis of threshold scan reduced data. (b) The same spectra on logarithmic scale including a fit extrapolation to the end points (Fermi plot).

summed 25 ADC values of the clusters. The same data on logarithmic scale is shown in Fig 8.7 (b) and allows a linear fit extrapolation to the endpoints (Fermi plot). Thus the relative alignment of this characteristic feature can be derived as the endpoint ratio $800/100=8$, which is in good agreement with the ratio of the literatures values $156/18.6 = 8.4$. The large low energy gap in the ^{14}C spectrum originates from a chosen high hit threshold, because the data was recorded with the threshold scan reduction. Some artifacts in the distribution tails results from an insufficient bad pixels masking and an additional row wise common mode noise, which also appears as dots and lines in the images of Fig 8.4. But these artifacts vanished after a bug fixes for the common mode noise and bad pixel suppression in the latest software version.

8.5 Sensor resolution vs. object distance

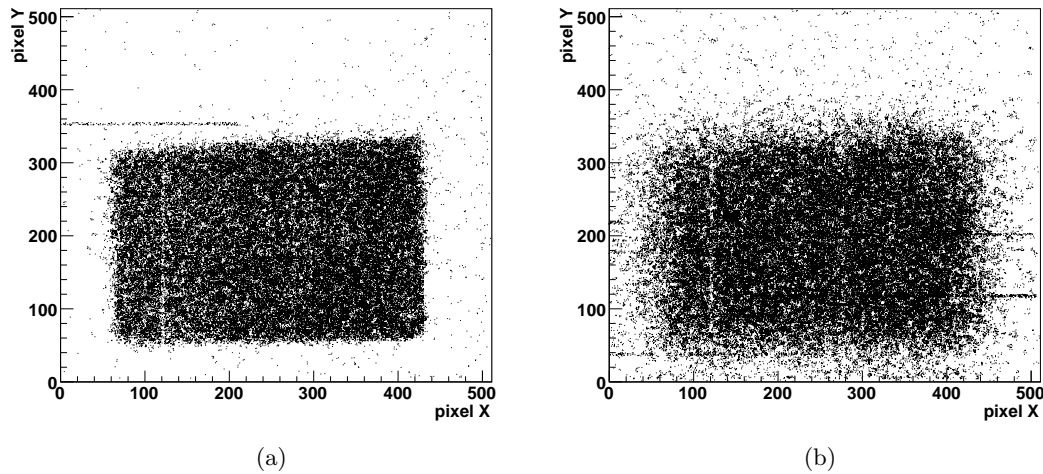


Figure 8.8: Image of a 489.1 nCi/mg tritium dot with a source to sensors distance of $620 \mu\text{m}$ (a) and $1250 \mu\text{m}$ (b).

The experimental setup used for the REGINS project, depicted in Fig 8.1, allowed to reach sensor to standard dot distances down to $620 \mu\text{m}$. Such short distances are necessary to avoid stopping in the air and to diminishes particle tracks with flat angles to the sensor surface. Absorbtion in the air reduces the detection efficiency, while flat angle tracks lead to smeared out edges of detected areas. Thus the sharpness of images decreases with rising distances between source and sensor, as visible in the images taken for the same tritium standard dots at a distance of $650 \mu\text{m}$ and $1250 \mu\text{m}$ in Fig 8.8. Only distances of a few hundred μm lead to sharpness efficient to distinguish 1 mm^2 or even smaller pixel sizes on microarrays.

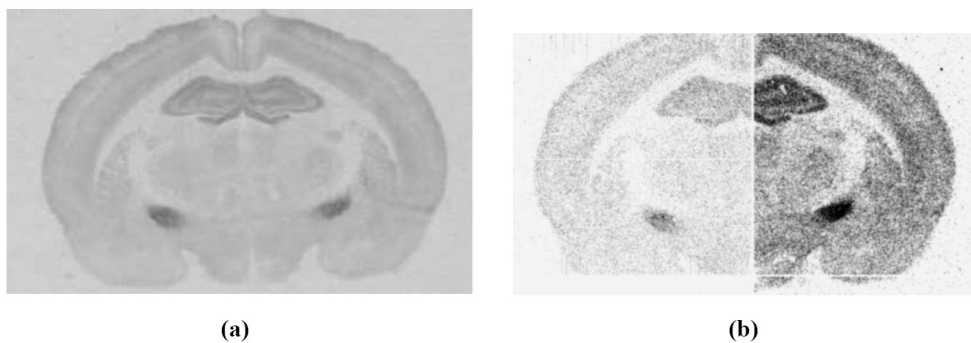


Figure 8.9: Tritium labeled slices of a mouse brain recorded with a film in a week at room temperature (a) and with MIMOSA-V in 10 hours at 4°C (b). [Cac07]

For the same reasons the imaging of radioactively labeled tissue slices needs short sensor to slice distances. But additionally the slice thickness is limited, otherwise images of different depths

overlay. This constraint is true for most slice imaging techniques and might be weakened for tritium autoradiography due to the short range of its β -particles. Despite these problems the back-thinned MIMOSA-V reaches a better detection efficiency for tritium labeled tissue sample than conventional film imaging. The two images of mouse brain slices with same activity in Fig 8.9 have a similar contrast and sharpness, though the exposure time for the MIMOSA-V image was 10 hours compared to a week for the film. The contrast shift between the two columns of the MIMOSA-V image originates from the different diode dimensions of the sensor.

Chapter 9

Summary

The construction of most parts of the Alpha Magnetic Spectrometer (AMS-02) detector is finished, except for the superconducting magnet for the Tracker, which is being tested and will be available at the end of 2008. All subdetectors and final electronics were pre-integrated in a clean room at CERN and went through a successful test in a cosmic ray test stand. At the moment AMS-02 is disassembled again for the installation of the magnet, only the TRD still operates and takes data. As soon as the magnet is delivered, the final detector will be assembled at CERN. In case the integration stays on schedule, a beamtest with the whole detector is foreseen at the CERN SPS accelerator. Otherwise AMS-02 will be directly transported to the ESA ESTEC facilities in Noordwijk, Netherlands and will go through a final TVT and EMI-test. After all tests the detector will be flown to the NASA, Kennedy Space Center and then will wait for the launch to the ISS until enough transport volume of the Space Shuttle is available.

This thesis presents extensive tests of the AMS-02 TRD board-level electronics to guarantee a 3 years maintenance-free operation in space. The tests were performed in specialized laboratories equipped with TVT (Thermo Vacuum Test), ESS (Environmental Stress Screening) and EMI-test (Electro Magnetic Interference) facilities. They included qualification tests of the readout and slow control electronic boards housed in a crates (U-crate) as well as qualification and acceptance test of the power supply DC/DC-converters and their control board assembled to the Power Distribution box (UPD-box). The qualified UPD production then was assembled to a first UPD-box¹. With the gained experience an assembly document was written, that guided the assembly of the flight model UPD-boxes at the Chungshan Institute of Science and Technology (CSIST) in Taiwan. For electrical tests of all TRD electronic boards a LabView test software was implemented and successfully used for all tests up to the complete FM/FS board production. It helped to identify shorts on the data reduction boards, measured the stability of the readout front end supply voltages at the occurring temperatures in space and detected defects of the boards protection circuits. All performed DC/DC-converter tests included efficiency curve measurements, that helped to estimate the total AMS-02 power consumption and to find the necessary supply voltage achieving a stable operation of the UPSFE-board in the U-crate. The large amount of FM/FS DC/DC-converters were comfortably tested with a specially developed variable load system controlled by the LabView test software. All tested U-crate and UPD boards passed the functional and the qualification and acceptance requirements and the later assembled U-crate and UPD-box achieved the same.

As discussed in this thesis AMS-02 will search for antimatter locations in the universe, determine the mean density of interstellar matter as well as the composition and the age of cosmic ray

¹The QM2 UPD assembly was done in cooperation with Florian Hauler and Andreas Sabellek, IEKP

fluxes and among further measurement it can do an indirect search of dark matter. In the nowadays commonly agreed universe model dark matter makes up a fraction of 80% of the total universe mass. Dark matter could be indirectly detected by its annihilation end products showing up in the cosmic ray spectra of hadrons, leptons and gamma rays. The leptons are electrons and positrons. Electrons are lost in the sea of the large cosmic ray flux, but positrons might be detectable, if they can be discriminated against protons. The difficulty is that both particles have the same charge and the $\sim 10^5$ times more frequent protons may be often detected as positrons. Therefore AMS-02 provides a powerful proton rejection of about 10^5 , reached by the ECAL (10^3) and the TRD ($10^2 - 10^3$).

Unfortunately the measured TRD proton rejection power, derived from an analysis of beamtest data taken with a prototype, was significantly lower than the one gained from a GEANT3 simulation of this detector for proton energies above 160 GeV. Since GEANT3 is an unsupported detector simulation framework with an old hadron physics parametrization (GEISHA), a solution was found by implementing a further process generating a diffractive background as: $p + C \rightarrow p + C + \pi^+ + \pi^-$ in the organic (^{12}C) material of the TRD (prototype). Because the TRD selects light leptons by additional energy deposition of generated transition radiation in forward direction, the simulated rejection power shrank due to the energy deposition of protons and additional pions in forward direction. But the motivation of the necessary cross sections (≤ 15 mb) was not proven and the parametrization of only two pions with energies in range of a few MeV was quite simple. Altogether this motivated the implementation of a new simulation based on the GEANT4 detector simulation framework (C⁺⁺). A framework, that is commonly used in HEP experiments, like the LHC detectors, and continuously supported. Furthermore it includes a variety of new hadron physics approaches. But the proton rejection power derived from GEANT4 simulations showed the same deviation, though all available hadron physics approaches suitable for our needs were tested.

Therefore the motivation for the diffractive process hypothetically introduced to the GEANT3 simulation was studied for available data and theoretical predictions. It concluded that diffractive cross sections permit the assumed background and led to a further analysis of diffractive events generated by the particle event generator PYTHIA. This analysis code was used for a FORTRAN based fast simulation of the TRD prototype and included the same algorithms as used for beamtest data and simulation analysis. Since PYTHIA simulates only nucleon interactions, the background was extracted from pure diffractive $p + p$ events providing the kinematics and the result was scaled with a theoretically predicted cross section dependency from the nucleon to the $p + C$ case. The background derived in this way agrees with the observed rejection power deviation up to 200 GeV proton energies. Only for the highest energy of 250 GeV this could not be achieved. The reason may be related to a different beam setup used for this energy, providing a lower beam purity or to the approximated kinematics used for this analysis, resulting in a pion rate with strong forward direction smaller than for the about twelve times heavier ^{12}C . The particle multiplicities of the selected events strongly peak for two pions. Thus the simple two pion approximation inside the parameterized process for the GEANT3 simulation seems to be acceptable. Only the assumed energy range of a few MeV disagrees with the energies of the selected pion of tens of GeV. Nevertheless the result hints to a diffractive background shrinking the TRD proton rejection power, which is not described by the available GEANT4 hadron physics approaches. The presented results were transmitted to the GEANT4 collaboration and a possible solution was promised.

The knowledge gained from the development of the LabView test software and the beamtest

analysis with ROOT was directly used for the implementation of a LabView DAQ-Software to readout a backthinned MIMOSA-V within the REGINS project. A part of the used algorithms were additionally implemented as a C++ code for a post processed cluster search of some of the recorded data. The REGINS project aimed at the development of a silicon imaging device for autoradiography on microarrays. Therefore tritium and ^{14}C standards images were recorded with activities (8 nCi/mg to 489.1 nCi/mg) down to the typical ones of radioactive labeled molecules on microarrays. Thus the expected decays rates per frame were extremely low and a data reduction to a manageable size was required, since significant images require an information contained in 10^5 to 10^6 frames or a raw data size of about 1 TB for a megapixel sensor like MIMOSA-V.

In contrast to AMS-02, the used DAQ-system consists of a single board, the SUCIMA-Imager, and a further attached piggy bag board to repeat the small signals of the MIMOSA-V CMOS sensor. A data reduction was not possible by hardware according to missing mathematical processing features of the DAQ board and its too small memory. Therefore as particular difference to AMS-02 the acquired data was reduced by the LabView DAQ software running on a Windows PC. All sparsification algorithms were exclusively implemented in LabView with some sophisticated approaches to achieve a fast data flow. The software provides a graphical user interface to apply necessary settings and to display the recorded image as well as the single frame images and some further statistical analysis. With the implemented algorithms frame rates up to 10/s were reached and after the measurement sharp images of the standards dots were displayed.

Typical pixel dimensions on microarrays of 1 mm^2 or smaller force a sensor granularity at the level of 20-25 μm and the MIMOSA-V has a granularity of 17 μm . The recorded images with the DAQ software document an imaging of standard dots down to activities of 8 nCi/mg with sufficient resolution for the envisaged task. Thereby the sharpness of the images is correlated with the sensor to source distance, which allows only distances of a few hundred μm . A further analysis of the recorded data derived the energy spectra of the particle hit clusters measured with the sensor. These spectra describe the shapes and the endpoint alignment of the expected ^{14}C and tritium β -spectra. Since the spectra of these two sources clearly separate, even differential imaging of molecules variably labeled with ^{14}C and tritium is offered by the used sensor design.

Appendix A

Measured inclusive cross sections of $pp \rightarrow pX$ and $pA \rightarrow pX$

TABLE II. (Continued.)

P_t		0.18 GeV/c				0.3 GeV/c				0.5 GeV/c			
		p (GeV/c)	50	80	30	40	50	60	70	80	88	30	50
$pp \rightarrow pX$				5.68 ± 0.29	6.47 ± 0.33	8.59 ± 0.40	10.10 ± 0.20	10.82 ± 0.21	11.87 ± 0.18	13.74 ± 0.28	2.93 ± 0.18	3.82 ± 0.12	4.173 ± 0.066
$pC \rightarrow pX$				43.2 ± 2.4	49.2 ± 1.2	49.9 ± 1.5	54.4 ± 2.3	61.0 ± 1.4	58.8 ± 1.2	61.66 ± 0.95	25.7 ± 1.6	29.6 ± 1.6	24.1 ± 1.0
$pAl \rightarrow pX$				76.1 ± 3.3		83.2 ± 2.8	82.9 ± 3.4	95.9 ± 4.1	87.6 ± 3.5	89.9 ± 1.6			
$pCu \rightarrow pX$				127.4 ± 5.2	133.2 ± 4.6	131.8 ± 4.3	129.0 ± 5.4	132.3 ± 3.9	137.2 ± 3.6	137.6 ± 2.9	74.6 ± 5.0	81.2 ± 5.1	53.9 ± 2.5
$pAg \rightarrow pX$				176.0 ± 8.3		175.5 ± 6.5	179.2 ± 8.5	193 ± 11	178.6 ± 6.4	171.5 ± 4.7			
$pPb \rightarrow pX$				242 ± 13	248 ± 11	228.2 ± 9.6	225 ± 11	249 ± 17	247.7 ± 7.9	217.7 ± 6.8	138 ± 11	115.1 ± 9.6	89.4 ± 5.4
σ_0 (mb)				10.11 ± 0.93	11.89 ± 0.67	13.28 ± 0.77	15.5 ± 1.2	18.2 ± 1.1	16.71 ± 0.77	19.94 ± 0.69	5.94 ± 0.80	8.8 ± 1.0	7.66 ± 0.71
α				0.605 ± 0.022	0.574 ± 0.016	0.546 ± 0.015	0.509 ± 0.020	0.487 ± 0.017	0.506 ± 0.012	0.457 ± 0.009	0.597 ± 0.034	0.501 ± 0.031	0.465 ± 0.024

Figure A.1: Capture of a invariant cross sections ($E \frac{d\sigma}{dp^3}$) table from reference [Bar83]. Measured cross sections for the inclusive processes $pp \rightarrow pX$ and $pA \rightarrow pX$ with momentum p and transversal momentum p_T of the secondary proton are listed. The data was derived with a 100 GeV proton beam on fixed targets at the Fermilab M6E beam line.

Appendix B

Parameters of the TRD prototype simulation

The following lines include the source code of the parameter list "DetectorParameterDef.icc" used for the AMS-02 TRD prototype simulation:

```
// Material Environment for Gas Mixtures
//pressure    = 0.963*bar;//1013.e+2*pascal;//mean pressure for the beam test
pressure      = 1.013*bar;//1013.e+2*pascal;
temperature   = 293.5*kelvin;//room temp. //273.5*kelvin;//STP

////////////////////////////////////
//Radiator Definitions
////////////////////////////////////
FoilDensity    = 0.91*g/cm3; //Atlas Polypropylene
RadiatorDensity = 0.06*g/cm3;
//Air density
//GasDensity    = 1.165*mg/cm3;//density as for G3
GasDensity      = 1.193*mg/cm3;
//GasDensity    = 1.236*mg/cm3;//density at 1013mbar 293.5K
//GasDensity    = 1.2928*mg/cm3;//STP

RadiatorLength = 2500.*mm; //only Initilsation value for World construction
RadiatorWidth  = 100.1*mm; //test beam 2000 // 100.8*mm; // TRD modul
RadiatorThick  = 21.*mm;

GapThick       = ((FoilDensity-RadiatorDensity)
                  /(RadiatorDensity-GasDensity))*FoilThick;
FoilGasRatio   = FoilThick/(GapThick+FoilThick);
FoilNumber     = G4int(RadiatorThick/(GapThick+FoilThick));
//extra Radiators 2000 beam test
exFoilNumber   = G4int(RadiatorThick/(3.5*(GapThick+FoilThick)));

////////////////////////////////////
//Octagon honeycomb structure (Testbeam correction, not used)
////////////////////////////////////
TestGap        = 20.*cm;
OktagonCThick  = 2.0*mm;
OktagonAlThick = 0.5*mm;
Carb1Place     = 0.0*mm;
Carb2Place     = 20.0*mm;
AlPlace        = 10.0*mm;
```

```

////////////////////////////////////
//Straw Tube Module Definitions
////////////////////////////////////
//XeCO2 density
//TubeGasDensity = 4.46*mg/cm3;//calibrated mean density for 2000 Testbeam
//TubeGasDensity = 4.58*mg/cm3;//density taken for 2000 Testbeam G3
TubeGasDensity = 4.72*mg/cm3;
//TubeGasDensity = 4.75*mg/cm3;
//TubeGasDensity = 4.78*mg/cm3;
//TubeGasDensity = 5.0818*mg/cm3;//STP

//Tube-Wall Definitions
WallThick      = 0.0724*mm;
CarbFoilRatio  = 0.012*mm/WallThick;
AluFoilRatio   = 0.0004*mm/WallThick;
KapFoilRatio   = 0.05*mm/WallThick;
UreFoilRatio   = 0.01*mm/WallThick;

//Tube-Wire Definitions
WireThick      = 0.0303*mm;
GoldRatio      = 0.03*mm/WireThick;
WolfRatio      = 0.0003*mm/WireThick;

//radiants for tube-foil layers
outWallRad     = 3.0724*mm;
inWallRad      = 3.*mm;
outGasRad      = 3.*mm; //small Gap to avoid numerical problems
inGasRad       = 0.0303*mm; //small Gap to avoid numerical problems
outWireRad     = 0.0303*mm;
inWireRad      = 0.*mm;

//
TubeLength     = RadiatorLength;
StartAngel     = 0.*deg ;
SpanningAngel  = 360.*deg ;
TubeNumber     = 16;

//-----
//Tables of tubes/stiffeners positions in one module
//-----

//beamtest 2000 Modul-Geometry (use this for beam test 2000)
//with 3mm inner diameter tubes,100.1 cm width, 3x0,3mm stiffener
//(described by Thorsten Siedenbug)
//-----

ModuleWidth    = 100.1*mm;

TubeDist[0]    = -46.95;
TubeDist[1]    = -40.75;

```

```

TubeDist[2] = -34.55;
TubeDist[3] = -28.35;

TubeDist[4] = -21.85;
TubeDist[5] = -15.65;
TubeDist[6] = -9.45;
TubeDist[7] = -3.25;

TubeDist[8] = 3.25;
TubeDist[9] = 9.45;
TubeDist[10] = 15.65;
TubeDist[11] = 21.85;

TubeDist[12] = 28.35;
TubeDist[13] = 34.55;
TubeDist[14] = 40.75;
TubeDist[15] = 46.95;

//Transvers Stiffener Definitions
//-----
TStiffNumber      = 5;
TStiffThick       = 0.6*mm;
TStiffDist        = 10*cm;
//StiffX = outWallRad+TStiffThick/2.+coating;//coating used for some tubes
TStiffX = outWallRad+TStiffThick/2.;

///Longitudinal Stiffener Definitions
//-----
LStiffNumber      = 3;

//Distances along module
LStiffDist[0]    = 25.1*mm;
LStiffDist[1]    = 0.*mm;
LStiffDist[2]    = -25.1*mm;

/*
//TRD Modul-Geometry (use this for final TRD)
//-----

ModuleWidth     = 100.8*mm;

//Tube positions
//-----
TubeDist[0]     = -47.4*mm;

TubeDist[1]     = -40.9*mm;
TubeDist[2]     = -34.7*mm;
TubeDist[3]     = -28.5*mm;

TubeDist[4]     = -22.0*mm;

```

```

TubeDist [5] = -15.8*mm;
TubeDist [6] = -9.6*mm;

TubeDist [7] = -3.1*mm;
TubeDist [8] = 3.1*mm;

TubeDist [9] = 9.6*mm;
TubeDist [10] = 15.8*mm;
TubeDist [11] = 22.0*mm;

TubeDist [12] = 28.5*mm;
TubeDist [13] = 34.7*mm;
TubeDist [14] = 40.9*mm;

TubeDist [15] = 47.4*mm;

//Transvers Stiffener Definitions
//-----
TStiffNumber = 5;
TStiffThick = 0.6*mm;
TStiffDist = 10*cm;
//StiffX = outWallRad+TStiffThick/2.+coating;
TStiffX = outWallRad+TStiffThick/2.;

//Longitudinal Stiffener Definitions
//-----
LStiffNumber = 6;

//Distance along module
LStiffDist[0] = 44.1*mm;
LStiffDist[1] = 25.2*mm;
LStiffDist[2] = 6.3*mm;
LStiffDist[3] = -6.3*mm;
LStiffDist[4] = -25.2*mm;
LStiffDist[5] = -44.1*mm;

*/

////////////////////////////////////
//general TRD Element Definitions for the Placing
////////////////////////////////////
ElementNumber = 20; //only initialisation value (changed by geometry readin)
ModuleThick = 2.*(outWallRad+TStiffThick);

//numeric safety margin for rotation is 0.001*mm
ElementThick = 28.999*mm; //RadiatorThick+ModuleThick+1.*mm;
RadPlace = (RadiatorThick-ElementThick)/2.+0.2*mm;
ModulePlace = (ElementThick-ModuleThick)/2.-0.2*mm;

```

Appendix C

Additional comparison plots between data and simulations of the TRD prototype beamtest.

C.1 Proton beam profiles inside the TRD prototype

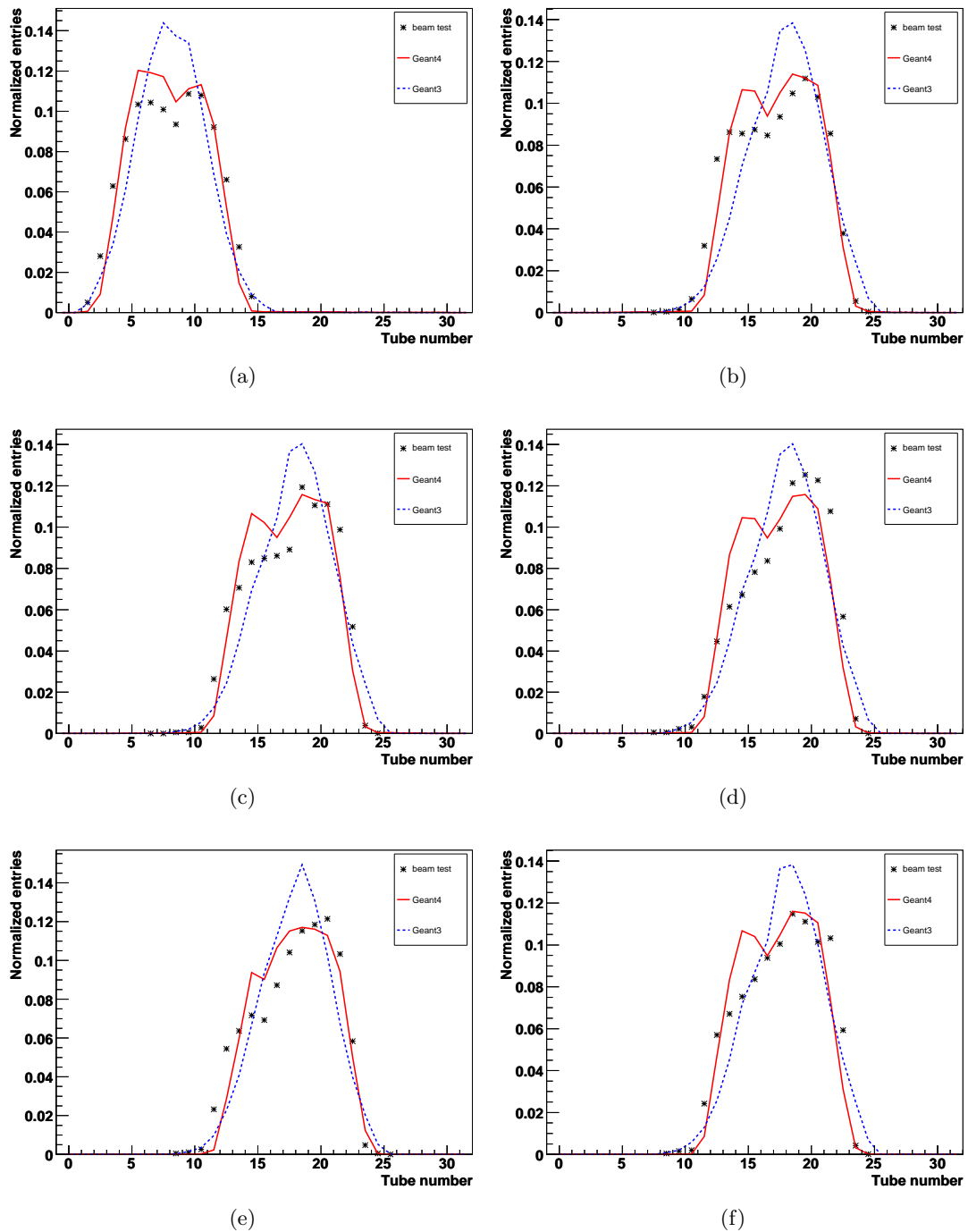


Figure C.1: Proton beam profiles inside the TRD prototype for the central layer 10 and beam energies of: (a) 20, (b) 40, (c) 60, (d) 80, (e) 100, and (f) 120 GeV.

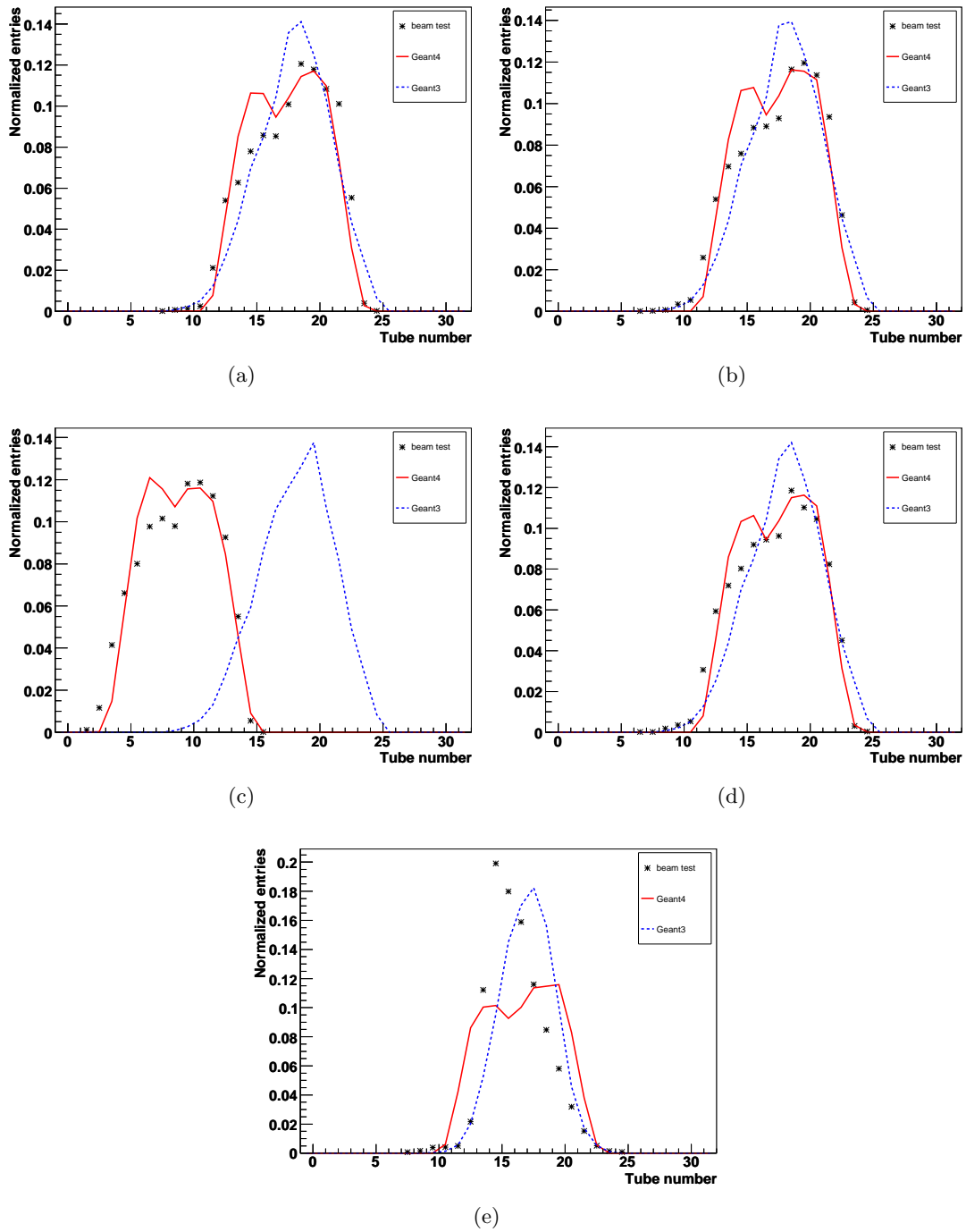


Figure C.2: Proton beam profiles inside the TRD prototype for the central layer 10 and beam energies of: (a) 140, (b) 160, (c) 180, (d) 200, and (e) 250 GeV. The quite narrow beam profile for the 250 GeV data file with a beam angle of 8.3° was not adjusted, since the file with an angle of -1.5° and a wide profile, but low statistics, gave the same result for the rejection power. The deviation of GEANT3 for 180 GeV results from a missing file for a beam angle of -1.5° , instead a beam angle of 7.5° is used.

C.2 Plots for a detector gas density of 4.72 mg/cm^3

C.2.1 Accumulated proton energy depositions in the TRD prototype

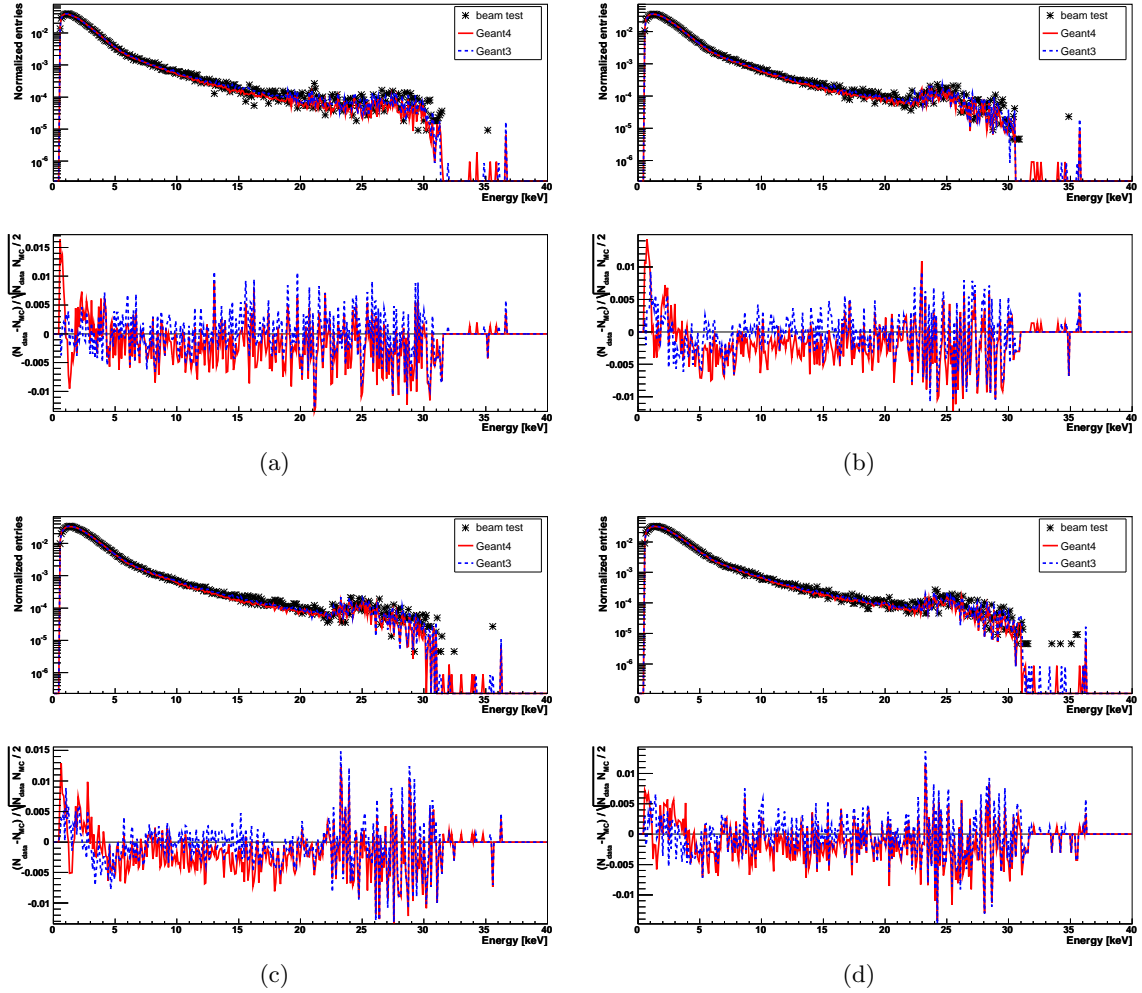


Figure C.3: (top) Energy depositions of protons accumulated for the whole detector on a logarithmic scale. (bottom) Differences between the simulations and the data. For beam energies of: (a) 20, (b) 40, (c) 60 and (d) 80 GeV.

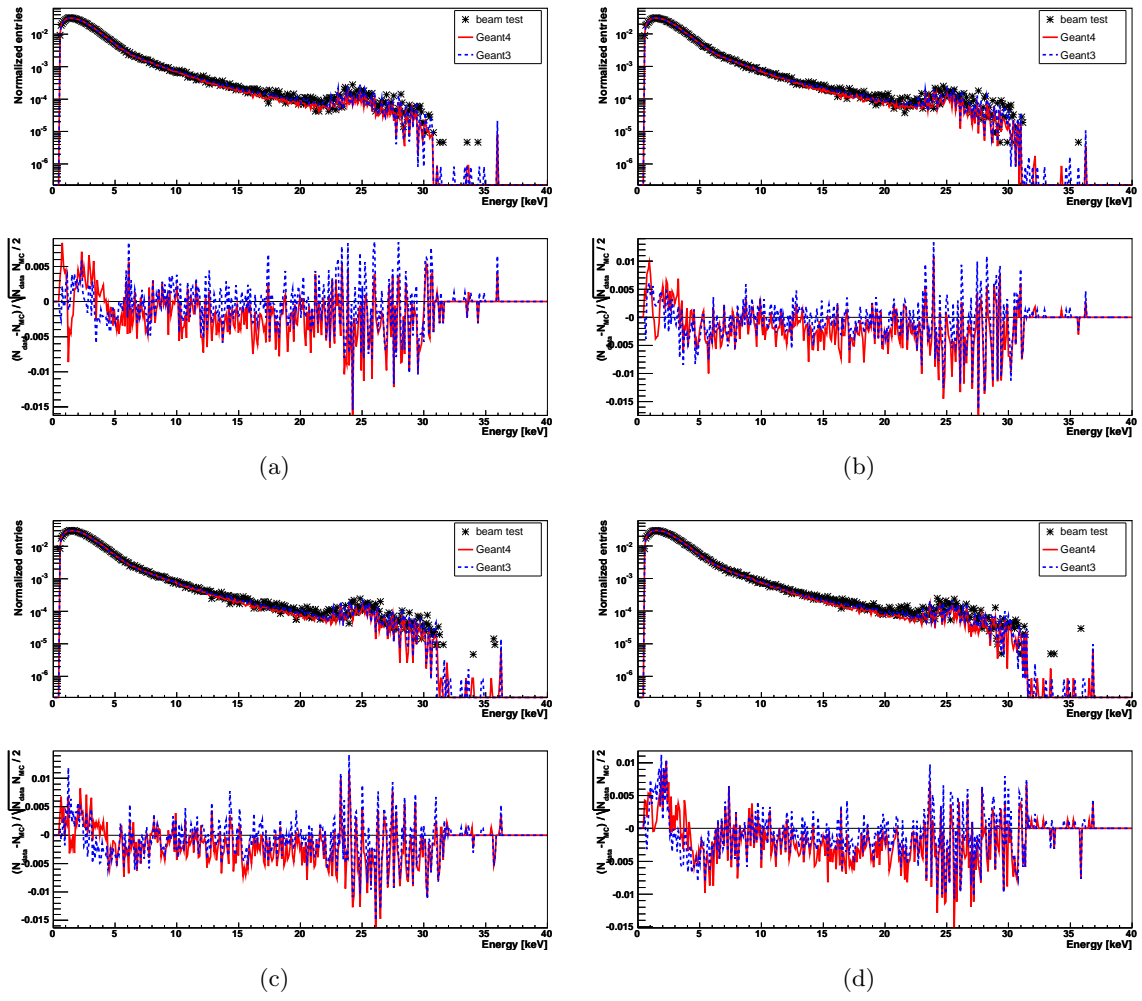


Figure C.4: (top) Energy depositions of protons accumulated for the whole detector on a logarithmic scale. (bottom) Differences between the simulations and the data. For beam energies of: (a) 100, (b) 120, (c) 140 and (d) 160 GeV.

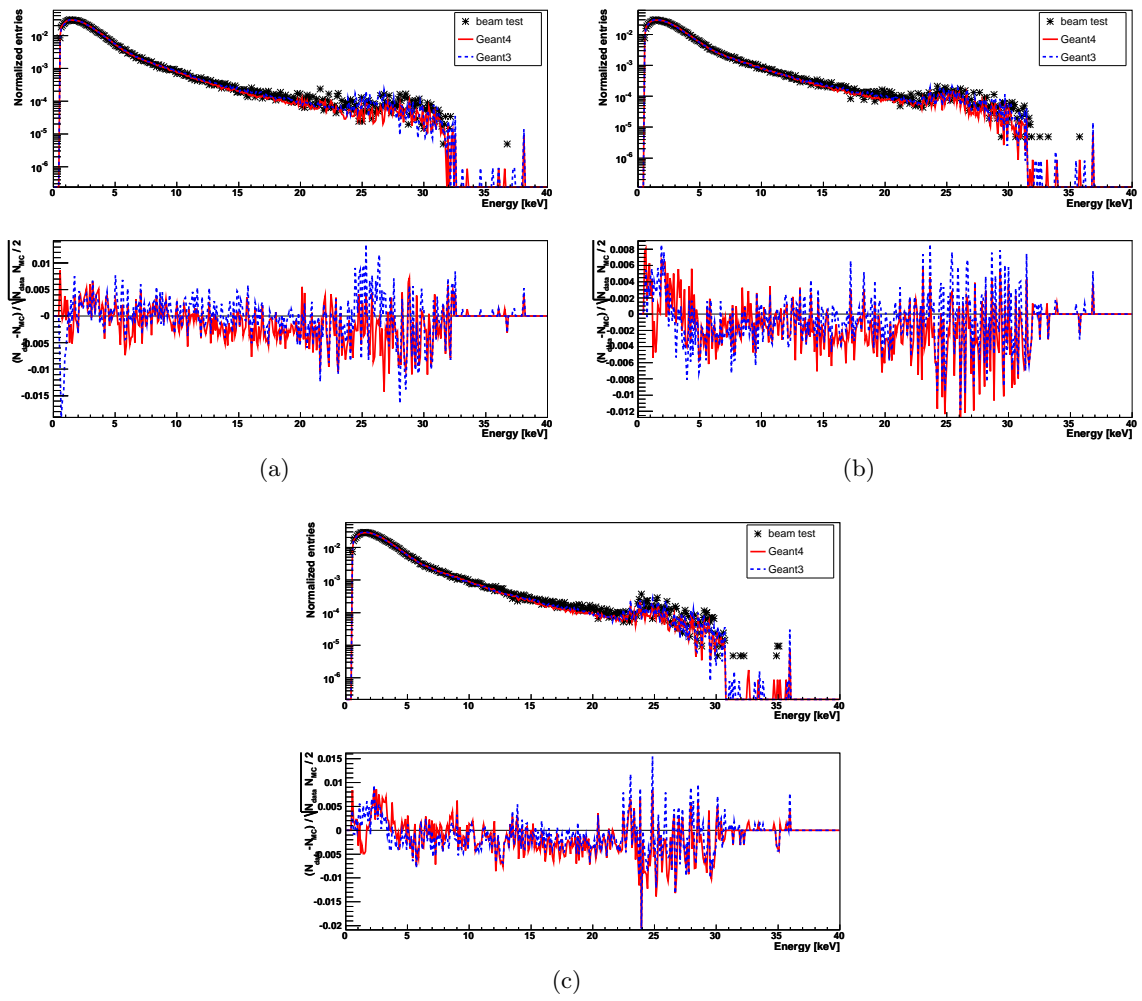


Figure C.5: (top) Energy depositions of protons accumulated for the whole detector on a logarithmic scale. (bottom) Differences between the simulations and the data. For beam energies of: (a) 180, (b) 200 and (c) 250 GeV.

C.2.2 Mop values of the accumulated proton layer distributions

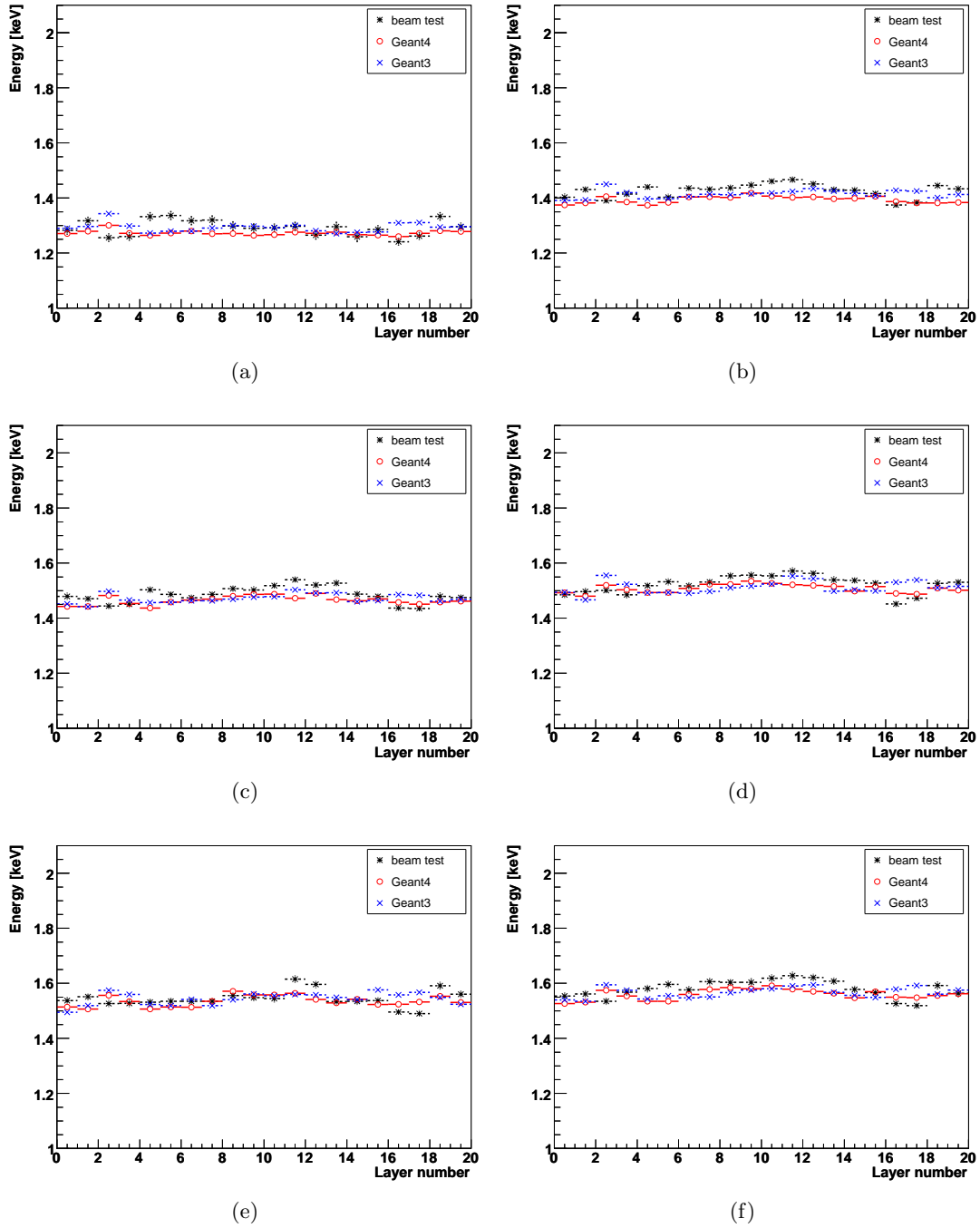


Figure C.6: Landau fit MOP values to the energy depositions accumulated for each layer and the detector (layer number 20) of protons for each prototype layer and beam energies of: (a) 20, (b) 40, (c) 60, (d) 80, (e) 100 and (f) 120 GeV.

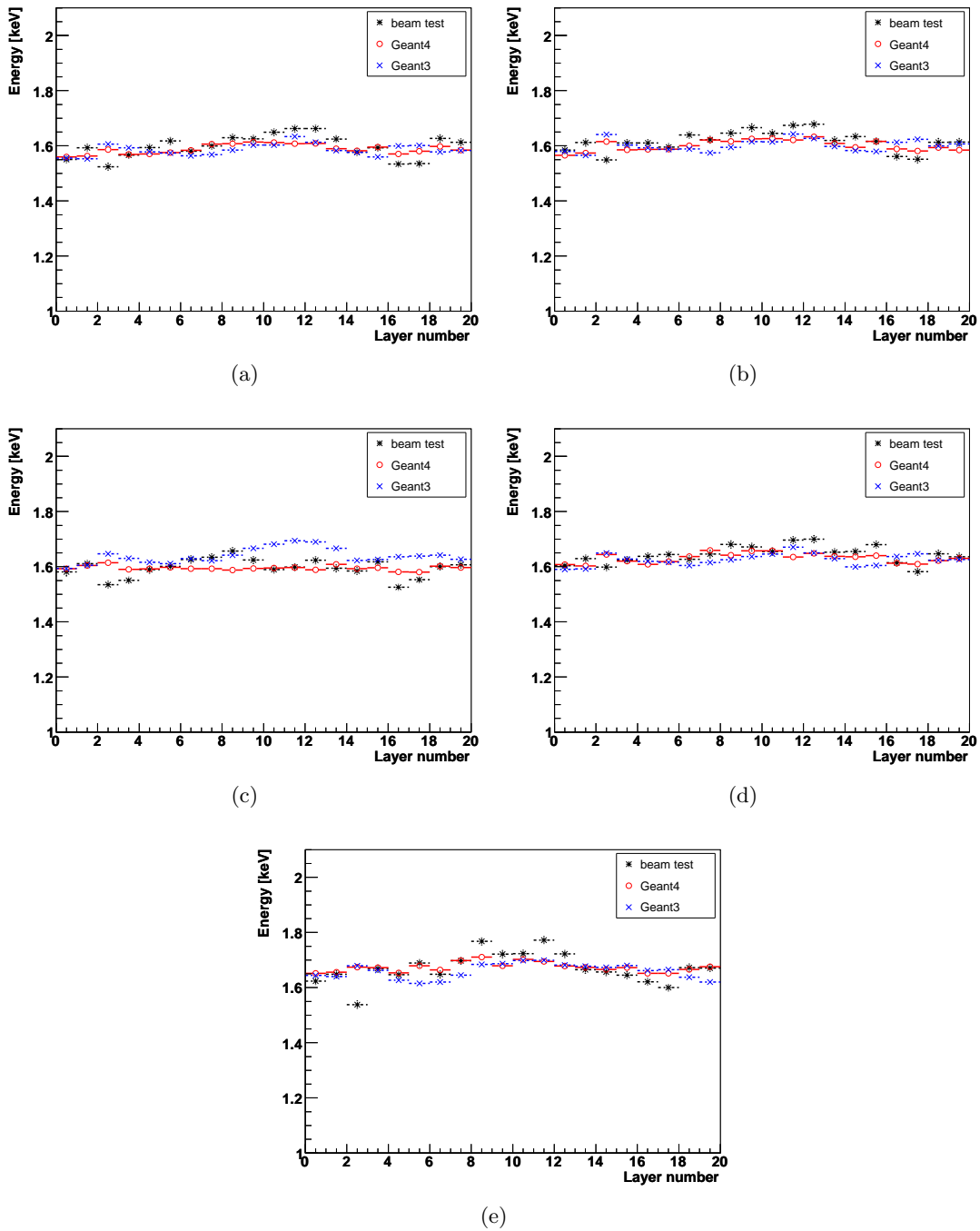


Figure C.7: Landau fit MOP values to the energy depositions accumulated for each layer and the detector (layer number 20) of protons for each prototype layer and beam energies of: (a) 140, (b) 160, (c) 180, (d) 200 and (e) 250 GeV.

C.2.3 Likelihood distributions

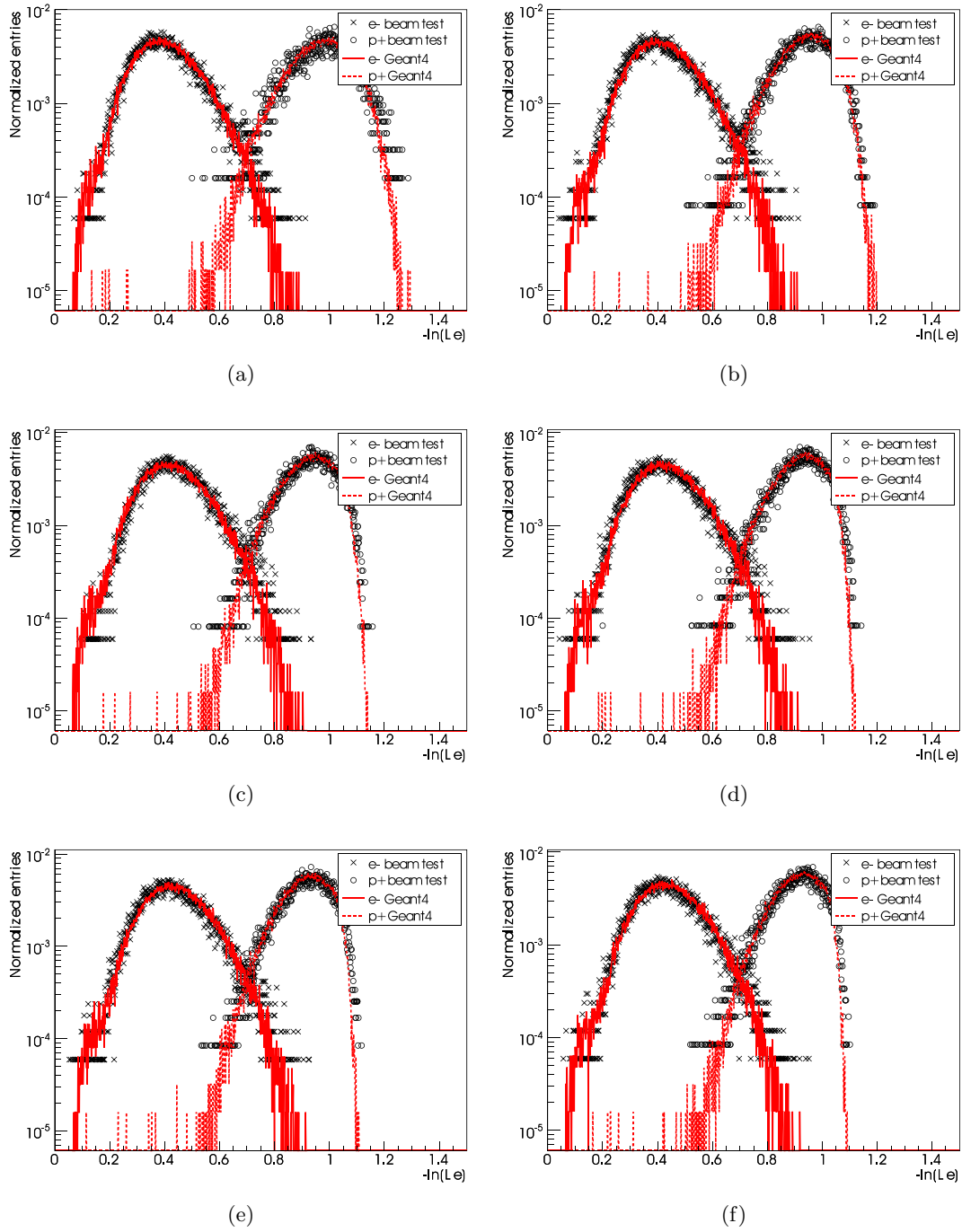


Figure C.8: Likelihood distributions for electrons of 20 GeV energy and protons of: (a) 20, (b) 40, (c) 60, (d) 80, (e) 100 and (f) 120 GeV.

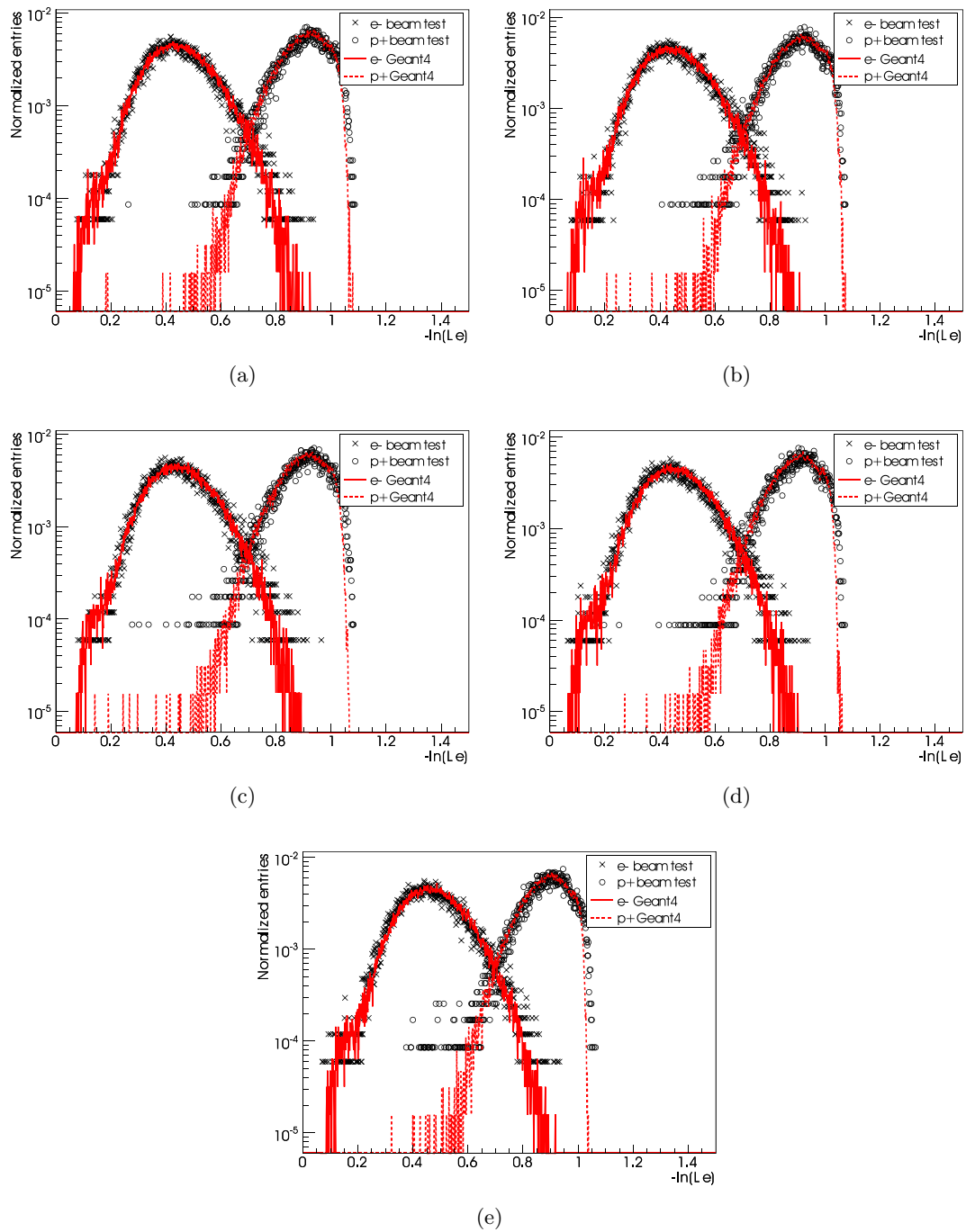


Figure C.9: Likelihood distributions for electrons of 20 GeV energy and protons of: (a) 140, (b) 160, (c) 180, (d) 200 and (e) 250 GeV.

C.3 Plots for a detector gas density of 4.78 mg/cm³

C.3.1 Accumulated proton energy depositions in the TRD prototype

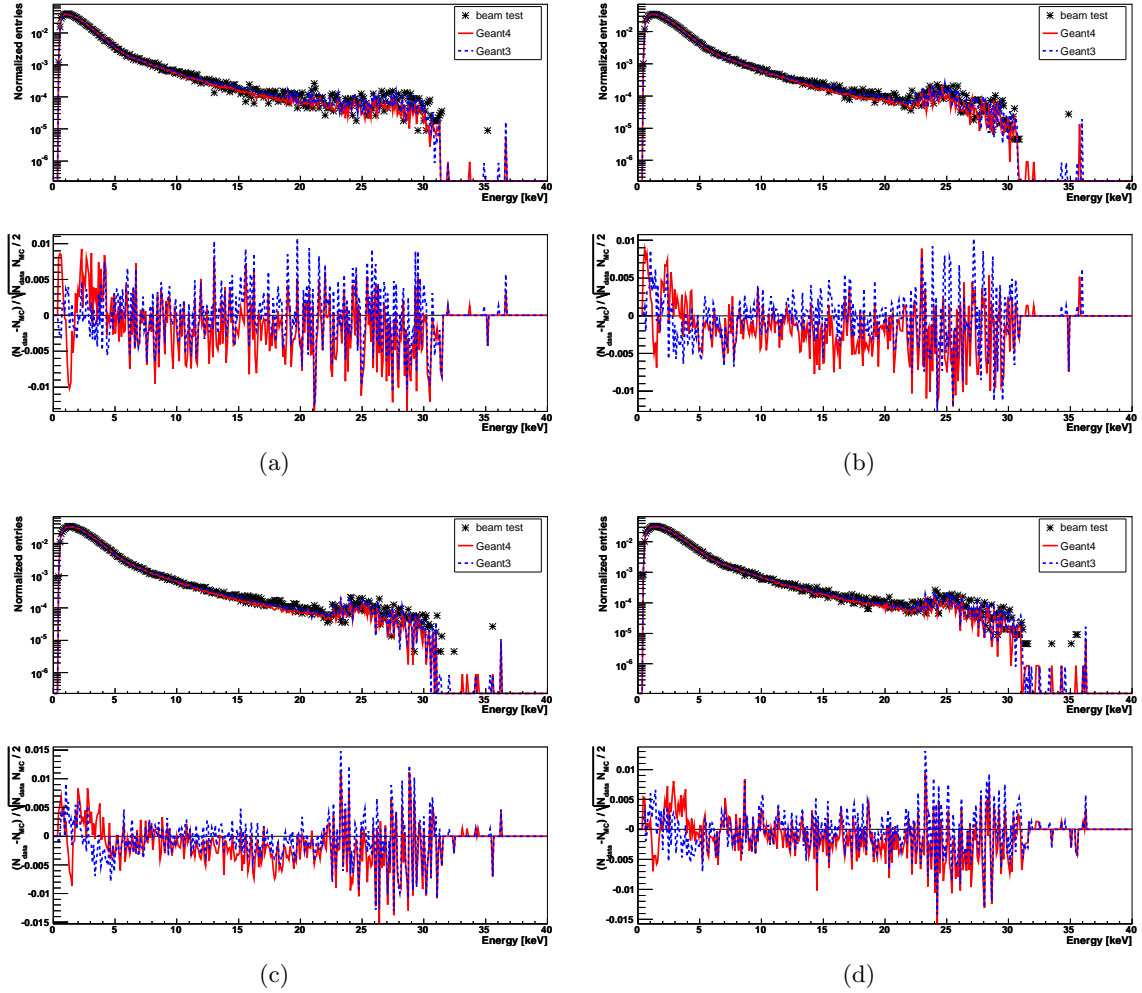


Figure C.10: (top) Energy depositions of protons accumulated for the whole detector on a logarithmic scale. (bottom) Differences between the simulations and the data. For beam energies of: (a) 20, (b) 40, (c) 60, (d) 80 GeV.

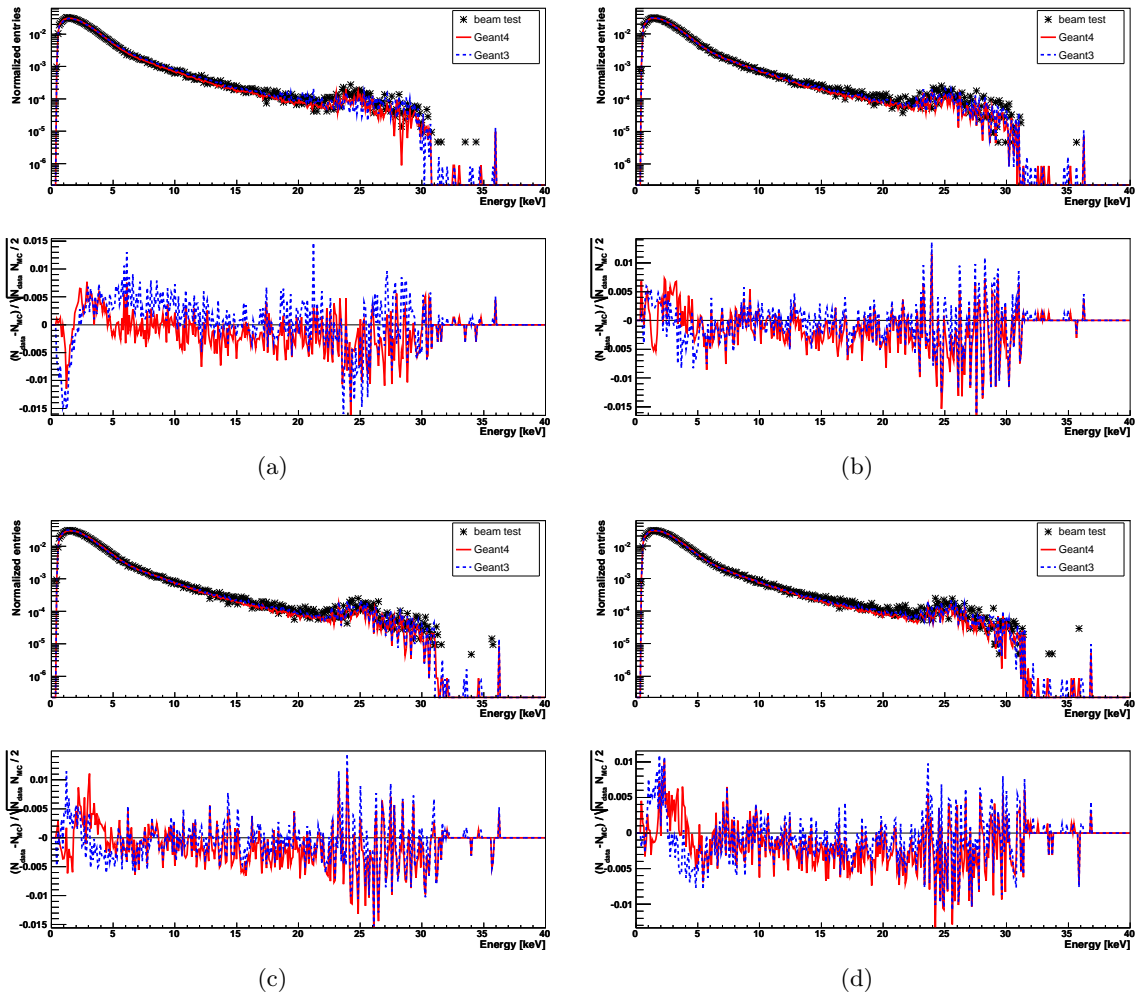


Figure C.11: (top) Energy depositions of protons accumulated for the whole detector on a logarithmic scale. (bottom) Differences between the simulations and the data. For beam energies of: (a) 100, (b) 120, (c) 140 and (d) 160 GeV.

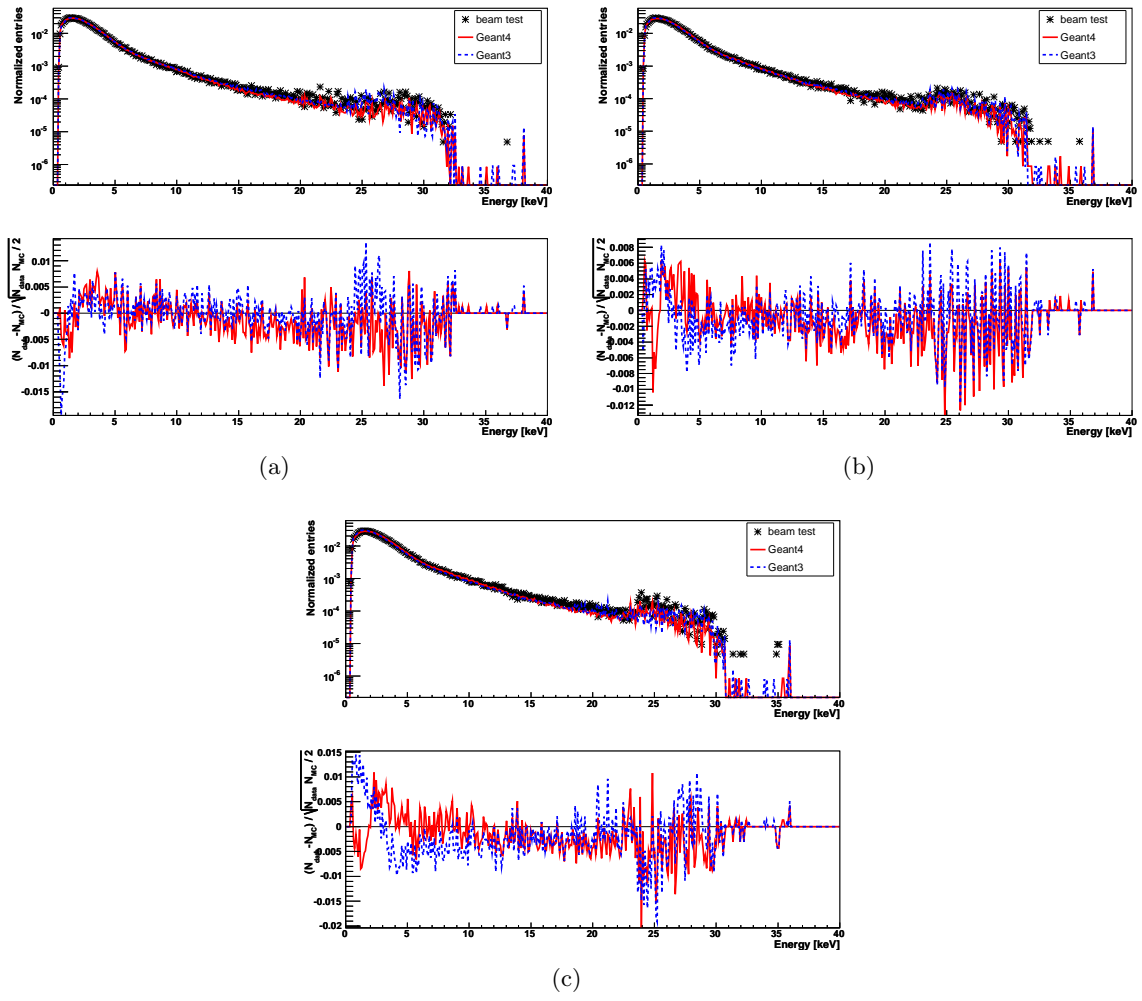


Figure C.12: (top) Energy depositions of protons accumulated for the whole detector on a logarithmic scale. (bottom) Differences between the simulations and the data. For beam energies of: (a) 180, (b) 200 and (c) 250 GeV.

C.3.2 Mop values of the accumulated proton layer distributions

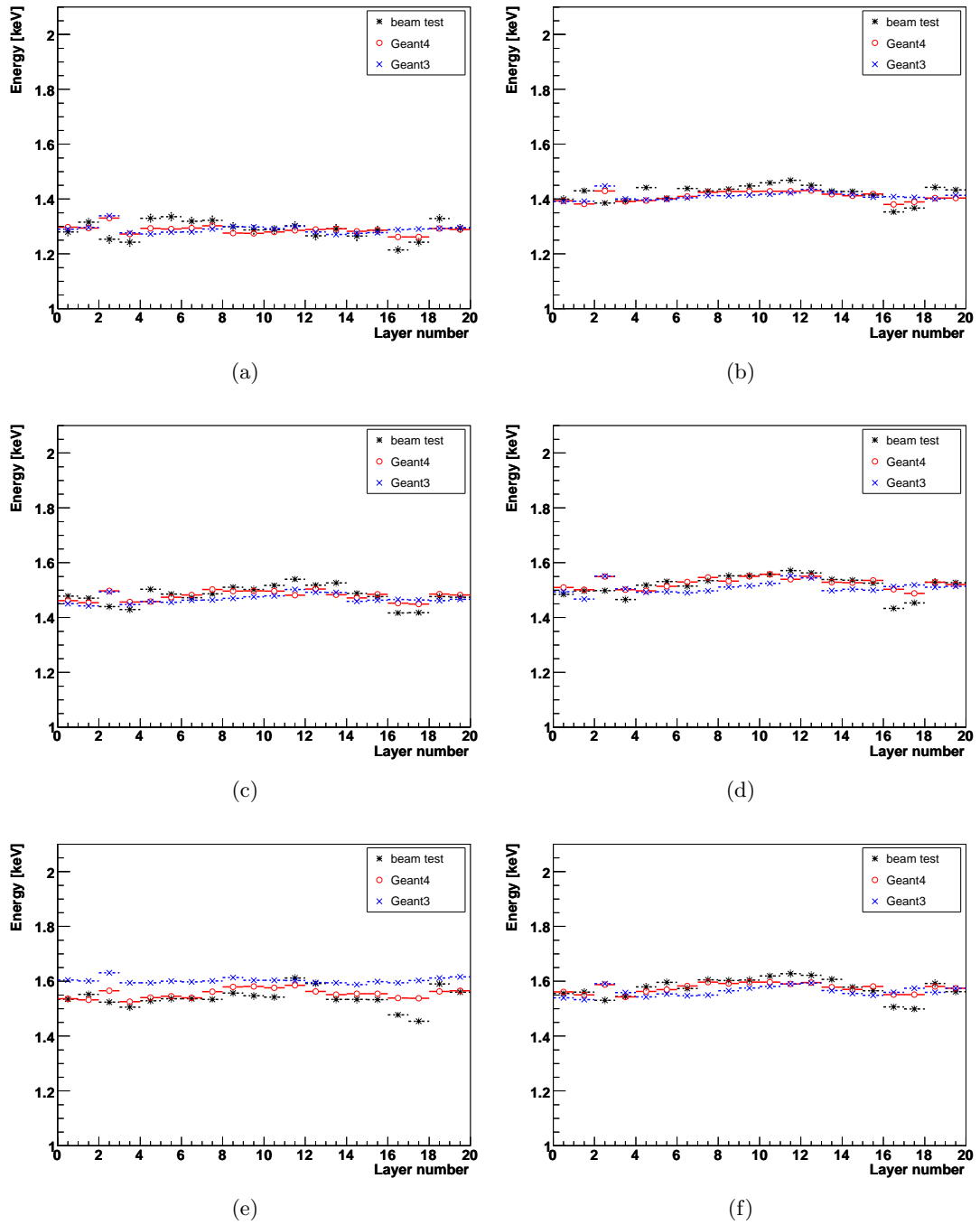


Figure C.13: Landau fit MOP values to the energy depositions accumulated for each layer and the detector (layer number 20) of protons for each prototype layer and beam energies of: (a) 20, (b) 40, (c) 60, (d) 80, (e) 100 and (f) 120 GeV.

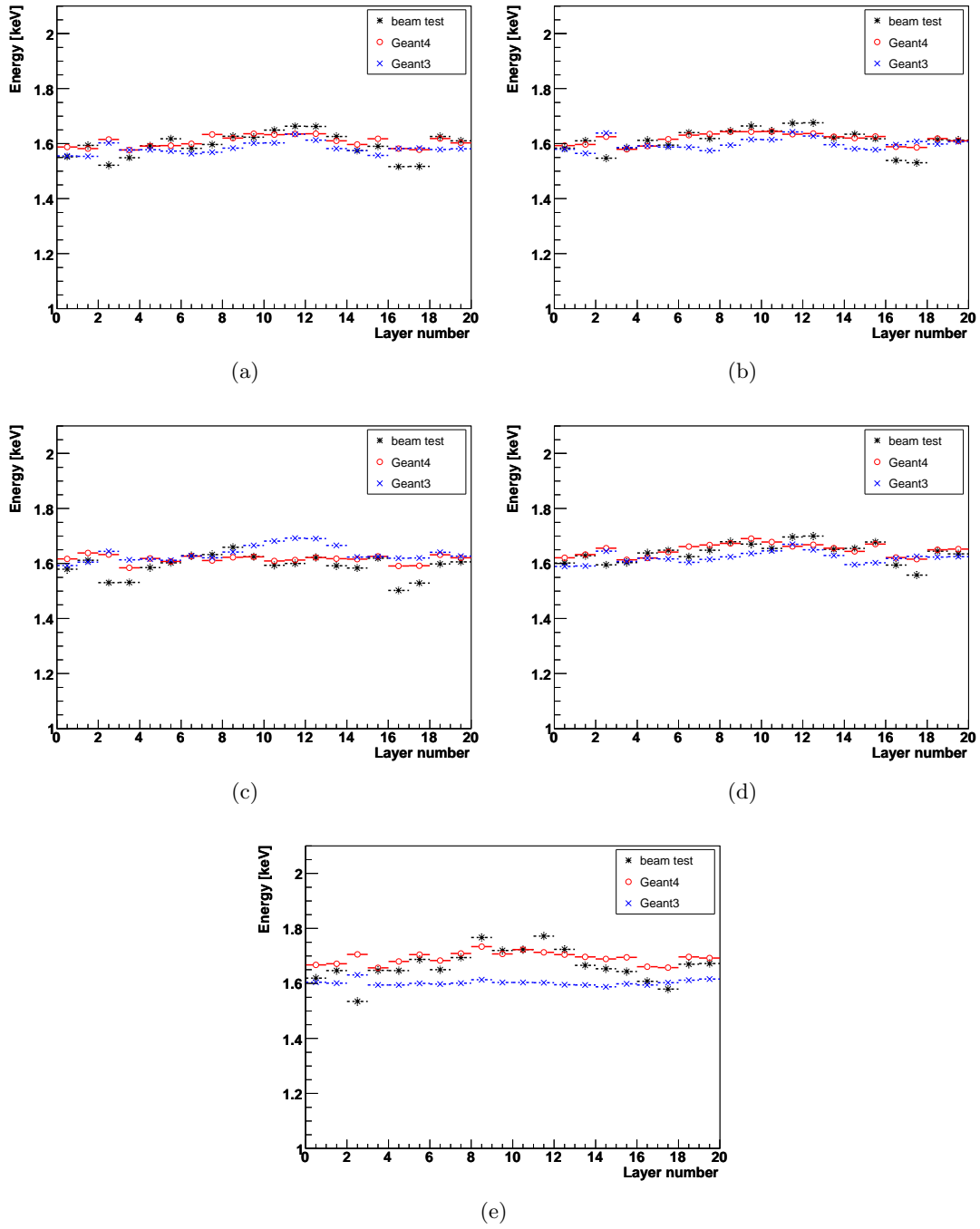


Figure C.14: Landau fit MOP values to the energy depositions accumulated for each layer and the detector (layer number 20) of protons for each prototype layer and beam energies of: (a) 140, (b) 160, (c) 180, (d) 200 and (e) 250 GeV.

C.3.3 Likelihood distributions

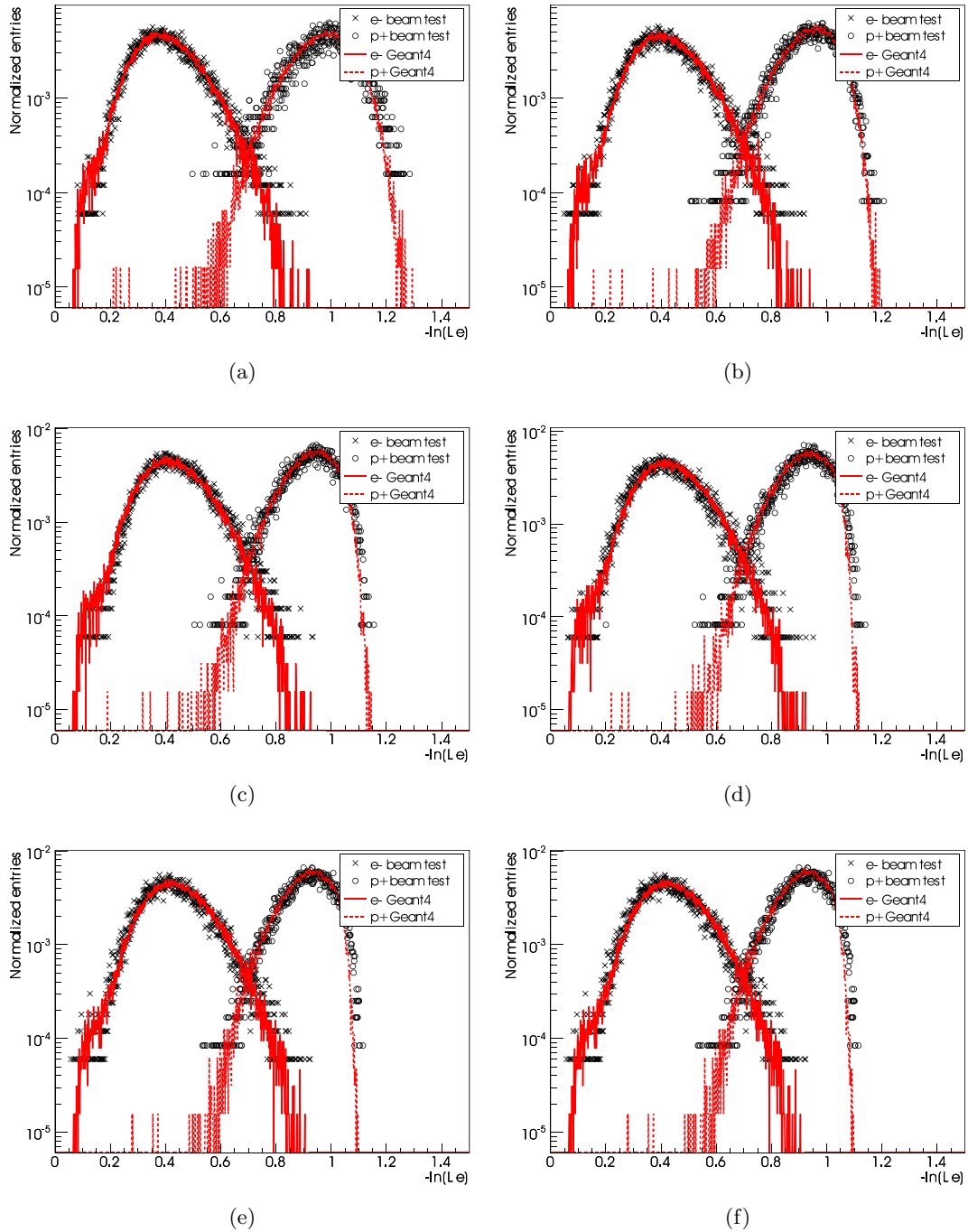


Figure C.15: Likelihood distributions of electrons with 20 GeV energy and protons with energies of: (a) 20, (b) 40, (c) 60, (d) 80, (e) 100 and (f) 120 GeV.

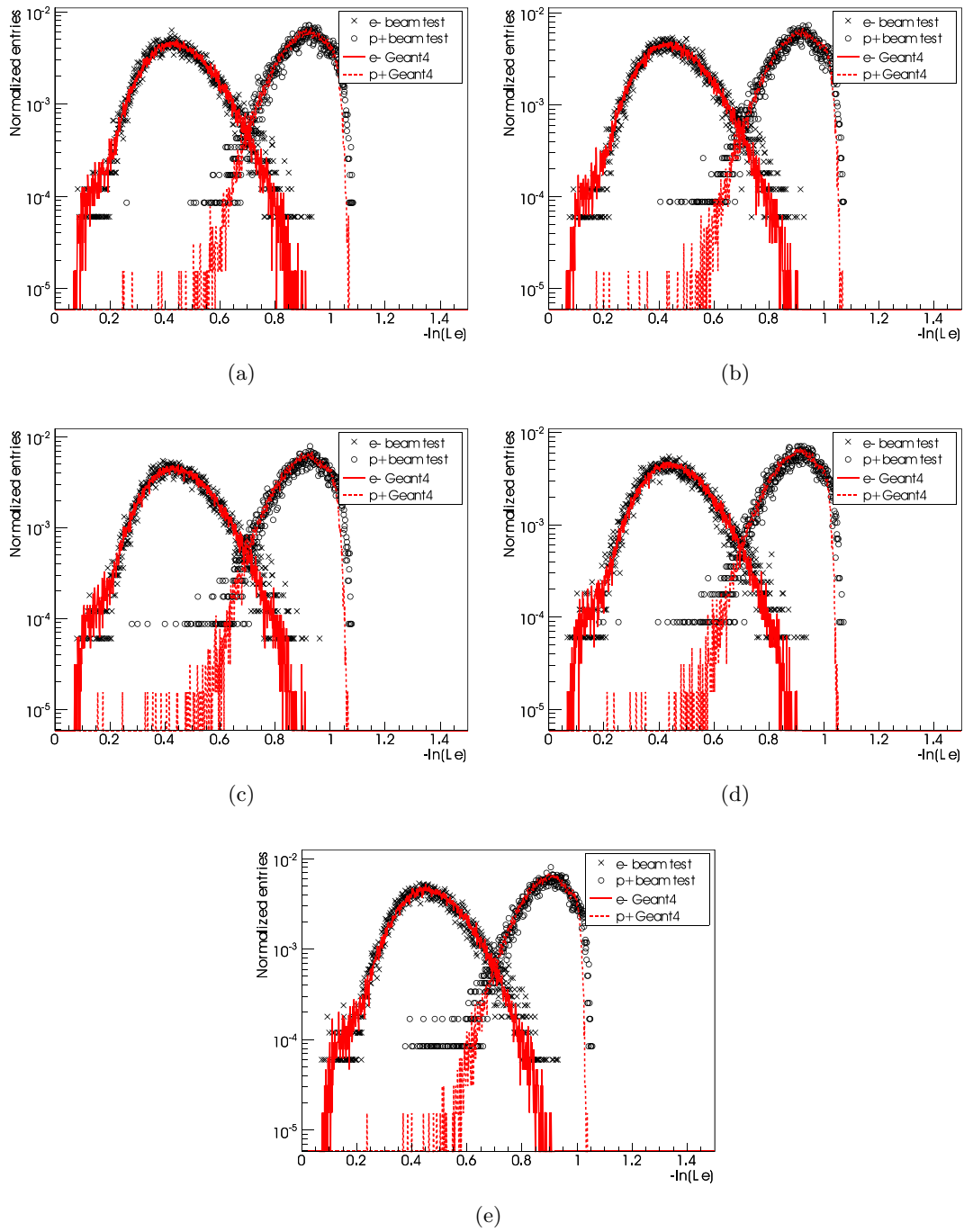


Figure C.16: Likelihood distributions of electrons with 20 GeV energy and protons with energies of: (a) 140, (b) 160, (c) 180, (d) 200 and (e) 250 GeV.

Acknowledgements

First of all I like to thank Prof. Dr. Wim de Boer for giving me the opportunity to prepare this thesis. His encouraging advice was a great help especially for the analysis of the TRD beamtest data and the simulations. For taking over the Korreferat and discussions about diffraction my thanks go to Prof. Dr. Thomas Müller.

Many thanks go to my doctorate companions Dr. Levin Jungermann, Dr. Hannes Bol, Dr. Florian Hauler and Dipl.-Phys. Andreas Sabellek. It was a pleasure to work with you for performing space qualification tests of the AMS-02 electronics or measurements with the MIMOSA-V detector.

As well, I like to thank the staff of our institute. Dr. Hans-Jürgen Simonis for keeping computers and printers running, Dr. Peter Blüm and Dr. Alexander Dierlamm for discussions about various physics topics. Tobias Barvich and Pia Steck for technical support. Herr Atz and the Azubis from the electronic workshop for their assistance in the cabling work for DC/DC-converter tests and the UPD assembly. Frau Haas, Frau Schulz and Frau Fellner for support in administrative questions. Dr. Valery Zhukov and Dipl.-Phys. Iris Gebauer for discussions about cosmic rays and AMS-02.

From the RWTH Aachen I would like to thank Prof. Dr. Klaus Lübelmeyer for performing DC/DC-converter vibrations. Dr. Thorsten Siedenburg for his assistance in recovering all necessary parameters for the beamtest analysis and simulations. Dr. Chanhoon Chung for operating the TVT-chamber for DC/DC-converter tests.

Many thanks to my family for their support in my years of education. The most grateful I am to my wife Kathrin who was always on my side. Your understanding for my overtime work and the many trips to Taiwan, CERN, Aachen or the US was a substantial contribution to this thesis.

List of Figures

1.1	A drawing of the AMS-02 experiment mounted to the International Space Station (ISS) (by Lockheed Martin).	1
2.1	The mean energy loss of particles in matter described by the Bethe Bloch formula. This plot shows the loss for muons. For other particle masses the energy scale is just shifted and the radiative loss (Bremsstrahlung) is small for heavy particles [PDG02].	6
2.2	Polarization of media by traversing charged particles with different speed.	8
2.3	Constructive interference of TR photons from two interfaces of a material layer.[Hau05]	9
2.4	Rising TR yield by cascading many material layers.[Hau05]	10
2.5	Dominating regimes of photon process dependent on their energy and the charge number of the absorber material. [Gru93]	11
2.6	Contribution of photon processes to the interaction coefficient in Xenon gas. [NIS]	11
2.7	Compton scattering of a photon on an electron [].	12
3.1	A cross section of AMS-02. It shows all subdetectors, the Unique Support Structure (USS) to mount AMS-02 to the ISS, thermal radiators, debris shields and electronic crates.	15
3.2	Projected AMS-02 limits on the $\bar{H}e/He$ ratio compared to previous measurements.	16
3.3	Projected AMS-02 measurement of the $^{10}Be/^{9}Be$ ratio.	17
3.4	Projected AMS-02 measurement of the B/C ratio.	17
3.5	The gamma ray excess measured by EGRET. It can be explained by adding a signal of DMA and fitting the complete output between 0.1 GeV and 0.5 GeV to the data [dBSZ+05].	19
3.6	Halo profile in the xy-plane of the galactic disc [dBSZ+05].	20
3.7	Halo profile in the xz-plane of the galactic disc [dBSZ+05].	20
3.8	Rotation velocity with contributions from the inner and outer DM ring [dBSZ+05].	20
3.9	Simulated \bar{p} flux with DMA contribution for isotropic and anisotropic propagation compared to data [dB08].	21
3.10	Simulated $e^+/e^+ + e^-$ fraction with DMA contribution for anisotropic propagation and averaged data.[dB08].	21
3.11	AMS-02 and the detectable particle signatures with its subdetectors.	22
3.12	Drawing of the Time Of Flight detector.	23
3.13	Drawing of the Time Of Flight detector paddle.	23
3.14	Time resolution of the TOF (in [ns]) taken with two counters during a beamtest in 2003.	23
3.15	Combined charge measurement of TOF and RICH taken with a beamtest in 2002.	23
3.16	Drawing of the ACC. The light is guided in fibers to PMTs on the vacuum case [Doe07].	24
3.17	One of the 16 ACC scintillator panels with grooves for wavelength shifting fibers.	24

3.18	Drawing of the TRD. The TRD is supported by an M shaped structure. Inside it carries 328 sandwiches of straw modules and fleece radiator.	25
3.19	(a) Short prototype straw tube module. (b) Sandwich of fleece radiators and straw modules. The TRD layers show alternating shifts.	25
3.20	Cross section of the straw tube walls.	25
3.21	The TRD octagon support structure during module assembly. The large amount of module slots in the walls is still visible.	26
3.22	TRD gas supply system. Box S consists of a Xenon and a CO_2 vessel. Vessel D is on the back and cannot be seen.	26
3.23	Tracker layer 2 completely equipped with ladders. A ladder is composed of double-sided silicon strip sensors	27
3.24	Tracker rigidity resolution for protons and helium [Bat02].	27
3.25	Drawing of the Tracker Thermal Control System (TTCS). Thermal bars conduct heat from the readout hybrids to evaporator rings, where some CO_2 evaporates. The liquid/vapure mixture is pumped to the wake and ram radiator to be cooled below the boiling point.	28
3.26	Tracker laser Alignment System. (a) TAS components in the M-Crate. (b)The laser beams are injected on the upper and lower Tracker plate by two times five beamport boxes. (c) Micrograph of Anti Reflex (AR) area.	29
3.27	AMS-02 superconducting magnet together with the helium tank inside the vacuum case.	30
3.28	Field configuration of the AMS-02 magnet.	30
3.29	Cross-section of a magnet coil.	30
3.30	Mechanics of the magnet supporting straps.	30
3.31	Schematic drawing of the phase separation done by the porous plug. [NAS05] .	31
3.32	Drawing of the RICH detector.	31
3.33	Velocity resolution of the RICH.	31
3.34	Cherenkov rings plotted for single $A/Z=2$ ion events.	32
3.35	Charge distribution for $Z > 1$ measured during a beamtest in 2002 with a $n=1.03$ radiator.	32
3.36	Mechanical layout of the ECAL. The active detector is labeled pancake. PMTs are mounted to the side panels. ECAL is fixed to the USS with corner brackets	33
3.37	Energy resolution of the ECAL. The resolution is parameterized by the formula given in the plot.	33
3.38	ECAL longitudinal shower profiles for 6 GeV and 180 GeV electrons.	33
3.39	One edge of three ECAL layers. Red dots are out coming fibers.	34
3.40	Light collection system of the ECAL. A magnetic shielding covers the light guides, the HV divider and the front end electronics.	34
3.41	AST, AMICA Star Tracker system. (a) AST optics. (b) AST support and readout structure. (c) AST position on AMS-02.	35
4.1	AMS-02 DAQ structure. First the detector data is reduced in xDR nodes and then gather and buffered by JINFs in the subdetector crates. On request it is send send to JINJ and from there to the JMDC. It least the data is linked to the HRDL and from there via RS422 to the ISS data infrastructure. All links are bidirectional. [AMS09]	37

4.2	Slow control commands are transmitted on two different paths. The TOF, TRD, Tracker, ECAL, RICH subdetectors receive LeCroy commands by AMSWire links, all other subsystems are controlled via CAN-Bus. [AMS09]	38
4.3	The Common Digital Part consists of an Analog Device Digital Signal Processor (ADSP), a flash memory, an SRAM, LVDS driver/receiver and a Field Programmable Gate Array (FPGA).	40
4.4	Schematic drawing of the TRD DAQ system. The system consists of front end electronics, two U-Crates and two UPD-Boxes. The front end electronics are mounted to the detector, close to groups of always four straw modules. A U-Crate and a UPD-Box build a fully functional readout set. One of the two sets is mounted to the wake the other one on the ram radiator.	42
4.5	Photo of the UTE mounted to the end of a straw module.	43
4.6	Photo of the UHVD board.	43
4.7	Picture of the UFE.	43
4.8	Scheme of the TRD front end electronics.	43
4.9	Readout sequence defined for the UFE boards.	44
4.10	Board placement on the UBPv2.	45
4.11	Top view on the UBPv2.	45
4.12	Power taps and slow control connector on bottom of the UBPv2.	45
4.13	Front side of a JINFv2 board. Two CDDCs feature a two fold redundancy.	46
4.14	Front side of a UDR2 board. Two CDPs feature a two fold redundancy.	47
4.15	Front side of a UPSFEv2 board. The board houses two times 7 linear regulators and two Actel FPGAs on the front and back side to achieves a two fold redundancy.	48
4.16	Front side of a UHVG board. The board houses two times 7 linear Cockcroft Walton high voltage elevators controlled by LeCroy MHV100 chips to feature a two fold redundancy.	49
4.17	Board placing inside the UPD-Box.	50
4.18	Power connection scheme between the UPD-Box and the U-Crate.	50
4.19	Photo of the UPD box. Visible is the right main wall with the 28 V supply and the HV as well as digital 3.3 V output connectors.	51
4.20	Top view of an open UPD box. Visible are the four terminal blocks in the center, all input and output connectors and the huge amount of cabling.	51
4.21	Block diagram of the S9056 DC/DC-converter. The diagram of other converters only differ in the part from the secondary transformer up to the outputs [CAE03].	52
4.22	Top view of a S9053U DC/DC-converter on its I-Frame. All cabling to the output connectors and the terminal blocks is shown.	53
4.23	Top view of a S9048 DC/DC-converter on its I-Frame. All cabling to the output connectors and the terminal blocks is shown.	54
4.24	Top view of a S9056 DC/DC-converter on its I-Frame All cabling to the output connectors and the terminal blocks is shown.	55
4.25	Top view of a S9011AU control board on its I-Frame. Visible are the DC/DC-converter control connections on the I-Frame, the two LeCroy connections on the panel and the voltage supply wires to the terminal blocks.	55
4.26	Top view of a S9011B filter board on its I-Frame. All cabling to the input connectors and the terminal blocks is shown.	56
4.27	Conducted susceptibility of the S9011B filter [CAE04].	57
4.28	Conducted emission of the S9011B and the required limits [CAE04].	57
4.29	Qualification/acceptance procedure for the board level production. [Hau05]	57

4.30	Plot of the thermal-cycling profile for the board level tests. Right corner: Photo of boards inside the temperature chamber. [Hau05]	58
4.31	Plot of the ESS temperature profile. [Hau05]	59
4.32	Vibration test of a QM1 DC/DC-converter at the RWTH Aachen.	60
4.33	Random vibration spectrum used for vibration tests.	60
4.34	Plot of the TVT temperature profile. [Hau05]	61
4.35	Photo of the QM1 test backplane including a feature description. [Hau05]	62
4.36	Schematic of the digital SSF test circuit. A microcontroller sends sequences to a digital potentiometer, that defines the current through a MAX890L current limiter.	63
4.37	Plot of the Solid State Fuse (SSF) tests current versus time. After the SSF is disabled the current drops to zero.	63
4.38	Photo of the UPSFE test backplane including a feature description. [Hau05]	64
4.39	Variable load circuit on the UPSFE test backplane. It consists of MAX980L MOSFETs, a digital potentiometer and optocouplers.	64
4.40	Photo of the variable load system for DC/DC-converter test including a component description.	65
4.41	Schematic of the control circuit inside the control box.	66
4.42	Schematic of the variable load circuit. A triple Darlington circuit with a high power transistor as last stage operates as load for a DC/DC-converter.	66
4.43	Overview of the TRD Test Environment. This software controlled the test devices and log the data of most electrical tests performed for the TRD QM2 and FM/FS board production.	67
4.44	TRD Test Environment settings tab.	68
4.45	TRD Test Environment current monitor tab.	68
4.46	TRD Test Environment voltage monitor tab.	69
4.47	TRD Test Environment digital SSF test tab.	69
4.48	TRD Test Environment UPSFE regulator SSF test tab.	70
4.49	TRD Test Environment DC/DC-converter test tab.	70
4.50	Photo of three resistor chains used for manual efficiency measurements of the DC/DC-converters.	71
4.51	Bad component on UDR2 93005 during production. The component failed visual inspection and was replaced before board level functional tests.	73
4.52	DSP solder problem on UDR2 93005, 93006 and 93009 during production. The problem was hard to detect since normally the area is covered by the DSP.	73
4.53	Efficiency curves for each tested FM/FS DC/DC-converter type with nominal efficiencies measured during ESS. The S9054, S9053, S9055 belong to the TRD Gas System and the Tracker. The ESS of the S9053 was done separate from the UPD production one.	76
5.1	Beamtest setup and trigger logic used at the X7 beamline. [Orb03]	79
5.2	Photo of the 20-layer TRD prototype. [Orb03]	80
5.3	(a) Gain linearity of the VA32HDR2 used for the prototype. (b) Gain linearity of the VA32HDR12 used for the final TRD. [Orb03]	81
5.4	Pedestal width distribution of all 640 channels. [Orb03]	82
5.5	Overlay of the accumulated energy deposition distribution for e^- and p . All single track event hits of a sample are accumulated in one histogram. [Orb03]	82

5.6	Likelihood distributions, for 20 GeV electrons and 160 GeV proton samples. [Orb03]	83
5.7	(a) Rejections factors versus p^+ energies by 3 methods: cluster counting (blank stars), geometric mean (Def.I) and arithmetic mean (Def.II) likelihoods.(b) Comparison of likelihood rejections versus p^+ energies derived with the X7- and H6-beamline data. [Orb03].	84
5.8	(a) Rejection factors versus the p^+ energies for the data and the GEANT3 MC gained by different methods and electrons energies of 20 GeV and 40 GeV. (b) Likelihood rejections factors versus p^+ energies above 100 GeV for the X7 data, the original (MC) and the adjusted GEANT3 MC (MC2). Inserted are the likelihood distributions for Def. I. [Orb03]	85
5.9	Feynman graphs for coherent single and double diffraction. (a) Target single diffraction, (b) projectile single diffraction, (c) double diffraction. [Sch83] . . .	86
5.10	The parameterization of the most important Regge trajectories: pion (π), reggeon (\mathbb{R}) and pomeron (\mathbb{P}). [Bor05]	87
5.11	Measured total SD cross section in pp and $\bar{p}p$ scattering as function of \sqrt{s} compared to standard (dashed) and renormalized predictions from Regge theory. [Bor05]	87
5.12	(a) Coherent diffraction cross section of protons and neutrons on nuclei versus the atomic number A . Data points: $n + A \rightarrow p + \pi^- + A$ (stars), emulsion targets (triangles), $A = 4$ (4He)(circle), theoretical prediction for 4He (broken line). [FGS00] (b) Double diffraction cross section measured by UA5 compared to the cross section used by the MC particle event generators PYTHIA and PHOJET. [FS04]	88
5.13	Drawing of the TRD prototype geometry and one of the front scintillators as it is used inside the GEANT4 simulation. This drawing was generated for detector to beam angle of 7.5°	89
5.14	Data and simulation (G3,G4) beam profiles inside the first (a) and the last (b) prototype layer for proton energies of 200 GeV and a detector to beam angle of 7.5°	90
5.15	(top) Data and simulation energy depositions of 160 GeV protons accumulated for the whole prototype. (bottom) Differences between the simulations and the data.	91
5.16	Data and simulation MOP values of a Landau fit to the accumulated layer energy depositions of protons. They are plotted for a GEANT4 Xe/CO ₂ density of 4.78 mg/cm ³ and 20 GeV (a) as well as 250 GeV (b) (slightly overestimated) protons, and for a density of 4.72 mg/cm ³ and 20 GeV (c) (slightly underestimated) as well as 250 GeV (d).	92
5.17	Data and simulation (G3,G4) total event energy depositions on track (a) and hit number on track per event (b) for 80 GeV protons.	93
5.18	(top) Data and simulation energy deposition of 20 GeV electrons accumulated for the whole prototype. (bottom) Differences between the simulations and the data.	94
5.19	(top) Data and simulation (G3,G4) energy depositions of 20 GeV electrons accumulated for the first (a) and the last layer (b). (bottom) Differences between the simulation and the data.	95
5.20	Data and GEANT4 simulation likelihood distributions for 20 GeV electrons and 20 GeV protons (a) as well as 250 GeV protons (b).	99

5.21	Energy dependence of the rejections factors for the data the standard and adjusted GEANT3 simulation and the GENAT4 simulation. The different plots are derived for the GEANT4 hadron physics approaches: (a) no hadron physics, (b) LHEP, (c) QGSC and (d) FTFP.	100
5.22	Energy dependence of the selection efficiencies for the data the standard and adjusted GEANT3 simulation and the GEANT4 simulation. The different plots are derived for the GEANT4 hadron physics approaches: (a) no hadron physics, (b) LHEP, (c) QGSC and (d) FTFP.	101
5.23	TR-cluster count distribution of 20 GeV electrons for a TR-cluster cut of 6.5 keV on the energy depositions on track.	104
5.24	Expectations of a Poisson fit to the cluster count distribution of protons for all tested beam energies and TR-cluster cut of 6.5 keV.	104
5.25	Selected TRD prototype backgrounds from a PHYTIA diffraction with a TR-cluster cut of 5 and 6. They are compared to the ones needed to describe the rejection power deviation between the data and a GEANT4 simulation without hadronic physics (a) and with FTFP physics (b).	105
5.26	Multiplicity distribution of a certain particle inside the selected diffractive PHYTIA events. Particle ID: 1= p , 2= π^+/π^- , 3= γ , 4= e^-/e^+ , 5= μ^-/μ^+	106
5.27	Energy distribution of all on track pions inside the selected diffractive PHYTIA events with a primary proton energy of 250 GeV.	106
6.1	Schematic drawing of a CMOS pixel read out. M1 is the reset transistor, M2 one part of the source follower of the amplifier and M3 the select switch. [Dep04]	108
6.2	Schematic cross-section through of a CMOS pixel with the electronics (top), the collecting diode (top and middle), the epitaxial layer (middle) and the substrate (bottom). [Dul05]	108
6.3	(a) Picture of a MIMOSA-V detector. [Jun05] (b) Sensor electronics schematic depicting the sub-matrices and the analog and digital read out parts. [Dep04]	109
6.4	Illustrations of the back-thinning process used on the MIMOSA-V. (a) The CMOS pixel sensor in its standard configuration. (b)The process of smoothing the surface, glueing the handle wafer, removing of the bulk material and drilling access holes to the bond pads. (c) The resulting CMOS sensor with a very thin dead layer. [Jun05]	111
6.5	(a) A cross-section of a n-MOS transistor, with a positive gate voltage applied. (b) The band structure in the MOS contact for a positive gate voltage. It illustrates the hole capturing in the Si-SiO ₂ interface. Taken from reflavin . . .	113
7.1	The SUCIMA Imager card houses a FPGA that reads analog data via 4 ADCs, generates the digital signals for the sensor and has a USB interface chip for data transmission to and communication with a PC.	116
7.2	The repeater for the SUCIMA Imager. On the top and left side it has two connectors for fast analogue and digital signals, at the bottom a ribbon cable to connect the hybrid and on the right the power input. The digital control signals and the power lines are connected by interconnection pins.	117
7.3	The MIMOSA-V hybrid with a back-thinned sensor mounted on top.	118

7.4	The frontpanel of the MIMOSA-V DAQ software with displays for the recorded Hitmap (integrated clusters), the Eventmap (single event hits), the actual noise and further frame dependent images. On the lower left can be entered some often adjusted data reduction settings, while on top a part of the analysis algorithms can be switch on/off, the data size and file path can be set and the initialization of analysis and sensors setting as well the pedestal and the noise can be performed.	119
7.5	The settings panel of the MIMOSA-V DAQ software. The different applicable settings are ordered on separate tabs reflecting their functionality.	120
8.1	Experimental setup used for the low activity measurements with the back-thinned MIMOSA-V.	125
8.2	Illustration of the 3H and the ^{14}C β -spectra with marked endpoint energies.	126
8.3	Illustration of a protein chip production flow and a detected image, including the substrate and pixel dimensions. [ZKC ⁺ 00]	128
8.4	Off line analysis image of 3H dots with 8 nCi/mg (a) and 489.1 nCi/mg (b) and sizes of $\sim 6 \times 4$ mm ² as well as of ^{14}C dots with 18 nCi/mg (c) and 220 nCi/mg (d) and sizes of $\sim 6 \times 5$ mm ² .	129
8.5	Images of 3H dots with 8 nCi/mg (a) and 489.1 nCi/mg (b) and sizes of $\sim 6 \times 4$ mm ² as well as of ^{14}C dots with 18 nCi/mg (c) and 220 nCi/mg (d) and sizes of $\sim 6 \times 5$ mm ² captured from the DAQ software display.	130
8.6	Images of RPA506 and RPA507 standards with activities from 0.48 nCi/mg to 109.4 nCi/mg recorded at 4°C. [Cac07]	131
8.7	(a) Measured tritium and ^{14}C energy spectra of the standard dots, derived by the off line analysis of threshold scan reduced data. (b) The same spectra on logarithmic scale including a fit extrapolation to the end points (Fermi plot).	131
8.8	Image of a 489.1 nCi/mg tritium dot with a source to sensors distance of 620 μ m (a) and 1250 μ m (b).	132
8.9	Tritium labeled slices of a mouse brain recorded with a film in a week at room temperature (a) and with MIMOSA-V in 10 hours at 4°C (b). [Cac07]	132
A.1	Capture of a invariant cross sections ($E \frac{d\sigma^3}{dp^3}$) table from reference [Bar83]. Measured cross sections for the inclusive processes $pp \rightarrow pX$ and $pA \rightarrow pX$ with momentum p and transversal momentum p_T of the secondary proton are listed. The data was derived with a 100 GeV proton beam on fixed targets at the Fermilab M6E beam line.	139
C.1	Proton beam profiles inside the TRD prototype for the central layer 10 and beam energies of: (a) 20, (b) 40, (c) 60, (d) 80, (e) 100, and (f) 120 GeV.	146
C.2	Proton beam profiles inside the TRD prototype for the central layer 10 and beam energies of: (a) 140, (b) 160, (c) 180, (d) 200, and (e) 250 GeV. The quite narrow beam profile for the 250 GeV data file with a beam angle of 8.3° was not adjusted, since the file with an angle of -1.5° and a wide profile, but low statistics, gave the same result for the rejection power. The deviation of GEANT3 for 180 GeV results from as missing file for a beam angle of -1.5°, instead a beam angle of 7.5° is used.	147
C.3	(top) Energy depositions of protons accumulated for the whole detector on a logarithmic scale. (bottom) Differences between the simulations and the data. For beam energies of: (a) 20, (b) 40, (c) 60 and (d) 80 GeV.	148

C.4	(top) Energy depositions of protons accumulated for the whole detector on a logarithmic scale. (bottom) Differences between the simulations and the data. For beam energies of: (a) 100, (b) 120, (c) 140 and (d) 160 GeV.	149
C.5	(top) Energy depositions of protons accumulated for the whole detector on a logarithmic scale. (bottom) Differences between the simulations and the data. For beam energies of: (a) 180, (b) 200 and (c) 250 GeV.	150
C.6	Landau fit MOP values to the energy depositions accumulated for each layer and the detector (layer number 20) of protons for each prototype layer and beam energies of: (a) 20, (b) 40, (c) 60, (d) 80, (e) 100 and (f) 120 GeV.	151
C.7	Landau fit MOP values to the energy depositions accumulated for each layer and the detector (layer number 20) of protons for each prototype layer and beam energies of: (a) 140, (b) 160, (c) 180, (d) 200 and (e) 250 GeV.	152
C.8	Likelihood distributions for electrons of 20 GeV energy and protons of: (a) 20, (b) 40, (c) 60, (d) 80, (e) 100 and (f) 120 GeV.	153
C.9	Likelihood distributions for electrons of 20 GeV energy and protons of: (a) 140, (b) 160, (c) 180, (d) 200 and (e) 250 GeV.	154
C.10	(top) Energy depositions of protons accumulated for the whole detector on a logarithmic scale. (bottom) Differences between the simulations and the data. For beam energies of: (a) 20, (b) 40, (c) 60, (d) 80 GeV.	155
C.11	(top) Energy depositions of protons accumulated for the whole detector on a logarithmic scale. (bottom) Differences between the simulations and the data. For beam energies of: (a) 100, (b) 120, (c) 140 and (d) 160 GeV.	156
C.12	(top) Energy depositions of protons accumulated for the whole detector on a logarithmic scale. (bottom) Differences between the simulations and the data. For beam energies of: (a) 180, (b) 200 and (c) 250 GeV.	157
C.13	Landau fit MOP values to the energy depositions accumulated for each layer and the detector (layer number 20) of protons for each prototype layer and beam energies of: (a) 20, (b) 40, (c) 60, (d) 80, (e) 100 and (f) 120 GeV.	158
C.14	Landau fit MOP values to the energy depositions accumulated for each layer and the detector (layer number 20) of protons for each prototype layer and beam energies of: (a) 140, (b) 160, (c) 180, (d) 200 and (e) 250 GeV.	159
C.15	Likelihood distributions of electrons with 20 GeV energy and protons with energies of: (a) 20, (b) 40, (c) 60, (d) 80, (e) 100 and (f) 120 GeV.	160
C.16	Likelihood distributions of electrons with 20 GeV energy and protons with energies of: (a) 140, (b) 160, (c) 180, (d) 200 and (e) 250 GeV.	161

List of Tables

4.1	Temperature levels for the crate level ESS.	59
4.2	Time table of the QM2 U-Crate and UPD S9011AU board level ESS tests at CSIST	73
4.3	Time table of the DC/DC-converter vibration and TVT tests	74
4.4	Time table of the QM2 DC/DC-converter ESS tests at CSIST	75
4.5	Time table of the FM/FS DC/DC-converter ESS tests at CSIST	75
5.1	Event numbers recorded for the beamtest in 2000. Suffix k denotes $\times 1000$. . .	78
5.2	List of tested GEANT4 hadronic physics models suitable for an energy range of 20 GeV – 250 GeV including their features and the GEANT3 GHEISHA model.	96
5.3	List of cuts applied for the event selection.	98

Bibliography

- [AFG⁺07] J. Apostolakis, G. Folger, V. Grichine, V. Ivanchneko, M. Kossov, and A. Ribon. Hadronic Shower Shape Studies in Geant4. CERN-LCGAPP-2007-02, 2007.
- [AMS09] AMS-02 collaboration. AMS on ISS, Construction of a particle physics detector on the International Space Station. to be published, 2009.
- [Bar83] D.S. Barton et. al. Experimental study of the A dependency in inclusive hadron fragmentation. *Physical Review D*, Vol 27, No 11, June 1983.
- [Bat02] R. Battiston. Astroparticle Physics in Space with AMS-02. Talk at the 1st Space Part Conference, Elba, May 2002. <http://www.pg.infn.it/spacepart/presentazioni/presentazioni.html>.
- [BH34] H. Bethe and W. Heitler. On the Stopping of Fast Particles and on the Creation of Positive Electrons. *Proceedings of the Royal Society of London. A* Vol. 146, Iss. 856, 83-112, 1934.
- [Bla00] B. Blau et al. Status of AMS02 detectors and the superconducting magnet. *Grav. Cosmol. Suppl.*, 6:168179, 2000.
- [Bla02] B. Blau et al. The superconducting magnet of AMS-02. *Nucl. Phys. Proc. Suppl.*, 113:125132, 2002.
- [Bla04] B. Blau et al. The superconducting magnet system of the Alpha Magnetic Spectrometer AMS-02. *Nucl. Phys. Proc. Suppl.*, 113:125132, 2004.
- [Bor05] K. Borras. Hard diffraction at HERA and the Tevatron. *ACTA PHYSICA POLONICA B*, Vol 36, No 2, 2005.
- [Bov82] C. Bovet et al. The CEDAR Counters for Particle Identification in the SPS secondary Beams: A Description and an operational Manual. Technical report, CERN 82-13, 1982.
- [Brü03] M. Brückel. The Transition Radiation Detector of the AMS-02 Experiment – Development and test of Read-out Electronics. Diploma thesis, IEKP Karlsruhe, 2003.
- [Bu03] M. Buenerd et al. The AMS-02 RICH Imager Prototype In-Beam Tests with 20 GeV/c per Nucleon Ions. In 28th International Cosmic Ray Conference (ICRC). Universal Academy Press Inc., 2003.
- [Cac07] M. Caccia et al. Tritium imaging with a CMOS active pixel detector. September 2007.
- [Cad02] F. Cadoux et al. The AMS-02 electromagnetic calorimeter. *Nucl. Phys. Proc. Suppl.*, 113:159165, 2002.

- [CAE03] CAEN SpA. Technical Information Manual Mod S9056. Rev. 0. Technical report, September 2003.
- [CAE04] CAEN SpA. Technical Information Manual Mod S9011. Rev. 1. Technical report, 2004.
- [Car05] Center for Advanced Research in Space Optics. Carso. Amica - Astro Mapper for Instrument Check of Attitude., 2005. <http://carso.area.trieste.it/>.
- [Cas03] D. Casadei et al. The AMS-02 Time of Flight System. Final Design. In 28th International Cosmic Ray Conference (ICRC). Universal Academy Press Inc., 2003.
- [Cec03] C. Cecchi. The AMS-02 tracker. In 28th International Cosmic Ray Conference (ICRC). Universal Academy Press Inc., 2003.
- [Cec04] C. Cecchi. The silicon tracker of the AMS02 experiment. Nucl. Instrum. Meth., A518:145146, 2004.
- [Cor03] E. Cortina et al. The AMS-02 Tracker Performance. In 28th International Cosmic Ray Conference (ICRC). Universal Academy Press Inc., 2003.
- [Cze01] A. Czermak et al. Data acquisition system for silicon ultra fast cameras. Proc. 7th International Conference on Advanced Technology and Particle Physics, October 2001.
- [dB94] W. de Boer. Grand unified theories and supersymmetry in particle physics and cosmology. Prog. Part. Nucl. Phys., 33:201302, 1994.
- [dB03] W. de Boer. Is dark matter supersymmetric? Talk IETP Winterschool, February 2003. <http://home.cern.ch/~deboerw>.
- [dB08] W. de Boer. Indirect Dark Matter Signals, October 2008. arXiv: 0810.1472v3 [astro-ph].
- [dBHSZ04] W. de Boer, M. Herold, C. Sander, and V. Zhukov. Indirect evidence for neutralinos as dark matter. Eur. Phys. J. C33:s981, 2004. arXiv.org hep-ph/0312037.
- [dBSZ⁺05] W. de Boer, C. Sander, V. Zhukov, A.V. Gladyshev, and D.I. Kazakov. EGRET Excess of Diffuse Galactic Gamma Rays as Tracer of Dark Matter. Astron. Astrophys. 444 51, 2005. arXiv:astro-ph/0508617v1.
- [Dep02] G. Deptuch. New Generation of Monolithic Active Pixel Sensors for Charged Particle Detection. PhD thesis, Universite Louis Pasteur Strassbourg - University of Mining and Metallurgy Cracow, 2002.
- [Dep04] G. Deptuch et. al. Tritium autoradiography with thinned and back-side illuminated monolithic active pixel sensor device. Submitted to Computer Physics Communications, 2004.
- [Doe07] P. Doetinchem. AMS-02 Anticounter. RWTH seminar talk, Bad Honnef, August 2007. <http://www1b.physik.rwth-aachen.de/~kolleg/fileadmin/data/gk/de/badhonnef/2007/vonDoetinchem.pdf>.
- [Dul05] W. Dulinski et al. Tests of a backside illuminated monolithic CMOS pixel sensor in an HPD set-up. Nucl. Instr. and Meth., A(546):274280, 2005.

-
- [Egg04] R. Eggert. Development of a Fuse-Test Backplane for a Multi-Channel Power Supply (UPSFE) within the AMS Project. Master thesis, IEKP Karlsruhe, 2004.
- [ESA00] V. Egoritshev, V. Saveliev, and S. J. Aplin. Particle identification via transition radiation and detectors. Nucl. Instrum. Meth., June 2000.
- [Eve08] J. E. Everett et. al. Astrophys. J. 674, 258, 2008.
- [FGS00] L. Frankfurt, V. Guzey, and M. Strikman. Colour coherent phenomena on nuclei and the QCD evolution equation. J. Phys. G: Nucl. Part. Phys. 27 (2001) R23R68, October 2000.
- [Fol07] G. Folger et al. Reference Physics Lists. Geant4 Online Physics Reference Manual, November 2007. http://geant4.web.cern.ch/geant4/support/proc_mod_catalog/physics_lists/referencePL.shtml.
- [Fop04] S. Fopp. Entwicklung und Bau eines auf Proportionalkammern basierenden Übergangsstrahlungsdetektors für das AMS-02-Weltraumexperiment. PhD thesis, RWTH Aachen, 2004.
- [FS04] F. Ferro and A. Sobol. Simulation of diffractive and non-diffractive processes at the LHC energy with the PYTHIA and PHOJET MC event generators. TOTEM-NOTE, May 2004.
- [Gen03] S. Gentile et al. The Performance of the Transition Radiation Detector of the AMS-02 Experiment. In Nuclear Science Symposium, Portland, Oregon, USA, 2003.
- [Gou95] K. Goulianos. The structure of the Pomeron. RU 95/E-26 (arXiv:hep-ph/9505310v1), May 1995.
- [Gri01] V.M. Grichine. X-ray transition radiation energy loss of relativistic charge in absorbing media. Nucl. Instrum. Meth. A 484 (2002) 573586, August 2001.
- [Gru93] C. Grupen. Teilchendetektoren. BI Wissenschaftsverlag, ISBN 3-411-16571-5, 1993.
- [GS04] V.M. Grichine and S.S. Sadilov. Geant4 models for X-ray transition radiation. Nucl. Instrum. Meth. A 522 122125, 2004.
- [GS06] V.M. Grichine and S.S. Sadilov. GEANT4 X-ray transition radiation package. Nucl. Instrum. Meth. A 563 (2006) 299302, March 2006.
- [GW05] V. Grichin and D.H. Wright. Photoabsorption Ionization Model. Geant4 Online Physics Reference Manual, 2005. <http://geant4.web.cern.ch/geant4/UserDocumentation/UsersGuides/PhysicsReferenceManual/html/node41.html>.
- [Haa04] D. Haas. The Silicon Tracker of AMS02. Nucl. Instrum. Meth., A530:173177, 2004.
- [Ham01] T. Hams et al. $^{10}\text{Be}/^{9}\text{Be}$ ratio up to 1.0 GeV/nucleon measured in the ISOMAX 98 balloon flight. In Proc. of the 27th ICRC, Hamburg, volume 5, page 1655, 2001.
- [Ham04] T. Hams et al. Measurement of the abundance of radioactive Be-10 and other light isotopes in cosmic radiation up to 2-GeV/nucleon with the balloon-borne instrument ISOMAX. Astrophys. J., 611:892905, 2004.

- [Hau05] F. Hauler. Development of the Space Qualified Data Acquisition for the Transition Radiation Detector of the AMS-02 Experiment on the International Space Station. PhD thesis, IEKP Karlsruhe, December 2005.
- [Hei54] W. Heitler. The Quantum Theory of Radiation. Clarendon Press., 1954.
- [Jun05] L. Jungermann. Space-Qualified Electronics for the AMS02 Experiment and Medical Radiation Imaging. PhD thesis, IEKP Karlsruhe, May 2005.
- [Kir04] T. Kirn et al. Status of the AMS-TRD-Straw Modules. Nucl. Instrum. Methods., A522:6972, 2004.
- [KS04] T. Kirn and T. Siedenburger et al. The AMS-02 Transition Radiation Detector. In 10th Vienna Conference on Instrumentation, Austria, 2004.
- [Mon03] B. Monreal et al. Gas Slow Control System for AMS-02 Transition Radiation Detector on ISS. Poster, presented on the Nuclear Science Symposium, Portland, Oregon, USA, 2003.
- [NAS05] National Aeronautics and Space Administration, NASA. Introduction to Liquid Helium in Space, May 2005. <http://cryowwwwebber.gsfc.nasa.gov/introduction/heliumspace.html>.
- [NIS] National Institut of Standards and Technology, NIST. Online Data Base. <http://physics.NIST.gov/PhysRefData/contents.html>.
- [Orb03] J. Orboeck. The final 20-Layer-Prototype for the AMS Transition Radiation Detector: Beamtests, Data-Analysis, MC-Studies. PhD thesis, RWTH Aachen, May 2003.
- [PDG02] K. Hagiwara et al., Particle Data Group, PDG. Review of Particle Physics. Physical Review Letters, 2002.
- [Sab08] A. Sabellek. The Space Qualified Data Acquisition for the Transition Radiation Detector of the AMS-02 Experiment on the international Space Station. PhD thesis, IEKP Karlsruhe, December 2008.
- [Sch83] M. Schmelling. MINT - A Simple Model for Low Energy Hadronic Interactions. Talk, June 1983.
- [Sch07] M. Schmanau. AMS TRD Power Distribution Box, V1.9. AMS-02 assembly procedure document, April 2007. http://www-ekp.physik.uni-karlsruhe.de/~amswww/downloads/assembly_docs/UPD_Assemblyv01.9.pdf.
- [Sie02] T. Siedenburger et al. A Transition Radiation Detector For AMS. Nucl. Phys. Proc. Suppl., 113:154158, 2002.
- [Spe03] D. N. Spergel et al. First Year Wilkinson Microwave Anisotropy Probe (WMAP) Observations: Determination of Cosmological Parameters. Astrophys. J. Suppl., 148:175, 2003.
- [VB02] E. Predazzi V. Barone. High-Energy Particle Diffraction. Springer-Verlag, ISBN 3-540-42107-6, 2002.
- [VGB⁺84] P. Venkataramaiah, K. Gopala, A. Basavaraju, S. S. Suryanarayana, and H. Sanjeeviah. A simple relation for the Fermi function. J. Phys. G: Nucl. Part. Phys. 11 (1985) 359364, September 1984.

- [WM02a] D.H. Wright and M. Maire. Compton scattering. Geant4 Online Physics Reference Manual, 2002. <http://geant4.web.cern.ch/geant4/UserDocumentation/UsersGuides/PhysicsReferenceManual/html/node27.html>.
- [WM02b] D.H. Wright and M. Maire. e^+e^- Annihilation. Geant4 Online Physics Reference Manual, 2002. <http://geant4.web.cern.ch/geant4/UserDocumentation/UsersGuides/PhysicsReferenceManual/html/node46.html>.
- [ZKC⁺00] H. Zhu, J. F. Klemic, S. Chang, P. Bertone, A. Casamayor, K. G. Klemic, D. Smith, M. Gerstein, M. A. Reed, and M. Snyder. Analysis of yeast protein kinases using protein. *Nature Genetics*, Vol 26, November 2000.

